Innovative Self-assembling Nanodelivery Systems to Combat Bacterial Infections

by

Mohammed Abdeen Mohammed Salih

(M. Pharm, National Ribat University, Sudan)

Submitted as fulfilment of the requirements for the degree of Doctor of Philosophy in Pharmaceutics at the Discipline of Pharmaceutical Sciences of the School of Health Sciences at the University of KwaZulu-Natal

Supervisor: Professor Thirumala Govender
(PhD, University of Nottingham, United Kingdom)

Date submitted: 23 July, 2020

“The ultimate pursuit of learning is to be able to ask better questions. The one who is able to do so, will equip himself to explore the answers”

-Ahmed Salem-

"***This thesis is dedicated to my beloved parents and family for their endless love, support and encouragement.”***

Declaration 1-Plagiarism

I, Mr. Mohammed Abdeen Mohammed Salih, declare that

1. The research data reported in this thesis, except where otherwise indicated is my own original work.
2. This thesis has not been submitted for any degree or examination at any other university.
3. This thesis does not contain data, pictures, graphs, or other information belonging to other people, unless specifically acknowledged as being sourced from other people.
4. This thesis does not contain any other person's writing, unless specifically acknowledged as being sources from other researchers. Where other written sources have been quoted, then:
    a. Their words have been rephrased but the general information attributed to them has been referenced;
    b. Where their exact words have been used, their writing has been placed inside quotation marks, and referenced.
5. Where I have reproduced a publication of which I am an author, co-author, or editor, I have indicated in detail which part of the publication was written by myself alone and have fully referenced such publications.
6. This dissertation does not contain any graphics, text or tables copied from the internet, unless specifically acknowledged, and the source being detailed in the reference sections of the dissertation.

Signed:  Date: **23 July 2020**

I, Professor Thirumala Govender as supervisor of the Ph.D. studies hereby consent to the submission of this Ph.D. thesis.

Signed: 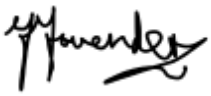 Date: **23 July 2020**

Declaration 2-Publications

Mr. Mohammed Salih contributed to the literature search and evaluations, conceptualization, design of the projects, modification, optimization of methods, preparation, characterization in terms of synthesis and structural elucidation techniques such as Fourier-transform infrared (FT-IR) spectroscopy, Proton and ^{13}Carbon nuclear magnetic resonance spectroscopy (^{1}H NMR and C^{13} NMR), 2D Nuclear Overhauser Effect measurements (NOESY spectrum), and the bio-safety of all the materials synthesized for the studies in this thesis. He also contributed to the formulation and characterization of the nano-based drug delivery system that was formulated from the synthesized materials in terms of particle size, polydispersity index, zeta potential, surface morphology, entrapment efficiency, *in vitro* drug release, differential scanning calorimetry (DSC), protein binding with Microscale Thermophoresis (MST) technique, *in vitro* and *in vivo* antimicrobial activity, the mathematical modeling in terms of the *in vitro* release kinetics data and stability studies and molecular dynamics (MD) simulations studies. Mr. Mohammed Salih also wrote the first drafts of all the first authored papers and undertook all revisions. Dr. Mr. C.A Omolo assisted with the inception, overall design of the project, solving any technical problems and supervision of the studies. Dr. Nikita Devnarain assisted in performing the cytotoxicity studies of the synthesized materials, assisted by performing MD simulation studies and proof reading of manuscripts and thesis chapters. Dr. Ayman Y. Waddad assisted in the characterization of the synthesized materials and proofreading of manuscripts. Dr. Pavan Walvekar assisted in the synthesis of the PEGylated fusidic acid and formulation. Dr. C. Mocktar supervised the *in vitro* and *in vivo* antibacterial activity studies. Prof. T. Govender served as supervisor and was responsible for project conceptualization, problem-solving, editing of papers and abstracts as well as general supervision of all studies.

Research output from the dissertation

1. First authored Publications

The following research papers were published as results generated from specific objectives from this study and they include:

- Salih M, Omolo CA, Agrawal N, Walvekar P, Waddad A.Y, Mocktar C, Ramdhin C, Govender T. 2020. Supramolecular amphiphiles of Beta-cyclodextrin and Oleylamine for enhancement of vancomycin delivery. International Journal of Pharmaceutics. 574:118881. (Impact factor = 4.320). DOI: 10.1016/j.ijpharm.2019.118881.

- Salih, M., Omolo, C. A., Devnarain, N., Elrashedy, A. A., Mocktar, C., Soliman, M. E. S., & Govender, T. (2020). Supramolecular Self-Assembled Drug Delivery System (SADDs) of Vancomycin and Tocopherol Succinate as an Antibacterial Agent: In vitro, In silico and In vivo Evaluations. Pharmaceutical Development and Technology. (Impact factor 2.374) doi:10.1080/10837450.2020.1797786
- Salih M, Walvekar P, Omolo CA, Elrashedy A. A, Devnarain N, Waddad A.Y, Fasiku V, Mocktar C, Govender T. A Self-Assembled Polymer Therapeutic for Simultaneously Enhancing Solubility and Antimicrobial Activity and Lowering Serum Albumin Binding of Fusidic acid. Journal of Biomolecular Structure & Dynamics (Impact Factor 3.22) (manuscript ID: TBSD-2020-1529). (In Press).

2. Conference Presentations

The following local and international conference presentations were produced from the data generated during the doctoral study:

- **Salih M**, Omolo CA, Agrawal N, Walvekar P, Waddad A.Y, Mocktar C, Ramdhin C, Govender T. 2020. Supramolecular amphiphiles of Beta-cyclodextrin and Oleylamine for enhancement of vancomycin delivery. UKZN Nanotechnology Platform Symposium, 9th October 2018, Durban, South Africa (**Poster Presentation**).
- **Salih M**, Omolo CA, Agrawal N, Walvekar P, Waddad A.Y, Mocktar C, Ramdhin C, Govender T. 2020. Supramolecular amphiphiles of Beta-cyclodextrin and Oleylamine for enhancement of vancomycin delivery. ICONAN 2019, 16-18 October 2019, Munich, Germany (**Poster Presentation**).
- **Salih M**, Omolo CA, Devnarain N, Elrashedy A. A, Mocktar C, Mahmoud E. S. Soliman M. E, Govender T. Supramolecular Self-Assembled Drug Delivery System (SADDs) of Vancomycin and Tocopherol Succinate as an Antibacterial Agent: *in vitro*, *in silico* and *in vivo* Evaluations. College of Health Sciences Annual Research Symposium, University of KwaZulu Natal, 1st November 2019 Durban, South Africa. (**Oral presentation**).

3. Co-authored publications

The following are co-authored publications related to the studies on the synthesis of advanced materials for combating antimicrobial resistance.

- Walvekar P, Gannimani R, Salih M, Makhathini S, Mocktar C, Govender T. Self-assembled oleyl amine grafted hyaluronic acid polymersomes for delivery of vancomycin against methicillin-resistant Staphylococcus aureus (MRSA). *Colloids and Surfaces B: Biointerfaces*. 2019 Oct 1;182:110388. (Impact Factor = 3.973) DOI: 10.1016/j.colsurfb.2019.110388.

- Nikita Devnarain, Nawras Osman, Victoria Fasiku, Sifiso Makathini, Mohammed Salih, Usri Ibrahim and Thirumala Govender. (2020). Intrinsic Stimuli-Responsive Nanocarriers for Smart Drug Delivery of Antibacterial Agents – An In-Depth Review of the Last Two Decades. *WIREs Nanomedicine & Nanobiotechnology*. Manuscript ID: NANOMED-651. (Impact Factor = 7.689) (In press).

Abstract

The rising surge of bacterial resistance puts an immense economic and social strain on the healthcare system worldwide. Unfortunately, the production of new antibiotics is significantly outstripped by existing therapies that are losing their effectiveness. Limitations associated with conventional dosage forms are one of the main contributing factors for increasing antimicrobial resistance. Novel nano-drug delivery systems have immense potential for overcoming antimicrobial resistance. This study broadly aimed to design advanced materials and explore nano-based strategies for preparation of self-assembling delivery systems to combat *Staphylococcus aureus* (*S. aureus*) and methicillin-resistant *Staphylococcus aureus* (MRSA) infections. In this study, three novel self-assembling systems; supramolecular amphiphilic Beta-cyclodextrin and Oleyl amine (BCD-OLA), supramolecular self-assembled drug delivery system (SADDs) for enhancement of vancomycin (VCM) delivery, and self-assembling PEGylated Fusidic acid (PEG-FA) as a polymer therapeutic were designed, synthesized and employed for the formulation of nano-drug delivery systems for efficient delivery of antibiotics. All the newly synthesized systems were confirmed and characterized by FTIR, DSC, NMR and molecular dynamic (MD) simulations. The synthesized materials and the formulated delivery system were found to be biosafe after exhibiting cell viability above 75% in all human cell lines tested using the MTT assay. The formulated nano-based systems were evaluated for sizes, polydispersity indices (PDI), zeta potential (ZP), surface morphology, drug release, *in vitro* and *in vivo* antibacterial activity. The formulated BCD-OLA nanovesicles size was shown to be 119.8 ± 1.12 nm with a PDI of 0.220 ± 3.98, and ZP of 25.8 ± 6.96 mV. The formulated SADDs for VCM delivery displayed a size of 85.15 ± 0.4 nm with PDI of 0.131 ± 0.017 and ZP of -27 ± 1.3 mV. The encapsulation efficiency of VCM in both formulated BCD-OLA and VCM/TS nano-system was 40.2 ± 4.5% and 68.8 ± 2.8%, respectively. The release profile of the encapsulated drug from both systems was found to have sustained release over a 48 h period. The self-assembled PEG-FA conjugate showed an average hydrodynamic diameter of 149.3 ± 0.21 nm with PDI of 0.267 ± 0.012 and ZP of 5.97 ± 1.03 mV. HRTEM images revealed vesicular structure for supramolecular BCD-OLA, and a homogenous spherical morphology for formulated VCM/TS and PEG-FA nanoparticels (NPs). *In vitro* antibacterial activity for the BCD-OLA nanovesicles, VCM/TS NPs and PEG-FA (NPs) showed enhancement in antibacterial activity by 2- to 4-fold reduction in MIC against *S. aureus* and MRSA when compared to the bare drug. Further intracellular and macrophage studies showed that VCM-

loaded BCD-OLA nanovesicles had an 8- and 459-fold reduction of intracellular bacteria compared to the bare drug, respectively. There was a 9.5-fold reduction in the MRSA load in mice skin treated with VCM/TS NPs in comparison with bare VCM (p = 0.0077). Human serum albumin (HSA) binding studies using *in silico* molecular docking and Microscale Thermophoresis showed that PEG-FA had very weak or no interaction with HSA (K_d = 14999 μM), which could prevent bilirubin displacement and reduce side effects. In summary, these novel nano-drug delivery systems show potential for improving the treatment of bacterial infections, which will be useful for addressing the crisis of resistant bacteria and declining new antibiotics. The data from this study has resulted in three first-authored international publications.

Acknowledgments

Firstly, I would like to express my sincere gratitude to Prof. Thirumala Govender, my supervisor, for her continued support during my Ph.D. Her encouragement, inspiration, persistence and enormous expertise enabled me to write the articles and this thesis at all times of the study. I couldn't have imagined a better supervisor and mentor for my doctoral studies.

Thank you to Dr. Chunderika Mocktar for her caring support, advice, creative criticism, and approachable nature that has allowed me to learn valuable lab techniques and skills in general from her. Her motivation, assistance, support, and guidance throughout the project has been of great importance and I'm grateful for that.

Special thanks go to my mentor and previous colleague Dr. Calvin Omolo for his assistance in the design of these projects as well as his continued guidance and motivation. Also, great thanks to my post-doctoral mentors Dr. Ayman Waddad, and Dr. Nikita Devnarain. I will forever be indebted to them, for being with me every step of the way, helping me tackle any problem encountered along the way and instilling invaluable skills that will be crucial in my career ahead.

Special mention goes to my colleagues, Mr. Sifiso Makhatini, Dr. Pavan Walvekar, Dr. Ruma Maji, Dr Andile Mbuso Faya, Ms. Nawras Abdelmoniem, Ms.Victoria Fasiku, Dr. Daniel Hassan, Melissa Ramtahal and Leslie Murugan for all their support, technical assistance in the lab and life-long friendship.

My sincere thanks go to all the organizations that gave me their indispensable generous resources, including the UKZN Nanotechnology Platform and the College of Health Sciences at UKZN. Without their support, facilities and financial help, it would not have been possible for me to pursue and to complete this Ph.D project successfully. My appreciation goes to the Electron Microscope Unit, and Biomedical Resource Unit at UKZN for their technical support.

Thank you to my parents, family and friends, for their complete support and motivation throughout my studies. You have molded me into the person that I am today, and I will continue to pursue my dreams and I hope to make you proud. Thank you for always believing in me and pushing me for greatness. Last but not least I give my thanks to the Almighty ALLAH for the gift of life, wisdom, grit, perseverance, health and humility as I travelled this journey.

Table of Contents

Declaration 1 – Plagiarism i
Declaration 2 –Publications ii
Research output from the dissertation ii
Abstract v
Acknowledgements vii
List of Abbreviations.....x
List of Figures and Tables.....xii
CHAPTER 1, INTRODUCTION 1
1.1 Introduction 1
1.2 Background 1
1.3 Problem statement 9
1.4 Aims and objectives of this study 10
1.5 Novelty of the study 12
1.6 Significance of the study 13
1.7 Overview of dissertation 14
1.8 References……...…...16
CHAPTER TWO: EXPERIMENTAL PAPER ONE
2.1 Introduction.....24
2.2 Graphical Abstract..... 25
2.3 Published Manuscript.....26
2.4 Abstract 26
2.5 Materials, Instrumentation and Methods.....27

2.6 Results and Discussion 30
2.7 Conclusions.....39
2.8 References……..……..40
CHAPTER THREE: EXPERIMENTAL PAPER TWO
3.1 Introduction.....43
3.2 Graphical Abstract.....44
3.3 Published Manuscript.....45
3.4 Abstract 46
3.6 Materials and Methods.....49
3.7 Results and Discussion.....57
3.8 Conclusion 76
3.9 References.....77
CHAPTER FOUR: EXPERIMENTAL PAPER THREE
4.1 Introduction.....86
4.2 Graphical Abstract.....87
4.3 Accepted Manuscript.....88
4.4 Abstract 89
4.6 Materials and Methods.....92
4.7 Results and Discussion.....100
4.8 Conclusion 114
4.9 References.....115
CHAPTER 5, CO-AUTHORED PAPERS
5.1 Introduction 122
5.2 Published co-authored paper 1 123
5.2.1 Abstract 123
5.3 Published co-authored paper 2 124
5.3.1 Abstract 124
CHAPTER 6, CONCLUSION
6.1 General conclusions 126

6.2 Significance of the findings in the study 128
6.3 Recommendations for future studies 130
6.4 Conclusion 131
Appendix I 133
Appendix II 135
Appendix III 140
Appendix IV 144
Appendix V 154
Appendix VI 155

List of Abbreviations

^{1}H NMR	Proton Nuclear Magnetic Resonance	MHB	Mueller-Hinton Broth
^{13}C NMR	Carbon 13 Nuclear Magnetic Resonance	MHD	Mean Hydrodynamic Diameter
6-AHA	6-Aminohexanoic Acid	MIC	Minimum Inhibitory Concentration
A-549	Adenocarcinoma Human Alveolar Epithelial	MRSA	Methicillin-Resistant *Staphylococcus Aureus*
BCD	Beta-Cyclodextrin	MST	Microscale Thermophoresis
BOC	Di-Tert-Butyldicarbonate	MTT	3-(4,5-Dimethylthiazol-2-Yl)-2,5-Diphenyltetrazolium Bromide
CDC	Centers for Disease Control and Prevention	NCEs	New Chemical Entities
CDs	Cyclodextrins	NOESY	2D Nuclear Over-Hauser Effect Measurements Spectrum
CFUs	Colony Forming Units	NPs	Nanoparticles
CHPC	Centre For High Performance Computing	OLA	Oleyl Amine
DCC	N,N'-Dicyclohexylcarbodiimide	PBS	Phosphate Buffer Saline
DCM	Dichloromethane	PDI	Polydispersity Index
DDS	Drug Delivery Systems	PEG	Polyethylene Glycol
DL	Drug Loading	PI	Propidium Iodide
DLC	Drug Loading Capacity	PME	Particle Mesh Ewald
DLS	Dynamic Light Scattering	Ps	Picoseconds
DMSO	Dimethyl Sulfoxide	R^2	Correlation Coefficient
DSC	Differential Scanning Calorimetry	RBC	Red Blood Cell
DMAP	P-Dimethylaminopyridine	RMSE	Root Means Square Error
EE	Encapsulation Efficiency	RMSF	Root-Mean-Square Fluctuation
EUCAST	European Committee of Antimicrobial Susceptibility Testing	RT	Room Temperature
FA	Fusidic Acid	SADDs	Self-Assembled Drug Delivery System
FACS	Fluorescence-Activated Cell Sorting	SA	*Staphylococcus Aureus*
FBS	Fetal Bovine Serum	SDS	Sodium Dodecyl Sulphate
FT-IR	Fourier Transform-Infrared	SCVs	Small Colony Variants
HEK-293	Human Embryonic Kidney Cells	TEM	Transmission Electron Microscopy.
HeLa	Human Cervical Cancer Cells	THP-1	Human Myelomonocytic Cell Line
HSA	Human Serum Albumin	TFA	Trifluoroacetic Acid
HRTEM	High Resolution Transmission Electron Microscope	TTC	Tetracycline

IR	Infrared	TS	D-α-tocopherol Succinate
MCF-7	Liver Hepatocellular Carcinoma Cell Lines.	VCM	Vancomycin
MD	Molecular Dynamics	Vdw	Van Der Waals Force
MFS	Facilitator Super Family.	WHO	World Health Organization
MHA	Mueller-Hinton Agar	ZP	Zeta Potential

List of Figures and Tables

NUMBER	TITLE	PAGE
CHAPTER ONE: Introduction (Figures)		
Figure 1	Timeline for the history of antibiotics, year of discovery and year of introduction to the market.	**2**
Figure 2	Death from AMR infections and other causes in 2050	**3**
Figure 3	Novel FDA-approved antibacterial and non-bacterial drugs	**5**
CHAPTER TWO: Experimental Paper 1 (Figures)		
Figure 1	Proposed mechanism for the formation of the amphiphile via inclusion complexation.	**30**
Figure 2	FT-IR of OLA (A), BCD (B) and BCD-OLA (C).	**31**
Figure 3	Schematic representation of BCD showing the inner and outer proton orientation.	**31**
Figure 4	^{1}H NMR (400 MHz) spectra in D_2O at 300 K of OLA, BCD and BCD-OLA complex.	**32**
Figure 5	2D NOESY spectrum (400 MHz) in D_2O at 300 K of BCD-OLA complex.	**33**
Figure 6	The two possible orientations of OLA in the BCD cavity.	**34**
Figure 7	Job's plot using differences in absorbance for the determination of BCD-OLA complex stoichiometry.	**34**
Figure 8	Representative images from OLA and BCD simulation A) t= 0 ns. B) t = 12.7 ns. C) t = 42.6 ns. D) t = 100 ns.	**34**
Figure 9	A) Time evolution of COM distance between BCD and OLA. B) Time evolution of interaction energy between BCD and OLA and its components.	**35**
Figure 10	A-D) Representative image of self-assembly simulation at different time points E) Time evolution of number aggregates formed during simulation.	**35**
Figure 11	MTT assay for evaluation of cytotoxicity of BCD-OLA against A549, HEK 293 and Hela cell lines.	**35**

Figure 12	Morphology of non-drug loaded BCD-OLA nanovesicles (A and B), VCM loaded nanovesicles (C and D) and histogram showing size distribution by intensity (C).	**36**
Figure 13	DSC thermogram of BCD, OLA and BCD-OLA (A) and VCM, BCD-OLA, physical mixture and freeze-dried formula (B).	**36**
Figure 14	Cumulative release profile of VCM and BCD-OLA/VCM	**36**
Figure 15	HRTEM for MRSA; untreated (A1 and A2), VCM treated (B1 and B2) and BCD-OLA/VCM treated (C2 and C2)	**38**
Figure 16	Dot plot and histogram from the flow cytometry analysis A) untreated MRSA (live cells); B, C and D represents percentage dead cells in the MRSA population after incubation with VCM at (7.81µg/mL), VCM at its MIC (31.25 µg/mL) and VCM loaded BCD-OLA nanovesicles at its MIC (7.81 µg/mL), respectively.	**39**
Figure 17	Bacterial killing kinetics of 5x MIC of BCD-OLA nanovesicles and VCM against MRSA. Sample treated with sterile water were used as control. The results are given as means SD (n = 3; data without error bars indicate that the SD is too small to be seen).	**39**
Figure 18	Intracellular MRSA CFU recovered after treating infected (HEK 293) cells. *** denotes statistical significance for BCD-OLA 5x MIC versus untreated control MRSA, *denotes significant difference between BCD-OLA 1 MIC versus bare VCM 1MIC and control MRSA. while for infected Macrophage (THP-1) ****denotes significant difference between BCD-OLA 5 MIC versus control MRSA, *** denotes statistical significance for BCD-OLA 1 MIC versus control MRSA and **denotes significant difference between BCD-OLA 1 MIC versus bare VCM 1 MIC.	**40**
CHAPTER TWO: Experimental Paper 1 (Tables)		
Table 1	Size, PDI, ZP, EE% and DL% for the different ratio of BCD-OLA used in formulation with VCM. The values are expressed as mean ± SD (n = 3).	**35**
Table 2	MIC values for bare VCN, BCD-OLA/VCM and BCD-OLA.	**36**
Table 3	Stability study on BCD-OLA nanovesicles over three months at 4°C	**40**

	and RT. All the samples were studied in triplicate and the data were presented as mean ± SD (n = 3).	
CHAPTER THREE: Experimental Paper 2 (Figures)		
Figure 1	Morphology of VCM/TS NPs from HRTEM and histogram for sample measurement showing size distribution measured via DLS.	**59**
Figure 2	A: Effect of DMEM containing 10 % FBS on particle size distribution measured by intensity for VCM/TS NPs. Figure B and C: Effect of storage time at RT over one month on size and charge, respectively.	**60**
Figure 3	Molecular visualization of interaction between VCM and three TS molecules TS 1, TS 2 and TS 3.	**61**
Figure 4	a-d: Representative image of self-assembly simulation at different time intervals.	**62**
Figure 5	MTT assay for evaluation of cytotoxicity of VCM/TS against A549, HEK 293 and MCF-7 cell lines.	**63**
Figure 6	RBCs exposed to varying concentration of VCM/TS NPs and centrifuged.	**64**
Figure 7	FT-IR spectrum of VCM, TS and VCM/TS NPs.	**64**
Figure 8	DSC thermogram of (A) TS, (B) VCM, (C) physical mixture of VCM/TS and (D) freeze-dried VCM/TS NPs.	**65**
Figure 9	Cumulative release profile of VCM from VCM solution and VCM/TS NPs.	**67**
Figure 10	The potential hydrophobic binding sites on NorA and NorB, identified by MetaPocket, with corresponding binding site amino acid residues.	**69**
Figure 11	Docking poses of TS bound to binding pockets of NorA (left) and NorB (right) with best binding affinities.	**70**
Figure 12	Time evolution of the simulation of TS bound to NorA (green) and NorB (maroon), and the root-mean-square fluctuation of the 100ns simulation of TS bound to NorA and NorB.	**71**
Figure 13	Thermodynamic energy calculations and per-residue energy decomposition analysis of TS binding to NorA and NorB. **A, F.** Residue-ligand interaction diagram of TS forming hydrophobic	**73**

	interactions and hydrogens bond with NorA and NorB amino acid residues, respectively. **B, D.** Thermodynamic energy calculations of binding site residues of NorA and NorB, respectively. **C, E.** Per-residue energy decomposition analysis of TS bound to NorA and NorB, respectively.	
Figure 14	Images from fluorescence microscopy for MRSA biofilms represent the untreated (A1 and A2), VCM-treated (B1 and B2) and VCM/TS NPs-treated (C1 and C2) biofilm. Live cells are stained with green and dead cells in red.	**75**
Figure 15	Evaluation of MRSA burden post 48 hr treatment. **denotes significant difference for VCM/TS NPs versus bare VCM. ***denotes significant difference between untreated versus bare VCM and also denotes a significant difference between untreated and VCM/TS NPs. Data are represented as means ± SD (n = 3).	**76**
CHAPTER THREE: Experimental Paper 2 (Tables)		
Table 1	Size, PDI, ZP, EE % and DL % for the different molar ratios of TS used in formulation with VCM. The values are expressed as mean ± SD, (n=3).	**58**
Table 2	The binding energies (kcal/mol) for the VCM/TS computed from MD trajectories.	**61**
Table 3	Drug release kinetics data for VCM/TS NPs.	**67**
Table 4	MIC values for bare VCM, VCM/TS NPs and TS.	**68**
CHAPTER FOUR: Experimental Paper 3 (Figures)		
Scheme 1.	Synthesis of PEG-FA. I) Methanol, room temperature, 24 h; II) EDC, DMAP, DCM, room temperature, 24 h; III) TFA, DCM, room temperature, 2 h; IV) EDC, DMAP, DCM, room temperature, 24 h.	**93**
Figure 1	The 3-D crystal structure of human serum albumin (PDB code: 2VUE).	**98**
Figure 2	DSC thermogram of **A)** 6AHA, PEG and PEG-6AHA. **B)** PEG-6AHA, FA and PEG-FA.	**102**
Figure 3	^{1}H-NMR spectra of FA, PEG-6AHA, and PEG-FA in $CDCl_3$	**102**
Figure 4	The solubility of FA and PEG-FA in water (n=3).	**103**

Figure 5	MTT assay for evaluation of cytotoxicity of A) PEG-FA and B) FA, against HeLa, HEK 293 and MCF-7 cell lines.	**104**
Figure 6	Haemolysis assay of FA and PEG-FA A) Images of RBCs treated with FA and PEG-FA at various concentrations. B) % of haemolysis after exposure to various concentrations of FA and PEG-FA. Data are expressed as mean ± SD, n=3.	**105**
Figure 7	A) Morphology of the self-assembled PEG-FA conjugate from HRTEM. B) Histogram for sample measurement showing size distribution measured via DLS.	**106**
Figure 8	Representation of the self-assembly of PEG-FA conjugates via MD simulation at a different time points (t).	**108**
Figure 9	Molecular visualization of bilirubin, FA and 2-PEG-FA at the sub-domain IB of HSA [A1], [B1] and [C1], respectively. Inter-molecular interactions between bilirubin, FA and 2-PEG-FA with sub-domain IB of HSA are shown in [A2], [B2] and [C2], respectively.	**110**
Figure 10	Structural orientation of the 7-PEG-FA at the sub-domain IB of HSA showing the unfavorable binding site.	**111**
Figure 11	**A)** The plot of the normalized fluorescence F_{norm} (%) vs. the concentration of FA, bilirubin, and PEG-FA from MST experiments. Data were derived from the T-Jump signal. Lines represent fits of the data points using the K_d model. **B)** Quantitative comparison of the different ligands shown in (A) to the HSA in fraction bound, (n=3).	**113**
CHAPTER FOUR: Experimental Paper 3 (Tables)		
Table 1	Haemolysis (%) for different concentrations of FA and PEG-FA, PBS (pH 7.4) and distilled water	**105**
Table 2	The binding energies (kcal/mol) of PEG-FA conjugates computed from the MD trajectories.	**107**
Table 3	Binding affinity parameters of FA, bilirubin and PEG-FA with HSA protein.	**112**
Table 4	The effect of HSA on self-assembled PEA-FA conjugate after incubation.	**113**
Table 5	MIC values for bare FA and PEG-FA.	**114**

CHAPTER 1

INTRODUCTION

1.1 Introduction

This chapter provides a brief background to the study which incorporates the current status of infectious diseases and various limitations associated with current antibiotic therapy. Furthermore, it emphasizes the role of nano-drug delivery systems in the advancement of antibiotic therapy and provides the aims, objectives, novelty and significance of the study.

1.2 Background

For decades before the discovery of antimicrobial agents, pathogenic microorganisms such as bacteria, viruses, fungi and parasites posed a significant threat to global health, resulting in the development of numerous life threatening diseases [1]. These microorganisms have the potential to spread disease directly or indirectly and from one person to another [2]. In addition to being a cause of mortality, infectious diseases also contribute greatly to opportunistic infections in immunocompromised people, which further increases the mortality rates [3, 4]. The rapid evolution of infectious diseases globally in both nosocomial and community settings has created an urgent need for newer effective therapeutic interventions in both developed and developing countries [5]. This evolution has also posed a threat to global trade, population growth and further escalated the disease burden in developing countries [6, 7]. Amongst various infectious diseases, bacterial infections have risen to be of global concern because of their significantly high numbers and severity [8]. Therefore, various novel strategies to circumvent the spread of infectious diseases are required.

The first drug used in hospital, now call an antibiotic was initially known as pyocyanase, derived from *Pseudomonas aeruginosa* (*P. aeruginosa*) and prepared by Emmerich and Löw in 1899 (formerly *Bacillus pycyaneus*) [9]. However, the treatment was eventually banned from use due to inconsistency and toxicity of the preparation to humans. Further investigations confirmed the production of antibiotic substances from *P. aeruginosa* [10]. Decades later, on September 3rd , 1928, a serendipitous event occurred, which led to the discovery of penicillin by Alexander Fleming (1929) [11]. This breakthrough was considered a landmark in human progress, as it saved millions of lives and significantly contributed to the control of infectious diseases, as they were the leading cause of human morbidity and

mortality for much of human history. The continued work of succeeding researchers resulted in the production of several new antibiotics, some of which had gone up to the patient's bedside. The era between the 1950s and 1970s was indeed the golden age of discovery of new classes of antibiotics [9] (**Figure 1)**. However, Fleming himself was among the first researchers who cautioned about the potential resistance to penicillin by bacteria if usage is abused during treatment [9, 12].

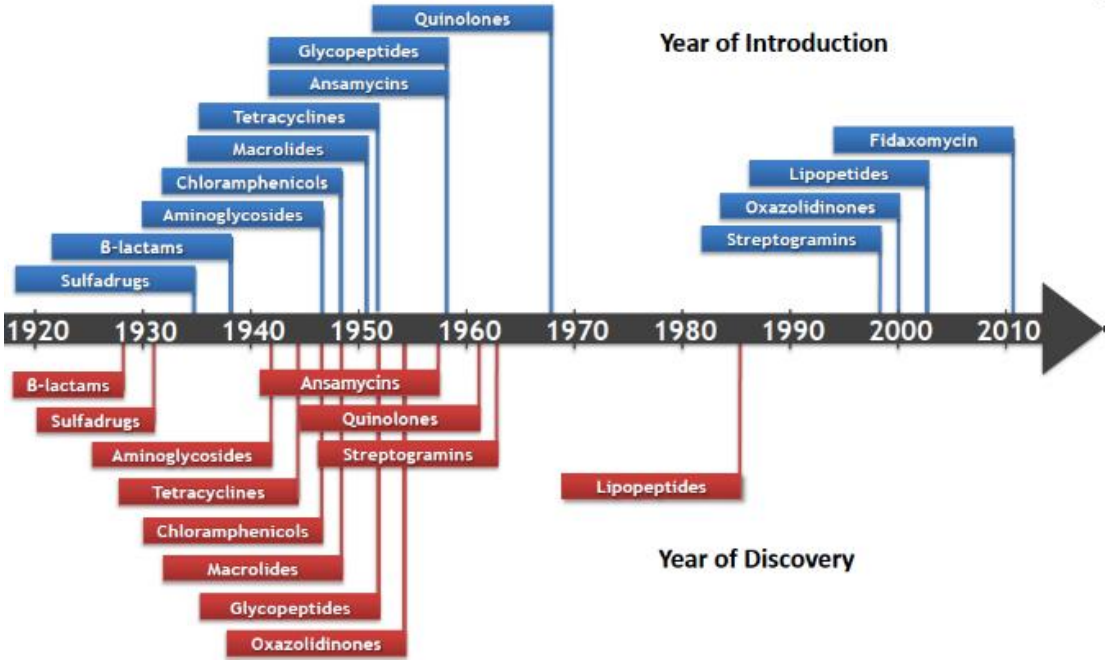

Figure 1. Timeline for the history of antibiotics, year of discovery and year of introduction to the market [13].

Antimicrobial resistance is not new, but the number of resistant species, the geographical locations affected by drug resistance and the level of resistance in single species is unprecedented and growing [14]. Currently, multidrug-resistant (MDR) bacteria continue to be extremely challenging in community health care [15]. Bacteria have developed various ways by which they gain resistance to antimicrobials. Among those mechanisms are enzyme inactivation, decreased cell permeability, target protection, increased efflux due to over-expression of efflux pumps, target overproduction and altered target site/enzyme [16, 17]. The statistics of infections produced by such resistant strains are growing globally. Recent statistics showed an estimated 700,000 annual death rate worldwide [18]. Additionally, in 2019, bacterial resistance led to 2.8 million severe illnesses cases and 35,000 deaths in the United States, which is significantly higher than the previous report in 2013. Over half the world's population is projected to be at risk of infectious diseases, causing a disproportionate

disease burden [8]. The World Health Organization (WHO) has declared antimicrobial resistance (AMR) as one of the thirteen most urgent health challenges for the next decade [19]. Additionally, they estimated that by 2050, antibiotic resistance would result in approximately 10 million deaths, causing nearly $100 trillion global economic loss (**Figure 2**) [20]. The challenge of MDR bacteria is gaining more attention as the novel coronavirus (COVID-19) continues to cause secondary lung infection in susceptible patients [21]. Patients with such infections require strong antibiotics, however, complications arise due to the presence of MDR bacteria. Doctors are faced with making split-second decisions, on which antibiotic has the greatest chance of treating each patient effectively. This reveals the desperate need for new innovative approaches before we hit a tipping point.

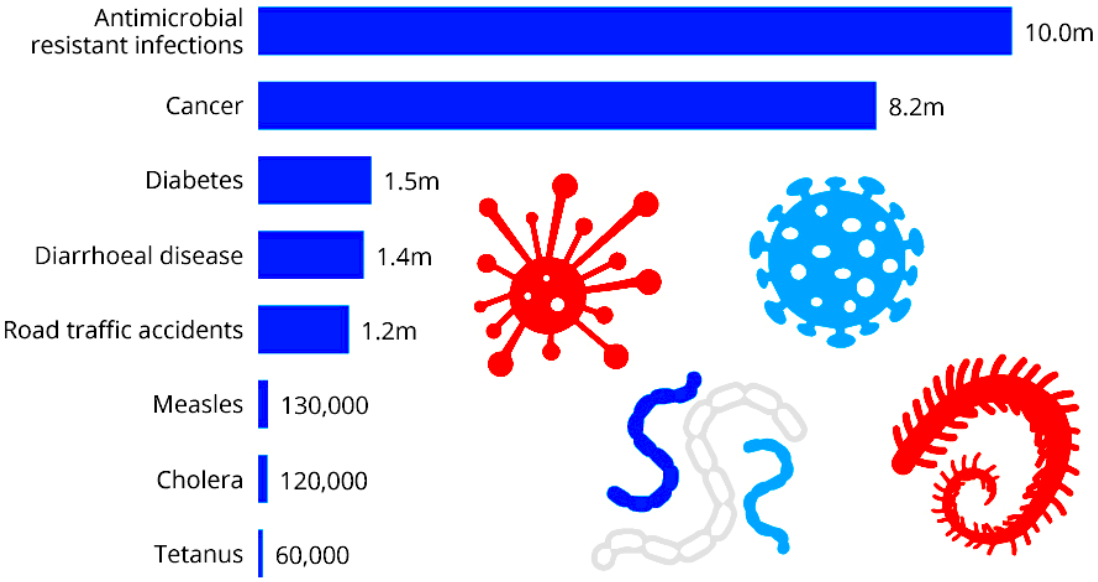

Figure 2. Death from AMR infections and other causes in 2050 [22].

One of the most serious resistant strains of bacteria that has risen to be of global concern is methicillin-resistant *Staphylococcus aureus* (MRSA). Since its discovery in a London hospital in 1960, MRSA has become a superbug of global concern [23]. MRSA infections have contributed to serious morbidity and mortality worldwide and can cause different organ-specific infections. The most common infections involving the skin and soft tissue, followed by invasive infections, such as lung abscess, pneumonia, empyema, sepsis, meningitis and other metastatic complications [23, 24]. A recent study by Wozniak *et al.* (2019) for the estimation of health and economic burden of AMR infections in Australian hospitals, found that the cost of treating MRSA patients is nearly AUD$5.5 million per year [25]. In Europe, MRSA accounts for over 40 % of healthcare-associated infections and has led to an excess of

EUR 380 million in-hospital costs [26, 27]. Furthermore, according to the Center for Disease Control and Prevention (CDC) in 2019, the cost of healthcare due to MRSA infections in the United States is approximately $1.7 billion annually, with an annual infection rate of 323,700 cases in hospitals [28]. WHO has previously listed MRSA as a superbug that needs to be prioritized for research to develop new alternative treatments [29]. Even though vancomycin (VCM) is effective and considered to be the last resort for the treatment of MRSA infections, some emerging strains are already resistant to VCM [30]. The evolving resistance of bacterial strains to the available antibiotic currently in use, accompanied by the possibility of emerging resistance to new antimicrobial drugs, calls for an urgent need to develop novel tactics for treating resistant bacterial infections.

Since the introduction of antibiotics to the market in 1945, they have been delivered via conventional dosage forms. These conventional dosage forms display several limitations, which are not due to the ineffectiveness of the antibiotics. These limitations include inadequate uptake at the infection site, insufficient targeting of bacteria, exposure of healthy cells to antibiotics, rapid degradation and elimination from the bloodstream. These factors lead to suboptimal therapeutic effects, side effects, increased frequency of administration and poor patient compliance [31-34]. These limitations also have been identified as major contributing factors to the development of antibiotic resistance and have led to the reduced period between introduction of antibiotics and the development of resistance, resulting in depletion of the antibiotic pipeline (**Figure 3**). Paradoxically, over the past three decades, the AMR crisis has been further compounded by pharmaceutical companies withdrawing or downgrading their antibiotic research and development (R&D) programs [35]. The short treatment courses, coupled with the possible short lifespan of an antibiotic's utility owing to the rapid development of resistance has rendered investment into research and development of new antibiotics insufficiently rewarding in today's business model [15, 35, 36].

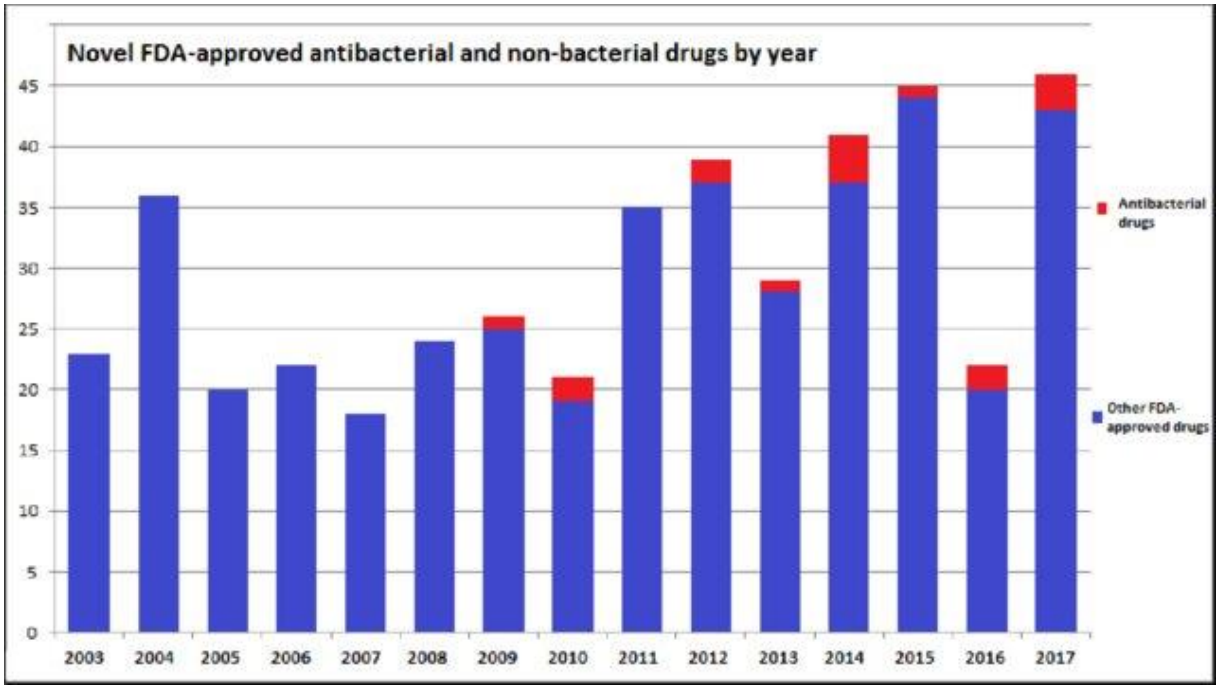

Figure 3. Novel FDA-approved antibacterial and non-bacterial drugs [37].

Recent nanotechnology advances have presented exciting opportunities for the production of new formulations based on distinct forms of nano-drug delivery systems with varying sizes, shapes and versatile antimicrobial properties. Nano-drug delivery systems can provide a promising alternative as they may not only be bactericidal, but also serve as carriers of antibiotics and natural antimicrobials [33, 38, 39]. Nanotechnology is confirmed to be an effective strategy in enhancing antibacterial activity, protecting the antibiotics in the market and addressing the problems of bacterial resistance, with some antibacterial nano-drug delivery systems already in the market [33, 40, 41]. These various nanoantibiotics offer several advantages, such as i) targeting the site of infection, ii) preventing exposure of the drug to healthy cells, iii) enhanced solubility, iv) sustained and controlled drug release, v) uniform distribution of the drug in the target tissue, and vi) improved cellular internalization.[42, 43]. Moreover, the required effective dose can be significantly reduced by enhancing the pharmacokinetic profile and therapeutic index of the encapsulated drugs as opposed to free drugs. This advantage can, in turn, reduce the toxicity and adverse side effects associated with high systemic drug and frequent dosing [44, 45]. Antibiotics such as vancomycin, fusidic acid, teicoplanin, linezolid, daptomycin, clarithromycin, amongst others, have been encapsulated into various nano-systems to overcome MRSA infections [34, 46, 47]. However, the application of nanotechnology for antibiotic therapy is still in its early stages compared to other medical conditions, such as cardiovascular disease and cancer [33,

48]. Therefore, to address the limitations associated with conventional dosage forms of antibiotics and the growing bacterial resistance to antibiotics, novel nano-antibiotic approaches are necessary.

Amongst various nanoparticulated systems, self-assembling amphiphiles designed through conjugation of hydrophilic and hydrophobic components via chemical modification or physical interaction, are considered to be one of the most prominent and promising candidates for drug delivery applications [49-51]. Under aqueous conditions, the amphiphiles can self-assemble to form various nano-aggregates, such as vesicles, micelles, spheres, lamellae, rods and other complex structures [52]. In addition to all advantages of nano-carriers, self-assembled amphiphiles have two unique attributes that make them superior in drug delivery. Firstly, they have the ability to assume complex structures that are difficult to attain via chemical synthesis. Secondly, the dissociation of self-assembled structures can be triggered by external stimuli, which can serve as a mechanism of payload release [53]. Also, more precise concentrations of drugs can be directly encapsulated within the self-assembled structure [54]. Self-assembled amphiphiles offer an attractive alternative to crosslinked polymers, rubbers, and metallics. Currently, there are commercially available therapeutics based on self-assembled amphiphiles [54]. Most reports for self-assembling delivery systems focus on anticancer research, rather than drug delivery for the treatment of antibiotic resistance. Due to their unique structure and extraordinary functions, which have been exploited as therapeutic and diagnostic agents [55, 56], self-assembling amphiphiles are promising systems that can aid in restoring the effectiveness of existing antibiotics. Moreover, a self-assembling system with intrinsic antibacterial activity was shown to expand the spectrum of currently available antibiotics [57, 58]. In the present work, we have developed three self-assembling drug delivery systems to effectively target and treat methicillin-susceptible and resistant *S. aureus* infections; namely i) supramolecular amphiphiles of Beta-cyclodextrin and Oleyl amine (BCD-OLA), ii) supramolecular Self-assembled Drug Delivery System (SADDs) of Vancomycin and Tocopherol Succinate (VCM/TS) as an antibacterial agent and iii) Pegylated Fusidic acid (PEG-FA) as a self-assembling polymer therapeutic.

Cyclodextrins (CDs) are cyclic oligosaccharides covalently connected by α(1–4) ether linkages, derived from bacterial degradation of starch [59, 60]. The most popular CDs are α-, β- and γ-CD, which are composed of six, seven and eight units of glucose, respectively [60-62]. Owing to its solubilizing properties, low toxicity and low inflammatory response, CDs

are widely used as excipients in pharmaceutical formulations [63]. The hydrophobic inner cavity and the external hydrophilic surface of CDs with their ability to interact with different molecules make CDs extremely desirable for use in the delivery of drugs [64-68]. The complexation of CDs with hydrophobic compounds creates supramolecular amphiphiles via chemical modification [69] or host-guest interaction using their hydrophobic cavities through non-covalent bonds, which can self-assemble to form various nanoparticles (NPs) such as monolayers, micelles, bilayer vesicles, or liquid-crystalline NPs [70]. Vesicles derived from the self-assembly of supramolecular amphiphiles can mimic the biological membrane and simultaneously regulate the release of the encapsulated drug [71]. The majority of amphiphilic CDs derivatives used in the delivery of drugs were synthesized by chemical modification of CDs [72]. Complexes of CDs have been introduced for several applications such as drug delivery, antimicrobial coatings on devices (e.g. biomedical instruments and implants) and antimicrobial dressings that help avoid wound infections [63, 73, 74]. Interestingly, CDs are recognized as 'trojan horses' for antibacterial drugs [75, 76], while OLA is an unsaturated fatty amine derived from the fatty acid, oleic acid, which have been used to synthesize various NPs as a solvent and reducer agent [77]. Furthermore, OLA has shown to have intrinsic antimicrobial activity and has been used for synthesis of intracellular delivery systems [78, 79]. The use of a nano-delivery system with intrinsic antibacterial activity has been shown to broaden the range of antibiotics currently available [57], thereby showing potential for combating antibacterial resistance. Therefore, the production of simple CD-amphiphiles with OLA via inclusion complexation will result in a superior drug delivery system with inherent antimicrobial activity and little or no toxicity. This will serve as a highly useful tool for combating antimicrobial resistance. Although there are many analogous drug delivery systems of BCD and hydrophobic guest molecules [80, 81], to the best of our knowledge, there have been no reports of this cationic amphiphile (BCD-OLA) for the delivery of any class of drug using this novel material. Despite the reported uses of BCD as a stabilizer for magnetic NPs through inclusion complex with surface bound OLA and oleic acid [82], there have been no reports on such cationic amphiphiles with self-assembling properties without chemical modification of the original structure of the parent compounds.

Amphiphilic conjugation, whereby the drug forms the building blocks of the delivery system, results in self-delivery with significant enhanced drug activity and loading efficiency without the use of non-therapeutic carriers [58, 83, 84]. However, this strategy is still dependent on chemical modifications of the drug, which relies on the use of toxic reagents and organic

solvents. Recently, a new strategy to build SADDs by producing NPs composed only of therapeutic molecules without any chemical bonds, based on supramolecular interactions was developed [85-88]. This technique focuses on producing complex structures assembled from molecular subunits through weak interactions, such as hydrophobic-hydrophilic bonds, hydrogen-bonding, metal-ligand coordination, π–π stacking and van der Waal's (vdW) forces [89]. These supramolecular complexes are identified by their unique structure and extraordinary functions [90], which make them useful in building advanced biomaterials [55, 56]. Such biomaterials have been employed as therapeutic and diagnostic agents, including the production of new antibacterial compounds [91]. One of the last resort treatments being used for MRSA is the glycopeptide antibiotic, vancomycin (VCM) [92]. These bacteria have acquired resistance to a number of antibiotics due to improper use, inactivation of the drug through hydrolysis or chemical modification, genetic mutation. This has resulted in modification of the drug's target and reduced intracellular accumulation of the antibiotic due to increased cell wall thickness or over-expression of efflux pumps[93, 94]. Efflux pumps have been pointed out as major contributors to multidrug resistance in gram-positive and -negative bacteria, as they extrude a wide variety of toxic compounds, including antibiotics from bacterial cells [95, 96]. Based on these facts, a delivery system comprising of compounds with the ability to interact with and/or inhibit these efflux pumps and lower the minimum inhibitory concentration (MIC) of the antibiotic, can be considered a promising therapeutic agent that will aid in restoring the effectiveness of existing antibiotics [97-99]. D-α-tocopherol succinate (TS) is an FDA approved derivative of α-tocopherol, which is known also as vitamin E. Tocopherol is known for its high lipid solubility and ability to modify the permeability of bacterial cell membranes, causing damage in the essential elements and collapse of proton pumps, leading to enhanced permeability and intracellular accumulation of various substances, including antibiotics [100, 101]. Therefore, recent studies have tested the potential of α-tocopherol as an efflux pump inhibitor [101, 102]. Interestingly, the use of α-tocopherol in combination with antibiotics has been described to enhance the sensitivity of drug-resistant bacteria to antibiotics [102-105], thus highlighting the usefulness of this compound for the development of innovative antibacterial-resistant preparations. Therefore, we are reporting a novel SADDs, composed of TS as the hydrophobic component and VCM as the hydrophilic element (VCM/TS complex), that will self-assemble into NPs; and we explore its potential for enhancing the antibacterial activity of VCM against *S. aureus* and MRSA. This is the first SADD formulation with TS for any class of drug, and the first SADD formulation with VCM.

Another vital part of modern therapeutics, which also forms part of nanomedicine, is "polymer therapeutics". This is a branch of drug delivery using polymers that covalently bind to a drug, such as poly(ethyl)ene glycol (PEG) [106]. Furthermore, polymer therapeutics that have the ability to self-assemble into nanosized particles have shown to be efficient in drug delivery. PEGylation has been reported to be a suitable technique for formulating polymer therapeutics. with several products such as Pegasys®, Mircera® and Cimzia® already available in the market [107]. PEGylated polymer therapeutics have shown to enhance the water solubility of poorly soluble drugs, reduce uptake by the reticulo-endothelial system, target the delivery of drugs to specific sites of action and reduce human serum albumin (HSA) binding [47, 108, 109]. Consequently, PEGylation seems to be a promising technique for modifying the therapeutic performance of antibiotics and overcoming bacterial resistance [110, 111]. There are several reports supporting the improvement of antibiotic delivery through polymeric conjugation, including penicillin [112, 113], fluoroquinolones [114-117], aminoglycoside [110, 118] and sulfonamides [119]. Fusidic acid (FA) is an antibiotic belonging to the fusidane group, which was first isolated from *Fusidium coccineum* fungus in 1962 [120]. FA is available in different conventional dosage forms, including; tablets and suspension for oral, cream and ointment for topical and also for intravenous administration [121]. The poor water solubility and the high affinity of HSA binding of FA limit its formulation and therapeutic efficacy [121, 122]. Although, there have been reports of FA conjugation with small molecules in order to enhance and broaden its spectrum [123, 124], there are no reports on polymer FA conjugation to form a self-assembling polymer therapeutic. Therefore, polymeric conjugation of FA with a biodegradable polymer such as PEG, can potentially enhance the solubility, bioavailability as well as antimicrobial activity of FA.

1.3 Problem statement

Antibiotic resistance has significantly threatened the management of infectious diseases. Moreover, it has rendered many antibiotics ineffective towards specific bacterial strains. This has led to a rise in mortality and morbidity rates, especially in developing countries. Current drug delivery formulations present many drawbacks, such as insufficient concentration of drugs at infection/target sites, exposure of the drug to healthy cells, rapid degradation and limited bloodstream circulation which lead to suboptimal therapeutic effects, serious side effects, poor patient compliance and drug resistance. All of these factors suggest the immense need for the production of novel therapeutic compounds and approaches to curb the increase

in drug resistance. Nano-drug delivery systems are showing significant potential for overcoming the limitations associated with conventional dosage forms. The identification of novel nano-based strategies to enhance antibacterial activity and to target infection sites, can therefore, contribute to enhancing patient therapy and disease treatments. The design and synthesis of advanced materials and nano-based strategies for developing self-assembling nano-carriers are necessary to improve the antibacterial activity of currently available antibiotics. Furthermore, synthesis of novel self-assembling amphiphiles having inherent antibacterial effects and their investigation as nano-carriers to improve the activity of antibiotics remain to be explored.

1.4 Aims and objectives of this study

The broad aim of this study was to design advanced materials and explore nano-based strategies for preparations of self-assembling delivery systems to treat *S. aureus* and MRSA infections. The specific research aims of the three novel nano-formulations developed in this study for enhancing antibacterial activity are further highlighted, with their respective objectives.

Aim 1

This study aimed to synthesize and formulate a novel supramolecular amphiphile, BCD-OLA, via inclusion complexation for the enhancement of VCM delivery.

To achieve this aim, the objectives of the study were to:

1. Use a single step synthetic method to form the supramolecular inclusion complex for synthesis of BCD-OLA amphiphile.
2. Determine the stoichiometry of BCD-OLA complexes using Job's method.
3. Characterize BCD-OLA using structural elucidation techniques such as Fourier transform-infrared spectroscopy (FT-IR), ^{1}H NMR and 2D NMR (NOESY spectrum).
4. Determine the *in vitro* cytotoxicity of the synthesized BCD-OLA to confirm its safety in biological systems.
5. Formulate VCM-loaded nanovesicles from BCD-OLA amphiphile and evaluate the formulated nanovesicles in terms of size, polydispersity index (PDI), zeta potential (ZP), morphology, entrapment efficiency, *in vitro* drug release, flow cytometry, *in vitro* antibacterial activity and bacterial killing kinetics.
6. Perform molecular dynamics (MD) simulations to understand the molecular mechanism of the inclusion complex and nanovesicle's formation.

7. Determine the efficacy of the VCM-loaded BCD-OLA nanovesicles in eradicating intracellular MRSA in macrophages (TPH-1) and human embryonic kidney (HEK 293) cells.

Aim 2

This study aimed to synthesize and formulate a SADDs composed of two components, hydrophobic TS and hydrophilic VCM, as well as to explore its potential for enhancing the antibacterial activity of VCM against *S. aureus* and MRSA.

To achieve this aim, the objectives of the study were to:

1. Use the solvent evaporation method to screen different ratios of TS and VCM to form NPs with the desirable size, PDI, ZP and loading capacity.
2. Determine the *in vitro* cytotoxicity and haemolytic effect of the synthesized VCM/TS NPs to confirm its safety in biological systems.
3. Perform MD simulations to understand the mechanism of the complex and self-assembly into NPs.
4. Determine the structural change in VCM and TS before and after self-assembly into NPs using FT-IR and differential scanning calorimetry (DSC).
5. Evaluate the formulated VCM/TS NPs in terms of size, PDI, ZP, morphology, entrapment efficiency, *in vitro* drug release, *in vitro* and *in vivo* antibacterial activity.
6. Investigate the potential of TS to block the outer membrane channel of NorA and NorB efflux pumps and possibly prevent extrusion of antibiotics via MD simulations.

Aim 3

This study aimed to synthesize and formulate a novel PEGylated fusidic acid (PEG-FA), conjugated through a small spacer with an amide bond and to explore its potential for simultaneously enhancing the solubility and antimicrobial activity of FA and lowering its binding to HSA.

To achieve this aim, the objectives of the study were to:

1. Synthesize PEG-FA conjugate and confirm its structure using structural elucidation techniques such as FT-IR, ^{1}H NMR, and DSC.
2. Determine the *in vitro* cytotoxicity and haemolytic effect of the synthesized PEG-FA to confirm its safety in biological systems.

3. Evaluate the formulated PEG-FA NPs in terms of size, PDI, ZP, and morphology.
4. Evaluate the enhancement in water solubility and *in vitro* antibacterial activity compared to the bare FA.
5. Perform MD simulations to understand the mechanism of PEG-FA self-assembly.
6. Determine the binding affinity of FA, bilirubin and PEGylated FA molecules with HSA using Microscale Thermophoresis (MST) and molecular docking studies.

1.5 Novelty of the Study

The novelty of the project for the three experimental studies is presented hereunder.

Aim 1

The experimental research performed in this study, which is presented in **Chapter Two,** is novel for the following reasons:

- There are several reports of amphiphilic CDs synthesized via chemical modification. This study reports the first amphiphilic CDs coined from BCD and OLA via inclusion complexation that are able to self-assemble into nanovesicles.
- This is the first nanovesicle assembled from cationic amphiphile (BCD-OLA) for the delivery of any class of drug.
- This is the first supramolecular complex with inherent antibacterial activity for the delivery of antibiotics.
- Intracellular bacterial infections are difficult to treat, as bare drugs do not penetrate effectively into the cells. Intracellular bacteria use acidic phagolysosomes and endosomes as reservoirs. There have been several reports to address this problem using nano-drug delivery systems. This paper reports for the first time the targeting of intracellular bacterial infections using amphiphilic supramolecular complex, which has never been reported before.

Aim 2

The experimental research performed in this study, which is presented in **Chapter Three,** is novel for the following reasons:

- This study reports the first SADDs formulated with TS for any class of drug.
- This is the first SADD formulation of VCM.
- This is the first report of the potential of TS to block the outer membrane channel of NorA and NorB bacterial efflux pumps and the binding potential of TS to NorA and NorB efflux pumps at a molecular level via MD simulations.

- This study reports the first antibacterial SADDs formulation, that has been characterized and confirmed to have antibiofilm activity compared to the bare drug.

Aim 3

The experimental research performed in this study, which is presented in **Chapter Four,** is novel for the following reasons:

- This is the first report of FA conjugation with a biodegradable polymer.
- This is the first self-assembling polymer therapeutic of FA.
- This research is the first report of the quantitative binding of FA, bilirubin and PEGylated FA molecules with HSA using MST.

1.6 Significance of the study

The nano-drug delivery systems developed in this study are novel and can contribute to overcoming the problems of bacterial resistance to antibiotics and limitations associated with their conventional dosage forms. The significance of this study are highlighted below:

New pharmaceutical products: The proposed BCD-OLA, VCM/TS and PEG-FA are new pharmaceutical products not yet reported in the literature. They have the potential to stimulate the local pharmaceutical industries to manufacture cost-effective superior medicines.

Improved patient therapy and disease treatment: The proposed formulations can improve both patient therapy and treatment of various diseases associated with bacterial infections by enhancing antibacterial performance, minimizing doses, lowering side effects and improving patient compliance. Hence, it will lead to improving the quality of patients life and saving lives.

Creation of new knowledge to the scientific community: These studies proposed can lead to new knowledge being generated in pharmaceutical sciences. It can include the following:

- Synthesis schemes for new materials, preparation procedures for the novel drug delivery systems and their *in vitro*, *in silico* and *in vivo* properties will be identified.
- The detailed MD simulations for self-assembly of amphiphilic materials into nano-systems can contribute to a better mechanistic understanding of nano-formulations.
- The combined effects of these novel antibacterial materials with antibiotics can identify the synergistic or additive antibacterial effects.
- The extensive *in vivo* testing of these novel systems can provide knowledge for *in vitro in vivo* correlations.

Stimulation of new research: The proposed BCD-OLA, VCM/TS, and PEG-FA as strategies to improve activity against methicillin-susceptible and resistant *S. aureus* infections, can stimulate further studies on their clinical evaluation, potential for other applications and design of new materials.

1.7 Overview of dissertation

The research work performed is presented in this thesis in the publication format, according to University of Kwa-Zulu Natal, College of Health Sciences guidelines. It specifies the inclusion of a brief introductory chapter, published papers and a final chapter on the conclusions. A Ph.D. study requires at least three first-authored papers, two of which must be experimental.

CHAPTER TWO: EXPERIMENTAL PAPER ONE: This chapter addresses Aim 1, Objectives 1-7 and is a first-authored experimental article published in an ISI International Journal: International Journal of Pharmaceutics (Impact Factor = 4.320). This article highlights the formulation of the novel amphiphilic BCD-OLA supramolecular complex, the *in vitro* toxicity evaluation and formulation of the BCD-OLA nanovesicles to deliver VCM. It also highlights the molecular dynamics simulation of the self-assembly of nanovesicles, characterization of its physical properties, *in vitro* antibacterial properties and eradication of intracellular MRSA in macrophages and HEK 293 cells.

CHAPTER THREE: EXPERIMENTAL PAPER TWO: This chapter addresses Aim 2, Objectives 1–6 and is a first-authored experimental article published in an ISI international journal: Pharmaceutical Development and Technology (Impact Factor 2.374). This article highlights the formulation development of the novel SADDs through supramolecular complexation to deliver VCM, the *in vitro* toxicity evaluation, molecular dynamics simulation of the self-assembly of NPs, characterization of its physical properties, *in vitro* and *in vivo* antibacterial properties.

CHAPTER FOUR: EXPERIMENTAL PAPER THREE: This chapter addresses Aim 3, Objectives 1–6 and is a first-authored experimental article accepted in Journal of Biomolecular Structure & Dynamics (Impact Factor 3.22) an ISI international journal (manuscript ID: TBSD-2020-1529). This article highlights the synthesis of a novel polymeric conjugation of FA with a biodegradable polymer; PEG, the *in vitro* toxicity

evaluation, molecular dynamics simulation of the self-assembly of NPs, characterization of its physical properties, binding check for FA, bilirubin and PEG-FA molecules with HSA using MST, and *in vitro* antibacterial properties.

CHAPTER FIVE: CO-AUTHORED PAPERS: In addition to the first authored experimental papers in Chapters, 2, 3 and 4 focusing on aims 1, 2 and 3, I have also been involved in other papers within our group as a Ph.D. student. As these papers also focused on the broad aim of this PhD project to improve treatment of bacterial infections, these papers have been included in the thesis. This chapter therefore includes published one experimental paper and one review article in an ISI International Journals: Colloids and Surfaces B: Biointerfaces (Impact Factor = 3.973) and WIREs Nanomedicine & Nanobiotechnology (Impact Factor = 7.689).

CHAPTER SIX: CONCLUSION: This chapter includes the overall conclusions from research findings in the study, provides information on the potential significance of the findings and makes recommendations for future research work in the field of strategic solutions to combat bacterial resistance to antibiotics.

References

1. Morens, D.M., G.K. Folkers, and A.S. Fauci, The challenge of emerging and re-emerging infectious diseases. Nature, 2004. 430(6996): p. 242-249.
2. Lindahl, J.F. and D. Grace, The consequences of human actions on risks for infectious diseases: a review. Infection Ecology & Epidemiology, 2015. 5(1): p. 30048.
3. Shahapur, P.R. and R.C. Bidri, Recent trends in the spectrum of opportunistic infections in human immunodeficiency virus infected individuals on antiretroviral therapy in South India. Journal of Natural Science, Biology, and Medicine, 2014. 5(2): p. 392.
4. Rali, P., et al., Opportunistic pulmonary infections in immunocompromised hosts. Critical Care Nursing Quarterly, 2016. 39(2): p. 161-175.
5. Ayukekbong, J.A., M. Ntemgwa, and A.N. Atabe, The threat of antimicrobial resistance in developing countries: causes and control strategies. Antimicrobial Resistance & Infection Control, 2017. 6(1): p. 47.
6. Bhutta, Z.A., et al., Global burden, distribution, and interventions for infectious diseases of poverty. Infectious Diseases of Poverty, 2014. 3(1): p. 21.
7. Neiderud, C.-J., How urbanization affects the epidemiology of emerging infectious diseases. Infection Ecology & Epidemiology, 2015. 5(1): p. 27060.
8. Chen, H., et al., Point of care testing for infectious diseases. Clinica Chimica Acta, 2019. 493: p. 138-147.
9. Aminov, R.I., A brief history of the antibiotic era: lessons learned and challenges for the future. Frontiers in Microbiology, 2010. 1: p. 134.
10. Hays, E.E., et al., Antibiotic Substances produced by Pseu-domonas aeruginosa. Biological Chemistry, 1945. 159(3): p. 725-50.
11. Mahoney, J.F., R.C. Arnold, and A. Harris, Penicillin treatment of early syphilis—a preliminary report. American Journal of Public Health and the Nations Health, 1943. 33(12): p. 1387-1391.
12. Sir Alexander Fleming. Nobel Lecture: Penicillin. 1945 [cited 2020 30 April]; Available from: https://www.nobelprize.org/prizes/medicine/1945/fleming/lecture/.
13. Lewis, K., New approaches to antimicrobial discovery. Biochemical Pharmacology, 2017. 134: p. 87-98.
14. Levy, S.B. and B. Marshall, Antibacterial resistance worldwide: causes, challenges and responses. Nature Medicine, 2004. 10(12): p. S122-S129.
15. Boucher, H.W., et al., White paper: developing antimicrobial drugs for resistant pathogens, narrow-spectrum indications, and unmet needs. J. Infect. Dis, 2017. 216(2): p. 228-236.
16. Jacoby, G.A. and G.L. Archer, New mechanisms of bacterial resistance to antimicrobial agents. New England Journal of Medicine, 1991. 324(9): p. 601-612.
17. Davies, J., Inactivation of antibiotics and the dissemination of resistance genes. Science, 1994. 264(5157): p. 375-382.

18. Willyard, C., The drug-resistant bacteria that pose the greatest health threats. Nature News, 2017. 543(7643): p. 15.

19. World Health Organization. Urgent health challenges for the next decade. 2020 [cited 2020 30 April]; Available from: https://www.who.int/news-room/photo-story/photo-story-detail/urgent-health-challenges-for-the-next-decade.

20. Organization, W.H., No time to wait: securing the future from drug-resistant infections. Report to the Secretary-General of the United Nations. World Health Organization, Geneva, 2019.

21. Lupia, T., et al., 2019-novel coronavirus outbreak: A new challenge. Journal of Global Antimicrobial Resistance, 2020.

22. Statista. Deaths From Drug-Resistant Infections. 2015 [cited 2020 30 March]; Available from: https://www.statista.com/chart/3095/drug-resistant-infections/.

23. Turner, N.A., et al., Methicillin-resistant Staphylococcus aureus: an overview of basic and clinical research. Nature Reviews Microbiology, 2019. 17(4): p. 203-218.

24. Hassoun, A., P.K. Linden, and B. Friedman, Incidence, prevalence, and management of MRSA bacteremia across patient populations-a review of recent developments in MRSA management and treatment. Critical Care, 2017. 21(1): p. 211.

25. Wozniak, T.M., E.J. Bailey, and N. Graves, Health and economic burden of antimicrobial-resistant infections in Australian hospitals: a population-based model. Infection Control & Hospital Epidemiology, 2019. 40(3): p. 320-327.

26. Schubert, M., et al., Prevalence and predictors of MRSA carriage among employees in a non-outbreak setting: A cross-sectional study in an acute care hospital. Journal of Occupational Medicine and Toxicology, 2019. 14(1): p. 7.

27. Köck, R., et al., Systematic literature analysis and review of targeted preventive measures to limit healthcare-associated infections by meticillin-resistant Staphylococcus aureus. 2014. 19(29): p. 1-27.

28. Centres for Disease Control and Prevention, Antibiotic resistance threats in the United States, 2019. 2019: Centres for Disease Control and Prevention, US Department of Health and Human Services.

29. World Health Organisation. WHO publishes list of bacteria for which new antibiotics are urgently needed. 2017 [cited 2020 5, Jan]; Available from: https://www.who.int/news-room/detail/27-02-2017-who-publishes-list-of-bacteria-for-which-new-antibiotics-are-urgently-needed.

30. Monaco, M., et al., Worldwide epidemiology and antibiotic resistance of Staphylococcus aureus, in Staphylococcus aureus. 2016, Springer. p. 21-56.

31. Nguyen, H.M. and C.J. Graber, Limitations of antibiotic options for invasive infections caused by methicillin-resistant Staphylococcus aureus: is combination therapy the answer? Journal of Antimicrobial Chemotherapy, 2010. 65(1): p. 24-36.

32. Karpecki, P., M.R. Paterno, and T.L. Comstock, Limitations of current antibiotics for the treatment of bacterial conjunctivitis. Optometry and Vision Science, 2010. 87(11): p. 908-919.

33. Gupta, A., et al., Combatting antibiotic-resistant bacteria using nanomaterials. Chemical Society Reviews, 2019. 48(2): p. 415-427.

34. Zaidi, S., L. Misba, and A.U. Khan, Nano-therapeutics: a revolution in infection control in post antibiotic era. Nanomedicine: Nanotechnology, Biology and Medicine, 2017. 13(7): p. 2281-2301.

35. Singer, A.C., C. Kirchhelle, and A.P. Roberts, (Inter) nationalising the antibiotic research and development pipeline. Lancet Infect. Dis., 2019. 20(2): p. 54-62.

36. Nathan, C., Resisting antimicrobial resistance. Nature Reviews Microbiology, 2020. 18(5): p. 259-260.

37. Andrei, S., et al., New FDA approved antibacterial drugs: 2015-2017. Discoveries, 2018. 6: p. e81.

38. Brooks, B.D. and A.E. Brooks, Therapeutic strategies to combat antibiotic resistance. Advanced Drug Delivery Reviews, 2014. 78: p. 14-27.

39. Wang, Y., et al., Antibiotic- Free Antibacterial Strategies Enabled by Nanomaterials: Progress and Perspectives. Advanced Materials, 2019: p. 1-21.

40. Caster, J.M., et al., Investigational nanomedicines in 2016: a review of nanotherapeutics currently undergoing clinical trials. Wiley Interdiscip. Rev. Nanomed. Nanobiotechnol., 2017. 9(1): p. 1416.

41. Hamblin, K.A., et al., Inhaled liposomal ciprofloxacin protects against a lethal infection in a murine model of pneumonic plague. Frontiers in Microbiology, 2017. 8(1): p. 91.

42. Pissuwan, D., T. Niidome, and M.B. Cortie, The forthcoming applications of gold nanoparticles in drug and gene delivery systems. Journal of Controlled Release, 2011. 149(1): p. 65-71.

43. Barth, J.V., G. Costantini, and K. Kern, Engineering atomic and molecular nanostructures at surfaces, in Nanoscience and Technology: a Collection of Reviews from Nature Journals. 2010, World Scientific p. 67-75.

44. Gao, W., et al., Nanoparticle-based local antimicrobial drug delivery. Advanced Drug Delivery Reviews, 2018. 127: p. 46-57.

45. Liu, P.-F., et al., Use of nanoparticles as therapy for methicillin-resistant Staphylococcus aureus infections. Current Drug Metabolism, 2009. 10(8): p. 875-884.

46. Omolo, C.A., et al., Formulation and Molecular Dynamics Simulations of a Fusidic Acid Nanosuspension for Simultaneously Enhancing Solubility and Antibacterial Activity. Molecular Pharmaceutics, 2018. 15(8): p. 3512-3526.

47. Omolo, C.A., et al., A hybrid of mPEG-b-PCL and G1-PEA dendrimer for enhancing delivery of antibiotics. Journal of Controlled Release, 2018. 290(1): p. 112-128.

48. Rizvi, S.A. and A.M. Saleh, Applications of nanoparticle systems in drug delivery technology. Saudi Pharmaceutical Journal, 2018. 26(1): p. 64-70.

49. Rösler, A., G.W. Vandermeulen, and H.-A. Klok, Advanced drug delivery devices via self-assembly of amphiphilic block copolymers. Advanced Drug Delivery Reviews, 2012. 64: p. 270-279.

50. Sun, T., et al., Self-assembled vesicles prepared from amphiphilic cyclodextrins as drug carriers. Langmuir, 2012. 28(23): p. 8625-8636.

51. Prakash Jain, J., W. Yenet Ayen, and N. Kumar, Self assembling polymers as polymersomes for drug delivery. Current Pharmaceutical Design, 2011. 17(1): p. 65-79.

52. Du, J. and Y. Chen, Organic–inorganic hybrid nanoparticles with a complex hollow structure. Angewandte Chemie International Edition, 2004. 43(38): p. 5084-5087.

53. Chen, M., et al., Nanoscale Self-Assembly for Delivery of Therapeutics and Imaging Agents. Technology & Innovation, 2011. 13(1): p. 5-25.

54. Branco, M.C. and J.P. Schneider, Self-assembling materials for therapeutic delivery. Acta biomaterialia, 2009. 5(3): p. 817-831.

55. Lehn, J.-M., Supramolecular chemistry. Science, 1993. 260(5115): p. 1762-1764.

56. Amabilino, D.B., D.K. Smith, and J.W. Steed, Supramolecular materials. Chemical Society Reviews, 2017. 46(9): p. 2404-2420.

57. Fernandes, M.M., et al., Nanotransformation of vancomycin overcomes the intrinsic resistance of gram-negative bacteria. ACS Appl. Mater. Interfaces, 2017. 9(17): p. 15022-15030.

58. Cheetham, A.G., et al., Self-assembling prodrugs. Chemical Society Reviews, 2017. 46(21): p. 6638-6663.

59. Szejtli, J., Introduction and general overview of cyclodextrin chemistry. Chemical Reviews, 1998. 98(5): p. 1743-1754.

60. Loftsson, T. and M.E. Brewster, Pharmaceutical applications of cyclodextrins. 1. Drug solubilization and stabilization. Journal of Pharmaceutical Sciences, 1996. 85(10): p. 1017-1025.

61. Martín, V.I., et al., Host-guest interactions between cyclodextrins and surfactants with functional groups at the end of the hydrophobic tail. Journal of colloid and interface science, 2017. 491: p. 336-348.

62. Hedges, A., Cyclodextrins: properties and applications, in Starch. 2009, Elsevier. p. 833-851.

63. Wong, C.E., et al., Cyclodextrins: a weapon in the fight against antimicrobial resistance. Journal of Molecular and Engineering Materials, 2017. 5(01): p. 1740006.

64. Brewster, M.E. and T. Loftsson, Cyclodextrins as pharmaceutical solubilizers. Advanced Drug Delivery Reviews, 2007. 59(7): p. 645-666.

65. Carrier, R.L., L.A. Miller, and I. Ahmed, The utility of cyclodextrins for enhancing oral bioavailability. Journal of Controlled Release, 2007. 123(2): p. 78-99.

66. Uekama, K., F. Hirayama, and T. Irie, Cyclodextrin drug carrier systems. Chemical Reviews, 1998. 98(5): p. 2045-2076.

67. Hirayama, F. and K. Uekama, Cyclodextrin-based controlled drug release system. Advanced Drug Delivery Reviews, 1999. 36(1): p. 125-141.

68. Davis, M.E. and M.E. Brewster, Cyclodextrin-based pharmaceutics: past, present and future. Nature Reviews Drug Discovery, 2004. 3(12): p. 1023.

69. Li, J. and X.J. Loh, Cyclodextrin-based supramolecular architectures: syntheses, structures, and applications for drug and gene delivery. Advanced Drug Delivery Reviews, 2008. 60(9): p. 1000-1017.

70. Sallas, F. and R. Darcy, Amphiphilic cyclodextrins–advances in synthesis and supramolecular chemistry. European Journal of Organic Chemistry, 2008. 2008(6): p. 957-969.

71. Allen, T.M. and P.R. Cullis, Drug delivery systems: entering the mainstream. Science, 2004. 303(5665): p. 1818-1822.

72. Varan, G., et al., Development of polycationic amphiphilic cyclodextrin nanoparticles for anticancer drug delivery. Beilstein Journal of Nanotechnology, 2017. 8(1): p. 1457-1468.

73. Dong, C., et al., Antibacterial modification of cellulose fibers by grafting β-cyclodextrin and inclusion with ciprofloxacin. Cellulose, 2014. 21(3): p. 1921-1932.

74. Thatiparti, T.R., A.J. Shoffstall, and H.A. Von Recum, Cyclodextrin-based device coatings for affinity-based release of antibiotics. Biomaterials, 2010. 31(8): p. 2335-2347.

75. Santos, R.S., et al., Nanomaterials and molecular transporters to overcome the bacterial envelope barrier: Towards advanced delivery of antibiotics. Advanced Drug Delivery Reviews, 2017. 136: p. pp.28-48.

76. Nardello-Rataj, V. and L. Leclercq, Encapsulation of biocides by cyclodextrins: toward synergistic effects against pathogens. Beilstein Journal of Organic Chemistry, 2014. 10(1): p. 2603-2622.

77. Mourdikoudis, S. and L.M. Liz-Marzan, Oleylamine in nanoparticle synthesis. Chemistry of Materials, 2013. 25(9): p. 1465-1476.

78. Cioffi, N. and M. Rai, Nano-antimicrobials: progress and prospects. 2012: Springer Science & Business Media.

79. Lim, Y.T., et al., Simultaneous intracellular delivery of targeting antibodies and functional nanoparticles with engineered protein G system. Biomaterials, 2009. 30(6): p. 1197-1204.

80. Shi, Y., et al., Entirely oligosaccharide-based supramolecular amphiphiles constructed via host–guest interactions as efficient drug delivery platforms. Chemical Communications, 2017. 53(91): p. 12302-12305.

81. Sun, T., et al., Strategy of directly employing paclitaxel to construct vesicles. The Journal of Physical Chemistry B, 2012. 116(50): p. 14628-14636.

82. MORI, K. and H. YAMASHITA, Design of colloidal and supported metal nanoparticles: Their synthesis, characterization, and catalytic application. Journal of The Japan Petroleum Institute, 2011. 54(1): p. 1-14.

83. Huang, P., et al., Combination of small molecule prodrug and nanodrug delivery: amphiphilic drug–drug conjugate for cancer therapy. Journal of The American Chemical Society, 2014. 136(33): p. 11748-11756.

84. Xie, S., et al., Design and synthesis of theranostic antibiotic nanodrugs that display enhanced antibacterial activity and luminescence. Proceedings of the National Academy of Sciences, 2017. 114(32): p. 8464-8469.

85. Kulkarni, A., et al., Combining immune checkpoint inhibitors and kinase-inhibiting supramolecular therapeutics for enhanced anticancer efficacy. Acs Nano, 2016. 10(10): p. 9227-9242.

86. Liu, K., et al., Simple peptide- tuned self- assembly of photosensitizers towards anticancer photodynamic therapy. Angewandte Chemie International Edition, 2016. 55(9): p. 3036-3039.

87. Shimanovich, U., et al., Tetracycline Nanoparticles as Antibacterial and Gene-Silencing Agents. Advanced Healthcare Materials, 2015. 4(5): p. 723-728.

88. Semiramoth, N., et al., Self-assembled squalenoylated penicillin bioconjugates: an original approach for the treatment of intracellular infections. ACS Nano, 2012. 6(5): p. 3820-3831.

89. Lehn, J.M., Supramolecular chemistry—scope and perspectives molecules, supermolecules, and molecular devices (Nobel Lecture). Angewandte Chemie International Edition in English, 1988. 27(1): p. 89-112.

90. Ganewatta, M.S. and C. Tang, Controlling macromolecular structures towards effective antimicrobial polymers. Polymer, 2015. 63: p. A1-A29.

91. Webber, M.J., et al., Supramolecular biomaterials. Nature Materials, 2016. 15(1): p. 13.

92. Binda, E., F. Marinelli, and G. Marcone, Old and new glycopeptide antibiotics: action and resistance. Antibiotics, 2014. 3(4): p. 572-594.

93. Slama, T.G., Gram-negative antibiotic resistance: there is a price to pay. Critical Care, 2008. 12(4): p. S4.

94. Blair, J.M., et al., Molecular mechanisms of antibiotic resistance. Nature Reviews Ricrobiology, 2015. 13(1): p. 42.

95. Saiful, A.J., et al., Efflux genes and active efflux activity detection in Malaysian clinical isolates of methicillin- resistant Staphylococcus aureus (MRSA). Journal of Basic Microbiology, 2008. 48(4): p. 245-251.

96. Sołoducho, J., et al., Recent Advances of Modern Protocol for CC Bonds–The Suzuki Cross-Coupling. Advances in Chemical Engineering and Science, 2013. 3(3A): p. 19-32.

97. Van Bambeke, F. and V.J. Lee, Inhibitors of bacterial efflux pumps as adjuvants in antibiotic treatments and diagnostic tools for detection of resistance by efflux. Recent Patents on Anti-infective Drug Discovery, 2006. 1(2): p. 157-175.

98. Lomovskaya, O., et al., Identification and characterization of inhibitors of multidrug resistance efflux pumps in Pseudomonas aeruginosa: novel agents for combination therapy. Antimicrobial Agents and Chemotherapy, 2001. 45(1): p. 105-116.

99. Sharma, A., V.K. Gupta, and R. Pathania, Efflux pump inhibitors for bacterial pathogens: From bench to bedside. The Indian Journal of Medical Research, 2019. 149(2): p. 129–145.

100. Nielsen, P., et al., The effect of α-tocopherol on the in vitro solubilisation of lipophilic drugs. International Journal of Pharmaceutics, 2001. 222(2): p. 217-224.

101. Tintino, S.R., et al., Action of cholecalciferol and alpha-tocopherol on Staphylococcus aureus efflux pumps. EXCLI Journal, 2016. 15: p. 315.

102. Abd El-Tawab, A.A., et al., Efflux Pump Inhibitors, Alpha-Tocopherol and Aspirin: Role in Campylobacter jejuni and Campylobacter coli Fluoroquinolone Resistance. Microbial Drug Resistance, 2018. 25: p. 203-211.

103. Andrade, J.C., et al., Enhancement of the antibiotic activity of aminoglycosides by alpha-tocopherol and other cholesterol derivates. Biomedicine & Pharmacotherapy, 2014. 68(8): p. 1065-1069.

104. Tintino, S.R., et al., Vitamin K enhances the effect of antibiotics inhibiting the efflux pumps of Staphylococcus aureus strains. Medicinal Chemistry Research, 2018. 27(1): p. 261-267.

105. Du, Y., et al., Tocopherol polyethylene glycol succinate modified hollow silver nanoparticles for combating bacteria-resistance. Biomaterials Science, 2019.

106. Knop, K., et al., Poly (ethylene glycol) in drug delivery: pros and cons as well as potential alternatives. Angew. Chem. Int. Ed., 2010. 49(36): p. 6288-6308.

107. Duncan, R. and M.J. Vicent, Polymer therapeutics-prospects for 21st century: the end of the beginning. Adv. Drug Deliv. Rev., 2013. 65(1): p. 60-70.

108. Banerjee, S.S., et al., Poly (ethylene glycol)-prodrug conjugates: concept, design, and applications. J. Drug Deliv., 2012. 2012(1): p. 1-17.

109. Owens III, D.E. and N.A. Peppas, Opsonization, biodistribution, and pharmacokinetics of polymeric nanoparticles. International Journal of Pharmaceutics, 2006. 307(1): p. 93-102.

110. Bahamondez-Canas, T.F., et al., PEGylation of tobramycin improves mucus penetration and antimicrobial activity against Pseudomonas aeruginosa biofilms in vitro. Mol. Pharm., 2018. 15(4): p. 1643-1652.

111. Du, J., et al., Improved biofilm antimicrobial activity of polyethylene glycol conjugated tobramycin compared to tobramycin in pseudomonas aeruginosa biofilms. Molecular Pharmaceutics, 2015. 12(5): p. 1544-1553.

112. Nathan, A., et al., Copolymers of lysine and polyethylene glycol: a new family of functionalized drug carriers. Bioconjugate Chemistry, 1993. 4(1): p. 54-62.

113. Turos, E., et al., Antibiotic-conjugated polyacrylate nanoparticles: new opportunities for development of anti-MRSA agents. Bioorganic & Medicinal Chemistry Letters, 2007. 17(1): p. 53-56.

114. Gac-Breton, S., et al., Norfloxacin-poly (L-lysine citramide imide) conjugates and structure-dependence of the drug release. Journal of Drug Targeting, 2004. 12(5): p. 297-307.

115. Sobczak, M., Synthesis and characterization of polyester conjugates of ciprofloxacin. European Journal of Medicinal Chemistry, 2010. 45(9): p. 3844-3849.

116. Sobczak, M., et al., Synthesis and study of controlled release of ofloxacin from polyester conjugates. International Journal of Pharmaceutics, 2010. 402(1-2): p. 37-43.

117. Kugel, A., et al., Antimicrobial polysiloxane polymers and coatings containing pendant levofloxacin. Polym. Chem., 2010. 1(4): p. 442-452.

118. Chen, M., et al., Multifunctional hyperbranched glycoconjugated polymers based on natural aminoglycosides. Bioconjugate Chemistry, 2012. 23(6): p. 1189-1199.

119. Chang, H.-P., et al., Synthesis and characterization of a new polymer–drug conjugate with pH-induced activity. Polymer, 2012. 53(16): p. 3498-3507.

120. Godtfredsen, W., et al., Fusidic acid: a new antibiotic. Nature, 1962. 193(4819): p. 987-987.

121. Curbete, M.M. and H.R.N. Salgado, A critical review of the properties of fusidic acid and analytical methods for its determination. Crit. Rev. Anal. Chem., 2016. 46(4): p. 352-360.

122. Rieutord, A., et al., In vitro study of the protein binding of fusidic acid: a contribution to the comprehension of its pharmacokinetic behaviour. International Journal of Pharmaceutics, 1995. 119(1): p. 57-64.

123. Njoroge, M., et al., Semisynthetic Antimycobacterial C-3 Silicate and C-3/C-21 Ester Derivatives of Fusidic Acid: Pharmacological Evaluation and Stability Studies in Liver Microsomes, Rat Plasma, and Mycobacterium tuberculosis culture. ACS Infect. Dis, 2019. 5(9): p. 1634-1644.

124. Espinoza-Moraga, M., et al., Synthesis and biological characterisation of ester and amide derivatives of fusidic acid as antiplasmodial agents. Bioorganic & Medicinal Chemistry Letters, 2017. 27(3): p. 658-661.

CHAPTER 2, EXPERIMENTAL PAPER 1

3.1 Introduction

This chapter addresses Aim 1, Objectives 1 - 7 and is a first-authored experimental published in an ISI International Journal: International Journal of Pharmaceutics (Impact Factor = 4.320). This article highlights the formulation of the novel amphiphilic BCD-OLA supramolecular complex, the *in vitro* toxicity evaluation and formulation of the BCD-OLA nanovesicles to deliver VCM. It also highlights the molecular dynamics simulation of the self-assembly of nanovesicles, characterization of its physical properties, *in vitro* antibacterial properties and eradication of intracellular MRSA in macrophages and HEK 293 cells.

Graphical bstract

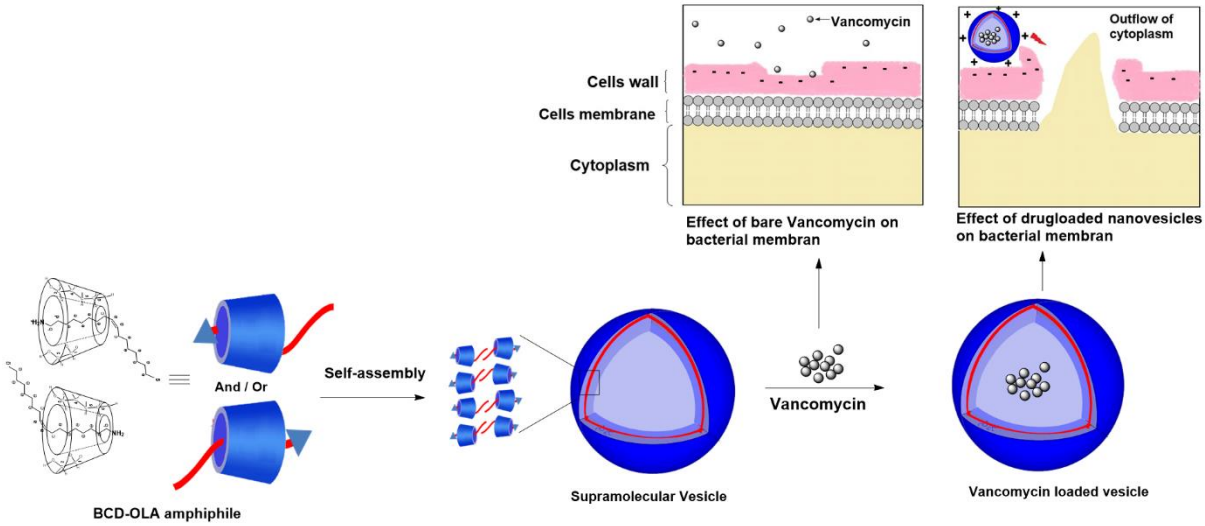

International Journal of Pharmaceutics 574 (2020) 118881

Contents lists available at ScienceDirect

International Journal of Pharmaceutics

journal homepage: www.elsevier.com/locate/ijpharm

Supramolecular amphiphiles of Beta-cyclodextrin and Oleylamine for enhancement of vancomycin delivery

Mohammed Salih[a], Calvin A. Omolo[a,b,*], Nikhil Agrawal[a], Pavan Walvekar[a], Ayman Y. Waddad[a], Chunderika Mocktar[a], Charlotte Ramdhin[a], Thirumala Govender[a,*]

[a] Discipline of Pharmaceutical Sciences, College of Health Sciences, University of KwaZulu-Natal, Private Bag X54001, Durban, South Africa
[b] School of Pharmacy and Health Sciences, United States International University, P.O. BOX 14634 – 00800, Nairobi, Kenya

ARTICLE INFO

Keywords:
Supramolecular amphiphiles
Cyclodextrin
MRSA
Nanovesicles
Inclusion complex

ABSTRACT

The global threat of antimicrobial resistant strains calls for innovative strategies to utilize nano drug delivery systems to enhance the delivery of antibiotics, thus reducing the development of resistance. Supramolecular amphiphiles that can self-assemble into nanostructures are one such nano delivery system, that are showing potential for effective drug delivery. The aim of this study was to synthesize and formulate a novel sugar-based cationic amphiphile (BCD-OLA) derivative from a Beta-cyclodextrin (BCD) head and long C18 carbon chain with a terminal amine; oleylamine (OLA), using inclusion complexation for application in antibiotic delivery. A suspension method was used for preparing the BCD-OLA amphiphile, which was then utilized for the formulation of nanovesicles. The complexation of BCD-OLA was confirmed by FTIR, ^{1}H NMR, 2D NMR NOESY spectrum and molecular dynamic (MD) simulations. Thereafter, biosafety was evaluated using the *in vitro* MTT cytotoxicity assay. Size, zeta potential (ZP), polydispersity index (PDI), entrapment efficiency, *in vitro* drug release and antimicrobial activity of BCD-OLA-loaded nanovesicles was also evaluated. MD of the BCD-OLA simulation showed that the mechanism responsible for amphiphile formation was through hydrophobic inclusion of OLA in BCD. MTT results showed cell viability of 75–100%, thus affirming biosafety of BCD-OLA complex. TEM images showed the self-assembled structures to be vesicles. The formulated nanovesicles size was shown to be 125.1 ± 8.30 nm with a PDI of 0.231 ± 0.05, and ZP of 19.3 ± 9.20mv. The encapsulation efficiency of vancomycin was 40.2 ± 4.5%. Vancomycin release from the nanovesicles was found to be sustained, with an 80% release over a 48 h period. The *in vitro* antibacterial test showed that the BCD-OLA had a 2- and 4-fold lower MIC against *Staphylococcus aureus* (SA) and Methicillin-resistant *Staphylococcus aureus* (MRSA), respectively, compared to bare vancomycin. Further, intracellular and macrophage studies showed that the system had a 459-fold reduction of intracellular bacteria using infected human embryotic kidney cells (HEK), and an 8-fold reduction in infected macrophages, contrast with bare vancomycin. These discoveries affirmed the potential of the BCD-OLA complex as a promising biosafe effective nanocarrier for antibiotic delivery.

1. Introduction

Despite the immense progress achieved in the management and treatment of infectious diseases, antimicrobial resistance is on the rise (Butler et al., 2017), and has significantly impacted global health, development and economy (Padiyara et al., 2018). It is estimated that by 2050, approximately 10 million lives per year with a total 100 trillion USD of economic output are in danger, because of the rise in drug resistant infections (O'Neill, 2016). Furthermore, the choice of antibiotics for use in conventional therapy has been limited, with first and second line antibiotic options being ineffective, thus health care providers are forced to use more toxic and expensive antibiotics. The world health organization (WHO) has predicted that if no proactive solutions are taken to slow down the process of drug resistance, the return to the pre antibiotic era is eminent (Arias-León, 2018). Methicillin-resistant *Staphylococcus aureus* (MRSA) is an infectious disease causing pathogen that has acquired considerable concern in the public health sector during the past two decades as the second leading cause of infectious disease, after *Clostridium difficile* (Magill et al., 2014). Recent studies have shown that isolated MRSA strains are less sensitive to Vancomycin

* Corresponding authors at: Discipline of Pharmaceutical Sciences, College of Health Sciences, University of KwaZulu-Natal, Private Bag X54001, Durban, South Africa. School of Pharmacy and Health Sciences, United States International University, P.O. BOX 14634 – 00800, Nairobi, Kenya (C.A. Omolo).
E-mail addresses: comolo@usiu.ac.ke (C.A. Omolo), govenderth@ukzn.ac.za (T. Govender).

https://doi.org/10.1016/j.ijpharm.2019.118881
Received 11 August 2019; Received in revised form 12 November 2019; Accepted 13 November 2019
Available online 09 December 2019
0378-5173/ © 2019 Elsevier B.V. All rights reserved.

(VCM), which is one of last resort antibiotic treatment for this bacterial strain (Marston et al., 2016). Furthermore, the decline of 56% of market-approved antibiotics in the last 20 years (Conly and Johnston, 2005) has been attributed to decreased product life cycle and increased production cost, compared to drugs for chronic diseases, which has led to a decline in antibiotic research (Slama, 2008), Thus, innovative strategies are needed to combat antibacterial resistance and protect current commercially available antibiotics.

Novel drug delivery systems such as liposomes, solid lipid nanoparticles, polymersomes, and dendrimers, have been reported to offer numerous advantages over conventional dosage forms. This includes; site specific drug release, intracellular drug delivery, controlled release, performance enhancement of the encapsulated drug, and improved therapeutic index (Xu et al., 2015; Kalhapure et al., 2015). The formulation of drug delivery systems with inherent antimicrobial activity will further potentiate the action of loaded antibiotics. There have been several reports of antibiotic drug delivery systems with inherent antimicrobial activity (Hussain et al., 2018; Álvarez-Paino et al., 2017). The utilization of a nano delivery system with inherent antibacterial activity has been shown to expand the spectrum of currently available antibiotic (Fernandes et al., 2017), thus showing potential to combat antibacterial resistance. Most of these systems have shown either toxicity or concentration dependent toxicity. Therefore, the synthesis of delivery systems with inherent antimicrobial activity and little or no toxicity will be an invaluable tool to combat antimicrobial resistance.

We herein report a novel amphiphile coined from Cyclodextrins (CDs) and Oleylamine (OLA) via supra molecular complexation with inherent antibacterial activity for the delivery of antibiotics. CDs are cyclic oligosaccharides linked covalently through α(1–4) ether linkages, produced by starch digestion by bacteria (Szejtli, 1998; Loftsson and Brewster, 1996). The most common CDs are α-, β- and γ-CD which are composed of six, seven and eight units of glucose, respectively. These are characterized by their crown shape with internal cavities ranging from 5 to 8 Å (Loftsson and Brewster, 1996; Martín et al., 2017; Hedges, 2009). The amphiphilic nature and ability to complex with different molecules make CDs highly attractive for use in the pharmaceutical industry (Brewster and Loftsson, 2007; Carrier et al., 2007; Uekama et al., 1998; Hirayama and Uekama, 1999; Davis and Brewster, 2004). In 2018 it was published that there are 56 CDs complex-based pharmaceutical products available in the market (Crini et al., 2018).

Complexation of CDs with hydrophobic compounds through chemical modification (Li and Loh, 2008) or through host-guest interaction using their hydrophobic cavities via non-covalent bonds have produced macrocyclic amphiphiles, which are self-assembling to form different nanoparticles such as micelles, monolayers, bilayer vesicles, or liquid-crystalline nanoparticles (Sallas and Darcy, 2008). Vesicles made from supramolecular amphiphiles through self-assembling are able to mimic the biological membrane and at the same time control the release of the loaded drug (Allen and Cullis, 2004). Despite the variety of CDs based materials that have been developed, most of amphiphilic cyclodextrin derivatives useful for drug delivery have been synthesized by covalent modification of cyclodextrin (Varan et al., 2017), which usually involve complex and expensive methods, use harmful solvents and have always resulted in formation of covalent bonds between the complex components. Thus, there is a need to develop simple CDs based amphiphiles to achieve maximum benefits from the unique structure of this compound for drug delivery.

Individual components of the proposed delivery system have distinct properties for application in antibiotic delivery. CDs are known as 'trojan horses' for antibacterial drugs (Santos et al., 2017), whilst OLA is an unsaturated fatty amine that belongs to oleic fatty acid, and is used as surfactant, solvent and reducing agent in the synthesis of different nanoparticles (Mourdikoudis and Liz-Marzan, 2013). It has also been shown to have inherent antimicrobial activity and it is used in the synthesis of intracellular delivery systems (Cioffi and Rai, 2012; Lim et al., 2009). Therefore, we envisage that the combination of BCD with OLA will result in a superior drug delivery system with enhanced antibacterial activity.

In this study, we propose a novel sugar-based amphiphile from Beta Cyclodextrin (BCD) head and long C18 carbon chain with a terminal amine (OLA) associated through non-covalent bonds. By using these pair of complementary partners, that associate strongly and selectively at molecular level to form a thermodynamically stable non-covalent complex, that resulted to an amphiphile (Schreiber and Smith, 2019). This amphiphile can be used to formulate a novel nano delivery system for antibiotics. We envisage the hydrophobic tail of OLA to be entrapped in BCD via inclusion complexation, forming a cationic amphiphile that has a BCD hydrophilic head and OLA hydrophobic tail with a free primary amine. The amphiphile is expected to self-assemble into nanoparticles wherein the model antibiotic can be loaded. Although there are many analogous systems for drug delivery using BCD and hydrophobic guest molecules (Shi et al., 2017; Sun et al., 2012), to the best of our knowledge, there have been no reports on this cationic amphiphile (BCD-OLA), for the delivery of any class of drug using this novel material. Despite the reported uses of BCD as a stabilizer for magnetic nanoparticles through inclusion complex with surface bound OLA and oleic acid (Mori and Yamashita, 2011), there have been no reports on such cationic amphiphiles with self assembling properties without chemical modification of the original structure of the parent compounds.

2. Materials and methods

2.1. Materials

B-Cyclodextrin and Oleylamine (≥98%) were purchased from Sigma-Aldrich (USA). Vancomycin hydrochloride acquired from Sinobright Import and Export Co., Ltd. (China) was converted to the VCM free base, according to a previously reported method (Kalhapure et al., 2014). 3-(4,5-dimethylthiazol-2-yl)-2,5-diphenyltetrazolium bromide (MTT) were purchased from Merck Chemicals (Germany). For bacterial cultures, Mueller-Hinton Broth (MHB), Nutrient Broth and Mueller-Hinton Agar (MHA) were purchased from Biolab (South Africa). *Staphylococcus aureus* (SA) (ATCC 25923) and methicillin-resistant *Staphylococcus aureus* (MRSA) (*Staphylococcus aureus* Rosenbach ATCC BAA 1683), Purified water used in the study was produced in the laboratory with a Milli-Q water purification system (Millipore corp., USA). for ^{1}H NMR and 2D NMR measurements Bruker 400 Ultra shield™ (United Kingdom) was used. All reagents and solvents used in this study were of analytical grade.

2.2. Synthesis of the BCD-OLA amphiphile

The inclusion complex suspension method (Lang et al., 2002) was employed to synthesize the BCD-OLA amphiphile. Briefly, BCD was dissolved in phosphate buffer saline (PBS) solution (0.1 M, pH 7.4) at a concentration of 10% (w/v). Thereafter OLA was added at equimolar concentration and the mixture was stirred at 55 °C, overnight. The final product was freeze dried and resulted in a white powder form.

2.3. Characterization of the BCD-OLA amphiphile

2.3.1. Fourier transform-infrared (FT-IR)

FT-IR analysis was performed on BCD, OLA and lyophilized BCD-OLA using a Bruker Alfa spectrophotometer (Germany) in order to understand the formation and effect of complexation on the functional groups.

2.3.2. NMR

^{1}H NMR and 2D Nuclear Overhauser Effect measurements (NOESY spectrum) of BCD, OLA and lyophilized BCD-OLA were recorded at 300 K, in deuterium water (D_2O, using a Bruker 400 Ultrashield™

(United Kingdom) NMR spectrometer. Samples for NMR were prepared with concentration of BCD (16 mg/mL), OLA (8 mg/mL) and BCD-OLA (16 mg/ mL) in D_2O. For 2D NOESY spectrum, the number of scans (ns) used was 18 and the mixing time was 200 ms.

2.3.3. Stoichiometry of the complex

The determination of the stoichiometries of complexes is paramount to determine their stability. Job's method is widely used to measure stoichiometries of complexes (Ghosh et al., 2018; Yang et al., 2018), where changes in analytical signals are measured and then plotted against the corresponding reagent molar fractions (Bosque-Sendra et al., 2003). In this study UV–Vis spectroscopy method was employed to measure the stoichiometry of the BCD-OLA complex. Different molar ratios of BCD and OLA ranging from 1:9 to 9:1 were prepared, at a constant total concentration of 0.48 mM; and the complex absorbance was measured at 268.5 nm. Job's plot was generated by plotting the difference in absorbance (ΔA) of the OLA with and without BCD versus the molar fraction of OLA in the complex. Molar fraction was calculated using the following equation:

$$\text{Molar fraction of OLA (r)} = \frac{\text{Molar concentration of OLA}}{\text{Total Molar concentration of the complex}}$$

2.3.4. All-atom molecular dynamics simulations

2.3.4.1. Molecular dynamics simulation of the formation of Oleylamine and β-cyclodextrin amphiphile formation. All atomic MD simulations were performed to understand the inclusion complexation mechanism of the OLA (guest) in BCD (host). OLA (PubChem ID: 5356789) and β-cyclodextrin (PubChem id: 444041) structures were downloaded from the PubChem database (Kim et al., 2015). The CHARMM General Force Field (CGenFF) force field (Vanommeslaeghe et al., 2010) parameters were used for both molecules, and the system was solvated using the TIP3P water model (Mark and Nilsson, 2001). The system containing a total of 7771 water molecules, 1 molecule of OLA and 1 molecule of BCD was used for the simulation. The steepest descent method was used to minimize the energy of the system (Bixon and Lifson, 1967) and two equilibration simulations were performed. The first used canonical ensemble (NVT), and the second used isobaric-isothermic ensemble (NPT), for 100 picoseconds (ps) each. For production of the simulation, NPT ensemble was used for 100 ns at temperature of 328.15 K and pressure of 1 atm. The velocity-rescale method (Bussi et al., 2007) was used for temperature coupling and Parrinello-Rahman method (Parrinello and Rahman, 1981) was employed for pressure coupling. The Particle Mesh Ewald (PME) method (Darden et al., 1993) was employed for long-range electrostatic interactions. 10 Å cut-off was employed for van der waals force (VdW) and short-range coulombic interaction.

2.3.4.2. Oleylamine and β-cyclodextrin amphiphile self-assembly simulation. The self-assembly mechanism of the BCD-OLA amphiphile was further investigated, using last frame (100 ns) of OLA and BCD inclusion complex simulation, as input for self-assembly simulation. For random insertion of 8 complexes of BCD-OLA, GROMACS insert-molecules tool was employed. The CHARMM General Force Field (CGenFF) parameters were used for molecules (Vanommeslaeghe et al., 2010), and the system was solvated using the TIP3P water model (Mark and Nilsson, 2001). The system contained a total of 8394 water molecules, 8 molecules of OLA and 8 molecules of BCD. The steepest descent method was used to minimize the energy of the system (Bixon and Lifson, 1967), and then two sequential equilibration runs were performed. The first used canonical ensemble (NVT), and the second used NPT, for 100 ps each. The production run was performed using NPT ensemble for 50 ns at temperature of 328.15 K and pressure of 1 atm. The velocity-rescale method (Bussi et al., 2007) was used for temperature coupling and the Parrinello-Rahman method (Parrinello and Rahman, 1981) was used for pressure coupling. For long-range electrostatic interactions, PME method was used. 10 Å cut-off was used for VdW and short-range coulombic interaction. GROMACS 5.1.2 was used for performing both simulations (Abraham et al., 2015).

2.3.4.3. Analysis. The center of mass distance between the molecules was calculated using *in-house* Tcl script. The binding energies and interaction energy were calculated using the g_mmpbsa tool and the number of aggregates in self-assembly simulation were determined using the g_aggregate tool (Barnoud et al., 2014).

2.3.5. In vitro cytotoxicity assay

The biosafety of BCD-OLA was measured using the MTT assay (Mosmann, 1983) on human embryonic kidney 293 (HEK 293), adenocarcinoma alveolar basal epithelial (A549) and human cervix cancer (Hela) cell-lines. Each cell line was seeded at a concentration of 2.5×10^3 cell/well into a 96-well plate containing 100 µL DMEM + 10% FBS and incubated for 24 h at 37 °C in a CO_2 humidified incubator. Thereafter, different concentrations of BCD-OLA (20, 40, 60, 80 and 100 µg/mL) was added and incubated for a further 48 h. Negative controls (blank) containing only culture medium, and positive controls containing culture medium and cells were also incubated under the same condition. Following the 48 h incubation period, the spent medium was replaced with a new 100 µL of fresh culture medium. Thereafter, 100 µL of MTT solution (5 mg/mL in PBS) was added to each well and incubated for 4 h. The spent media was then removed, and formazan crystals were solubilized using 100 µL of dimethyl sulfoxide. Microplate spectrophotometer (spectrostar nano, Germany) was used to measure the absorbance at 540 nm (proportional to the number of live cells), The following equation was used to calculate the percentage cell viability:

$$\%\ \text{Cell viability} = \left(\frac{\text{A540 nm treated cells}}{\text{A540 nm untreated cells}}\right) \times 100\%$$

2.4. Formulation and characterization of VCM loaded BCD-OLA nanovesicles

Drug loaded vesicles were formulated by dissolving 10 mg of VCM in 20 mL distilled water, then the lyophilized BCD-OLA powder was added portion wise under stirring, at room temperature and left to stir overnight. For preparation of the non-drug loaded nanovesicles, only water and lyophilized BCD-OLA powder were used. The size, PDI and ZP of BCD-OLA nanoparticles were analyzed by dynamic light scattering (DLS) using a Zetasizer Nano ZS90 (Malvern Instruments Ltd., UK). The BCD-OLA nanoparticles were diluted with milli-Q water in such a way that the scattering intensity was within the instrument's sensitivity range, after which it was analyzed. All measurements were performed in triplicate on three different batches that were prepared separately. The morphological investigations were performed using Jeol, JEM-1010 (Japan) transmission electron microscopy (TEM). BCD-OLA nanoparticles were diluted appropriately and mounted onto the surface of a copper grid, with the excess sample being removed by blotting off with filter paper, after which it was dried at ambient temperature and stained using 2% uranyl acetate solution before measurement. The images were captured at an accelerating voltage of 100 kV.

2.5. Entrapment efficiency (EE %) and drug loading (DL %)

Ultrafiltration method was used to determine the percentage of encapsulated VCM (Jadhav et al., 2018), 10 kDa molecular weight cut-off amicon®Ultra-4 centrifugal filter tubes were used. VCM loaded nanovesicles (2 mL) were placed into the upper chamber of the ultrafiltration centrifugal tube and centrifuged at 3000 rpm at room

temperature for 30 min. The concentration of free VCM in the ultrafiltrate was measured using a previously published HPLC method (Walvekar et al., 2018). The regression equation and linearity (r^2) were y = 138251x – 79,270 and 0.9998, respectively. All experiments were repeated three times at 25 °C. The EE % and DL % was calculated using the following equations:

$$\text{EE } \% = \left(\frac{\text{Weight of VCM in nanovesicles}}{\text{Weight of VCM added}}\right) \times 100\%$$

$$\text{DL } \% = \left(\frac{\text{Weight of VCM in nanovesicles}}{\text{Total weight of nanovesicles}}\right) \times 100\%$$

2.6. Differential scanning calorimetry (DSC)

The thermal profiles of the BCD, OLA, VCM, lyophilized BCD-OLA, lyophilized BCD-OLA/VCM and physical mixture were determined by DSC (Shimadzu DSC-60, Japan) (Omolo et al., 2018). Briefly, aluminum pan was loaded with samples (2 mg) and sealed using a crimper, followed by heating under nitrogen flow, at a constant rate of 10 °C/min to 300 °C. An empty pan was used as a reference.

2.7. In vitro drug release and release kinetics

Diffusion dialysis bag method was used to determine the release of VCM (Sonawane et al., 2016). Briefly, 2 mL of BCD-OLA-loaded nanovesicles and VCM solution were transferred into dialysis bags (cut-off: 14,000 Da) separately, followed by immersion in 40 mL PBS buffer, at 37 °C in a shaking incubator (100 rpm). A 3 mL sample was withdrawn from the 40 mL PBS solution and replaced with the same amount of the PBS, to keep a constant volume. The experiment was repeated in triplicate. The released VCM in the sample was quantified using a previously published HPLC method (Walvekar et al., 2018). Various mathematical models were used to study the drug release kinetics of BCD-OLA-loaded nanovesicles, including first order, Hixson-Crowell, Higuchi, Weibull and Korsmeyer–Peppas. To choose the best fit model, correlation coefficient (R^2) and root mean square error (RMSE) were calculated, while Korsmeyer–Peppas model was used to determine the release mechanism by calculating the value of the release exponent (n). DDSolver software program was used for analysis (Zhang et al., 2010).

2.8. Antibacterial activity

2.8.1. In vitro antibacterial activity

The minimum inhibitory concentration (MIC) values of VCM-loaded BCD-OLA nanovesicles against SA and MRSA were determined using broth microdilution method (Jorgensen and Turnidge, 2015). Briefly, an overnight culture in nutrient broth at 37 °C of SA and MRSA in a shaking incubator, was diluted to 0.5 McFarland standard. Specific volume of MHB was transferred to 96-well plate, followed by addition of equal volume of bare VCM (positive control), BCD-OLA solution (negative control) and BCD-OLA/VCM nanovesicles in the first well and then serially diluted. Then SA and MRSA at concentration of 5×10^5 colony forming units per mL (CFU/mL) were added to the 96 well plate containing the serially diluted samples and MHB. The broth mixture was incubated in a shaking incubator at 37 °C for 24 h, then spotted on MHA plates, and incubated for 24 h at 37 °C in order to observe the MIC values. The studies were performed in triplicate.

2.8.2. Synergism studies

Fractional inhibitory concentrations (FIC) was used to evaluate the combined effect of BCD-OLA and VCM in BCD-OLA laded nanovesicles, against SA and MRSA, based on the *in vitro* antibacterial activity results. According to the European Committee of Antimicrobial Susceptibility Testing (EUCAST) guidelines, the summation of both FICs was used to classify the interaction as synergistic, additive, indifferent, or antagonist (Microbiology et al., 2000).

The following equations were used to calculated ΣFIC:

$$\text{FIC (A)} = \text{MIC (A in presense of B)/MIC of (A) alone}$$

$$\text{FIC (B)} = \text{MIC (B in presense of A)/MIC of (B) alone}$$

$$\mathbf{\Sigma}\text{FIC} = \text{FIC (A)} + \text{FIC (B)}$$

The FIC index is shown in Table S1.

2.8.3. Bacterial membrane disruption

Bacterial membrane disruption was determined using a methodology developed by our group (Omolo et al., 2018). Briefly, MRSA (1.5×10^8 CFU/mL) suspension was incubated with BCD-OLA loaded with 500 μg/mL of VCM, in a 50:50 ratio with PBS for 4 h at 37 °C in a shaking incubator. High Resolution Transmission Electron Microscope (brightfield, darkfield, STEM diffraction) - JEOL HRTEM 2100 was used to examine the samples after being loaded onto a copper grid surface.

2.8.4. Bacterial cell viability

The viability of MRSA cells after treatment with BCD-OLA/VCM or bare VCM at their respective MIC, and bare VCM at MIC of loaded BCD-OLA nanovesicle for 18 h, was conducted using flow cytometry method, previously reported by our group (Omolo et al., 2018). Using untreated MRSA cells as a negative control. BD FACSCANTO II (Becton Dickinson, CA, USA) flow cytometer was used. All the setting of the instrument was kept the same as in the reported method.

2.8.5. Bacterial killing kinetics

MRSA from an overnight culture was diluted with phosphate buffer to a concentration of 5×10^5 CFU/mL. Equal volume of bacteria and VCM and VCM loaded nanovesicles at concentrations equivalent to 5x MIC were mixed and incubated in a shaking incubator at 37 °C. For negative control, sterile water was added. Samples were taken after 0, 1, 2, 4, 6, 8, 12 and 24 h of incubation and serially diluted in sterile water (10-fold dilution three times), and plated in triplicate on MHA plates and CFU were counted. The data were plotted using $\log_{10}$ of CFU number on Y axis against sampling time on X axis (Omolo et al., 2018).

2.8.6. In vitro intracellular activity

Human myelomonocytic cell line (THP-1) displaying macrophage like activity, and HEK 293 cells were used to study the intracellular activity of BCD-OLA. THP-1 cells were cultured as a loose suspension in RPMI 1640 medium, while HEK 293 cells were cultured in DMEM, without antibiotics. Both media were supplemented with 10% decomplemented fetal calf serum (FCS) and 2 mM glutamine. 5×10^5 cells/mL of either cell line was infected with MRSA as previously described (Seral et al., 2003; Carryn et al., 2002). Briefly, an overnight culture of MRSA was washed with sterile PBS and centrifuged at a 3000 rpm at 4 °C. Washing was repeated 3 times, thereafter bacterial cells were resuspended and diluted with the specified growth medium for each cell line. Bacterial cells were then added to the wells at a density of 2.5 $x10^6$ CFU/mL for THP-1 and 2.5 $x10^{12}$ CFU/mL for HEK 293, respectively. Plates were then incubated at 37 °C in a CO_2 humidified incubator for 2 h. Thereafter, the infected cells were washed with respective culture medium, HEK 293 was washed 7 times, to remove extracellular bacteria. THP-1 cells were centrifuged at 1,500 rpm for 7 min, four times, to remove any non-phagocytosed bacteria, followed by gentle resuspension of the THP-1 cell sediment in pre-warmed RPMI 1640 medium (Carryn et al., 2002). The last washing medium was then plated onto MHA plates, to ensure all extracellular bacterial cells had been removed and that no growth was observed. Thereafter, fresh medium was added to the cells, and either VCM loaded BCD-OLA (concentration of VCM 7.81 and 39.05 μg/mL, which represent the MIC and 5X MIC of BCD-OLA/VCM, respectively), or bare VCM (31.25 and

156.25 μg/mL, which represent the MIC and 5X MIC of bare VCM, respectively), was added and incubated for 24 h. Untreated cells were used as controls and incubated under the same conditions. Post infection and treatment, cells were lysed with 0.1% triton X in distilled water (Abed et al., 2015). The lysates for both cells were then plated onto MHA plates, at appropriate dilutions for 24 h in order to determine the number of viable bacteria cells by counting the colony forming units (CFU) (Carryn et al., 2002). The CFU/mL was calculated using the equation below:

$$\text{CFU/mL} = \frac{\text{number of colonies} \times \text{dilution factor}}{\text{volume of the culture plate}}$$

2.9. Effect of storage condition

The effect of storage on the physical stability of BCD-OLA nanovesicles was evaluated for 90 days, at room temperature (RT) and at 4 °C, respectively, by assessing the physical appearance, particle size, PDI, and ZP parameters (Omolo et al., 2018).

2.10. Statistical analysis

All values were represented as mean ± SD. Paired *t*-test was used to compare individual groups and p values < 0.05 were considered statistically significant. One-way analysis of variance (ANOVA), followed by Bonferroni's multiple comparison test, was used for statistical analysis. GraphPad Prism Version 6 (Graph Pad Software Inc., San Diego, CA) was used.

3. Results and discussion

3.1. Synthesis and characterization of the BCD-OLA complex

The BCD-OLA complex was prepared using a suspension method. BCD was dissolved in PBS buffer (0.1 M, pH 7.4) and the solution temperature was adjusted to 55 °C. To this, OLA was added dropwise, and a white foaming solution was formed directly. The mixture was left overnight under vigorous stirring. The newly formed mixture was physically different from its individual components. BCD is soluble in water and forms a clear solution, whilst OLA is hydrophobic and immiscible with water. Thus, the appearance of white foam showed that the inclusion complex that was formed is amphiphilic. The amphiphile could have been formed via a non-covalent host-guest interactions of OLA (guest) and BCD (host) resulting to molecular assembly of amphiphilic in nature (Fig. 1). Association between these complementary partners (OLA and BCD) could be attributed to hydrogen bonding and hydrophobic effects (Schreiber and Smith, 2019). Further confirmation of the complex formation was determined via ^{1}H NMR, FT-IR and MD simulation. For the final product, the mixture was then frozen and lyophilized to remove the water, and isolate.

3.2. Fourier transform-infrared (FT-IR)

FT-IR was used to study the molecular interaction of the BCD-OLA complex (Li and McGown, 1994). Spectral comparison for OLA, BCD and BCD-OLA is shown in (Fig. 2). Characteristic bands of OLA were obtained (the primary amine N-H symmetric and asymmetric stretching vibration at 3369 cm^{-1} and 3281 cm^{-1} respectively, bands around 3000 cm^{-1} are due to bending vibration of =C—H, symmetric and asymmetric vibration of C—H at 3004 cm^{-1}, 2851 cm^{-1} and 2920 cm^{-1} respectively, all the remaining bands are due to bending vibration of —C = C at 1644, NH_2 at 1586 cm^{-1}, CH_3 at 1461 cm^{-1}, C—N at 1064 cm^{-1} and C—C at 721 cm^{-1}), whilst BCD showed (O—H stretching broad band at 3300–3500 cm^{-1}, C—H stretching at 2923 cm^{-1} and C—O stretching at 1020). The spectrum obtained for BCD-OLA complex showed all the characteristic peaks for the individual components, BCD and OLA, with expected change in size and intensity. The reduction in the intensity of the symmetric and asymmetric vibration bands of C-H of OLA (indicated by dotted circle in Fig. 2C), could be due to insertion of the aliphatic chain of OLA inside BCD cavity. This result was further corelated with NMR and MD simulation which indicated that the formation of the novel amphiphile had occurred without any chemical change. This could be attributed to hydrophobic interaction between the BCD and C18 aliphatic chain of OLA (Martín et al., 2017; Sun et al., 2012).

3.3. NMR

^{1}H NMR is commonly employed for the detection of inclusion complex formation in solution because it affects the proton environment in both guest and host compound, which leads to variation in chemical shift of these protons (see Fig. 3).

Confirmation of OLA inclusion inside the BCD cavity was determined by proton NMR. As a result of inserting OLA inside the BCD cavity, distortion of the cavity protons was detected by ^{1}H NMR. Spectra was recorded under the same condition for BCD, OLA and BCD-OLA complex using D_2O as NMR solvent. Chemical shift of the solvent was used as a secondary standard.

As shown in Fig. 4, the characteristic resonances for OLA were identified at 5.344 ppm (vinyl, a) of the double bond, 2.041 ppm (allyl,

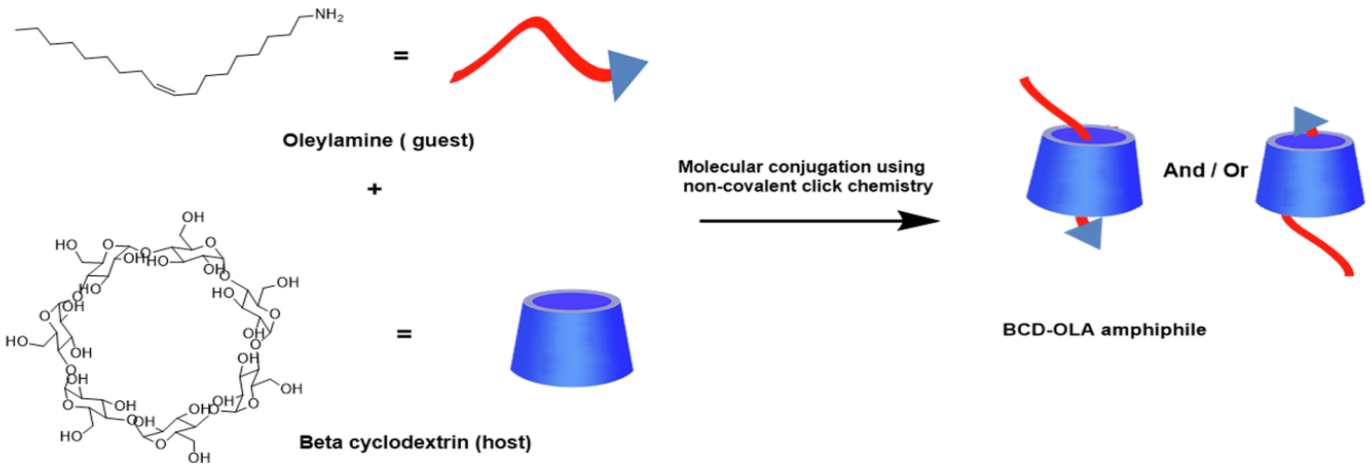

Fig. 1. Proposed mechanism for the formation of the amphiphile via inclusion complexation.

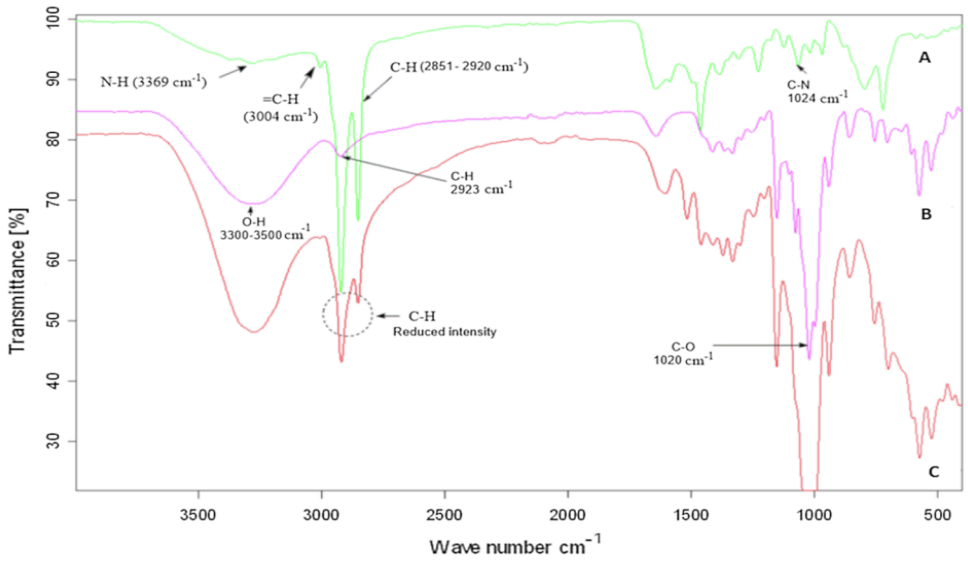

Fig. 2. FT-IR of OLA (A), BCD (B) and BCD-OLA (C).

c) and 0.929 ppm (methyl, g). Peaks for methylene protons were observed at 2.615 ppm (b), 1.426 ppm (d) and 1.313 ppm (e), while for the amine's peak (f) there was a broad peak that was seen to overlap with that of methylene protons (e). The peaks were not sharp and well-integrated in comparison to when OLA was dissolved in $CDCL_3$ (Fig. S1), due to the insolubility of the compound in water. All characteristic peaks for BCD were also identified. Protons inside the cavity of BCD were more sensitive to the complexation, specifically proton number H-3 and H-5 (Yao et al., 2014). The normal shift of these protons before complexation, was 4.008 ppm and 3.899 ppm, respectively. After complexation there was significant upfield chemical shifts (Table S2), in comparison to H-1, H-2 and H-4 protons, which showed a minor change in chemical shift of 5.111, 3.6941 and 3.628 ppm before complexation, respectively. The lack of shift in spectra of H-1, H-2 and H-4 protons could be because they are located outside the BCD cavity (Fig. 4). There was also upfield shifting of proton H-6, which is located on the narrow end of the BCD cavity rim. However, the shift was less significant when compared to H-3 and H-5. The upfield shifting resulted in increased shielding effect, caused by displacement of water molecules from the BCD cavity with OLA alkyl chain during the formation of the complex (Wilson et al., 1997). These results imply that OLA was successfully inserted in the cavity of BCD.

The changes in chemical shifts (Δδ) from ^{1}H NMR of the pure OLA and BCD portions of the complex, in comparison with the chemical shift in BCD-OLA complex were analyzed (Table S2). The results indicated that OLA methylene protons (b and d, protons adjacent to the amine terminal group) underwent considerable changes. These shifts could have been due to formation of inclusion complex with BCD, and formation of hydrophobic and hydrogen bonds. These chemical shifts indicated correlations between the H-3, H-5, and H-6 protons of the BCD and the protons at the carbon adjacent to the amine terminal group, and also the (—CH_2—) protons of the OLA.

2D NOESY NMR is a direct and powerful technique to study inclusion complexes, by examining the intermolecular dipolar cross-correlations of the host and the guest (Yao et al., 2014). 2D NMR was used for further confirmation and verification of inclusion complex formation between BCD and OLA. (Fig. 5) shows the 2D NOESY spectrum for BCD-OLA complex. Cross-peak interaction between the protons from the aliphatic chain of OLA $(—CH_2—)_n$. Dipolar interactions of the BCD cavity protons (H-3, H-5, and H-6), with the aliphatic backbone of OLA from the 2D NMR NOESY spectrum was noticed. It was concluded that there is no correlation of the OLA with external protons (H-2 and H-4) of the BCD. These results, suggest that part of the hydrocarbon chain that separates the amine group and the unsaturated double bond of the OLA was inside the BCD cavity, while the double bond and the amine group could be protruding outside (Fig. 6). Because of the conical shape of the BCD, two opposite orientations for the OLA in the complex were possible (Fig. 6), which indicate formation of pseudorotaxanes (orientational isomers) (Yamashina et al., 2018), where OLA could be threading through BCD either from the narrow or the wider side, in a ratio of 1:1. This resulted into amphiphilic pseudorotaxanes having a hydrophobic tail of OLA and BCD providing the hydrophilic portion that self assemble. This strategy has been reported widely where an inclusion complex of 1:1 between BCD and hydrophobic moieties has

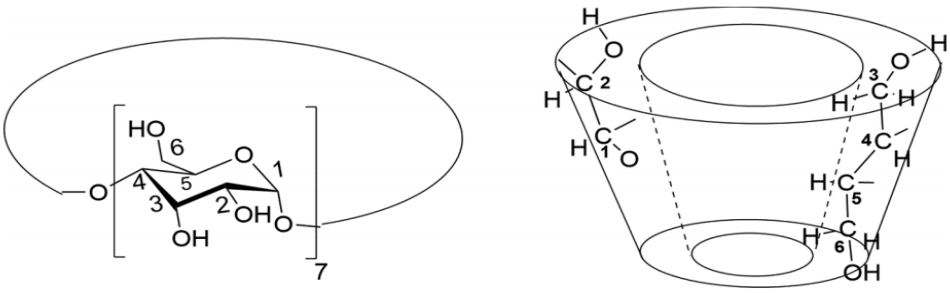

Fig. 3. Schematic representation of BCD showing the inner and outer proton orientation.

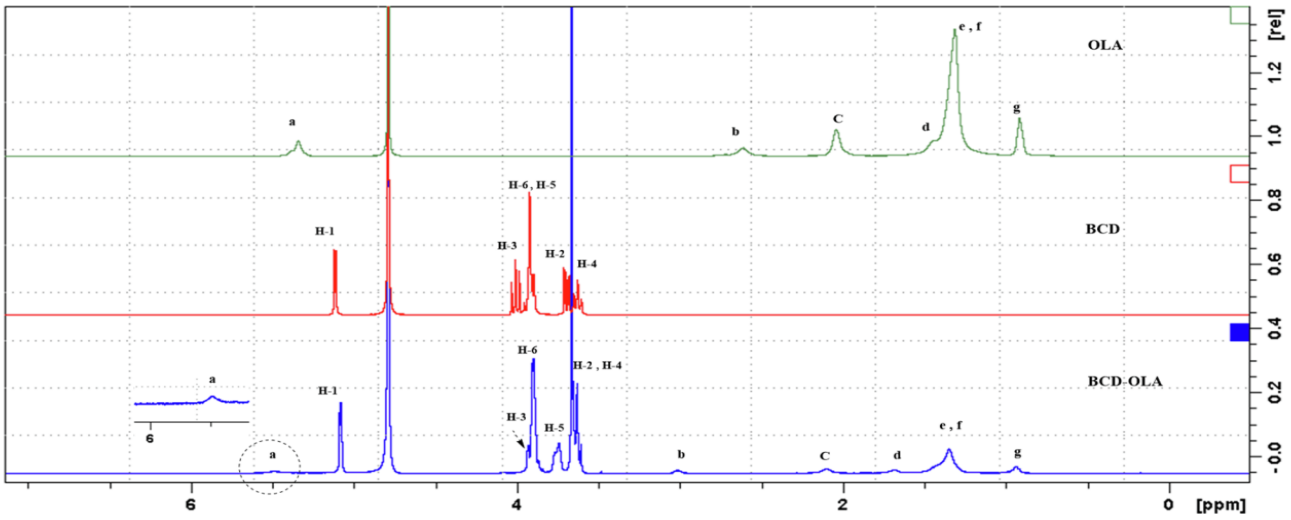

Fig. 4. ^{1}H NMR (400 MHz) spectra in D_2O at 300 K of OLA, BCD and BCD-OLA complex.

resulted in amphiphiles (Bojinova et al., 2003), and with other literature reporting formation vesicles (Zou et al., 2007; Sun et al., 2011). The interactions displayed by ^{1}H NMR and 2D NMR results indicated penetration OLA into the BCD cavity, leading to an amphiphile BCD-OLA.

3.4. Stoichiometry of the complex

Complex formation with cyclodextrin results in changes of the UV–vis absorption spectrum and can be employed to determine stoichiometry of the complex (Milcovich et al., 2018). Changes in analytical signals that occur due to formation of the complexes can then be employed to determine the stoichiometry of complexation via Job's plot (Bosque-Sendra et al., 2003). By plotting the difference in absorbance (ΔA) of OLA with and without BCD versus the molar fraction of OLA in the complex, the stoichiometry of BCD-OLA complex was calculated from the resultant Job's plot. It was observed that BCD in water formed a clear solution, however, there was a change in turbidity of the solution with variation of BCD - OLA ratios. This behavior could be attributed to the formation of the amphiphile due to BCD and OLA complexing, resulting in the formation of an amphiphilic system in water leading to the change in absorbance (Ghosh et al., 2018; Mele et al., 1998). Similar behavior has been reported for inclusion complexation between carotenoid and BCDs (Mele et al., 1998). Job's plot was generated by plotting differences in absorbance in Y axis and the value of molar fraction of OLA (r) in the X axis. The highest point in the curve from the plot which indicates the stoichiometric ratio of the inclusion complex was determined. From the calculations, r = 0.5, suggesting that a 1:1 complexation occurred, while r values of 0.33 and 0.66 indicates complexation ratios of 1:2 and 2:1 respectively. From (Fig. 7), the highest point of the curve resulted in r = 0.5, which suggested that the stoichiometric value for the BCD-OLA inclusion complex was 1:1. This result correlates with other reports from literature that employed Job's plot to confirm the stoichiometry of inclusion complexes (Martín et al., 2017; Ghosh et al., 2018).

3.5. MD simulation

3.5.1. Insertion of OLA into BCD core and self-assembly of inserted complexes

MD simulation of OLA with BCD for 100 ns was performed in order to understand their spontaneous binding and inclusion complexation. Time evolution of the center of mass (COM) distance between both molecules and interaction energy of the components were calculated. Time evolution of COM distance between BCD and OLA (Fig. 8A) showed that both molecules formed the first interaction (~12.5 ns) and continued bound until simulation time end (simulation video 1 in Supplementary material). The time evolution of interaction energy (Fig. 9B, [1]green line) showed that the interaction energy between both molecules fluctuated between ~70 kJ to ~100 kJ during binding. The interaction energy of the components also showed that Van der Waals (VdW) energy (Fig. 9B, black line) played a major role in the binding of both molecules. Visual inception of trajectory revealed that OLA first interacted with the core region of the BCD, after which the OLA rearranged its confirmations and became inserted into the core region of BCD (Fig. 8). The binding energy (ΔG_{total}) for the whole simulation trajectory was also calculated (Table S3). The VdW and electrostatic interactions contribution to the ΔG_{total} were represented by ΔE_{vdw} and ΔE_{elec} respectively, while the contributions of polar and nonpolar solvation energy to ΔG_{total} were represented by ΔG_{polar} and $\Delta G_{nonpolar}$, respectively. Binding between BCD and OLA was majorly governed by the hydrophobic interaction since ΔE_{vdw} was the most favorable contributor, followed by $\Delta G_{nonpolar}$. ΔE_{elec} and ΔG_{polar} were unfavorable for binding, however, favorable ΔE_{vdw} and $\Delta G_{nonpolar}$ lead to an overall favorable ΔG_{total}. This energetics further indicated the formation of a stable complex.

3.5.2. Oleylamine and β-cyclodextrin amphiphile self-assembly simulation

The last frame (100 ns) of the first simulation was taken, where there was inclusion complex of OLA into the core of BCD. This was replicated to make 8 complexes and 50 ns self-assembly simulations were performed (Fig. 10A–D). It was observed that these complexes started to assemble within a few nanoseconds (ns) after simulations (Fig. 10E). Simulation data revealed that there were three dimers formed around ~2 ns, two trimers around ~8.26 ns, two tetramers around ~16.15 ns, followed by a pentamer around ~17. 7 ns (simulation video 2 in Supplementary material). Overall, these results suggested that BCD-OLA complexes could self-assemble with the hydrophilic BCD retained on solvent accessible areas, while the hydrophobic OLA was on the core, away from the solvent (Microbiology et al., 2000). This result is similar to other simulation of BCD amphiphile self-assembly studies (Sun et al., 2011), and also in line with the experimental

[1] For interpretation of color in Figs. 9 and 16, the reader is referred to the web version of this article.

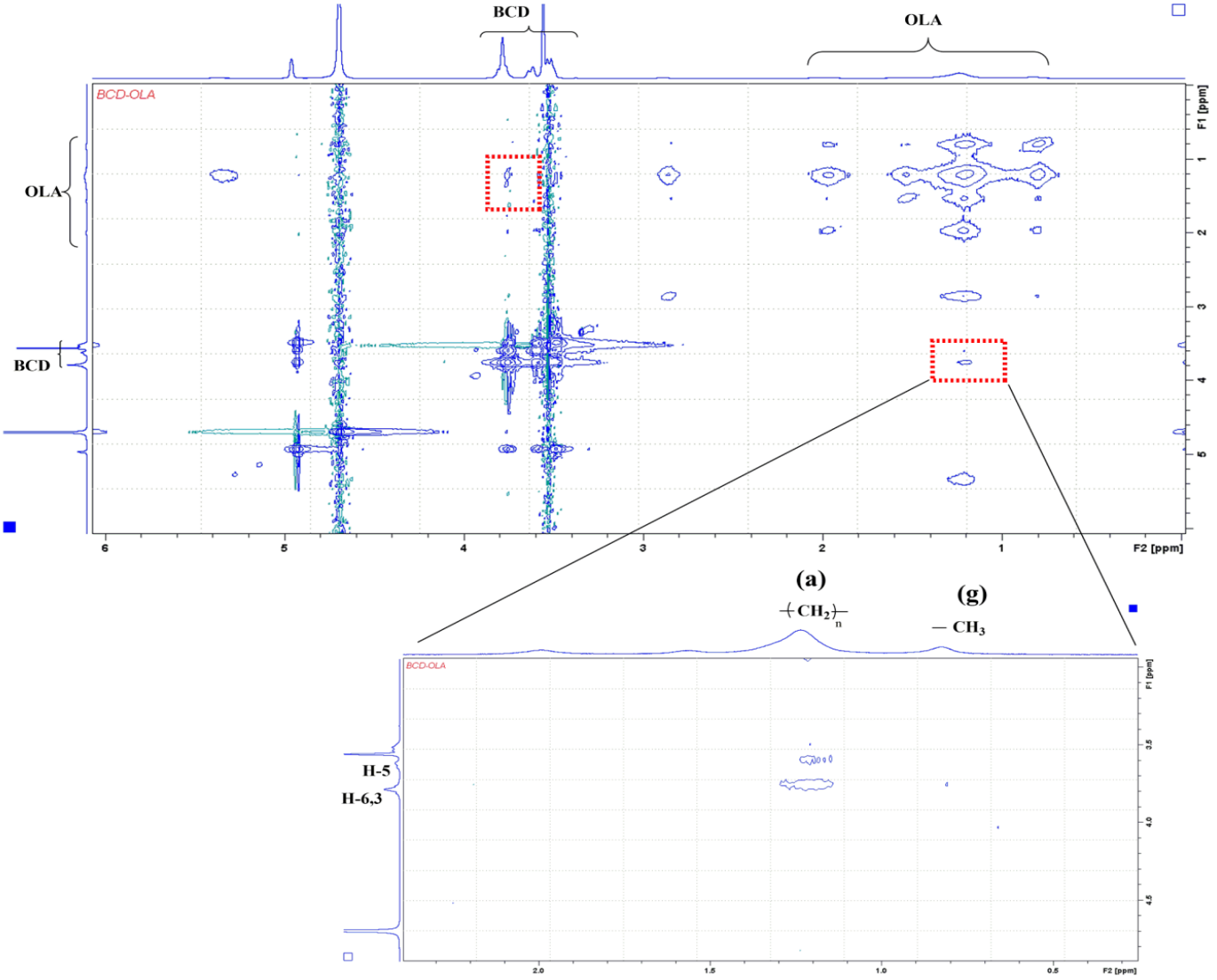

Fig. 5. 2D NOESY spectrum (400 MHz) in D_2O at 300 K of BCD-OLA complex.

results which showed BCD amphiphiles self-assembling.

3.6. In vitro cytotoxicity assay

The safety of BCD-OLA was evaluated by performing *in vitro* MTT cytotoxicity assay. Quantification of viable cells using the MTT assay is based on formation of insoluble crystalline formazan from metabolic reduction of tetrazolium salt by living mammalian cells (Mosmann, 1983). The number of viable cells is directly proportional to the quantity of formazan crystals formed. Three cell lines; A549, HEK 293 and Hela were used to determine the bio-safety of BCD-OLA. The results showed that cell viability ranged between 78.3 and 88.1 %, over all concentrations on all three tested cell lines (Fig. 11). This is in accordance with the minimum requirement guideline for biomedical products (> 75% cell viability) (Cao et al., 2010). No dose-dependent toxic effect to any of the tested cell lines, within the concentration range studied was observed. These results are consistent with previous findings in the literature, where BCD and OLA have been reported to be safe for biomedical application, thus indicating the biosafety of BCD-OLA amphiphile (Hamid et al., 2004; Riss et al., 2016).

3.7. Size, polydispersity index (PDI), zeta potential (ZP) and morphology of the optimal formulation

The formed amphiphile was evaluated for self-assembly vesicle formation. Drug loaded vesicles were formulated by dissolving VCM in 20 mL distilled water, then the lyophilized BCD-OLA powder was added portion wise. Lyophilized BCD-OLA was added to VCM in different ratios w/w (1:1, 1:2 and 1:3) under stirring, and the mixture was left to stir overnight. For preparation of the non-drug loaded nanovesicles (Blank), only water and lyophilized BCD-OLA powder were used Thereafter, the volume of the mixture was adjusted to the initial volume and filtered using 0.45 μm syringe filter. The resultant filtrate was subjected to characterization. Each experiment was prepared in triplicate. As shown in (Table 1), as the BCD-OLA concentration increased the size remained within the acceptable limit for nanoparticles (De Jong and Borm, 2008). However, PDI increased from 0.211 ± 0.04 to 0.433 ± 0.08 when the ratio changed from 1:1 to 1:6, respectively, whilst ZP was not highly affected by the amount of BCD-OLA in any tested ratio. The presence of highly positive charge on the surface of nanoparticles could be attributed to the primary amine group of OLA.

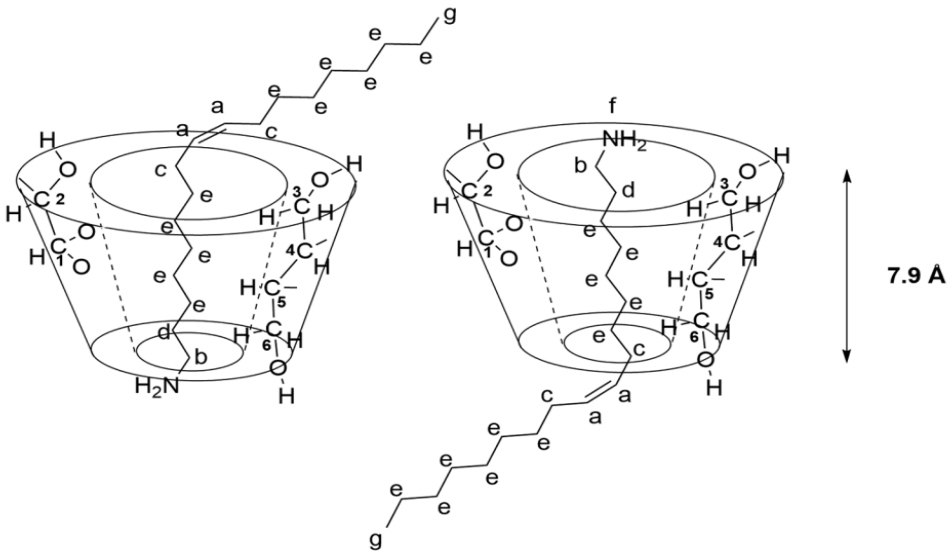

Fig. 6. The two possible orientations of OLA in the BCD cavity.

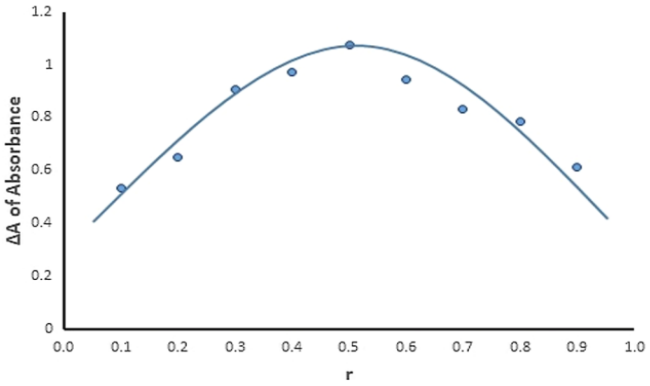

Fig. 7. Job's plot using differences in absorbance for the determination of BCD-OLA complex stoichiometry.

Although the EE % increased with increasing BCD-OLA ratio in formulation, however, high PDI values indicated non-uniformity of the particles, therefore, ratio1:3 was chosen as the optimal formulation.

TEM was used to observe the morphology of assembled nanoparticles. TEM images, (Fig. 12A and B) for non-drug loaded nanovesicles, and (Fig. 12C and D) for VCM loaded nanovesicles, showed core–shell spherical particles with distinct contrast between the center and the edge, which is a known feature of vesicular structure (Zou et al., 2007). The results were similar to those determined by the DLS technique (Fig. 11E) which showed uniform distribution of the nanovesicles with average size of approximately 125.1 ± 8.3 nm and PDI of 0.231 ± 0.05. This result is similar to a previously reported study by Jiong et al (Zou et al., 2007), where it was reported that formation of nanovesicles was due to supramolecular complexation of BCD and a hydrophobic compound, containing an azo head and three 18 C alkyl chains.

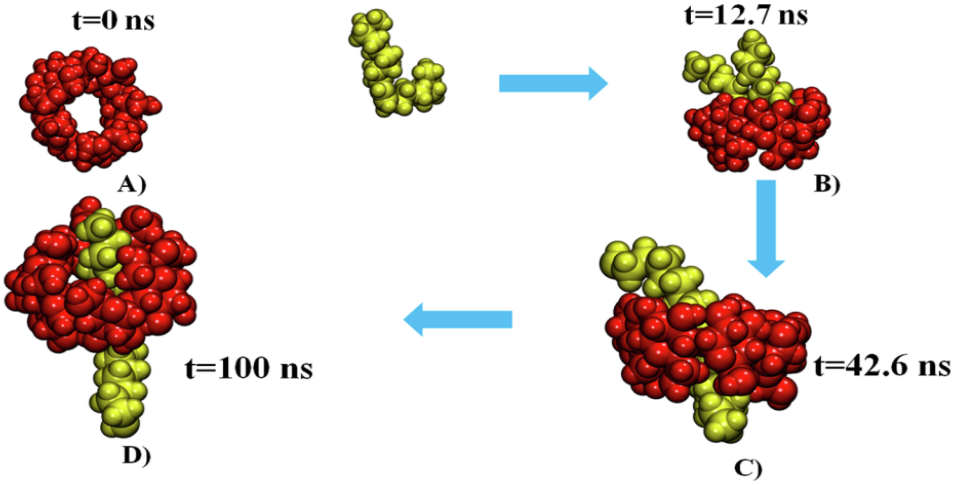

Fig. 8. Representative images from OLA and BCD simulation (A) t = 0 ns. (B) t = 12.7 ns. (C) t = 42.6 ns. (D) t = 100 ns.

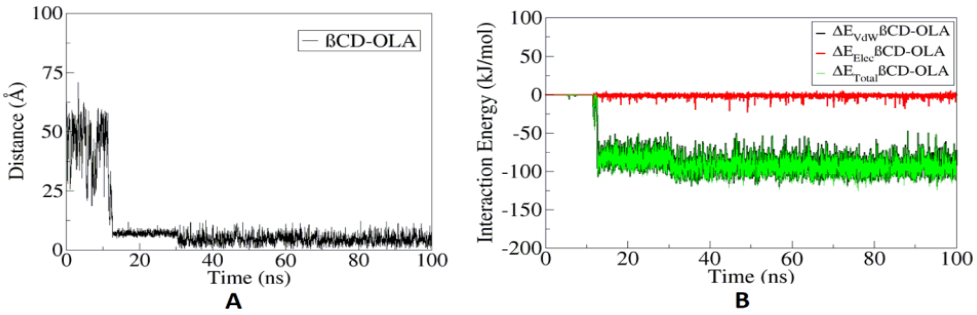

Fig. 9. (A) Time evolution of COM distance between BCD and OLA. (B) Time evolution of interaction energy between BCD and OLA and its components.

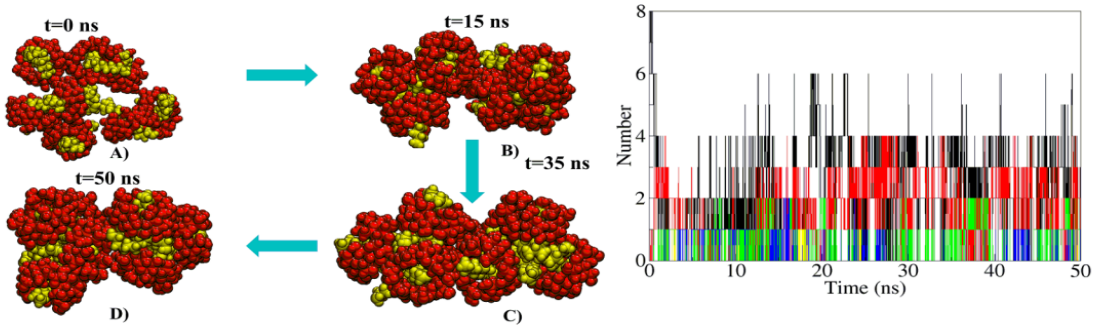

Fig. 10. (A–D) Representative image of self-assembly simulation at different time points (E) Time evolution of number aggregates formed during simulation.

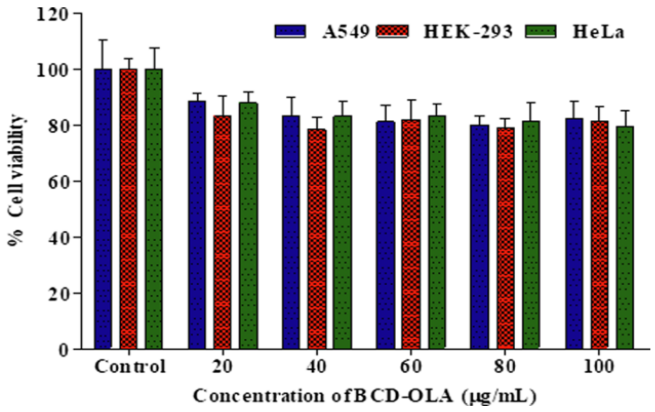

Fig. 11. MTT assay for evaluation of cytotoxicity of BCD-OLA against A549, HEK 293 and Hela cell lines.

3.8. Differential scanning calorimetry (DSC)

To investigate the melting and crystallization behavior of the BCD, OLA, VCM, physical mixture, lyophilized BCD-OLA and lyophilized BCD-OLA/VCM, thermal profiles were studied using DSC (Omolo et al., 2018). Two endothermic peaks of BCD were detected at 75.65 and 130.90 °C, respectively, whilst OLA did not show any peak within the range of the tested temperature. Interestingly, lyophilized BCD-OLA showed endothermic peak at 241.59 °C and no peak detected for BCD, which suggested the inclusion complex formation and change in the properties of the new material (Fig. 13). For VCM, the data showed a sharp peak at 126.74 °C which represents the decomposition of the glycopeptide antibiotic (Hoang Thi et al., 2010). The same peak appeared in the physical mixture of VCM with BCD-OLA, with a small peak near the region of the BCD-OLA peak (Fig. 13), whilst the individual component of the lyophilized BCD-OLA/VCM thermogram did not show any peak. This could be due to the encapsulation of non-crystalline form of VCM in the vesicles.

3.9. In vitro drug release

The drug release profiles of VCM and drug loaded BCD-OLA vesicles were determined using the dialysis method (Omolo et al., 2018). After 4 h, 45.31% of bare drug was released, while the release of VCM from the vesicles was 38.72%. Comparison of the release profile for the bare VCM and BCD-OLA/VCM nanovesicles are represented in (Fig. 14). The study revealed that the bare VCM quickly diffused out of the dialysis tube into the surrounding receiver compartment, and by 24 h all of the bare VCM had been released, whilst for BCD-OLA/VCM nanovesicles ~65% of the loaded drug was released after 24 h, and after 48 h the release was 80%. These results indicated that VCM release from the vesicles was slower when compared to the bare VCM, which is relatable to the findings in the literature (Guo et al., 2012).

Table 1
Size, PDI, ZP, EE% and DL% for the different ratio of BCD-OLA used in formulation with VCM. The values are expressed as mean ± SD (n = 3).

VCM: BCD-OLA	Size (nm)	PDI	ZP (mV)	EE%	DL%
Only BCD-OLA	104.6 ± 0.68	0.251 ± 0.01	45 ± 0.95	–	–
1 : 1	123.3 ± 10.50	0.211 ± 0.04	25.6 ± 1.50	31.0 ± 1.00	15.5 ± 1.00
1 : 3	125.1 ± 8.30	0.231 ± 0.05	19.3 ± 9.20	40.2 ± 4.50	10.0 ± 4.50
1 : 6	210.9 ± 50.00	0.433 ± 0.08	28.5 ± 6.00	51.6 ± 2.30	7.3 ± 2.30

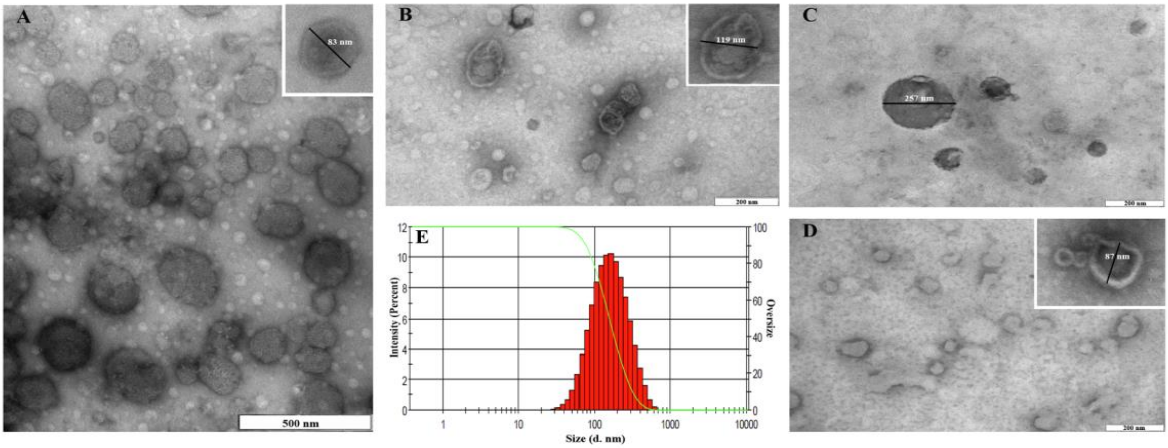

Fig. 12. Morphology of non-drug loaded BCD-OLA nanovesicles (A and B), VCM loaded nanovesicles (C and D) and histogram showing size distribution by intensity (C).

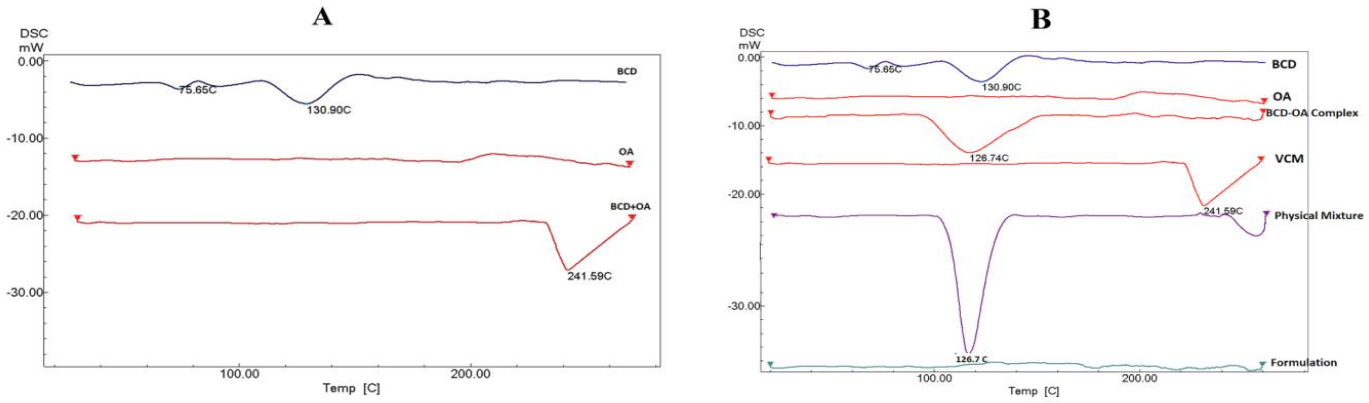

Fig. 13. DSC thermogram of BCD, OLA, VCM, BCD-OLA, physical mixture and freeze-dried formulation.

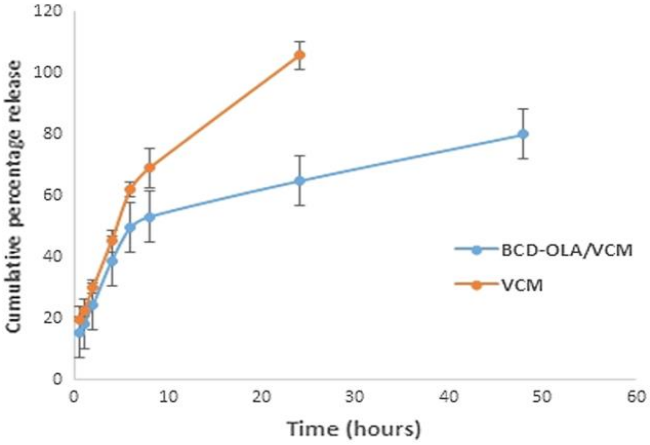

Fig. 14. Cumulative release profile of VCM and BCD-OLA/VCM.

The slower release of VCM from the vesicles in comparison to the bare drug, can be attributed to the entrapped drug at the core of the vesicles which led the drug to partition through the vesicle matrix before being released (Guo et al., 2012). This slow release profile of the drug from the formulation could be of high importance as it could extend the period of exposure of the bacteria to the killing dose of the drug, secure a prolonged antibacterial activity and enhance patient's compliance by reducing the dose frequency.

To understand the release kinetics of VCM from the BCD-OLA/VCM nanovesicles, five mathematical models were studied (Table S4). Weibull model was found to be the best fit model, with higher R^2 value of 0.978 and lowest root means square error (RMSE) value of 4.079. While the value of Weibull exponent parameter (β) was used to understand the drug release mechanism (Zhang et al., 2010), from the release kinetics analysis results, exponent parameter value (β) for BCD-OLA/VCM nanovesicle was found to be 0.473, indicating Fickian diffusion release mechanism. Furthermore, the (n) value of Korsmeyer-Peppas model was found to be 0.327, as the (n) value is less than 0.5, confirming that the release mechanism of VCM from the BCD-OLA/VCM nanovesicles is Fickian diffusion (Kalhapure et al., 2014).

Table 2
MIC values for bare VCN, BCD-OLA/VCM and BCD-OLA. (n = 3).

Time in hours	24	48	72	24	48	72
Material	SA (MIC μg/mL)			MRSA (MIC μg/mL)		
Bare VCM	3.90	3.90	3.90	31.25	31.25	31.25
(BCD + OLA)/VCM	1.95	3.90	3.90	7.81	7.81	7.81
BCD + OLA	93.75	187.5	187.5	93.75	187.5	187.5

3.10. Antibacterial activity

3.10.1. In vitro antibacterial activity

The MIC of the bare VCM, BCD-OLA and BCD-OLA/VCM was determined using microbroth dilution method against *SA* and MRSA. Data represented in (Table 2), revealed that the BCD-OLA/VCM had a 2- and 4-fold lower MIC against SA and MRSA, respectively, compared to the bare VCM. The MIC for BCD-OLA/VCM nanovesicles against SA and MRSA was 1.95 and 7.81 μg/mL, respectively, whereas for the bare VCM it was 3.90 μg/mL and 31.25 μg/mL, respectively, against the same bacteria. BCD-OLA was found to have some activity against the studied strains, MIC was found to be 93.75 μg/mL against SA in the first 24 h, which then became 187.5 μg/mL until the end of the study period. The same trend was noticed against MRSA, where MIC was initially 93.75 μg/mL but after 24 h it increased to 187.5 μg/mL, which indicated inherent antibacterial activity of BCD-OLA. The reduction of the MIC of VCM after loading in BCD-OLA nanovesicles was found to be 2- and 4-fold against SA and MRSA, compared to the bare VCM. This could be assigned to the ability of the nanovesicles to penetrate the bacterial cell, which led to overcoming the ion trapping of the peptidoglycan of the bacterial cell membrane (Chakraborty et al., 2012). These results indicated BCD-OLA/VCM could be a more efficient nanoantibiotic, compared to the bare drug. The reduction in the MIC could result in lowering the amount of drug required for SA and MRSA infections without affecting the intended therapeutic outcomes.

3.10.2. Synergism

To determine the synergism of these nanovesicles for enhancing antimicrobial activity, the FIC was calculated (Table S5). The FIC index values were used to determine the synergistic interactions between the antibacterial agents, as recommended by EUCAST guidelines (Microbiology et al., 2000). The synergistic interactions between VCM and BCD-OLA were found to be significant, when tested against SA and MRSA, where the FIC index for the loaded formula was found to be $\leq$ 0.5 against the both tested organisms. This synergistic effect on bacteria could be due to the inherent antibacterial activity of BCD-OLA (Santos et al., 2017; Cioffi and Rai, 2012), which acts via a mechanism different from that of VCM. BCD-OLA in combination with VCM resulted in enhanced antibacterial activity compared to VCM alone. Multiple mechanisms of action in a single delivery system with an increased concentration of the drug at the infection site, might help in reducing the development of antibacterial resistance (Huh and Kwon, 2011).

3.10.3. Bacterial membrane disruption

The disruption of MRSA membrane caused by BCD-OLA was evaluated using High Resolution Transmission Electron Microscope (HRTEM). The bacteria were incubated with BCD-OLA for 4 h, and thereafter examined using HRTEM (Fig. 15). The untreated MRSA bacteria (A1 and A2) showed intact cells and an integrated cell surface (red arrow A1) with homogenous cytosol distribution. VCM treated MRSA (B1 and B2) showed cell membrane deformation with a rough surface, whilst the BCD-OLA (C1 and C1) showed cracked and disrupted membrane and released cytoplasmic materials (red arrow in Fig. 14, C1 and C2). This could be due to the small size of the nanovesicles and the electrostatic attraction between the positively charged BCD-OLA and the oppositely charged bacterial cells (Abbaszadegan et al., 2015). This eventually resulted in maximum effective damage and it is sensible to assume that VCM loaded into BCD-OLA nanovesicles can reach the site of action more effectively than free VCM. This data is consistent with the MIC values, which showed the killing effect of the system.

3.10.4. Bacterial cell viability

Flow cytometry was used as a quantitative method to determine the bacterial cells killed at MIC of the bare VCM and BCD-OLA loaded nanovesicles, after 18 h incubation. Morphological changes that resulted from incubating of the bacteria with antibiotics was detected using specific dyes (Maglica et al., 2015). Internalization of PI and green fluorescing Syto9 were employed to detect the dead and live cells in the population of MRSA after treatment with the bare VCM, and the drug loaded BCD-OLA nanovesicles, respectively. PI dye, which cannot permeate through the intact bacterial cell, was used to detect damaged or dead cells, while Syto9 dye, which is non-selective cell wall permeant used for live cells (Fittipaldi et al., 2012). Kaluza flow cytometer software was used to analyze flow cytometry data (Fig. 16 **Dot plot**). Dot plot from the flow cytometry analysis showed that viable bacterial population with strong green fluorescent was limited in the quadrant 1, due to permeation of Syto9 dye, whilst a completely permeabilized population showed both red and green fluorescent and moved diagonally in the graph toward the upper right corner limited by the quadrant 3. This indicated high penetration of PI and Syto9 dye. The results of these two populations were also displayed by intensity histograms (Fig. 16 **Histogram**). This shift was an indication of bacterial cell death and increased cell wall destruction. Positively charged BCD-OLA nanovesicles may have induced binding to negatively charged teichoic acids in the bacterial cell membrane (Zhu et al., 2011), resulting in VCM delivery to site of action, thus negatively affecting the integrity of the treated cells. After MRSA treatment, there was a shift in PI fluorescence (Fig. 16B, C and D) and two distinct populations of dead and live cells were witnessed, while there was only one population of live cells for untreated MRSA (Fig. 16A). The bare VCM (Fig. 16C) and drug loaded BCD-OLA nanovesicles (Fig. 16D), at their respective concentration (31.25 μg/mL and 7.81 μg/mL, respectively), showed 91.01 $\pm$ 1.48% and 92.82 $\pm$ 0.56% dead MRSA cells in the population. On the other hand, when the bare VCM was used at the same concentration of VCM in the drug-loaded nanovesicles (7.81 μg/mL) to treat MRSA cells (Fig. 16B), only 47.18 $\pm$ 2.5% of cells were killed. From these results we can conclude that VCM loaded within BCD-OLA nanovesicles showed the same killing effect as the bare VCM, but at a 4-fold lower concentration. These results could translate to lower dose requirement for effective treatment, which will reduce dose-dependent VCM toxicity, such as nephrotoxicity and Redman's syndrome (Ingram et al., 2008; Sivagnanam and Deleu, 2002). These results combined with the previous results affirmed better antibacterial activity of the nanovesicles which further confirmed the superiority of BCD-OLA nanovesicles as a nanodelivey system for antibiotic.

3.10.5. Bacterial killing kinetics

Killing kinetic studies were performed to determine the rate and degree of killing of MRSA (5×10^5 CFU/mL) after 24 h exposure to VCM loaded BCD-OLA and the bare VCM at 5× MIC. (Fig. 17). Decrease of the MRSA CFUs was observed for both VCM and VCM loaded BCD-OLA. However, faster killing was observed with the samples treated with VCM loaded BCD-OLA, as shown by bacterial counts decreasing below the detection limit with a 3-log reduction by 8 h. Whereas, cells treated with VCM at 5× MIC were killed more slowly, and the bacterial count was still in the detection limit after 24 h. Notably, VCM loaded BCD-OLA nanovesicles at 4 times lower concentration than the bare VCM, was able to kill at a faster rate (8 h), compared to the bare drug. This could assist in rapid and complete removal of the bacteria from the body, thus lowering the dose and regiments required to attain successful therapy.

3.10.6. In vitro intracellular activity

Intracellular ability of bacteria to infect and establish life cycle inside the cell has been attributed to factors such as internalization by the host cell, the recognition of matching host cell "invasin" components, successful adhesion, formation of specific pathogen-containing vacuoles, avoidance of the host cell defense mechanisms, reprogramming of the host cell's metabolism, adaptation of the bacterial metabolism to that of the host cell and ability of the host cells to meet the metabolic requirements of the intracellular bacteria (Eisenreich et al., 2019; Escoll

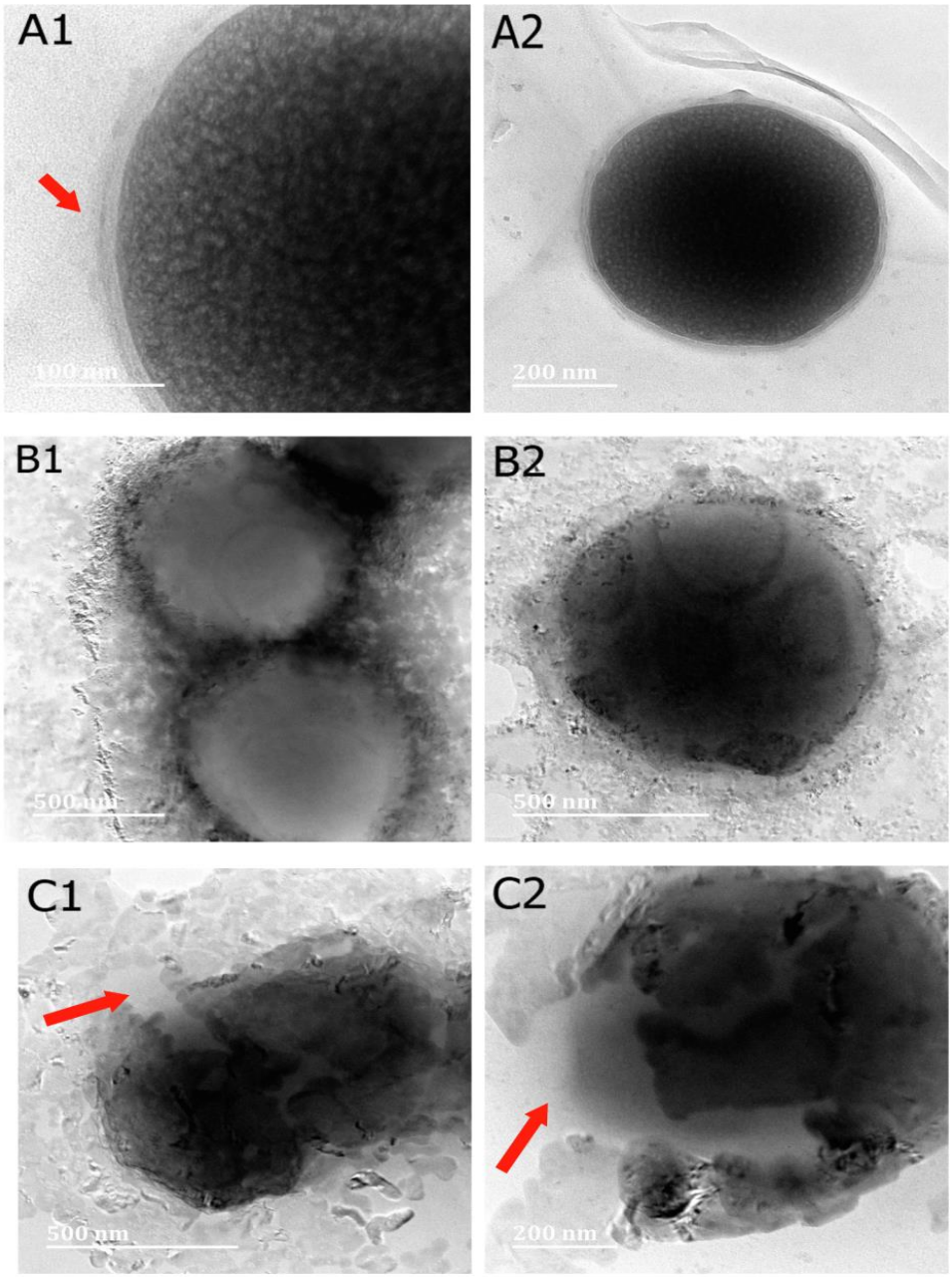

Fig. 15. HRTEM for MRSA; untreated (A1 and A2), VCM treated (B1 and B2) and BCD-OLA/VCM treated (C2 and C2).

et al., 2017). Epithelial and fibroblast cells are often colonized as they provide the above requirement for the bacteria to survive and replicate inside their cells. In this study, cell lines of THP-1 macrophages and HEK 293 cells were used as models to evaluate the ability of BCD-OLA system to eliminate intracellular bacterial infection, which is known as the main source of recurrent bacterial infection (Robino et al., 2013). After the infection process, treatment and lyses of the cell, the lysates were plated on MHA plates and quantified for CFU/mL and represented as $\log_{10}$ (Fig. 18). One-way ANOVA showed there was statistically significant reduction in the bacterial load ($P = 0.0033$ and $P < 0.0001$, $P = 0.0314$ and $P < 0.0001$) in THP-1 and HEK 293 cells, respectively, when treated with the bare VCM and the drug loaded BCD-OLA at their respective MICs and at 5x MIC. VCM showed some reduction in the bacterial load in the infected cell, but it was not statistically significant ($P > 0.05$), at both concentration used in both cell lines tested. On the other hand, drug loaded BCD-OLA system showed a 459-fold reduction of intracellular bacteria in infected HEK 293, and an 8-fold reduction in infected macrophages THP-1, compared to the bare VCM at MIC, while at 5x MIC BCD-OLA all the intracellular infections in both HEK 293 and TPH-1 cell lines were cleared. These results confirmed that the system is highly efficient in removing small colony variants in persistent infections (SCVs), which is a leading cause of chronic MRSA infection, treatment failure and source of evolving resistant strain of bacteria (Surewaard et al., 2016). More than 60% of current commercial antimicrobial drugs are now ineffective against intracellular pathogens (Abed and Couvreur, 2014). These results were

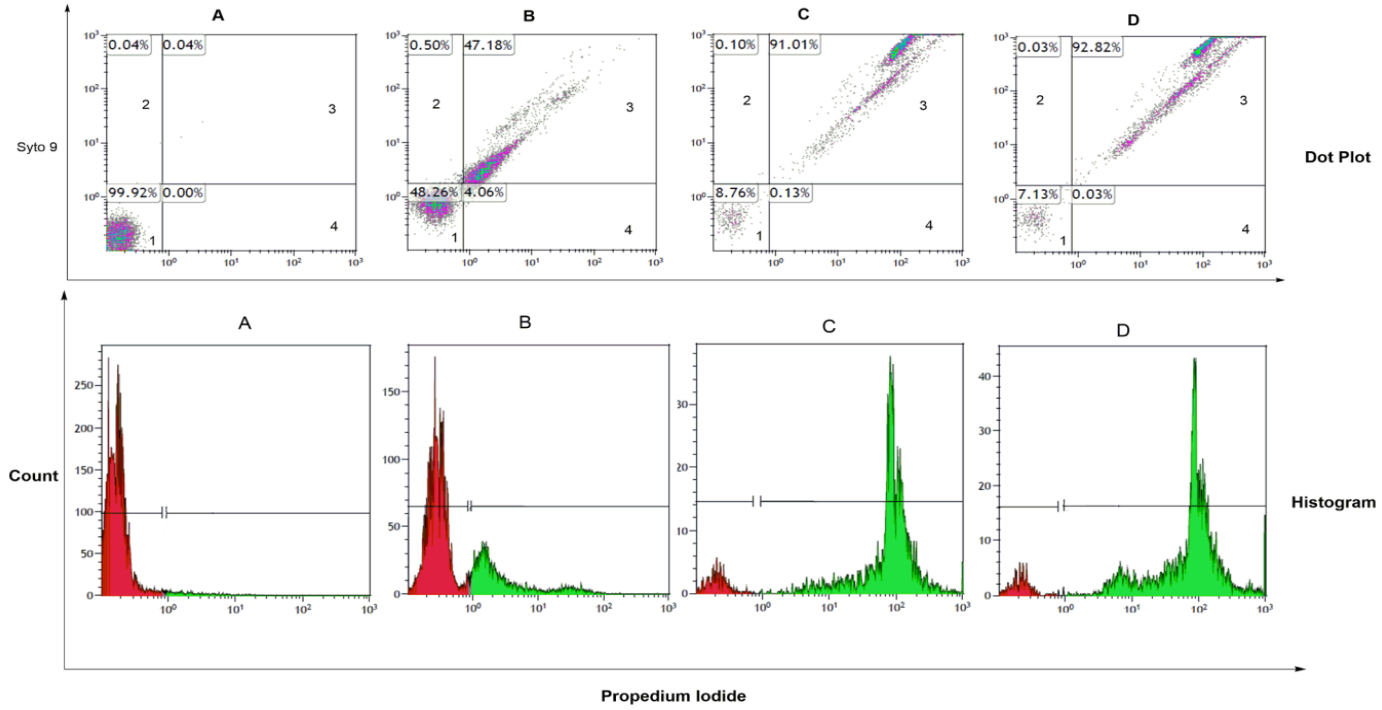

Fig. 16. Dot plot and histogram from the flow cytometry analysis A) untreated MRSA (live cells); B, C and D represents percentage dead cells in the MRSA population after incubation with VCM at (7.81 μg/mL), VCM at its MIC (31.25 μg/mL) and VCM loaded BCD-OLA nanovesicles at its MIC (7.81 μg/mL), respectively.

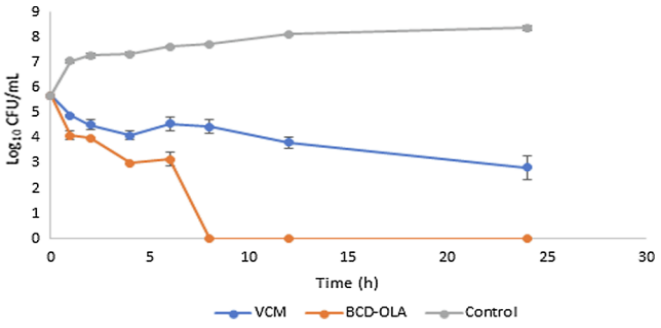

Fig. 17. Bacterial killing kinetics of 5 × MIC of BCD-OLA nanovesicles and VCM against MRSA. Sample treated with sterile water were used as control. The results are given as means SD (n = 3; data without error bars indicate that the SD is too small to be seen).

in line with other literature reports, which showed that amphiphilic cyclodextrin nanoparticles enhanced intracellular uptake of the encapsulated drug in these systems (Erdoğar et al., 2016). These findings support the applicability of BCD-OLA as a drug delivery system to eliminate these intracellular pathogens.

3.11. Effect of storage condition

To study the storage conditions effect on the BCD-OLA nanovesicles, fresh samples were prepared and characterized for their size, PDI and ZP. Thereafter samples were stored in sealed glass container at two different storage conditions; RT and 4 °C. Samples were removed at predetermined times and tested. The result is shown in Table 3. There was no change in color, phase separation or aggregation at any of the specified storage conditions or time periods. There was a slight decrease in BCD-OLA nanovesicles size from 139. 6 ± 0.82 to 113.9 ± 3.8 nm when stored at RT. However, at 4 °C, the size increased with time, coupled with higher RSD value. From this preliminary study we can conclude that RT is preferred over 4 °C as optimum storage condition for the BCD-OLA nanovesicles.

4. Conclusion

In this study, we proposed novel sugar-based amphiphile derivatives from BCD head and long C18 carbon chain with a terminal amine; OLA, using a simple suspension method. The complex was fully characterized with DSC, ^{1}H NMR, 2D NMR NOESY spectrum and FT-IR. MD simulation was used to elucidate the mechanism of complexation and the dominant binding energy, which was found to be the hydrophobic bond. The formulated nanovesicle size was shown to be 125.1 ± 8.30 nm with a PDI of 0.231 ± 0.05, and ZP of 19.3 ± 9.20 mv. The encapsulation efficiency of VCM was 40.2 ± 4.5%. VCM release from the nanovesicles was found to be sustained, with an 80% release over a 48 h period. The *in vitro* antibacterial test revealed that the BCD-OLA had a 2- and 4-fold lower MIC against SA and MRSA, respectively, compared to the bare VCM. Furthermore, intracellular and macrophage studies showed that the system had a 459-fold reduction of intracellular bacteria in infected human embryotic kidney cells (HEK), and an 8-fold reduction in infected macrophage cells (THP-1), These findings confirmed the potential of the BCD-OLA complex as a promising, biosafe, effective nanocarrier for antibiotic delivery to combat bacterial resistance to antibiotics, thus encouraging its application as a nanocarrier for delivery of other antibiotics classes.

CRediT authorship contribution statement

Mohammed Salih: Conceptualization, Methodology, Formal analysis, Investigation, Writing - original draft. **Calvin A. Omolo:** Conceptualization, Methodology, Writing - review & editing. **Nikhil Agrawal:** Software. **Pavan Walvekar:** Investigation. **Ayman Y. Waddad:** Formal analysis, Investigation, Writing - review & editing. **Chunderika Mocktar:** Resources. **Charlotte Ramdhin:** Writing -

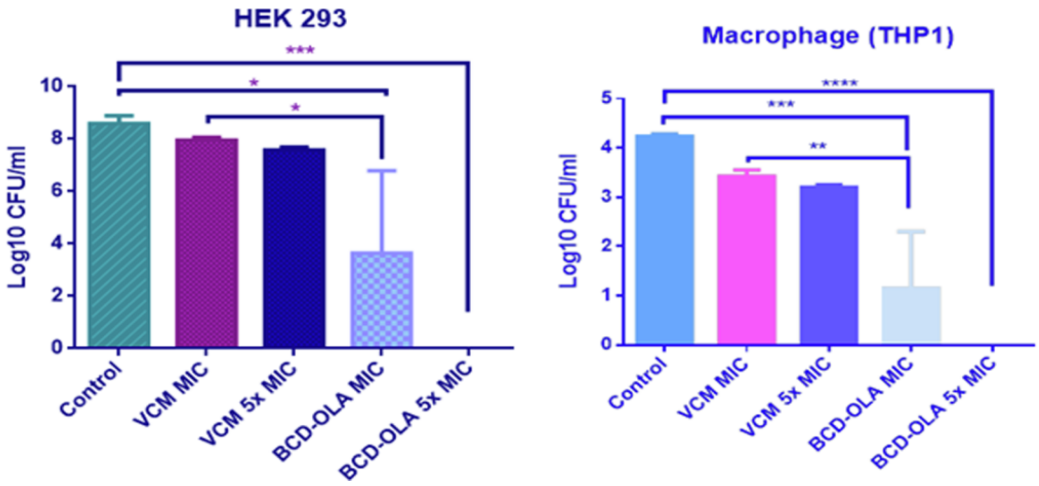

Fig. 18. Intracellular MRSA CFU recovered after treating infected (HEK 293) cells. *** denotes statistical significance for BCD-OLA 5x MIC versus untreated control MRSA, *denotes significant difference between BCD-OLA 1 MIC versus bare VCM 1MIC and control MRSA. while for infected Macrophage (THP-1) ****denotes significant difference between BCD-OLA 5 MIC versus control MRSA, *** denotes statistical significance for BCD-OLA 1 MIC versus control MRSA and **denotes significant difference between BCD-OLA 1 MIC versus bare VCM 1 MIC.

Table 3
Stability study on BCD-OLA nanovesicles over three months at 4 °C and RT. All the samples were studied in triplicate and the data were presented as mean ± SD (n = 3).

Storage condition	RT			4 °C		
Days	Size (nm)	PDI	ZP (mV)	Size (nm)	PDI	ZP (mV)
0	139.6 ± 0.8	0.206 ± 0.010	24.8 ± 7.0	139.6 ± 0.8	0.206 ± 0.010	24.8 ± 7.0
30	123.8 ± 1.8	0.241 ± 0.012	26.8 ± 8.7	151.1 ± 1.9	0.273 ± 0.015	17.4 ± 13.9
60	119.2 ± 2.9	0.224 ± 0.001	27.7 ± 1.3	144.2 ± 6.0	0.262 ± 0.005	28.6 ± 16.6
90	113.9 ± 3.8	0.221 ± 0.011	22.2 ± 1.4	155.5 ± 2.2	0.307 ± 0.031	22.3 ± 8.8

review & editing. **Thirumala Govender:** Supervision.

Declaration of Competing Interest

The authors declare that they have no known competing financial interests or personal relationships that could have appeared to influence the work reported in this paper.

Acknowledgement

The authors acknowledge the College of Health Sciences, University of KwaZulu-Natal (UKZN) and the UKZN Nanotechnology Platform, the National Research Foundation (NRF) of South Africa (Grant No. 106040) and the Medical Research Council (MRC) of South Africa for financial support. We also acknowledge the Microscopy and Microanalysis Unit (MMU) and the Department of Human Physiology at UKZN, for use of their facilities, as well as Centre for High Performance Computing (CHPC), Cape town for supercomputing resources.

Conflict of Interest

The authors declare that there is no conflict of interest.

Appendix A. Supplementary material

Supplementary data to this article can be found online at https://doi.org/10.1016/j.ijpharm.2019.118881.

References

Butler, M.S., Blaskovich, M.A., Cooper, M.A., 2017. Antibiotics in the clinical pipeline at the end of 2015. J. Antibiotics 70, 3.
Padiyara, P., Inoue, H., Sprenger, M., 2018. Global governance mechanisms to address antimicrobial resistance. Infectious Diseases: Res. Treatment 11 1178633718767887.
O'Neill, J., 2016. Tackling Drug-Resistant Infections Globally: Final Report and Recommendations: The Review On Antimicrobial Resistance Chaired By Jim O'Neill. Wellcome Trust and HM Government, London.
Arias-León, G., 2018. Resistance Mechanisms: A Problem and an Approach to the Solution. In: Sepsis. Springer, pp. 73–93.
Magill, S.S., Edwards, J.R., Bamberg, W., Beldavs, Z.G., Dumyati, G., Kainer, M.A., Lynfield, R., Maloney, M., McAllister-Hollod, L., Nadle, J., Ray, S.M., Thompson, D.L., Wilson, L.E., Fridkin, S.K., I. Emerging Infections Program Healthcare-Associated, T. Antimicrobial Use Prevalence Survey, 2014. Multistate point-prevalence survey of health care-associated infections. New England J. Med. 370, 1198–1208.
Marston, H.D., Dixon, D.M., Knisely, J.M., Palmore, T.N., Fauci, A.S., 2016. Antimicrobial resistance. JAMA 316, 1193–1204.
Conly, J.M., Johnston, B.L., 2005. Where are all the new antibiotics? The new antibiotic paradox. Canadian J. Infectious Diseases Med. Microbiol. 16, 159–160.
Slama, T.G., 2008. Gram-negative antibiotic resistance: there is a price to pay. Crit. Care 12, S4.
Xu, X., Ho, W., Zhang, X., Bertrand, N., Farokhzad, O., 2015. Cancer nanomedicine: from targeted delivery to combination therapy. Trends Mol. Med. 21, 223–232.
Kalhapure, R.S., Suleman, N., Mocktar, C., Seedat, N., Govender, T., 2015. Nanoengineered drug delivery systems for enhancing antibiotic therapy. J. Pharm. Sci. 104, 872–905.
Hussain, S., Joo, J., Kang, J., Kim, B., Braun, G.B., She, Z.-G., Kim, D., Mann, A.P., Mölder, T., Teesalu, T., 2018. Antibiotic-loaded nanoparticles targeted to the site of infection enhance antibacterial efficacy. Nat. Biomed. Eng. 2, 95.
Álvarez-Paino, M., Muñoz-Bonilla, A., Fernández-García, M., 2017. Antimicrobial polymers in the nano-world. Nanomaterials 7, 48.
Fernandes, M.M., Ivanova, K., Hoyo, J., Pérez-Rafael, S.I., Francesko, A., Tzanov, T., 2017. Nanotransformation of vancomycin overcomes the intrinsic resistance of gram-negative bacteria. ACS Appl. Mater. Interfaces 9, 15022–15030.
Szejtli, J., 1998. Introduction and general overview of cyclodextrin chemistry. Chem. Rev. 98, 1743–1754.
Loftsson, T., Brewster, M.E., 1996. Pharmaceutical applications of cyclodextrins. 1. Drug solubilization and stabilization. J. Pharm. Sci. 85, 1017–1025.
Martín, V.I., Ostos, F.J., Angulo, M., Márquez, A.M., López-Cornejo, P., López-López, M., Carmona, A.T., Moyá, M.L., 2017. Host-guest interactions between cyclodextrins and surfactants with functional groups at the end of the hydrophobic tail. J. Colloid Interface Sci. 491, 336–348.
Hedges, A., 2009. Cyclodextrins: properties and applications. In: Starch. Elsevier, pp. 833–851.
Brewster, M.E., Loftsson, T., 2007. Cyclodextrins as pharmaceutical solubilizers. Adv. Drug Deliv. Rev. 59, 645–666.
Carrier, R.L., Miller, L.A., Ahmed, I., 2007. The utility of cyclodextrins for enhancing oral bioavailability. J. Control. Release 123, 78–99.
Uekama, K., Hirayama, F., Irie, T., 1998. Cyclodextrin drug carrier systems. Chem. Rev.

98, 2045–2076.
Hirayama, F., Uekama, K., 1999. Cyclodextrin-based controlled drug release system. Adv. Drug Deliv. Rev. 36, 125–141.
Davis, M.E., Brewster, M.E., 2004. Cyclodextrin-based pharmaceutics: past, present and future. Nat. Rev. Drug Discovery 3, 1023.
Crini, G., Fourmentin, S., Fenyvesi, É., Torri, G., Fourmentin, M., Morin-Crini, N., 2018. Fundamentals and applications of cyclodextrins. In: Cyclodextrin Fundamentals, Reactivity and Analysis. Springer, pp. 1–55.
Li, J., Loh, X.J., 2008. Cyclodextrin-based supramolecular architectures: syntheses, structures, and applications for drug and gene delivery. Adv. Drug Deliv. Rev. 60, 1000–1017.
Sallas, F., Darcy, R., 2008. Amphiphilic cyclodextrins–advances in synthesis and supramolecular chemistry. Eur. J. Org. Chem. 2008, 957–969.
Allen, T.M., Cullis, P.R., 2004. Drug delivery systems: entering the mainstream. Science 303, 1818–1822.
Varan, G., Benito, J.M., Mellet, C.O., Bilensoy, E., 2017. Development of polycationic amphiphilic cyclodextrin nanoparticles for anticancer drug delivery. Beilstein J. Nanotechnol. 8, 1457–1468.
Santos, R.S., Figueiredo, C., Azevedo, N.F., Braeckmans, K., De Smedt, S.C., 2017. Nanomaterials and molecular transporters to overcome the bacterial envelope barrier: Towards advanced delivery of antibiotics. Adv. Drug Deliv. Rev. 136, 28–48.
Mourdikoudis, S., Liz-Marzan, L.M., 2013. Oleylamine in nanoparticle synthesis. Chem. Mater. 25, 1465–1476.
Cioffi, N., Rai, M., 2012. Nano-antimicrobials: progress and prospects. Springer Science & Business Media.
Lim, Y.T., Cho, M.Y., Lee, J.M., Chung, S.J., Chung, B.H., 2009. Simultaneous intracellular delivery of targeting antibodies and functional nanoparticles with engineered protein G system. Biomaterials 30, 1197–1204.
Schreiber, C.L., Smith, B.D., 2019. Molecular conjugation using non-covalent click chemistry. Nat. Rev. Chem. 1.
Shi, Y., Li, H., Cheng, J., Luan, T., Liu, D., Cao, Y., Zhang, X., Wei, H., Liu, Y., Zhao, G., 2017. Entirely oligosaccharide-based supramolecular amphiphiles constructed via host–guest interactions as efficient drug delivery platforms. Chem. Commun. 53, 12302–12305.
Sun, T., Yan, H., Liu, G., Hao, J., Su, J., Li, S., Xing, P., Hao, A., 2012. Strategy of directly employing paclitaxel to construct vesicles. J. Phys. Chem. B 116, 14628–14636.
Mori, K., Yamashita, H., 2011. Design of colloidal and supported metal nanoparticles: their synthesis, characterization, and catalytic application. J. Jpn. Pet. Inst. 54, 1–14.
Kalhapure, R.S., Mocktar, C., Sikwal, D.R., Sonawane, S.J., Kathiravan, M.K., Skelton, A., Govender, T., 2014. Ion pairing with linoleic acid simultaneously enhances encapsulation efficiency and antibacterial activity of vancomycin in solid lipid nanoparticles. Colloids Surf., B 117, 303–311.
Lang, M., Wong, R.P., Chu, C.-C., 2002. Synthesis and structural analysis of functionalized poly (?-caprolactone)-based three-arm star polymers. J. Polym. Sci., Part A: Polym. Chem. 40, 1127–1141.
Ghosh, R., Ekka, D., Rajbanshi, B., Yasmin, A., Roy, M.N., 2018. Synthesis, characterization of 1-butyl-4-methylpyridinium lauryl sulfate and its inclusion phenomenon with β-cyclodextrin for enhanced applications. Colloids Surf., A 548, 206–217.
Yang, L.-J., Chang, Q., Zhou, S.-Y., Yang, Y.-H., Xia, F.-T., Chen, W., Li, M., Yang, X.-D., 2018. Host–guest interaction between brazilin and hydroxypropyl-β-cyclodextrin: preparation, inclusion mode, molecular modelling and characterization. Dyes Pigm. 150, 193–201.
Bosque-Sendra, J.M., Almansa-López, E., García-Campaña, M., Cuadros-Rodríguez, L., 2003. Data analysis in the determination of stoichiometries and stability constants of complexes. Anal. Sci. 19, 1431–1439.
Kim, S., Thiessen, P.A., Bolton, E.E., Chen, J., Fu, G., Gindulyte, A., Han, L., He, J., He, S., Shoemaker, B.A., 2015. PubChem substance and compound databases. Nucleic Acids Res. 44, D1202–D1213.
Vanommeslaeghe, K., Hatcher, E., Acharya, C., Kundu, S., Zhong, S., Shim, J., Darian, E., Guvench, O., Lopes, P., Vorobyov, I., 2010. CHARMM general force field: A force field for drug-like molecules compatible with the CHARMM all-atom additive biological force fields. J. Comput. Chem. 31, 671–690.
Mark, P., Nilsson, L., 2001. Structure and dynamics of the TIP3P, SPC, and SPC/E water models at 298 K. J. Phys. Chem. A 105, 9954–9960.
Bixon, M., Lifson, S., 1967. Potential functions and conformations in cycloalkanes. Tetrahedron 23, 769–784.
Bussi, G., Donadio, D., Parrinello, M., 2007. Canonical sampling through velocity rescaling. J. Chem. Phys. 126, 014101.
Parrinello, M., Rahman, A., 1981. Polymorphic transitions in single crystals: A new molecular dynamics method. J. Appl. Phys. 52, 7182–7190.
Darden, T., York, D., Pedersen, L., 1993. Particle mesh Ewald: An N· log (N) method for Ewald sums in large systems. J. Chem. Phys. 98, 10089–10092.
Abraham, M.J., Murtola, T., Schulz, R., Páll, S., Smith, J.C., Hess, B., Lindahl, E., 2015. GROMACS: High performance molecular simulations through multi-level parallelism from laptops to supercomputers. SoftwareX 1, 19–25.
Barnoud, J., Rossi, G., Monticelli, L., 2014. Lipid membranes as solvents for carbon nanoparticles. Phys. Rev. Lett. 112, 068102.
Mosmann, T., 1983. Rapid colorimetric assay for cellular growth and survival: application to proliferation and cytotoxicity assays. J. Immunol. Methods 65, 55–63.
Jadhav, M., Kalhapure, R.S., Rambharose, S., Mocktar, C., Singh, S., Kodama, T., Govender, T., 2018. Novel lipids with three C18-fatty acid chains and an amino acid head group for pH-responsive and sustained antibiotic delivery. Chem. Phys. Lipids 212, 12–25.
Walvekar, P., Gannimani, R., Rambharose, S., Mocktar, C., Govender, T., 2018. Fatty acid conjugated pyridinium cationic amphiphiles as antibacterial agents and self-assembling nano carriers. Chem. Phys. Lipids 214, 1–10.
Omolo, C.A., Kalhapure, R.S., Agrawal, N., Rambharose, S., Mocktar, C., Govender, T., 2018. Formulation and molecular dynamics simulations of a fusidic acid nanosuspension for simultaneously enhancing solubility and antibacterial activity. Mol. Pharm. 15, 3512–3526.
Sonawane, S.J., Kalhapure, R.S., Rambharose, S., Mocktar, C., Vepuri, S.B., Soliman, M., Govender, T., 2016. Ultra-small lipid-dendrimer hybrid nanoparticles as a promising strategy for antibiotic delivery: In vitro and in silico studies. Int. J. Pharm. 504, 1–10.
Zhang, Y., Huo, M., Zhou, J., Zou, A., Li, W., Yao, C., Xie, S., 2010. DDSolver: an add-in program for modeling and comparison of drug dissolution profiles. AAPS J. 12, 263–271.
Jorgensen, J.H., Turnidge, J.D., 2015. Susceptibility test methods: dilution and disk diffusion methods. In: Manual of Clinical Microbiology, Eleventh ed. American Society of Microbiology, pp. 1253–1273.
E.C.f.A.S.T.o.t.E.S.o.C. Microbiology, I. Diseases, 2000. Terminology relating to methods for the determination of susceptibility of bacteria to antimicrobial agents. Clinical Microbiol. Infect. 6, 503–508.
Omolo, C.A., Kalhapure, R.S., Agrawal, N., Jadhav, M., Rambharose, S., Mocktar, C., Govender, T., 2018. A hybrid of mPEG-b-PCL and G1-PEA dendrimer for enhancing delivery of antibiotics. J. Control. Release 290, 112–128.
Seral, C., Van Bambeke, F., Tulkens, P.M., 2003. Quantitative analysis of gentamicin, azithromycin, telithromycin, ciprofloxacin, moxifloxacin, and oritavancin (LY333328) activities against intracellular Staphylococcus aureus in mouse J774 macrophages. Antimicrob. Agents Chemother. 47, 2283–2292.
Carryn, S., Van Bambeke, F., Mingeot-Leclercq, M.-P., Tulkens, P.M., 2002. Comparative intracellular (THP-1 macrophage) and extracellular activities of β-lactams, azithromycin, gentamicin, and fluoroquinolones against Listeria monocytogenes at clinically relevant concentrations. Antimicrob. Agents Chemother. 46, 2095–2103.
Abed, N., Saïd-Hassane, F., Zouhiri, F., Mougin, J., Nicolas, V., Desmaële, D., Gref, R., Couvreur, P., 2015. An efficient system for intracellular delivery of beta-lactam antibiotics to overcome bacterial resistance. Sci. Rep. 5, 13500.
Li, G., McGown, L.B., 1994. Molecular nanotube aggregates of β-and γ-cyclodextrins linked by diphenylhexatrienes. Science 264, 249–251.
Yao, Y., Xie, Y., Hong, C., Li, G., Shen, H., Ji, G., 2014. Development of a myricetin/hydroxypropyl-β-cyclodextrin inclusion complex: Preparation, characterization, and evaluation. Carbohydr. Polym. 110, 329–337.
Wilson, L.D., Siddall, S.R., Verrall, R.E., 1997. A spectral displacement study of the binding constants of cyclodextrin–hydrocarbon and–fluorocarbon surfactant inclusion complexes. Can. J. Chem. 75, 927–933.
Yamashina, M., Kusaba, S., Akita, M., Kikuchi, T., Yoshizawa, M., 2018. Cramming versus threading of long amphiphilic oligomers into a polyaromatic capsule. Nat. Commun. 9, 4227.
Bojinova, T., Coppel, Y., Lauth-de Viguerie, N., Milius, A., Rico-Lattes, I., Lattes, A., 2003. Complexes between β-cyclodextrin and aliphatic guests as new noncovalent amphiphiles: formation and physicochemical studies. Langmuir 19, 5233–5239.
Zou, J., Tao, F., Jiang, M., 2007. Optical switching of self-assembly and disassembly of noncovalently connected amphiphiles. Langmuir 23, 12791–12794.
Sun, T., Zhang, H., Yan, H., Li, J., Cheng, G., Hao, A., Qiao, H., Xin, F., 2011. Sensitive fluorescent vesicles based on the supramolecular inclusion of β-cyclodextrins with N-alkylamino-L-anthraquinone. Supramol. Chem. 23, 351–364.
Milcovich, G., Antunes, F.E., Grassi, M., Asaro, F., 2018. Stabilization of unilamellar catanionic vesicles induced by β-cyclodextrins: A strategy for a tunable drug delivery depot. Int. J. Pharm. 548, 474–479.
Mele, A., Mendichi, R., Selva, A., 1998. Non-covalent associations of cyclomaltooligosaccharides (cyclodextrins) with trans-β-carotene in water: evidence for the formation of large aggregates by light scattering and NMR spectroscopy. Carbohydr. Res. 310, 261–267.
Cao, X., Cheng, C., Ma, Y., Zhao, C., 2010. Preparation of silver nanoparticles with antimicrobial activities and the researches of their biocompatibilities. J. Mater. Sci. – Mater. Med. 21, 2861–2868.
Hamid, R., Rotshteyn, Y., Rabadi, L., Parikh, R., Bullock, P., 2004. Comparison of alamar blue and MTT assays for high through-put screening. Toxicol. In Vitro 18, 703–710.
Riss, T.L., Moravec, R.A., Niles, A.L., Duellman, S., Benink, H.A., Worzella, T.J., Minor, L., 2016. Cell viability assays. Assay Guidance Manual [Internet]. Eli Lilly & Company and the National Center for Advancing Translational Sciences.
De Jong, W.H., Borm, P.J., 2008. Drug delivery and nanoparticles: applications and hazards. Int. J. Nanomed. 3, 133.
Hoang Thi, T.H., Chai, F., Leprêtre, S., Blanchemain, N., Martel, B., Siepmann, F., Hildebrand, H.F., Siepmann, J., Flament, M.P., 2010. Bone implants modified with cyclodextrin: study of drug release in bulk fluid and into agarose gel. Int. J. Pharmaceutics 400, 74–85.
Guo, C., Zeng, L., Liu, S., Chen, Q., Dai, Z., Wu, X., 2012. In vitro evaluation and finite element simulation of drug release from polydiacetylene-polyethylene glycol stearate nanovesicles. J. Nanosci. Nanotechnol. 12, 245–251.
Chakraborty, S.P., Sahu, S.K., Pramanik, P., Roy, S., 2012. In vitro antimicrobial activity of nanoconjugated vancomycin against drug resistant Staphylococcus aureus. Int. J. Pharm. 436, 659–676.
Huh, A.J., Kwon, Y.J., 2011. "Nanoantibiotics": a new paradigm for treating infectious diseases using nanomaterials in the antibiotics resistant era. J. Control. Release 156, 128–145.
Abbaszadegan, A., Ghahramani, Y., Gholami, A., Hemmateenejad, B., Dorostkar, S., Nabavizadeh, M., Sharghi, H., 2015. The effect of charge at the surface of silver nanoparticles on antimicrobial activity against gram-positive and gram-negative bacteria: a preliminary study. J. Nanomater. 16, 53.
Maglica, Ž., Özdemir, E., McKinney, J.D., 2015. Single-cell tracking reveals antibiotic-induced changes in mycobacterial energy metabolism. MBio 6, e02236–02214.
Fittipaldi, M., Nocker, A., Codony, F., 2012. Progress in understanding preferential

detection of live cells using viability dyes in combination with DNA amplification. J. Microbiol. Methods 91, 276–289.
Zhu, C., Yang, Q., Liu, L., Lv, F., Li, S., Yang, G., Wang, S., 2011. Multifunctional cationic poly (p-phenylene vinylene) polyelectrolytes for selective recognition, imaging, and killing of bacteria over mammalian cells. Adv. Mater. 23, 4805–4810.
Ingram, P.R., Lye, D.C., Tambyah, P.A., Goh, W.P., Tam, V.H., Fisher, D.A., 2008. Risk factors for nephrotoxicity associated with continuous vancomycin infusion in outpatient parenteral antibiotic therapy. J. Antimicrob. Chemother. 62, 168–171.
Sivagnanam, S., Deleu, D., 2002. Red man syndrome. Crit. Care 7, 119.
Eisenreich, W., Rudel, T., Heesemann, J., Goebel, W., 2019. How viral and intracellular bacterial pathogens reprogram the metabolism of host cells to allow their intracellular replication. Front. Cell. Infect. Microbiol. 9.
Escoll, P., Song, O.-R., Viana, F., Steiner, B., Lagache, T., Olivo-Marin, J.-C., Impens, F., Brodin, P., Hilbi, H., Buchrieser, C., 2017. Legionella pneumophila modulates mitochondrial dynamics to trigger metabolic repurposing of infected macrophages. Cell Host Microbe 22, 302–316 e307.
Robino, L., Scavone, P., Araujo, L., Algorta, G., Zunino, P., Vignoli, R., 2013. Detection of intracellular bacterial communities in a child with Escherichia coli recurrent urinary tract infections. Pathogens Disease 68, 78–81.
Surewaard, B.G., Deniset, J.F., Zemp, F.J., Amrein, M., Otto, M., Conly, J., Omri, A., Yates, R.M., Kubes, P., 2016. Identification and treatment of the Staphylococcus aureus reservoir in vivo. J. Exp. Med. 213, 1141–1151.
Abed, N., Couvreur, P., 2014. Nanocarriers for antibiotics: A promising solution to treat intracellular bacterial infections. Int. J. Antimicrob. Agents 43, 485–496.
Erdoğar, N., Esendağlı, G., Nielsen, T.T., Şen, M., Öner, L., Bilensoy, E., 2016. Design and optimization of novel paclitaxel-loaded folate-conjugated amphiphilic cyclodextrin nanoparticles. Int. J. Pharm. 509, 375–390.

CHAPTER 3, EXPERIMENTAL PAPER 2

4.1 Introduction

This chapter addresses Aim .2, Objectives 1 - 6 and is a first-authored experimental article published in Pharmaceutical Development and Technology (Impact Factor 2.374), an ISI international journal (doi:10.1080/10837450.2020.1797786). This article highlights the formulation development of the novel SADDs through supramolecular complexation to deliver VCM, the *in vitro* toxicity evaluation, molecular dynamics simulation of the self-assembly of NPs, characterization of its physical properties, *in vitro* and *in vivo* antibacterial properties.

Graphical abstract

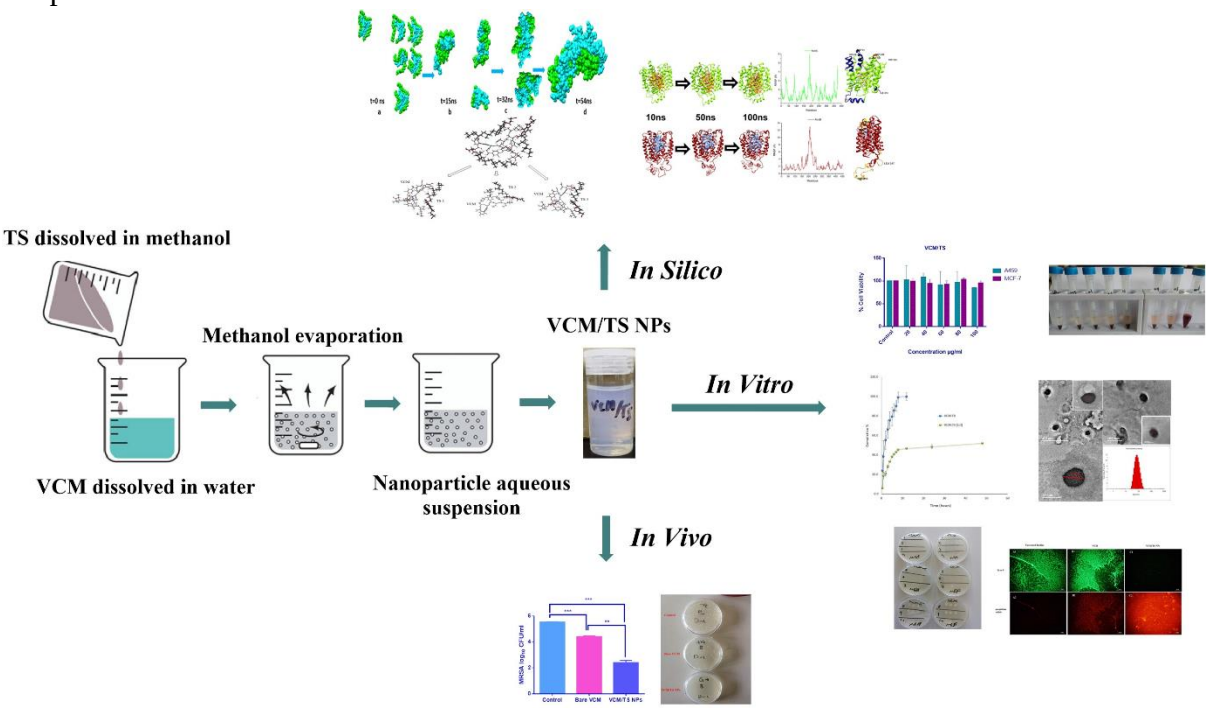

Supramolecular Self-Assembled Drug Delivery System (SADDs) of Vancomycin and Tocopherol Succinate as an Antibacterial Agent: *In vitro*, *In silico* and *In vivo* Evaluations

Mohammed Salih[a], Calvin A. Omolo[#,a,c], Nikita Devnarain[a], Ahmed A Elrashedy[b], Chunderika Mocktar[a], Mahmoud E. S. Soliman[b], Thirumala Govender[#,a]

[a]Discipline of Pharmaceutical Sciences, College of Health Sciences, University of KwaZulu-Natal, Private Bag X54001, Durban, South Africa

[b]Molecular Bio-computation and Drug Design Lab, School of Health Sciences, University of KwaZulu-Natal, Westville Campus, Durban 4001, South Africa

[c]School of Pharmacy and Health Sciences, United States International University, P.O. BOX 14634 - 00800 Nairobi, Kenya

corresponding author

Email address**:** govenderth@ukzn.ac.za; comolo@usiu.ac.ke

Graphical abstract:

Abstract

In this study self-assembled drug delivery system (SADDs) composed of a hydrophobic D-α-tocopherol succinate (TS) and a hydrophilic vancomycin (VCM) were formulated, and its potential for enhancing the antibacterial activity of VCM against Staphylococcus aureus (SA) and Methicillin-resistant Staphylococcus aureus (MRSA) were explored. The SADDs were synthesized via supramolecular complexation, then characterized for in silico, in vitro and in vivo studies. In silico studies confirmed the self-assembly of VCM/TS into NPs. The size, surface charge and drug loading of the SADDs was <100 nm, -27 mV and 68 %, respectively. The SADDs were non-haemolytic and biosafe. A sustained release of VCM from SADDs was noted, with 52.2 % release after 48 hr. The in vitro antibacterial test showed a two-fold decrease in MIC against SA and MRSA, and a significantly higher reduction in MRSA biofilms compared to bare VCM. Further, in silico studies confirmed strong and stable binding of TS to MRSA efflux pumps. The in vivo study using mice skin infection models showed a 9.5-fold reduction in bacterial load after treatment with SADDs, in comparison with bare VCM. These findings affirmed that VCM/TS NPs as a promising novel nano-delivery for treating bacterial infections.

Keywords: Self-assembled drug delivery system, D-α-tocopherol succinate, antibacterial, antimicrobial resistance, Vancomycin, Methicillin resistance *Staphylococcus aureus*, efflux pumps .

1- Introduction

The discovery and development of antibiotics has increased life expectancy and improved the quality of life over the last 75 years. However, improper use and sub-optimal delivery of antibiotics via conventional dosage forms have contributed to the development of antibiotic resistance [125]. The multidrug bacterial resistance explosion has led to the current serious challenges with the treatment of infectious diseases; thus new therapeutic approaches to combat multi-drug resistant pathogens are in high demand [126].

Innovative strategies are needed to combat antibacterial resistance. Nano-delivery systems and novel preparations that form chemical bonds or physical encapsulation of the drug can target drugs to infectious sites, decrease the exposure of healthy tissues and provide controlled drug release. They are, therefore, able to improve efficacy, and decrease doses and frequency of administration; hence improving patient compliance and acting as a potential tool to solve the problem of antibiotic resistance [127, 128]. Despite the huge array of nano-delivery systems and biomaterials that have been developed for drug delivery, combating bacterial resistance through these delivery systems is still challenging. The toxic and inflammatory effects of the nontherapeutic contents of drug delivery systems (DDS) and their metabolites are inherent drawbacks of DDS, apart from low drug loading and premature burst release prior to reaching the target site [129-131]. Innovative strategies to improve the drug loading and reduce nontherapeutic contents of DDS have been developed recently by researchers, where the drug was coupled, via cleavable bonds, with an amphiphilic system to form prodrugs [132-135].

Previously, various research groups have developed amphiphilic drug-drug conjugates, in which the drug forms the building blocks of the delivery system, resulting in self-delivery without the use of nontherapeutic carriers [83, 84]. Although the activity and drug loading are greatly enhanced, this strategy is still dependent on chemical modifications of the drug, which relies on the use of toxic reagents and organic solvents. An alternative to chemical modification is supramolecular chemistry, currently the most popular subfield of chemistry, which focuses on producing complex structures assembled from molecular subunits through weak interactions, such as hydrophobic-hydrophilic bonds, hydrogen-bonding, metal-ligand co-ordination, π–π stacking and van der Waal's (vdW) forces [136]. These supramolecular complexes are identified by their unique structure and extraordinary functions [90], which make them useful in building advanced biomaterials [55, 56] that have been employed as

therapeutic and diagnostic agents, including the production of new antibacterial compounds [91]. Recently, a new strategy to build self-assembled drug delivery systems (SADDs), based on supramolecular interactions, has been proposed, showing enhanced therapeutic efficacy by producing nanoparticles (NPs) composed only from therapeutic molecules without any chemical bonds [85-88]. An ideal example of this type of SADD is tetracycline (TTC) NPs, prepared using the sonochemical method [87]. The TTC NPs were formed through supramolecular hydrogen bonds between TTC molecules and showed enhanced antimicrobial activity [87]. Liu and co-workers reported SADDs based on supramolecular interactions between doxorubicin and chlorine e6, via π-π stacking, electrostatic and hydrophobic interactions [137]. The NPs produced were carrier-free, had the ability to improve the accumulation of drugs at a tumor site, enhance drug efficacy with reduced side effects and inhibit recurrence of tumors. This strategy of SADDs, based on supramolecular interactions, is relatively novel. Most reports focus on anticancer research as opposed to drug delivery in antibiotic resistance.

Vancomycin (VCM) is a glycopeptide antibiotic used as one of the last resort treatments for Methicillin-resistant *Staphylococcus aureus* (MRSA), which is a major source of nosocomial and community-acquired bacterial infections [92]. This bacteria has acquired resistance to many antibiotics, due to their inappropriate use, inactivation of the drug via hydrolysis or chemical modification, genetic mutation resulting in modification of the target of the drug, and decreased intracellular accumulation of the antibiotic because of increased cell wall thickness or over-expression of efflux pumps [93, 94]. Of these mechanisms, efflux pumps have been pointed out as major contributors of multi drug resistance in Gram-positive and -negative bacteria, as these efflux pumps extrude a wide variety of toxic compounds, including antibiotics from bacterial cells [95, 96]. In *Staphylococcus aureus* (SA), the predominant family of efflux pumps are Major Facilitator Super family (MFS) proteins, particularly NorA and NorB [138, 139]. Recently, Niranjana *et al.* reported the ability of a ferulic acid derivative to improve the antibacterial activity of ciprofloxacin against a NorA over-expressed strain of SA. They confirmed through *in vitro* and *in vivo* studies that this enhancement is due to the inhibition of the efflux effect of NorA [140]. In another study, silybin was shown to restore the sensitivity of antibiotics against MRSA by decreasing expression of NorA [141]. Based on these facts, any compound in delivery system that can show the ability to interact with and/or inhibit these efflux pumps and lower the minimum

inhibitory concentration (MIC) of the antibiotic, can be considered a promising therapeutic agent that will aid in restoring the effectiveness of existing antibiotics [97, 98].

Vitamin E is a naturally occurring antioxidant that is lipid-soluble and has the ability to solubilize several drugs that are hydrophobic [100]. D-α-tocopherol succinate (TS) is an FDA approved derivative of α-tocopherol, which is the most biologically active and abundant vitamin E isoform. Due to the high lipid solubility of α-tocopherol, it is able to modify the permeability of bacterial cell membranes, causing damage in the essential elements and collapse of proton pumps, leading to enhanced permeability and intracellular accumulation of different substances, including antibiotics [101]. Recent studies tested the effect of α-tocopherol as an efflux pump inhibitor [101, 102], and in addition to that, α-tocopherol in combination with antibiotics has been described to enhance the sensitivity of drug resistant bacteria to antibiotics [102-105]. These features of α-tocopherol highlight the usefulness of this compound for the development of innovative antibacterial-resistant preparations, demonstrating the potential of α-tocopherol and its derivatives against efflux pumps like NorA and Nor B.

Herein, we therefore report a novel SADD, composed of TS as hydrophobic part and VCM as hydrophilic part (VCM/TS complex), that will self-assemble into nanoparticles; and explore its potential for enhancing antibacterial activity of VCM against SA and MRSA, as well as for the eradication of biofilms. In this strategy, the antibiotic drug serves as building blocks to create well-defined NPs. The methods employed in the synthesis of the system have the potential for upscaling, commercialization and regulatory approval as no new chemical entities (NCEs) were formed among the approved excipients employed to synthesize the amphiphile. This is the first SADD formulation with TS for any class of drug, and the first SADD formulation of VCM. Additionally, in this study we aimed to investigate the potential of TS to block the outer membrane channel of NorA and NorB and possibly prevent extrusion of antibiotics via molecular dynamics (MD) simulations by determining the stable binding of TS to NorA and NorB efflux pumps at a molecular level.

2. Materials and Methods

2.1 Materials

D-α-tocopherol succinate was obtained from Sigma-Aldrich (USA). Vancomycin hydrochloride, acquired from Sinobright Import and Export Co., Ltd. (China), was converted to the VCM-free base, according to a previously reported method [142]. 3-(4,5-

dimethylthiazol-2-yl)-2,5-diphenyltetrazolium bromide (MTT) was purchased from Merck Chemicals (Germany). For cell culture, cells were purchased from Highveld Biologicals (Johannesburg, South Africa). Cell culture reagents were purchased from Whitehead Scientific (Johannesburg, South Africa). For bacterial cultures, Mueller-Hinton Broth (MHB), Nutrient Broth and Mueller-Hinton Agar (MHA) were purchased from Biolab (South Africa). SA (ATCC 25923) and MRSA (SA Rosenbach ATCC BAA 1683) were purchased from DLD Scientific (South Africa). Water was purified using a Milli-Q water purification system (Millipore corp., USA). For Fourier transform-infrared (FT-IR) spectroscopy, we used a Bruker Alpha-p spectrometer with a diamond ATR (Germany). All reagents and solvents used in this study were of analytical grade.

2.2 Preparation of Nanoparticles

The VCM/TS NPs were prepared using a solvent evaporation technique [143]. Briefly, 10 mg of VCM was initially dissolved in 10 ml of purified water (1 mg/ml), followed by the drop-wise addition of 1 ml of methanol (under stirring) containing dissolved TS in different molar ratios to VCM (1:1, 1:2, 1:3 and 1:6). The solution was left for at least 24 hours, to ensure evaporation of all methanol. The VCM/TS NPs were ultimately formed and characterized.

2.3 Characterization

2.3.1 Size, Polydispersity Index (PDI), Zeta Potential (ZP) and Morphology

The VCM/TS NPs were characterized for their average size, PDI and ZP using a dynamic light scattering method. Appropriate dilutions of the formula were made using PBS. Measurements were recorded at room temperature (25º C) using a Zetasizer Nano ZS90 (Malvern Instruments, UK) fitted with a 633 nm laser at 173° detection optics. All parameters were analyzed in triplicate. A High Resolution Transmission Electron Microscope (HRTEM, JEOL 2100) was used to study the morphological features of the NPs.

2.3.2 Dilution Effect

Dilution studies were implemented to establish the stability of the NPs at low concentrations [144]. The size and PDI of NPs diluted with PBS (for 0, 10, 100 and 1000 times), were measured using a Zetasizer. Furthermore, the colloidal stability of the NPs when diluted with cell culture medium was evaluated by measuring the change in the size after dilution [137].

2.3.3 Short-Term Physical Stability

Physical appearance, particle size and ZP parameters were monitored over one month at room temperature (RT) and at 4°C, for stability evaluation [47].

2.3.4 Entrapment Efficiency (EE) and Drug Loading (DL)

An ultrafiltration technique [145] was used to calculate the free VCM concentration by measuring absorbance at 280.4 nm and applying the Lambert-Beer law, to allow for the determination of drug loading (DL) and encapsulation efficiency (EE) of the NPs, according to the following equation:

$$EE\ \% = (\text{total drug} - \text{free drug})/\text{total drug} \times 100$$

$$DL\ \% = (\text{total drug} - \text{free drug})/\text{total weight of NPs} \times 100$$

2.3.5 Vancomycin and Tocopherol Succinate Complex Self-Assembly

2.3.5.1 Molecular dynamics of VCM/TS NPs complex

To study the self-assembly of the VCM/TS complex**,** the UCSF Chimera tool was used to initially bind VCM to three molecules of TS and, thereafter, used to randomly insert six complexes of VCM and TS. Molecular dynamic simulations represent a complete toolset that explore the atomic arrangement within molecules, thus offering new viewpoints on the structural landscape of molecular systems. The MD simulations were carried out using the PMEMD engine of the Amber software package [146]. The system was then minimized for 2500 steps with strong constraint on VCM, and TS for 1000 steps (500 steepest descent followed by 500 steps of the conjugate gradient), followed by 1000 steps of full minimization Langevin thermostat, with a collision frequency of 1.0 ps^{-1} with harmonic restraint of 5 $kcal.mol^{-1}$ $Å^{-2}$ on the solutes, applied during the gradual heating up of the systems to a temperature of 300 K in the canonical ensemble for 50 ps. This was followed by 50 ps of density equilibration in NPT ensemble and a final 500 ps equilibration at 300 K, 1 bar pressure and a coupling constant of 2 ps. MD production was carried out for 54 ns using classical MD with a time step of 2 fs, with the frame being recorded at every 500 steps of simulation. All the bond lengths involving hydrogen atoms were constrained using the SHAKE algorithm [147]. All the MD simulations were carried out using the GPU Amber 14 software package [148].

2.3.5.2 Binding free energy

To determine the binding free energy (ΔG_{bind}) of VCM to TS, molecular mechanics integrated with the Poisson-Boltzmann or generalized Born surface area continuum solvation (MM/PBSA and MM/GBSA) method was used [149].

The MD simulation produced a trajectory represented by 50,000 snapshots, which were averaged to generate ΔG_{bind}. The binding affinities between TS and the efflux pumps may be defined as:

(1) $\Delta G_{bind} = G_{complex} - G_{receptor} - G_{ligand}$

(2) $\Delta G_{bind} = E_{gas} + G_{sol} - TS$

(3) $E_{gas} = E_{int} + E_{vDW} + E_{ele}$

(4) $G_{sol} = G_{GB} + G_{SA}$

(5) $G_{SA} = \gamma SASA$

where:

E_{ele}	Electrostatic potential energy from Coulomb forces
E_{gas}	Gas-phase energy (based on FF14SB force field terms)
E_{int}	Internal energy
E_{vdW}	van der Waals energy
G_{sol}	Solvation free energy
G_{GB}	Polar solvation energy
G_{SA}	non-polar solvation energy
S	Total entropy of solute
SASA	Solvent accessible surface area (water probe radius of 1.4 Å)
T	Total entropy of temperature

A per-residue energy decomposition was used to predict the contribution of every residue to the total ΔG_{bind} at the ligand binding site, for significant residues of the pumps using the AMBER14 MM/GBSA method.

2.3.6 *In vitro* biosafety

2.3.6.1 Cytotoxicity and cell viability

The MTT assay was applied in the determination of biosafety of VCM/TS [150] on Michigan Cancer Foundation-7 (MCF-7) breast cancer, human embryonic kidney 293 (HEK 293) and adenocarcinoma alveolar basal epithelial (A549). Cells were seeded at a concentration of 2.5 x 10^3 cells/well into a 96-well plate containing 100 µl DMEM (HEK, MCF-7)/EMEM (A549), 10 % fetal bovine serum (FBS), 1 % pen-strep-fungizone and 1 % L-glutamine and incubated for 24 hr at 37 °C in a CO_2 humidified incubator. Thereafter, different

concentrations of VCM/TS (20, 40, 60, 80 and 100 µg/ml) were added and incubated for a further 24 hr. Following the 24 hr incubation period, media were substituted with 100 µl of MTT solution (5 mg/ml in PBS) per well and incubated for 4 hr. The supernatant was then aspirated, and formazan crystals were solubilized using 100 µl of dimethyl sulfoxide. A microplate spectrophotometer (spectrostar nano, Germany) read absorbances at 540 nm (proportional to the number of live cells). The following equation was used to calculate the percentage cell viability:

$$\% \text{ Cell viability} = \left(\frac{\text{A540 nm treated cells}}{\text{A540 nm untreated cells}}\right) \text{x } 100\%$$

2.3.6.2 Haemolysis

A previously described method was used for the determination of percentage haemolysis [58]. Briefly, freshly collected sheep's blood was washed three times with autoclaved phosphate buffer saline (PBS, pH 7.4) by centrifugation at 2800 rpm for 5 min. VCM/TS NPs were diluted with PBS to a concentration ranging from 0.05 to 0.5 mg/ml for each sample. The red blood cell (RBC) suspension (0.2 ml) was added to 1.8 ml of each sample and left for incubation at 37 ^{0} C for 30 min. Thereafter the samples were centrifuged at 3000 rpm for 10 min. Spectrophotometric readings of the supernatant of each sample at different concentrations were taken for the determination of haemoglobin release. To obtain 0 % and 100 % haemolysis, 0.2 ml of RBC suspension was added to 1.8 ml PBS and distilled water, respectively. The degree of haemolysis was calculated using the following equation:

$$\% \text{ Haemolysis } = \left(\frac{\text{ABS-ABS}_0}{\text{ABS100-ABS}_0}\right) \text{X } 100\%$$

where ABS100 and ABS_0 are the absorbances of the solution at 100% and 0% haemolysis, respectively.

2.3.7 Structural Changes

Fourier transform-infrared spectroscopy was performed to determine the structural change in VCM and TS before and after self-assembly into NPs.

2.3.8 Thermal Profiles

The thermal profiles of the TS, VCM, lyophilized and physical mixture VCM/TS were ascertained using differential scanning calorimetry (DSC) (Shimadzu DSC-60, Japan) [151]. Briefly, an aluminium pan was loaded with samples (2 mg) and sealed using a crimper,

followed by heating under nitrogen flow, at a constant rate of 10 °C/min to 300 °C. For reference purposes, an empty pan was used.

2.3.9 *In Vitro* Drug Release and Release Kinetics

The sustain-release property of the VCM/TS NPs was confirmed using the dialysis method. Into dialysis bags, 2 ml of VCM/TS NPs solution containing 1mg/ml of VCM was loaded (cut-off: 14,000 Da) and 2 ml of bare VCM solution was used as a control. Thereafter, the loaded dialysis bags were immersed in 40 ml PBS (pH 7.4), at 37 °C, in a shaking incubator (100 rpm). After each interval time, 3 ml of PBS were withdrawn, and immediately replaced with fresh PBS. The experiment was repeated in triplicate. The released VCM was determined using a UV-spectrophotometer by measuring the absorbance at 280.4 nm. The release kinetics of VCM from the VCM/TS NPs was studied using different mathematical models: first order, Higuchi, Weibull and Korsmeyer-Peppas. To find the best fit model, the root means square error (RMSE) and correlation coefficient (R^2) were determined, while the Korsmeyer-Peppas model was used to determine the release mechanism by calculating the value of the release exponent (n). The DDSolver software program was used for calculations [152].

2.4 Antibacterial Efficacy

2.4.1 *In Vitro* Antibacterial Activity

The broth microdilution technique was used to determine the MIC values of VCM/TS NPs against SA and MRSA [153]. Briefly, an overnight culture in nutrient broth at 37 °C of SA and MRSA, in a shaker incubator, was diluted to 0.5 McFarland standard, using a DEN-1B McFarland densitometer (Latvia). In a 96-well plate, a specific volume of MHB was added, followed by the addition of an equal volume of bare VCM (positive control), TS solution in 1% DMSO (negative control), and VCM/TS NPs in the first well; and then serially diluted. Then SA and MRSA were further diluted to 5×10^5 colony-forming units per ml (CFU/ml), and added to the 96-well plate containing the serially diluted samples and MHB [154]. The experiments were carried out in triplicate. The broth mixture was incubated for 24 hr in a shaking incubator at 37 °C, then spotted on MHA plates, and incubated for 24 hr at 37 °C to observe the MIC values.

2.4.2 *In Silico* Analysis of Tocopherol Succinate Binding to Efflux Pumps

To understand the dynamics and binding interactions of the TS/NorA and TS/NorB systems at a molecular level, homology models of NorA and NorB were created to further elucidate

the binding pockets, which enabled the determination of binding energies and molecular forces that contribute to binding using molecular docking, MD simulation, binding-free energy calculations, per-residue energy decomposition analyses and post-dynamic analyses.

2.4.2.1 Homology modelling and binding site determination of NorA and NorB

Computer-aided drug design requires crystal structures of biomolecules to analyze molecular dynamics and inter/intramolecular interactions. Due to the lack of available crystal structures of NorA and NorB efflux pumps, we undertook homology modelling as a tool to develop models that could be used to understand the binding interactions between TS with NorA and NorB, respectively. To construct the models, the amino acid sequences for NorA and NorB from MRSA were accessed from UniProt (accession numbers P0A0J6 and Q8NWQ5, respectively) [155]. Thereafter, the predictive 3D structures were generated using the SWISS-MODEL server (**Figure S1 and S2**) [156]. MolProbity was used to generate a Ramachandran Plot to assess and validate modified bond angles and torsional strain (**Figure S3**) [157]. Results revealed that for the NorA and NorB models, 94.35 % and 89.09 % of the respective protein's amino acid residues were in favoured regions. This left 4 and 14 outliers, respectively, none of which constituted the protein's active site.

The MetaPocket server [158] was used to predict potential binding pockets on the surfaces of NorA and NorB models. The most hydrophobic binding pockets (within the channel of the efflux pumps) were then chosen for docking.

2.4.2.2 Ligand acquisition and preparation

The 3D structures of TS and VCM were acquired from PubChem [159] and thereafter subjected to optimization using Avogadro [160]. The ligands were prepared for molecular docking via Chimera software [161].

2.4.2.3 Binding Affinity

Molecular docking is well-known technique in drug development [102]. To predict the conformation and binding affinity of TS to NorA and NorB, molecular docking was applied herein to determine the binding mode and binding affinities of TS to NorA and NorB, respectively. The molecular docking software employed herein comprised UCSF Chimera, AutoDock MGL tools [162], AutoDockVina [163] and Raccoon [164], with default docking parameters. For docking preparation of each compound, hydrogen atoms and Gasteiger charges were added. In this study, two systems were docked: TS to NorA; and TS to NorB.

The docking poses with the highest binding affinity (kcal.mol^{-1}) for each complex were then subjected to MD simulations.

2.4.2.4 Molecular dynamics

To determine the physical atomic motions that occur within the TS/NorA and TS/NorB systems, molecular dynamic simulations were performed on bound and unbound NorA and NorB systems. The MD simulations TS bound to NorA, TS bound to NorB and unbound NorA and NorB systems were performed using the PMEMD engine of the Amber software package [146]. Atomic partial charges were generated via ANTECHAMBER within the general Amber Force Field commands. The AMBER 14 Leap module immersed each system completely within a water box (10 Å TIP3P). For neutralization, Na^+ or Cl^- counter-ions were added. An initial 2500 step minimization was performed, with a restraint potential of 500 kcal/mol. Thereafter, a 1000-step full minimization was performed with no restraints. All systems were gradually heated to 300 K for 50 ps, such that each system provided a fixed number of atoms and volume. The solutes of the systems were subjected to a potential harmonic restraint of 10 kcal.mol^{-1}Å^{-2}. Thereafter, an equilibration step of 500 ps was conducted. An isobaric-isothermal ensemble (NPT) was imitated throughout the simulation (1 bar system pressure, constant number of atoms). The total simulation time of 100 ns for each system was performed, with the SHAKE algorithm to constrict hydrogen bonds, and a Langevin thermostat with collision frequency of 1 ps^{-1}.

2.4.2.5 Binding free energy and binding site residue identification

To determine the ΔG_{bind} of TS to NorA and NorB respectively, MM/GBSA was performed as mentioned in section 2.2.2. Thereafter, further analyses were carried out on the TS-NorA and TS-NorB complexes.

2.4.2.6 Post-dynamic analyses

The root-mean-square deviation (RMSD), root-mean-square fluctuation (RMSF) and thermodynamic energy of each system were then investigated to further understand the stability and energy contributions of the systems. All system co-ordinates were recorded in 1 ps intervals and the trajectories analyzed via the AMBER 14 CPPTRAJ module [165].

2.4.3 Reduction of MRSA Biofilm

Fluorescence microscopy was used to determine the potential of the VCM/TS NPS for eradication of MRSA biofilms [166]. MRSA biofilm was grown and treated with bare VCM and VCM/TS NPs following a previously published protocol by our group [47]. Briefly, biofilm was grown on cover slips. After formation of mature biofilm, the cover slips were washed and stained with Syto9 and propidium iodide (PI) dyes. Following 30 min. of incubation (dark), live (stained green) and dead cells (stained red) were detected using fluorescent optical microscopy (Nikon Eclipse 80i FM Japan). Three coverslips were observed for each sample.

2.4.4 *In Vivo* Antibacterial Activity

To further validate the therapeutic efficiency of VCM/TS NPs in depth, *in vivo* antibacterial activity of VCM/TS NPS was studied, using a MRSA skin infection model on BALB/c mice. The Animal Research Ethics Committee (AREC), University of KwaZulu-Natal (UKZN) has approved the protocol used for this study (Approval number: AREC/104/015PD) [167]. Compassionate care and treatment of the animals followed the regulations of the South African National Standard 10386:2008 and AREC of UKZN. BALB/c male mice weighing 18 - 20 g, were obtained from the Biomedical Research Unit, UKZN. Mice back skin hairs were removed 24 hr preceding the experiment and 70 % ethanol was used to disinfect the intact, exposed skin. The following day, the mice were injected intradermally with 50 µl of MRSA (1.5×10^8 CFU/ml) in saline. The mice were then divided into three groups: treatment, positive control and negative control groups (n = 4). Half an hour subsequent to infection, 50 µl of VCM/TS NPs formulation, free VCM, and saline, were injected intradermally at the same site of infection in the treatment, positive control, and negative control groups, respectively. The mice were observed for 48 hr with normal 12 hr light and dark conditions at 19-23 ^{0} C, and 55 ± 10 % relative humidity, with adequate ventilation. The mice were euthanized after 48 hr with halothane and the infected area of the skin was homogenized in PBS of pH 7.4 (5 ml). Tissue homogenates were serially diluted in PBS (pH 7.4), after which 20 µl was spotted on nutrient agar plates, incubated at 37 °C for 24 hr, and the CFU counted. The CFU/ml was calculated using the following equation:

$$\text{CFU/ml} = \frac{\text{number of colonies x dilution factor}}{\text{volume of the culture plate}}$$

3. Results and discussion

3.1 Preparation and Characterization of VCM/TS NPs

3.1.1 Size, PDI, ZP and Morphology

Spontaneous aggregation of amphiphiles that are formed with noncovalent interactions between hydrophilic and hydrophobic segments, through supramolecular complexation, are showing potential in drug delivery [151, 168, 169]. VCM/TS NPs were formulated in a similar way, since VCM is soluble in water and TS is hydrophobic. TS was dissolved in methanol and added to the VCM solution dropwise in H_2O under stirring. The mixture was left for a minimum of 24 hr to ensure evaporation of all methanol. As a control test, TS dissolved in methanol was added to pure distilled water under stirring, after which methanol evaporated and TS precipitated, due to the hydrophobicity of TS with no nanoaggregates forming. Different molar ratios of VCM and TS were determined to produce NPs with the desirable size, PDI, ZP and loading capacity. The sizes of the formed NPs were less than 100 nm in all VCM:TS ratios tested, except NPs obtained from the ratio of 1:6 (**Table 1**). Accumulation of bacterial components at the infection site causes enhanced vascular permeability which subsequently results in feasible passive targeting [170]. Moreover, dysfunctional lymphatic drainage has also been reported in bacterial infection, which potentially promotes nanoparticle accumulation at the sites of infection [171]. The smaller sizes displayed by VCM/TS NPs could lead to enhanced permeability and retention effect when administered intravenously [34, 172]. The surface charge of NPs was approximately -27 ± 1.3 mV. Previous studies showed that negatively charged NPs demonstration slow or reduced opsonization via the reticular endothelial system, which enhanced blood circulation time [109, 173-175]. The EE % increased with higher ratios of TS, as the highest EE% was observed with the ratio of 1:6 where it reached 75. 0 ± 3.5 %. In general, covalent linkage of drugs to carriers to form prodrugs is the most common strategy to get high drug loading [83, 84]. Here we are utilizing the drug as the building block of the delivery system, which significantly reduces the use of carrier material. Furthermore, the drug loading capacity exceeds 70 %, indicating the potential of VCM/TS NPs as a novel SADDs. Therefore, the ratio of 1:3 was preferred because the size was less than 100 nm; more importantly the EE% for the selected ratio was higher than the smaller ratios; 1:1 and 1:2. Although the ratio of 1:6 had higher EE%, the size of the formulated NPs were however more than 100 nm and the DL% was less than that for 1:3. A successful nanodelivery system should have a high drug loading capacity, thereby reducing the quantity of matrix materials for administration [176]. In addition, the PDI and ZP for the selected ratio were almost similar to the other ratio, hence, ratio of 1:3 was selected for further investigations [137, 177, 178]. HRTEM images showed

the selected formula of VCM/TS NPs to be solid spherical shapes (**Figure 1**), with the size almost similar to that measured using the DLS technique. The shape of the NPs is similar to other SADDs formulated via co-assembly of chlorine e6 and doxorubicin reported by Zhang *et al.* [137].

Table 1: Size, PDI, ZP, EE % and DL % for the different molar ratios of TS used in formulation with VCM. The values are expressed as mean ± SD, (n=3).

VCM:TS	Size (nm)	PDI	Zeta (mV)	EE%	DL%
1 to 1	69.14 ± 0.58	0.170 ± 0.003	-24 ± 0.12	45.5 ± 2.12	33.78 ± 2.12
1 to 2	62.05 ± 0.47	0.201 ± 0.008	-28 ± 0.01	65.0 ± 3.4	38.37 ± 3.40
1 to 3	85.15 ± 0.25	0.131 ± 0.017	-27 ± 1.30	68.8 ± 2.8	33.71 ± 2.80
1 to 6	110.3 ± 0.65	0.114 ± 0.017	-32 ± 1.50	75.0 ± 3.5	24.34 ± 3.50

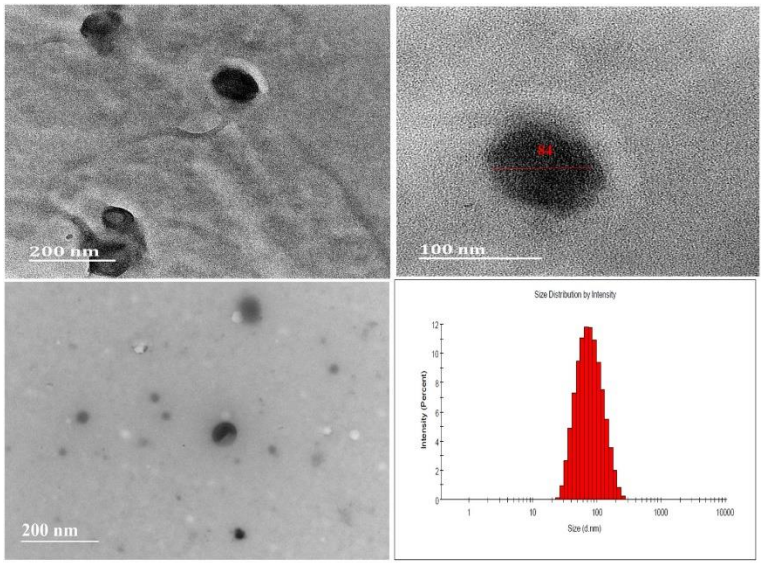

Figure 1: Morphology of VCM/TS NPs from HRTEM and histogram for sample measurement showing size distribution measured via DLS.

3.1.2 Dilution Effect

Most colloidal formulations when administered to the systemic circulation undergo considerable changes [179]. Dilution studies were carried out to establish the stability of the NPs at low concentrations [144]. After dilutions up to 10 µg/ml (100 times) of the system **(Table S1),** there were no differences in size or PDI of the NPs. This indicated that, on injection in the body, the nano particles might not breakdown due to blood dilution, thereby

avoiding dose dumping. These results indicated the potential for administration of NPs without causing dose dumping due to systemic dilution.

The surface adsorption of macromolecules, such as protein and lipids, onto the surface of NPs could lead to aggregation and colloidal destabilization when introduced into media or biological fluid [180]. The stability of the assembled NPs was tested when dispersed in DMEM supplemented with 10 % FBS, which indicated a slight increase in size by a shift in the distribution curve (**Figure 2 A)**; and no extra peak was observed which could result from aggregation. This result showed that the system retained acceptable colloidal stability in the cell culture medium [137, 180, 181], as well as the aqueous medium.

3.1.3 Short-Term Physical Stability

Preliminary physical stability studies were carried out at RT and 4 °C, over one month to determine the impact of storage conditions on the VCM/TS NPs. **Figures 2 B** and **C** show no significant deviations in size and ZP, respectively, when the samples were stored at RT over one month. Generally, an absolute ZP value ≥ 20 mV, could prevent particle aggregation upon storage [182-184], due to the repulsion forces caused by the surface charge, which can overcome attracting vdW forces between particles. This result is in accordance with other reports for SADDs [137, 185], and indicate acceptable stability of the VCM/TS NPs in the aqueous phase at both RT and 4 °C storage condition. Long-term physical and chemical stability studies using international council of harmonization (ICH) conditions to assess the physical and chemical stability of the system must be undertaken on future drugs encapsulated in this system to confirm the shelf life.

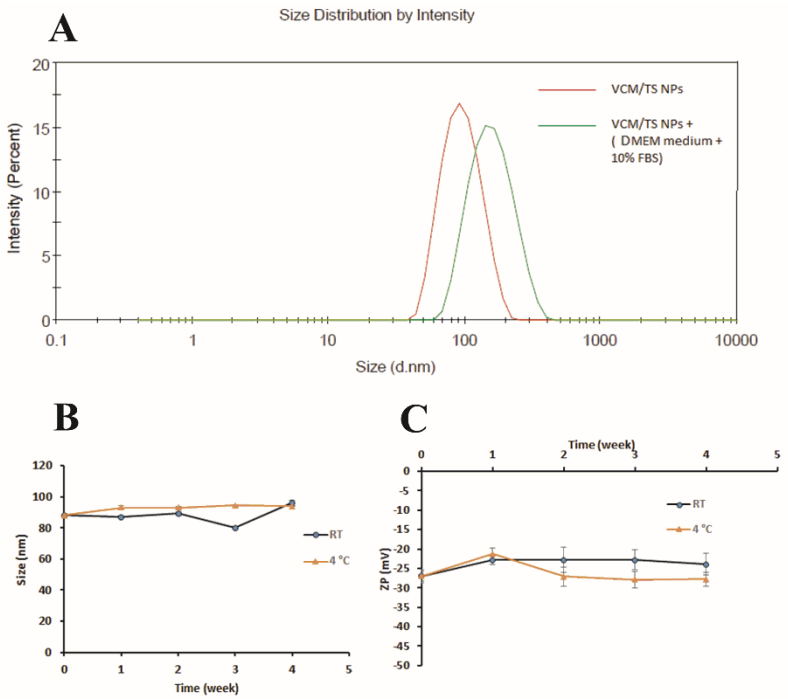

Figure 2 A: Effect of DMEM containing 10 % FBS on particle size distribution measured by intensity for VCM/TS NPs. Figure B and C: Effect of storage time at RT over one month on size and charge, respectively.

3.1.4 Molecular Dynamics of Self-Assembly of Vancomycin and Tocopherol Succinate

Molecular visualization of interactions between VCM and TS (**Figure 3**) showed the spatial arrangement of the two molecules and the different type of bonds that cause them to interact. The total binding free energy was evaluated to gain an enhanced perspective of the binding energetics of the VCM and TS complex. The MM/GBSA package in AMBER was utilized to calculate the binding free energies by obtaining snapshots from the trajectories of the simulations.

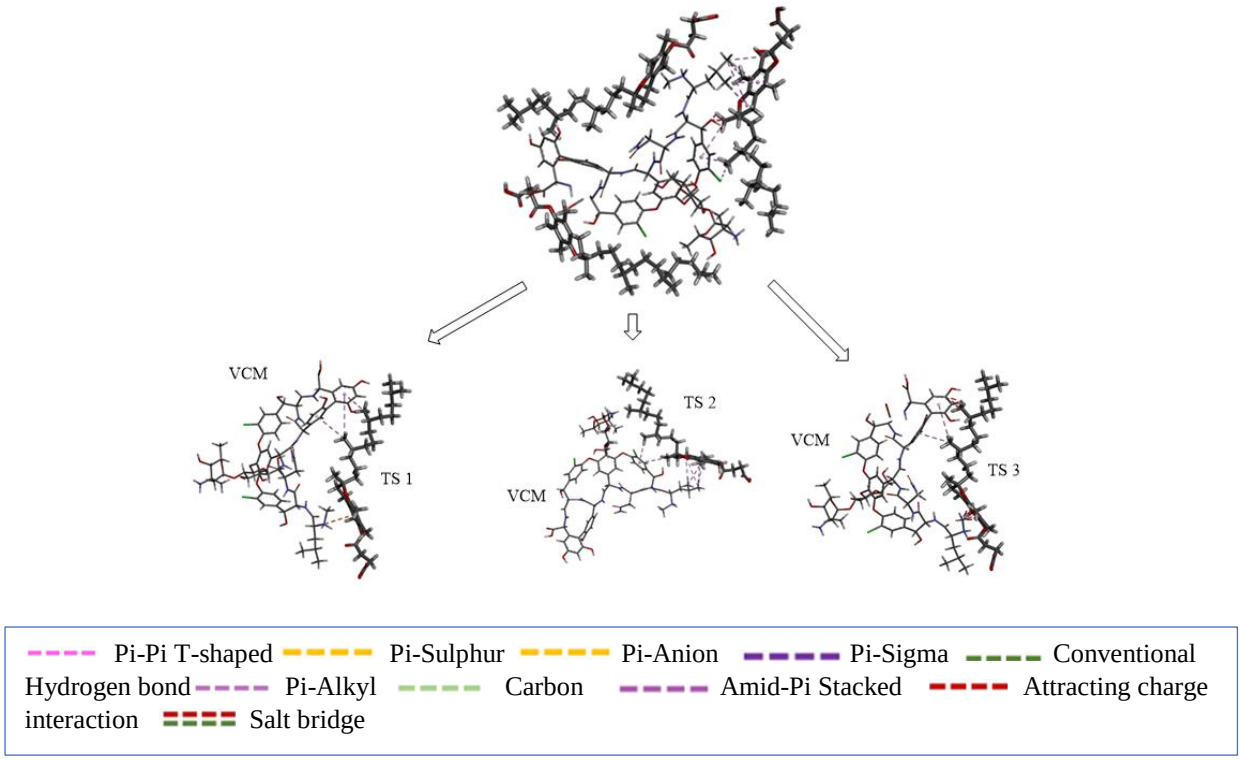

Figure 3: Molecular visualization of interaction between VCM and three TS molecules TS 1, TS 2 and TS 3.

Table 2: The binding energies (kcal/mol) for the VCM/TS computed from MD trajectories

Energy Components (kcal/mol)					
Complex	ΔE_{vdW}	ΔE_{elec}	ΔG_{gas}	ΔG_{solv}	ΔG_{bind}
VCM/TS1+ TS2+TS3	-56.83 ± 0.81	-15.48 ± 0.56	-72.32 ± 1.07	29.92 ± 0.64	-42.40 ± 0.63
VCM/TS1	-18.71 ± 0.34	-3.75 ± 0.41	-22.46 ± 0.56	7.63 ± 0.39	-14.82 ± 0.28
VCM/TS2	-29.66 ± 0.56	-3.93 ± 0.35	-33.60 ± 0.78	8.83 ± 0.36	-24.77 ± 0.28
VCM/TS3	-31.82 ± 0.43	-8.35 ± 0.50	-40.18 ± 0.60	15.51 ± 0.53	-24.66 ± 0.42

As shown in **Table 2**, the contribution to the ΔG total from the vdW and electrostatic interactions was represented by ΔE vdW and ΔE_{elec}. The polar and nonpolar solvation energy contributions to ΔG total were represented by ΔG gas and ΔG solvation, respectively. Binding between VCM and TS was mainly governed by the hydrophobic interaction, since ΔE gas

was most favourable contributor, followed by ΔG vdW and $\Delta E_{elec.}$ ΔG solvation was unfavourable for the binding; however, favourable ΔE gas and ΔG vdW lead to an overall favourable ΔG total.

The last frame (100 ns) of the first simulation, in which VCM interacted with TS, was taken and replicated to make six complexes and 54 ns self-assembly simulations were performed. It was observed that these complexes began to assemble within a few ns after simulations (**Figure 4**). Simulation data revealed that, at ~15 ns, there were three dimers formed. At 32 ns two trimers were formed and a hexamer was formed at 54 ns. Overall, this data suggests that VCM/TS complexes self-assemble in a way that has the hydrophilic VCM retained on solvent-accessible areas, while the hydrophobic TS was on the core, away from the solvent [186]. This result was similar to other simulation of complex amphiphile self-assembly studies [187], and also in line with the experimental results which showed these types of complexes are amphiphiles with self-assembling properties [185, 188]. The strong binding energies established between VCM and TS computationally correlate with the high experimental DL % and EE % reported in Table 1 [189].

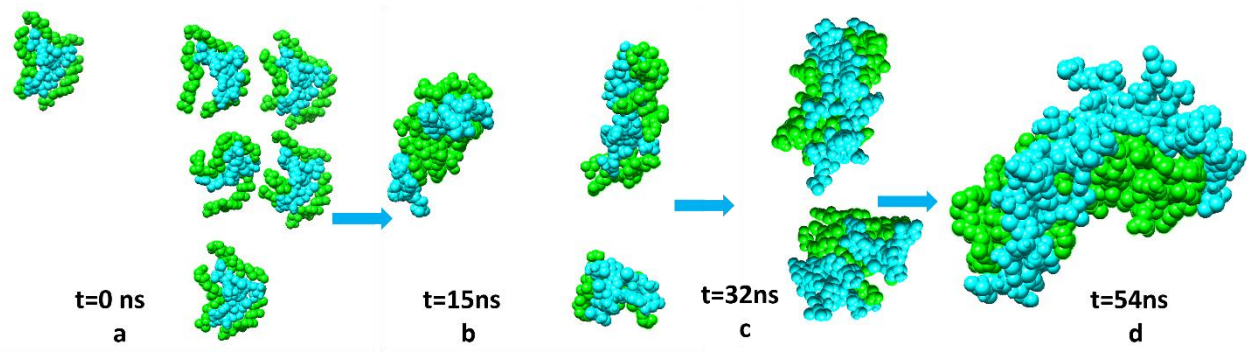

Figure 4 a-d: Representative image of self-assembly simulation at different time intervals.

3.1.5 *In Vitro* Biosafety

3.1.5.1 Cytotoxicity and cell viability

The cytotoxic effect of VCM/TS was determined via the *in vitro* MTT cytotoxicity assay. The MTT assay quantifies the number of healthy, living cells based on the metabolic reduction of yellow tetrazolium salt to crystalline formazan by living mammalian cells. The amount of formazan crystals produced is proportionate to viable cells present [150]. The results showed that cell viability ranged from 77.3 % to 108.5%, across all concentrations on all three tested cell lines (**Figure 5**). This is in accordance with the ISO norm for biomedical products (>70 % cell viability) [190]. In this study, no dose-dependent toxicity within the

concentration range to any of the three cell lines was reported. These results correlate with confirmed reports of biocompatibility and biosafety of TS [191], along with VCM as an FDA approved biosafe antibiotic, thus indicating the biosafety of the formulated VCM/TS NPs.

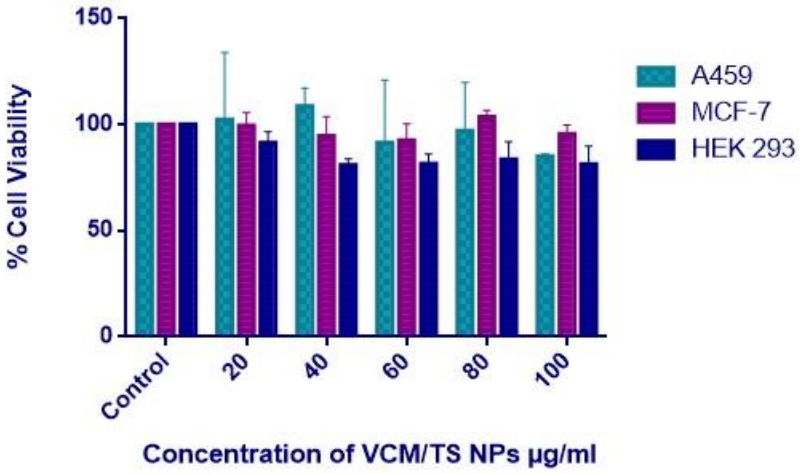

Figure 5: MTT assay for evaluation of cytotoxicity of VCM/TS against A549, HEK 293 and MCF-7 cell lines.

3.1.5.2 Haemolysis

Blood compatibility is an important factor for all intravenously administered pharmaceuticals, to ensure there are non-haemolytic properties [192]. The unique physicochemical characteristics and the small size of the NPs may lead to interference with red blood cells (RBCs) more than the conventional pharmaceuticals, and hence early preclinical study to establish their biocompatibility with the blood component is necessary [193]. Red blood cells collected from sheep's blood was used to evaluate the haemolytic properties of VCM/TS NPs (**Figure 6**). Among the different concentrations used in the study (**Table S2**), the highest concentration of VCM/TS NPs (0.5 mg/ml) resulted in less than 1 % haemolysis of RBCs, signifying the non-haemolytic nature of VCM/TS NPs.

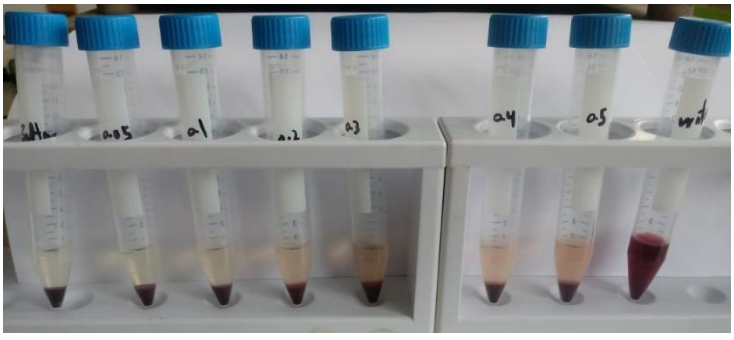

Figure 6: RBCs exposed to varying concentration of VCM/TS NPs and centrifuged.

3.1.6 Structural Changes

We further investigated whether the self-assembly of VCM with TS was accompanied by any structural or chemical modification. FT-IR spectra were acquired for VCM, TS and freeze-dried VCM/TS NPs (**Figure 7**). The spectrum obtained for VCM/TS NPs showed all the characteristic peaks for the individual components, VCM and TS, and no new peaks were detected. Therefore, we may conclude that the hydrophobic interaction inducing the formation of VCM/TS NPs led to stabilization of the nanosystem without the formation of NCEs. This result is similar to other VCM NPs formulated via hydrogen-bond with poloxamer and sunflower oil through an ultrasonic emulsification method [57]; and also observed during the formation of penicillin nanospheres and tetracycline nanoparticles [87, 194].

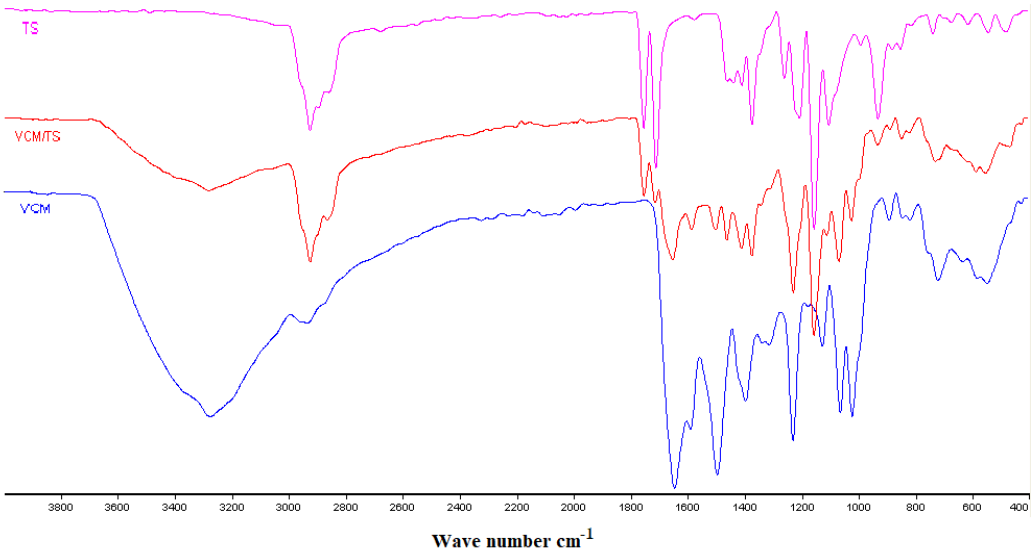

Figure 7: FT-IR spectrum of VCM, TS and VCM/TS NPs.

3.1.7 Thermal profiles

Differential scanning calorimetry is a useful technique to study the thermal behaviour of polyelectrolytes and biomaterials, which is correlated to their structure. DSC is highly utilized in drug delivery and formulation studies, since the endothermic and exothermic peak shifts are usually associated with interactions between drugs and the other components in the formula [195]. Thermal profiles for TS, VCM, a physical mixture of VCM/TS, and lyophilized VCM/TS NPs were recorded using DSC. Thermal profiles of both TS and VCM (**Figure 8A** and **8B**) showed endothermic peaks at 83.12 °C and 126.21 °C, respectively, which probably represents the melting point of those two biomolecules. We observed the

same peaks in the physical mixture of VCM/TS, which indicate the absence of any type of interaction between the two molecules. Interestingly, the thermogram of lyophilized VCM/TS NPs did not show any peak for the individual components of the mixture, which suggests a change in the physicochemical properties of the mixture component and the development of interaction and the formation of new bonds between them and the amorphous state of VCM/TS NPs [196].

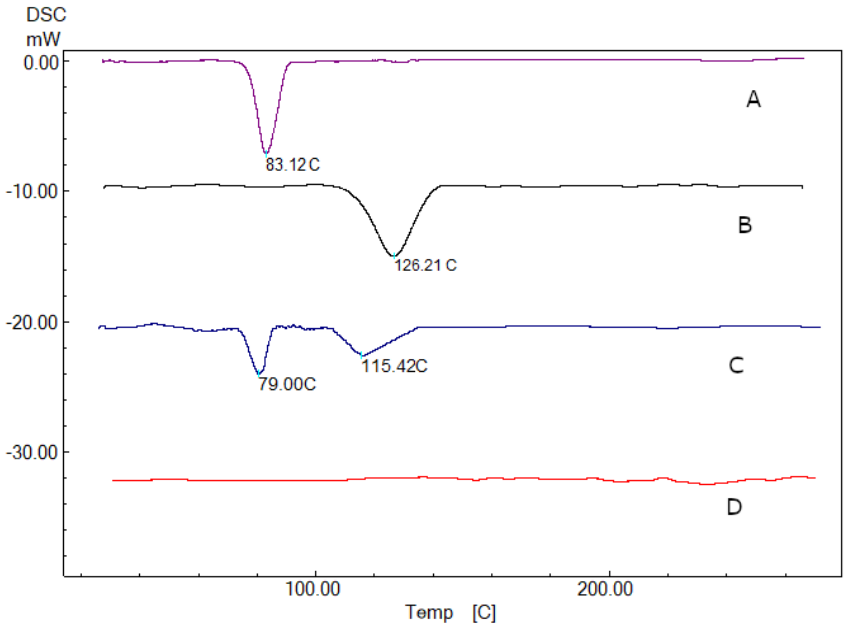

Figure 8 DSC thermogram of (A) TS, (B) VCM, (C) physical mixture of VCM/TS and (D) freeze-dried VCM/TS NPs.

3.1.8 *In Vitro* Drug Release from the VCM/TS NPs

An ideal nanodrug delivery system should have proper and stable nanosized particles and also be able to release the drug, because a system that cannot release the entrapped drug efficiently, or at all, is of no use [48]. The dialysis bag method was used to evaluate the releasing behaviour of VCM from the VCM/TS NPs, using bare VCM as the control. The result showed that the bare VCM was diffusing quickly through the dialysis bag membrane to the surrounding media until it was completely released after 8 hr (**Figure 9**), whilst the VCM/TS NPs release started quickly until it reached 45.6 % of the VCM in the system after 8 hr. After 48 hr, VCM/TS NPs had a 52.2 % release of VCM. The release profile of the system was seen to be biphasic in nature. A similar biphasic profile has been reported before in the literature [134, 197, 198]. The quick first phase of VCM release from VCM/TS NPs was probably due to VCM molecules adsorbed on and/or encapsulated near the nano aggregates

surface, which resulted in the initial faster release via dissociation [199]. Another reason could be explained by the Noyes Whitney equation. At the initial stage, since there is a much high concentration gradient between the dialysis bag and the receiver compartment, it translates to higher release rates [200].

To understand the releases kinetics of the VCM/TS NPs, the cumulative release percentage curve was fitted using different release models (**Table 3**). A goodness-of-fit test was used as a limiting criteria for selecting the appropriate release model [201]. It was found that the Weibull equation is the best-fitting model to describe the release, based on it having the higher regression coefficient, R2 value (R^2 = 0.933), compared to other models considered. In the Weibull model, the exponent parameter (β) value was found to provide a link with the drug release mechanism [202], which was found to be equal to 0.237 (**Table 3**), indicating Fickian diffusion as the release mechanism [202]. This result is also supported by the low (n) value (0.244) from the Korsmeyer-Peppas model, confirming the Fickian mechanism of release from the VCM/TS NPs, as the (n) value was less than 0.5 [142]. The Weibull model was used to describe the sustained release behaviour in many drug-loaded nanosystems [203-205].

The good sustained release behaviour of VCM/TS NPs will be beneficial in exposing the bacteria to a continuous lethal dose and will facilitate the improvement of patient compliance by reducing the frequency of administration.

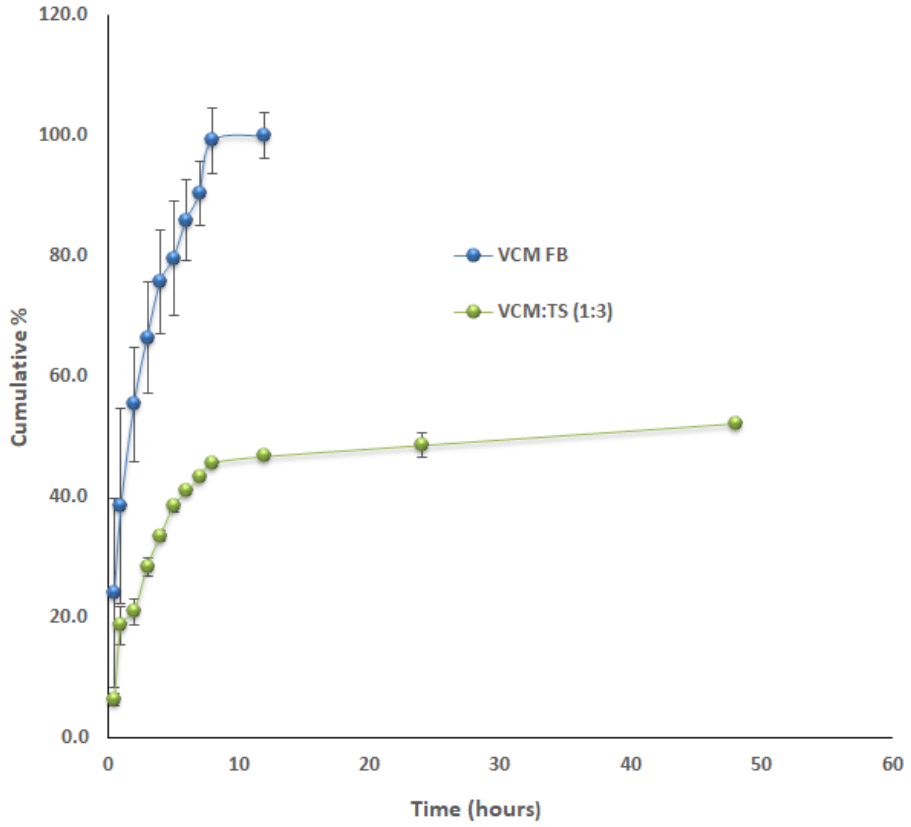

Figure 9: Cumulative release profile of VCM from VCM solution and VCM/TS NPs.

Table 3: Drug release kinetics data for VCM/TS NPs.

Model	Equation	R^2	Release exponent (n)	β
First Order	$Q = Q_0 . e^{kt}$	0.013	-	-
Higuchi	$Q = k. t^{½}$	0.503	-	-
Korsmeyer-Peppas	$Q = k . t^n$	0.756	0.244	-
Weibull	Q = 1 exp [-(t)a/b]	0.933	-	0.237

3.2 Antibacterial Activity

3.2.1 *In vitro* antibacterial activity

To evaluate the *in vitro* antibacterial activity of VCM/TS NPs against SA and MRSA, the broth dilution method was employed, and MICs were calculated for the bare VCM and NPs. Results (**Table 4**) indicated that the MICs for VCM and VCM/TS NPs against SA were 1.95 µg/ml and 0.97 µg/ml, respectively; while for MRSA they were 3.9 µg/ml and 1.95 µg/ml, respectively. A TS solution in 1 % DMSO showed no activity at the concentration used. This two-fold reduction in MIC against SA and MRSA, with VCM transformed into an SADD

with TS, could be due to several features: a) Antibiotic transformation into nanosized particles confers novel modes of action due to the smaller size of the NPs, with unique properties, and enhances activity against bacteria, unlike those of free molecules and bulk materials [57]; b) There are several studies confirming the ability of TS to modify the permeability of bacterial cell membranes, causing damage in the essential elements and collapse of proton pumps due to the lipophilic nature of TS [101]. TS has been reported to have antimicrobial activity in higher concentrations, however, in the concentrations tested in our studies it did not show any antibacterial activity [103]. The binding effect of TS on NorA and NorB efflux pumps, and possible inhibition, may therefore have also led to the enhancement of the permeability of VCM through the bacterial cell membrane. The outcomes of this assay indicate the ability of VCM/TS NPs to release the bare VCM in an active form, resulting in enhanced antibacterial activity, compared to that of bare VCM. Having demonstrated superior *in vitro* antimicrobial activity of VCM/TS NPs over bare VCM, we then proceeded to supplement our studies with *in silico* analyses to identify and understand the stability of molecular interactions between TS with NorA and NorB, respectively, as a potential mechanism for enhancing the antibacterial activity of the VCM/TS NPs.

Table 4: MIC values for bare VCM, VCM/TS NPs and TS.

Material	SA (MIC µg/ml)			MRSA (MIC µg/ml)		
Time in hours	**24**	**48**	**72**	**24**	**48**	**72**
Bare VCM	1.95	1.95	NA	3.9	3.9	NA
VCM/TS NPs	0.97	0.97	0.97	1.95	1.95	1.95
TS	NA	NA	NA	NA	NA	NA

NA = No activity

The values are expressed as mean, n = 3.

3.2.2 *In Silico* Analysis of Tocopherol Succinate Binding to Efflux Pumps

3.2.2.1 Predicted binding site determination

To determine the sites on NorA and NorB to which TS can bind, MetaPocket [158] was used to predict possible hydrophobic binding pockets. *Staphylococcus aureus* NorA and NorB are chromosomally encoded efflux pumps whose overexpression can confer multidrug resistance of the bacteria to several antibiotics [206]. Understanding the active sites of NorA and NorB could offer perspectives on how to inhibit them. The active pockets of the NorA and NorB efflux pump proteins consist of hydrophobic amino acids. This hydrophilic nature may stem

from the location of the active site at the surface of the protein. Potential ligands at these active sites possess specific moieties and characteristics to be able to form a stable inhibitory complex. MetaPocket predicted hydrophobic binding pockets on the NorA and NorB proteins, and the two most hydrophobic pockets on each protein are highlighted in (**Figure 10)**. Herein, is presented for the first time the homology models of MRSA NorA and NorB and their potential binding sites to which TS can bind, to perform its antibacterial activity.

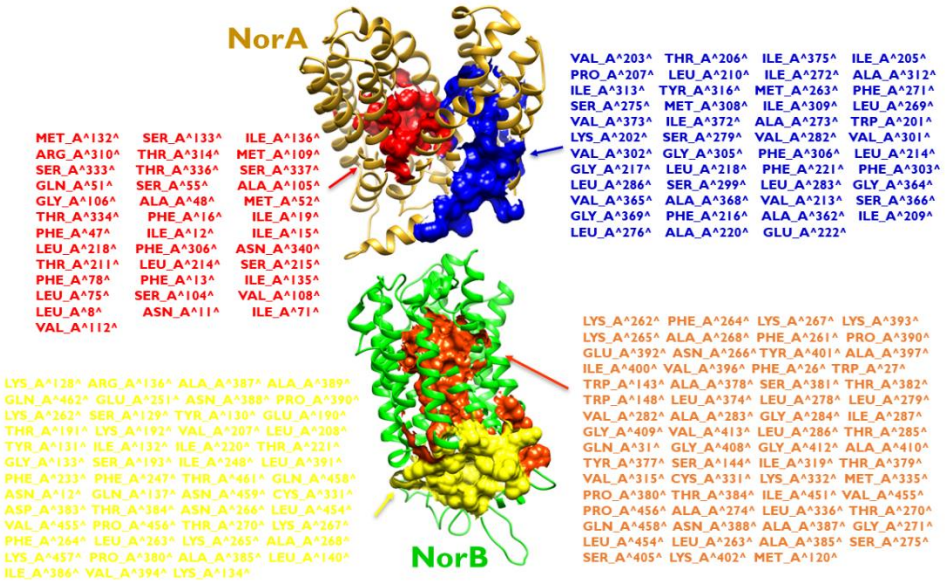

Figure 10: The potential hydrophobic binding sites on NorA and NorB, identified by MetaPocket, with corresponding binding site amino acid residues.

3.2.2.2 Binding affinity

Molecular docking is one of the most useful *in silico* methods in drug development, as it predicts the mode of ligand binding to a target protein [207]. Molecular docking was applied in this study to determine the potential binding mode and binding affinities of TS to NorA and NorB, respectively (**Figure 11**). The conformation of TS that bound to NorA and NorB with highest affinities were -5.8 kcal/mol and -7.2 kcal/mol, respectively. This is a prediction of the affinities with which TS may bind to NorA and NorB in a bacterial cell wall.

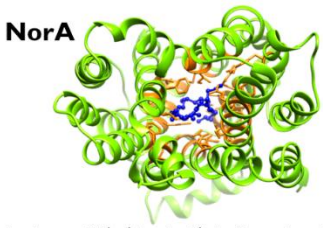

mode	affinity (kcal/mol)	dist from best mode rmsd l.b.	rmsd u.b.
1	-5.8	0.000	0.000
2	-5.7	25.180	28.267
3	-5.5	1.217	2.212
4	-5.5	27.411	29.896
5	-5.4	18.241	22.756
6	-5.4	25.104	27.781
7	-5.4	16.235	20.259
8	-5.3	17.737	20.300
9	-5.0	28.405	31.674

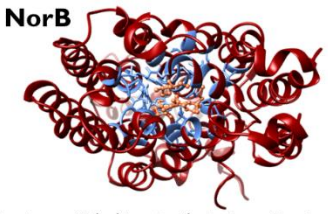

mode	affinity (kcal/mol)	dist from best mode rmsd l.b.	rmsd u.b.
1	-7.2	0.000	0.000
2	-6.2	9.541	14.136
3	-6.1	2.296	5.463
4	-6.0	31.375	35.871
5	-5.9	31.887	37.288
6	-5.8	32.234	36.998
7	-5.4	35.786	38.925
8	-5.4	28.797	34.488
9	-5.4	10.214	14.641

Figure 11: Docking poses of TS bound to binding pockets of NorA (left) and NorB (right) with best binding affinities.

3.2.2.3 Molecular dynamics

Even though the scoring algorithm of molecular docking attempts to represent experimental binding, software predictions remain inconsistent. Therefore, MD simulations were applied to each docked system for 100 ns to validate binding using virtual conditions identical to experimental conditions, elaborating further on the structural dynamics of TS binding to both NorA and NorB. The unbound NorA and NorB proteins, as well as TS bound to NorA and NorB, were simulated.

Throughout each simulation, TS remained stably bound to the proteins, without exiting the channel. The stability and convergence of each system were confirmed by analyzing the RMSD during the simulation. Both systems indicated stability – remained within a 2 Å range. Convergence in the TS-NorA and TS-NorB systems were reached after 45ns and 85ns, respectively (**Figure S4**). Increases in the radius of gyration of both systems upon binding (**Figure S5**) also confirmed the expansion of NorA and NorB to accommodate binding of TS. This, in turn, may block the efflux channel to prevent further efflux of compounds, including antibiotics, from the bacterial cell, which is seen as one of the main causes of resistance in gram-positive and gram-negative bacteria [95, 96].

Root-mean-square fluctuation (RMSF) revealed energy fluctuations of each amino acid residue of NorA and NorB when bound to TS, as in **Figure 12**, which shows a major shift in loop residues (175-200) and lower loop residues (193-259) of NorA and NorB, respectively. The fluctuations of these specific residues contribute the most to the adaption of NorA and

NorB upon TS binding. One can therefore postulate that these loops play major roles in allowing compounds, like TS, to enter the outer membrane channel of the pumps, thereby controlling the permeability of the bacterial cell wall.

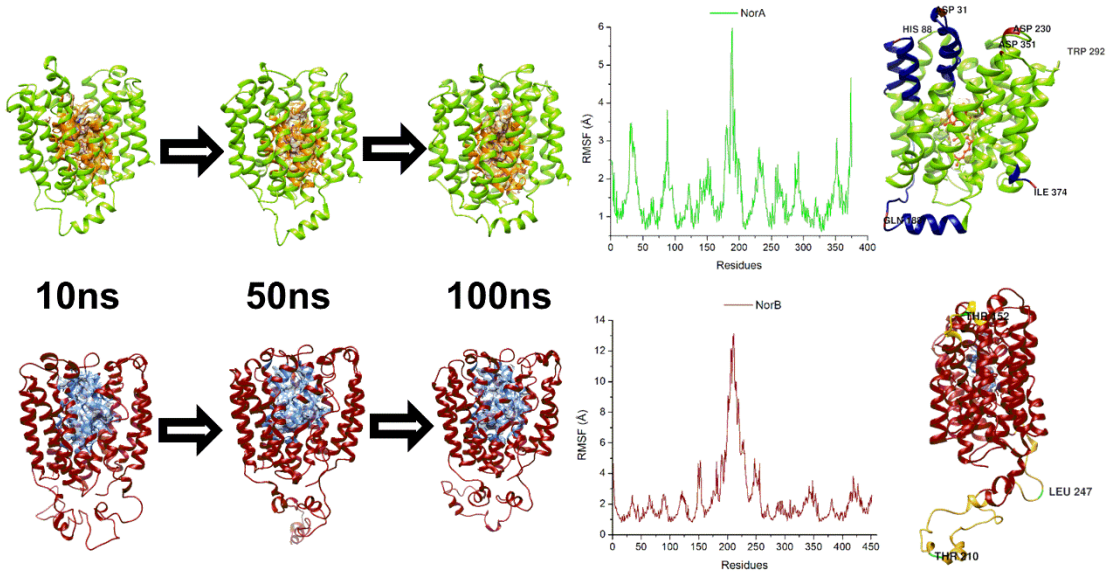

Figure 12: Time evolution of the simulation of TS bound to NorA (green) and NorB (maroon), and the root-mean-square fluctuation of the 100ns simulation of TS bound to NorA and NorB.

3.2.2.4 Thermodynamic binding free energy and binding site residue identification

To establish the forces and energies that contribute to the binding of TS to the efflux pumps situated in the bacterial cell wall, it is critical to calculate the binding free energy and per-residue decomposition analysis. **Figure 13** shows the amino acid residues of NorA and NorB that interact with TS after 100 ns of MD simulation. The ligand interaction diagram (**Figure 14A)** reveals that Thr112, Met108, Thr313, Ile135, Gln50, Ile14, Asn339, Leu217, Phe15 and Ile18 of NorA form hydrophobic interactions with TS; while Glu221 forms a stable intermolecular hydrogen bond with TS. **Figure 13F** shows that residues Gln283, Ser45, Asn41, Val402, Gln20, Asn279, Gly397, Ser394, Trp16, Gly398, Leu267, Ala48, Phe15 and Trp132 of NorB form hydrophobic interactions with TS; while Ser136 and Lys391 form hydrogen bonds with TS.

The energy components tables in **Figures 13B and 13D** provide a breakdown of energy contributions to binding, indicating that vdW forces and electrostatic energies play major roles in the binding of TS to NorA and NorB, respectively. The NorA and NorB proteins contribute more electrostatic energies toward binding (-26817.45 kcal/mol and -30572.07

kcal/mol, respectively) than vdW forces (-3036.37 kcal/mol and -3457.57 kcal/mol, respectively).

The per-residue energy decomposition graphs in **Figure 13** indicate that residues Phe15, Met108, Ile135, Thr335 and Asn339 of NorA are responsible for the high electrostatic energy contribution to binding shown in the table, while residues Ile135 and Arg309 provide most of the weak vdW forces involved in binding (**Figure 13C**). **Figure 13E** shows that residues Phe15, Trp16, and Asn279 contribute the most to the electrostatic binding of NorB to TS, while residues Trp132 and Ser136 bind with vdW forces.

From this MD study, one can hypothesize that TS binds stably and may inhibit antibiotic expulsion by blocking the efflux pumps, which further supports the enhancement of the activity and reduction in the MIC values for VCM. Thus, using TS as an excipient in the delivery of antibiotics to MRSA is promising in the enhancement of antimicrobial activity.

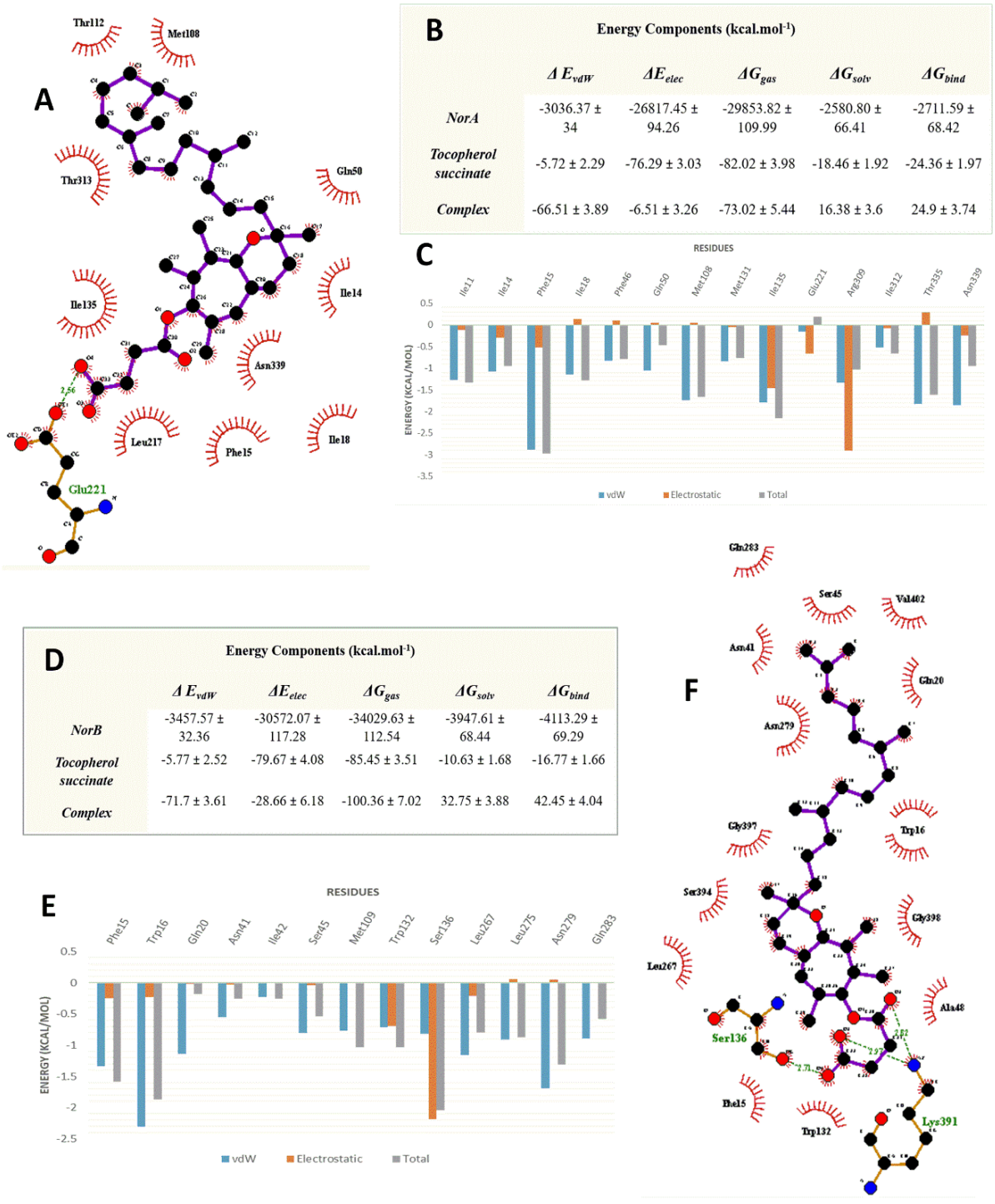

Figure 13: Thermodynamic energy calculations and per-residue energy decomposition analysis of TS binding to NorA and NorB. **A, F.** Residue-ligand interaction diagram of TS forming hydrophobic interactions and hydrogens bond with NorA and NorB amino acid residues, respectively. **B, D.** Thermodynamic energy calculations of binding site residues of NorA and NorB, respectively. **C, E.** Per-residue energy decomposition analysis of TS bound to NorA and NorB, respectively.

3.2.3 Reduction of MRSA Biofilm

Conventional antibiotics are not active against MRSA biofilm [208]. To determine the reduction effect of VCM/TS NPs on MRSA biofilm, untreated and treated biofilms were stained with Syto9 and PI and examined under a fluorescent microscope. For the untreated biofilms, the whole coverslip showed high intensity green colour when subjected to excitation at 488 nm, which is the range of Syto9; and since Syto9 is a cell permeant dye [209, 210], this is an indication of more living cells (**Figure 14**), compared to the dead cells (low intensity of red colour) that appeared when biofilms were stained and excited at the range of PI (**Figure 14**). Propidium iodide is a non-permeating dye and cannot penetrate an intact cell membrane [209]. Biofilms treated with VCM showed greater amounts of cells stained red compared to untreated biofilm, indicating more penetration of PI dye, due to ruptured and damaged cell walls caused by VCM treatment (**Figure 14. B1** and **B2**). The biofilm disruption was more pronounced upon treatment with VCM/TS NPs, indicated by the high intensity of red fluorescence and complete lack of the green, as compared to the bare VCM (**Figure 14. C1** and **C2**), confirming that there were many more dead cells than live ones, compared to the VCM treated biofilms. SA is one of the major biofilm-forming pathogens [211]. MRSA forms most of the adhered SA [212] and causes infections related to implanted medical devices. One of the features of biofilms is the extracellular polymeric substances, which play an important role in cell-surface or cell-cell attachment; and along with the intact biofilm structure, they act as a primary barrier for bacteria and prevent the entrance of the drug [213]. Bacteria embedded in biofilms are over 1000 times more resistant to antibiotics and the host immune system than those in culture [57]. The level of biofilm reduction caused by VCM/NPs indicates its superiority in eradication of MRSA biofilm compared to the bare VCM solution. This could be attributed to the fact that the nanoform of antibiotics usually leads to enhanced biofilm penetration, reaching the embedded bacteria more effectively than the drug solution [57]. It is possible that negatively charged VCM/TS NPs interact with the oppositely charged biofilm matrix electrostatically, and bind to the biofilm structure [214]. Additionally, TS has a significant anti-adhesive effect against SA biofilms [215], which could be due to interference with the initial event of biofilm formation. There could be a synergism between VCM and TS in planktonic bacteria via TS acting as an adjuvant to the antibiotic and efflux pump inhibitor, whilst the synergistic effect in biofilm inhibition could be via antiquorum sensing and enhanced transport of the drug across the biofilm protective barrier [103, 216]. Furthermore, there are reports of synergistic effects of efflux pump inhibitors and antibiotics against bacterial biofilms [217, 218]. There have been

detections of high levels of efflux pump (NorA and NorB) gene expression in biofilms. However, their influence on biofilm formation in MRSA is still largely unknown [219]. The frequent use of materials foreign to the body, such as contact lenses, prostheses and catheters highlights the necessity for, and enormous value of, a simple and effective system to treat biofilm-associated infections.

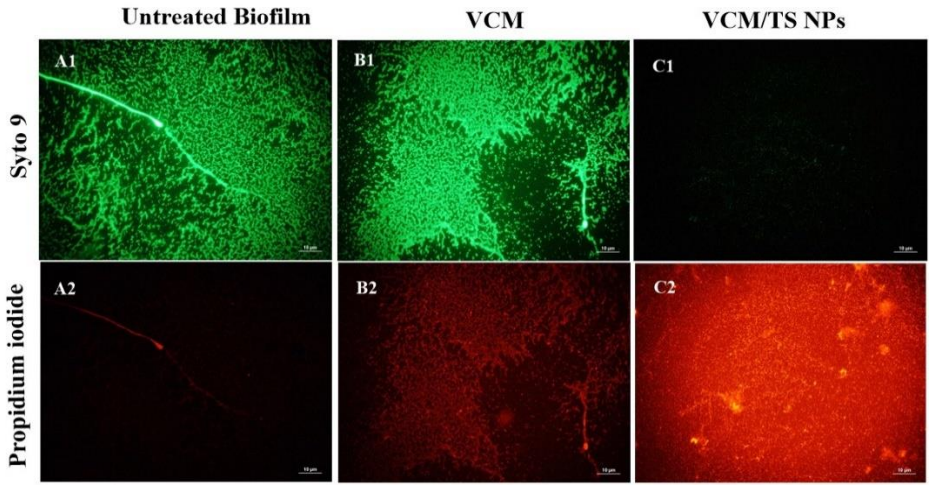

Figure 14: Images from fluorescence microscopy for MRSA biofilms represent the untreated (A1 and A2), VCM-treated (B1 and B2) and VCM/TS NPs-treated (C1 and C2) biofilm. Live cells are stained with green and dead cells in red.

3.2.4 *In Vivo* Antibacterial Activity

For further evaluation of the antibacterial activity of VCM/TS NPs, a skin infection model was used. Local intradermal MRSA injections were delivered between the epidermal and the subcutaneous layer of the skin. Skin was then harvested around the injection site and homogenized and the number of colony-forming units (CFUs) were quantified for each treatment group and represented as $\log_{10}$ **(Figure 15).** One-way ANOVA analysis between all the treatment groups revealed that there was a statistically significant reduction ($p < 0.0001$) in bacterial load of the skin**.** The mean bacterial loads ($\log_{10}$ CFU) recovered from the untreated and bare VCM groups were 5.52 ± 0.01 (338,000 CFU/ml) and 4.40 ± 0.05 (25,333.33 CFU/ml), respectively. These findings demonstrated that bare VCM had a 13.34-fold reduction in bacterial load, when compared to the untreated group ($p = 0.0007$). In the VCM/TS NP treated groups, the bacterial load was 2.4 ± 0.17 $\log_{10}$ CFU/ml (2,666.667 CFU/ml), which was 126-fold lower when compared to the untreated group ($p < 0.0008$). Furthermore, there was a 9.5-fold reduction in bacterial load after treatment with VCM/TS

NPs, compared to the bare VCM (p = 0.0077). This improvement in *in vivo* results compared to *in vitro* results for VCM/TS NPs could be due to enhanced penetration and retention of the nanosystem compared to the bare drug. Also, it could be due to enhanced drug release from the system in the *in vivo* conditions compared to the agar plate in the *in vitro* antibacterial study. A similar trend for superior *in vivo* results compared to *in vitro* results for nanodelivery systems have been reported [220]. These *in vivo* results demonstrated VCM/TS NPs as an effective drug delivery system for VCM.

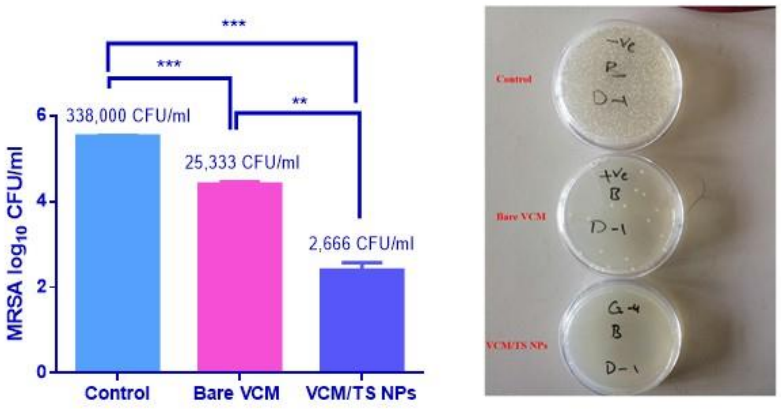

Figure 15: Evaluation of MRSA burden post 48 hr treatment. **denotes significant difference for VCM/TS NPs versus bare VCM. ***denotes significant difference between untreated versus bare VCM and also denotes a significant difference between untreated and VCM/TS NPs. Data are represented as means ± SD (n = 3).

4. Conclusion

In this study we described a method for the synthesis of a novel SADD comprising hydrophobic TS and hydrophilic VCM that self-assembled into NPs for delivery of VCM against SA and MRSA infections. The VCM/TS NPs self-assembly and stability were confirmed using MD simulation. The VCM/TS NP had a suitable size, surface charge and morphology for targeted antibiotic therapy. The NPs displayed an EE % of >60 % for VCM, which correlated with the strong binding established through MD. *In vitro* cell toxicity and haemolysis studies confirmed the biosafety of the system. The system showed a sustained release profile of VCM, which was ascribed to its enhanced and prolonged *in vitro* antibacterial effect when compared to bare VCM. Further, *in silico* studies showed the potential of TS to stably interact with MRSA NorA and NorB efflux pumps at a molecular level, indicating its potential as a constituent in a delivery system to inhibit efflux pumps for enhanced antibacterial activity. *In vivo* studies also confirmed the superiority of the NPs over the bare VCM by showing a significant reduction in bacterial load. The method employed in the synthesis of this SADD system with enhanced antibacterial activity

has the potential for upscaling, commercialization and regulatory approval as no NCEs were formed among the approved excipients used to synthesize the amphiphile. These findings indicate that VCM/TS NPs is a novel nano-delivery system that can be applied to improve treatment of bacterial infections and to fight bacterial resistance.

5. Acknowledgement

The authors acknowledge the College of Health Sciences, University of KwaZulu-Natal (UKZN), and the UKZN Nanotechnology Platform, the National Research Foundation (NRF) of South Africa (Grant No. 106040) and the Medical Research Council (MRC) of South Africa for financial support. We also acknowledge the Microscopy and Microanalysis Unit (MMU) and the Department of Human Physiology at UKZN, for use of their facilities, as well as the Centre for High Performance Computing (CHPC), Cape Town, for supercomputing resources.

6. Conflict of Interest

The authors declare that there is no conflict of interest.

5. References

1. English, B.K. and A.H. Gaur, The use and abuse of antibiotics and the development of antibiotic resistance, in Hot Topics in Infection and Immunity in Children VI. 2010, Springer. p. 73-82.

2. Matzov, D., A. Bashan, and A. Yonath, A bright future for antibiotics? Annual Review of Biochemistry, 2017. 86: p. 567-583.

3. Kalhapure, R.S., et al., Nanoengineered drug delivery systems for enhancing antibiotic therapy. Journal of Pharmaceutical Sciences, 2015. 104(3): p. 872-905.

4. Li, S., et al., Antibacterial hydrogels. Advanced science, 2018. 5(5): p. 1700527.

5. Lin, J., et al., Antibacterial zinc oxide hybrid with gelatin coating. Materials Science and Engineering: C, 2017. 81: p. 321-326.

6. Yu, D., et al., Antitumor activity of poly (ethylene glycol)–camptothecin conjugate: The inhibition of tumor growth in vivo. Journal of Controlled Release, 2005. 110(1): p. 90-102.

7. Knop, K., et al., Poly (ethylene glycol) in drug delivery: pros and cons as well as potential alternatives. Angewandte Chemie International Edition, 2010. 49(36): p. 6288-6308.

8. Sapra, P., et al., Novel delivery of SN38 markedly inhibits tumor growth in xenografts, including a camptothecin-11–refractory model. Clinical Cancer Research, 2008. 14(6): p. 1888-1896.

9. Feng, X., et al., Electrospun polymer micro/nanofibers as pharmaceutical repositories for healthcare. Journal of Controlled Release, 2019.

10. Wang, J., et al., Tumor redox heterogeneity- responsive prodrug nanocapsules for cancer chemotherapy. Advanced Materials, 2013. 25(27): p. 3670-3676.

11. Zhang, H., et al., Novel SN38 conjugate-forming nanoparticles as anticancer prodrug: in vitro and in vivo studies. Journal of Controlled Release, 2013. 166(2): p. 147-158.

12. Ding, J., et al., Electrospun polymer biomaterials. Progress in Polymer Science, 2019. 90: p. 1-34.

13. Huang, P., et al., Combination of small molecule prodrug and nanodrug delivery: amphiphilic drug–drug conjugate for cancer therapy. Journal of The American Chemical Society, 2014. 136(33): p. 11748-11756.

14. Xie, S., et al., Design and synthesis of theranostic antibiotic nanodrugs that display enhanced antibacterial activity and luminescence. Proceedings of the National Academy of Sciences, 2017. 114(32): p. 8464-8469.

15. Huang, H., et al., Facile modification of nanodiamonds with hyperbranched polymers based on supramolecular chemistry and their potential for drug delivery. Journal of colloid and interface science, 2018. 513: p. 198-204.

16. Ganewatta, M.S. and C. Tang, Controlling macromolecular structures towards effective antimicrobial polymers. Polymer, 2015. 63: p. A1-A29.

17. Lehn, J.-M., Supramolecular chemistry. Science, 1993. 260(5115): p. 1762-1764.

18. Amabilino, D.B., D.K. Smith, and J.W. Steed, Supramolecular materials. Chemical Society Reviews, 2017. 46(9): p. 2404-2420.

19. Webber, M.J., et al., Supramolecular biomaterials. Nature Materials, 2016. 15(1): p. 13.

20. Kulkarni, A., et al., Combining immune checkpoint inhibitors and kinase-inhibiting supramolecular therapeutics for enhanced anticancer efficacy. Acs Nano, 2016. 10(10): p. 9227-9242.

21. Shimanovich, U., et al., Tetracycline Nanoparticles as Antibacterial and Gene-Silencing Agents. Advanced Healthcare Materials, 2015. 4(5): p. 723-728.

22. Semiramoth, N., et al., Self-assembled squalenoylated penicillin bioconjugates: an original approach for the treatment of intracellular infections. ACS Nano, 2012. 6(5): p. 3820-3831.

23. Zhao, R., et al., Carrier-free nanodrug by co-assembly of chemotherapeutic agent and photosensitizer for cancer imaging and chemo-photo combination therapy. Acta biomaterialia, 2018. 70: p. 197-210.

24. Zhang, R., et al., Carrier-free, chemophotodynamic dual nanodrugs via self-assembly for synergistic antitumor therapy. ACS Applied Materials & Interfaces, 2016. 8(21): p. 13262-13269.

25. Binda, E., F. Marinelli, and G. Marcone, Old and new glycopeptide antibiotics: action and resistance. Antibiotics, 2014. 3(4): p. 572-594.

26. Slama, T.G., Gram-negative antibiotic resistance: there is a price to pay. Critical Care, 2008. 12(4): p. S4.

27. Blair, J.M., et al., Molecular mechanisms of antibiotic resistance. Nature Reviews Ricrobiology, 2015. 13(1): p. 42.

28. Saiful, A.J., et al., Efflux genes and active efflux activity detection in Malaysian clinical isolates of methicillin- resistant Staphylococcus aureus (MRSA). Journal of Basic Microbiology, 2008. 48(4): p. 245-251.

29. Sołoducho, J., et al., Recent Advances of Modern Protocol for CC Bonds–The Suzuki Cross-Coupling. Advances in Chemical Engineering and Science, 2013. 3(3A): p. 19-32.

30. Markham, P.N. and A.A. Neyfakh, Efflux-mediated drug resistance in Gram-positive bacteria. Current Opinion in Microbiology, 2001. 4(5): p. 509-514.

31. Sabatini, S., et al., Pyrazolo [4, 3-c][1, 2] benzothiazines 5, 5-dioxide: a promising new class of Staphylococcus aureus NorA efflux pump inhibitors. Journal of Medicinal Chemistry, 2012. 55(7): p. 3568-3572.

32. Sundaramoorthy, N.S., et al., Ferulic acid derivative inhibits NorA efflux and in combination with ciprofloxacin curtails growth of MRSA in vitro and in vivo. Microbial Pathogenesis, 2018. 124: p. 54-62.

33. Wang, D., et al., Inhibitory effects of silybin on the efflux pump of methicillin‑resistant Staphylococcus aureus. Molecular Medicine Reports, 2018. 18(1): p. 827-833.

34. Van Bambeke, F. and V.J. Lee, Inhibitors of bacterial efflux pumps as adjuvants in antibiotic treatments and diagnostic tools for detection of resistance by efflux. Recent Patents on Anti-infective Drug Discovery, 2006. 1(2): p. 157-175.

35. Lomovskaya, O., et al., Identification and characterization of inhibitors of multidrug resistance efflux pumps in Pseudomonas aeruginosa: novel agents for combination therapy. Antimicrobial Agents and Chemotherapy, 2001. 45(1): p. 105-116.

36. Nielsen, P., et al., The effect of α-tocopherol on the in vitro solubilisation of lipophilic drugs. International Journal of Pharmaceutics, 2001. 222(2): p. 217-224.

37. Tintino, S.R., et al., Action of cholecalciferol and alpha-tocopherol on Staphylococcus aureus efflux pumps. EXCLI Journal, 2016. 15: p. 315.

38. Abd El-Tawab, A.A., et al., Efflux Pump Inhibitors, Alpha-Tocopherol and Aspirin: Role in Campylobacter jejuni and Campylobacter coli Fluoroquinolone Resistance. Microbial Drug Resistance, 2018. 25: p. 203-211.

39. Andrade, J.C., et al., Enhancement of the antibiotic activity of aminoglycosides by alpha-tocopherol and other cholesterol derivates. Biomedicine & Pharmacotherapy, 2014. 68(8): p. 1065-1069.

40. Tintino, S.R., et al., Vitamin K enhances the effect of antibiotics inhibiting the efflux pumps of Staphylococcus aureus strains. Medicinal Chemistry Research, 2018. 27(1): p. 261-267.

41. Du, Y., et al., Tocopherol polyethylene glycol succinate modified hollow silver nanoparticles for combating bacteria-resistance. Biomaterials Science, 2019.

42. Kalhapure, R.S., et al., Ion pairing with linoleic acid simultaneously enhances encapsulation efficiency and antibacterial activity of vancomycin in solid lipid nanoparticles. Colloids and Surfaces B: Biointerfaces, 2014. 117: p. 303-311.

43. Rabani, E., et al., Drying-mediated self-assembly of nanoparticles. Nature, 2003. 426(6964): p. 271.

44. Zuo, H., et al., Crosslinking to enhance colloidal stability and redispersity of layered double hydroxide nanoparticles. Journal of Colloid and Interface Science, 2015. 459: p. 10-16.

45. Omolo, C.A., et al., A hybrid of mPEG-b-PCL and G1-PEA dendrimer for enhancing delivery of antibiotics. Journal of Controlled Release, 2018. 290(1): p. 112-128.

46. Sonawane, S.J., et al., Ultra-small lipid-dendrimer hybrid nanoparticles as a promising strategy for antibiotic delivery: In vitro and in silico studies. International Journal of Pharmaceutics, 2016. 504(1–2): p. 1-10.

47. Case, D., et al., AMBER 2018; 2018. University of California, San Francisco.

48. Ryckaert, J.-P., G. Ciccotti, and H.J. Berendsen, Numerical integration of the cartesian equations of motion of a system with constraints: molecular dynamics of n-alkanes. J. Comput. Phys., 1977. 23(3): p. 327-341.

49. Case, D.A., et al., The Amber biomolecular simulation programs. Journal of Computational Chemistry, 2005. 26(16): p. 1668-1688.

50. Devnarain, N. and M.E. Soliman, Molecular mechanism of resveratrol inhibition of Zika virus NS3 helicase: behind the scenes. Future Virology, 2019. 14(2): p. 73-84.

51. Mosmann, T., Rapid colorimetric assay for cellular growth and survival: application to proliferation and cytotoxicity assays. Journal of Immunological Methods, 1983. 65(1-2): p. 55-63.

52. Salih, M., et al., Supramolecular Amphiphiles of Beta-Cyclodextrin and Oleylamine for enhancement of Vancomycin delivery. International Journal of Pharmaceutics, 2019: p. 118881.

53. Zhang, Y., et al., DDSolver: An Add-In Program for Modeling and Comparison of Drug Dissolution Profiles. The AAPS Journal, 2010. 12(3): p. 263-271.

54. Jorgensen, J.H. and J.D. Turnidge, Susceptibility test methods: dilution and disk diffusion methods, in Manual of Clinical Microbiology, Eleventh Edition. 2015, American Society of Microbiology. p. 1253-1273.

55. Jorgensen, H., Methods for dilution antimicrobial susceptibility tests for bacteria that grow aerobically. Approved standard. National Committee for Clinical Laboratory Standards Antimicrobial Susceptibility Testing, 1993: p. NCCLS M7-A3.

56. Consortium, U., UniProt: a worldwide hub of protein knowledge. Nucleic Acids Research, 2018. 47(D1): p. D506-D515.

57. Waterhouse, A., et al., SWISS-MODEL: homology modelling of protein structures and complexes. Nucleic Acids Research, 2018. 46(W1): p. W296-W303.

58. Williams, C.J., et al., MolProbity: More and better reference data for improved all-atom structure validation. Protein Science, 2018. 27(1): p. 293-315.

59. Zhang, Z., et al., Identification of cavities on protein surface using multiple computational approaches for drug binding site prediction. Bioinformatics, 2011. 27(15): p. 2083-2088.

60. Kim, S., et al., PubChem substance and compound databases. Nucleic Acids Research, 2015. 44(D1): p. D1202-D1213.

61. Rayan, B. and A. Rayan, Avogadro Program for Chemistry Education: To What Extent can Molecular Visualization and Three-dimensional Simulations Enhance Meaningful Chemistry Learning. World Journal of Chemical Education, 2017. 5(4): p. 136-141.

62. Pettersen, E.F., et al., UCSF Chimera—a visualization system for exploratory research and analysis. Journal of Computational Chemistry, 2004. 25(13): p. 1605-1612.

63. Sanner, M.F., The Python interpreter as a framework for integrating scientific computing software-components. Scripps Res. Inst., 2008. 26(1): p. 1-12.

64. Trott, O. and A.J. Olson, AutoDock Vina: improving the speed and accuracy of docking with a new scoring function, efficient optimization, and multithreading. Journal of Computational Chemistry, 2010. 31(2): p. 455-461.

65. Ramírez, D. and J. Caballero, Is it reliable to use common molecular docking methods for comparing the binding affinities of enantiomer pairs for their protein target? International Journal of Molecular Sciences, 2016. 17(4): p. 525.

66. Roe, D.R. and T.E. Cheatham III, PTRAJ and CPPTRAJ: software for processing and analysis of molecular dynamics trajectory data. Journal of Chemical Theory and Computation, 2013. 9(7): p. 3084-3095.

67. Berlutti, F., et al., Influence of sub-inhibitory antibiotics and flow condition on Staphylococcus aureus ATCC 6538 biofilm development and biofilm growth rate: BioTimer assay as a study model. The Journal of Antibiotics, 2014. 67(11): p. 763.

68. Kugelberg, E., et al., Establishment of a superficial skin infection model in mice by using Staphylococcus aureus and Streptococcus pyogenes. Antimicrobial agents and chemotherapy, 2005. 49(8): p. 3435-3441.

69. Hamman, J.H., Chitosan based polyelectrolyte complexes as potential carrier materials in drug delivery systems. Marine Drugs, 2010. 8(4): p. 1305-1322.

70. Zarif, M., et al., Physicochemical characterization of vancomycin and its complexes with?-cyclodextrin. 2012.

71. Lee, W.L. and W.C. Liles, Endothelial activation, dysfunction and permeability during severe infections. Current opinion in hematology, 2011. 18(3): p. 191-196.

72. Gao, W., et al., Nanoparticle approaches against bacterial infections. Wiley Interdiscip. Rev. Nanomed. Nanobiotechnol., 2014. 6(6): p. 532-547.

73. Zaidi, S., L. Misba, and A.U. Khan, Nano-therapeutics: a revolution in infection control in post antibiotic era. Nanomedicine: Nanotechnology, Biology and Medicine, 2017. 13(7): p. 2281-2301.

74. Yang, L., et al., Triclosan-based supramolecular hydrogels as nanoantibiotics for enhanced antibacterial activity. Journal of Controlled Release, 2020.

75. Zhu, M., et al., Physicochemical properties determine nanomaterial cellular uptake, transport, and fate. Accounts of Chemical Research, 2012. 46(3): p. 622-631.

76. Owens III, D.E. and N.A. Peppas, Opsonization, biodistribution, and pharmacokinetics of polymeric nanoparticles. International Journal of Pharmaceutics, 2006. 307(1): p. 93-102.

77. Moghimi, S.M. and H. Patel, Serum-mediated recognition of liposomes by phagocytic cells of the reticuloendothelial system–the concept of tissue specificity. Advanced Drug Delivery Reviews, 1998. 32(1-2): p. 45-60.

78. Jahed, V., et al., NMR (1H, ROESY) spectroscopic and molecular modelling investigations of supramolecular complex of β-cyclodextrin and curcumin. Food chemistry, 2014. 165: p. 241-246.

79. Singh, R. and J.W. Lillard Jr, Nanoparticle-based targeted drug delivery. Experimental and molecular pathology, 2009. 86(3): p. 215-223.

80. Zhao, Y., et al., Novel carrier-free nanoparticles composed of 7-ethyl-10-hydroxycamptothecin and chlorin e6: Self-assembly mechanism investigation and in vitro/in vivo evaluation. Colloids and Surfaces B: Biointerfaces, 2020. 188: p. 110722.

81. Nel, A.E., et al., Understanding biophysicochemical interactions at the nano–bio interface. Nature Materials, 2009. 8(7): p. 543.

82. Moore, T.L., et al., Nanoparticle administration method in cell culture alters particle-cell interaction. Scientific Reports, 2019. 9(1): p. 900.

83. Kittler, S., et al., The influence of proteins on the dispersability and cell-biological activity of silver nanoparticles. Journal of Materials Chemistry, 2010. 20(3): p. 512-518.

84. Bose, S., et al., Formulation optimization and topical delivery of quercetin from solid lipid based nanosystems. International Journal of Pharmaceutics, 2013. 441(1-2): p. 56-66.

85. Katara, R., S. Sachdeva, and D.K. Majumdar, Design, characterization, and evaluation of aceclofenac-loaded Eudragit RS 100 nanoparticulate system for ocular delivery. Pharmaceutical development and technology, 2019. 24(3): p. 368-379.

86. Katara, R., S. Sachdeva, and D.K. Majumdar, Enhancement of ocular efficacy of aceclofenac using biodegradable PLGA nanoparticles: formulation and characterization. Drug Delivery and Translational Research, 2017. 7(5): p. 632-641.

87. Fan, L., et al., Carrier-free, pure nanodrug formed by the self-assembly of an anticancer drug for cancer immune therapy. Molecular Pharmaceutics, 2018. 15(6): p. 2466-2478.

88. Microbiology, E.C.f.A.S.T.o.t.E.S.o.C. and I. Diseases, Terminology relating to methods for the determination of susceptibility of bacteria to antimicrobial agents. Clinical Microbiology and Infection, 2000. 6(9): p. 503-508.

89. Sikwal, D.R., et al., Polyelectrolyte complex of vancomycin as a nanoantibiotic: Preparation, in vitro and in silico studies. Materials Science and Engineering: C, 2016. 63: p. 489-498.

90. Zhang, Z., et al., Construction of a supramolecular drug–drug delivery system for non-small-cell lung cancer therapy. ACS Applied Materials & Interfaces, 2017. 9(35): p. 29505-29514.

91. Gayathri, N.K., et al., Preparation, characterization, drug release and computational modelling studies of antibiotics loaded amorphous chitin nanoparticles. Carbohydr Polym, 2017. 177: p. 67-76.

92. Standard, I., Biological Evaluation of Medical Devices. Tests for in vitro Cytotoxicity. Switzerland, Geneva: ISO. TC, 2009. 194.

93. Kogure, K., et al., Cytotoxicity of α-tocopheryl succinate, malonate and oxalate in normal and cancer cells in vitro and their anti-cancer effects on mouse melanoma in vivo. Journal of Nutritional Science and Vitaminology, 2005. 51(6): p. 392-397.

94. Yalkowsky, S.H., J. Krzyzaniak, and G. Ward, Formulation- related problems associated with intravenous drug delivery. Journal of Pharmaceutical Sciences, 1998. 87(7): p. 787-796.

95. Dobrovolskaia, M.A., et al., Method for analysis of nanoparticle hemolytic properties in vitro. Nano Lett., 2008. 8(8): p. 2180-2187.

96. Fernandes, M.M., et al., Nanotransformation of vancomycin overcomes the intrinsic resistance of gram-negative bacteria. ACS Appl. Mater. Interfaces, 2017. 9(17): p. 15022-15030.

97. Fernandes, M.M., et al., Escherichia coli and Pseudomonas aeruginosa eradication by nano-penicillin G. Nanomedicine: Nanotechnology, Biology and Medicine, 2016. 12(7): p. 2061-2069.

98. Sarmento, B., et al., Characterization of insulin-loaded alginate nanoparticles produced by ionotropic pre-gelation through DSC and FTIR studies. Carbohydrate Polymers, 2006. 66(1): p. 1-7.

99. Saganowska, P. and M. Wesolowski, DSC as a screening tool for rapid co-crystal detection in binary mixtures of benzodiazepines with co-formers. Journal of Thermal Analysis and Calorimetry, 2018. 133(1): p. 785-795.

100. Rizvi, S.A. and A.M. Saleh, Applications of nanoparticle systems in drug delivery technology. Saudi Pharmaceutical Journal, 2018. 26(1): p. 64-70.

101. Liu, M., et al., Characterization and release of triptolide-loaded poly (D, L-lactic acid) nanoparticles. European Polymer Journal, 2005. 41(2): p. 375-382.

102. Arriagada, F., et al., Development and characterization of florfenicol-loaded BSA nanoparticles as controlled release carrier. AAPS PharmSciTech, 2019. 20(5): p. 202.

103. Zhu, D., et al., Folate-targeted polymersomes loaded with both paclitaxel and doxorubicin for the combination chemotherapy of hepatocellular carcinoma. Acta biomaterialia, 2017. 58: p. 399-412.

104. Smith, B.T., Remington education: physical pharmacy. 2015: Pharmaceutical Press.

105. Bamba, M., et al., Release mechanisms in gelforming sustained release preparations. International Journal of Pharmaceutics, 1979. 2(5-6): p. 307-315.

106. Papadopoulou, V., et al., On the use of the Weibull function for the discernment of drug release mechanisms. International Journal of Pharmaceutics, 2006. 309(1-2): p. 44-50.

107. Zhang, H., F.-M. Zhang, and S.-J. Yan, Preparation, in vitro release, and pharmacokinetics in rabbits of lyophilized injection of sorafenib solid lipid nanoparticles. International Journal of Nanomedicine, 2012. 7: p. 2901.

108. Adibkia, K., et al., Piroxicam nanoparticles for ocular delivery: physicochemical characterization and implementation in endotoxin-induced uveitis. Journal of Drug Targeting, 2007. 15(6): p. 407-416.

109. Ji, J., et al., Preparation, characterization and in vitro release of chitosan nanoparticles loaded with gentamicin and salicylic acid. Carbohydrate Polymers, 2011. 85(4): p. 803-808.

110. Costa, S.S., et al., Multidrug efflux pumps in Staphylococcus aureus: an update. The Open Microbiology Journal, 2013. 7: p. 59.

111. Mukesh, B. and K. Rakesh, Molecular docking: a review. International Journal of Research in Ayurveda & Pharmacy, 2011. 2(6): p. 1746-1751.

112. Kannappan, A., et al., Antibiofilm activity of Vetiveria zizanioides root extract against methicillin-resistant Staphylococcus aureus. Microbial Pathogenesis, 2017. 110: p. 313-324.

113. Mah, T.-F., et al., A genetic basis for Pseudomonas aeruginosa biofilm antibiotic resistance. Nature, 2003. 426(6964): p. 306.

114. Fittipaldi, M., A. Nocker, and F. Codony, Progress in understanding preferential detection of live cells using viability dyes in combination with DNA amplification. Journal of Microbiological Methods, 2012. 91(2): p. 276-289.

115. Archer, N.K., et al., Staphylococcus aureus biofilms: properties, regulation, and roles in human disease. Virulence, 2011. 2(5): p. 445-459.

116. Gad, G.F.M., et al., Detection of icaA, icaD genes and biofilm production by Staphylococcus aureus and Staphylococcus epidermidis isolated from urinary tract catheterized patients. The Journal of Infection in Developing Countries, 2009. 3(05): p. 342-351.

117. Macia, M., E. Rojo-Molinero, and A. Oliver, Antimicrobial susceptibility testing in biofilm-growing bacteria. Clinical Microbiology and Infection, 2014. 20(10): p. 981-990.

118. Ikuma, K., A.W. Decho, and B.L. Lau, When nanoparticles meet biofilms—interactions guiding the environmental fate and accumulation of nanoparticles. Frontiers in Microbiology, 2015. 6: p. 591.

119. Bidossi, A., et al., In vitro comparison between α-tocopheryl acetate and α-tocopheryl phosphate against bacteria responsible of prosthetic and joint infections. PloS One, 2017. 12(7): p. e0182323.

120. Gajdács, M. and G. Spengler, The role of drug repurposing in the development of novel antimicrobial drugs: Non-antibiotic pharmacological agents as quorum sensing-inhibitors. Antibiotics, 2019. 8(4): p. 270.

121. Memariani, H., M. Memariani, and A. Ghasemian, An overview on anti-biofilm properties of quercetin against bacterial pathogens. World Journal of Microbiology and Biotechnology, 2019. 35(9): p. 143.

122. Liu, Y., L. Yang, and S. Molin, Synergistic activities of an efflux pump inhibitor and iron chelators against Pseudomonas aeruginosa growth and biofilm formation. Antimicrobial agents and chemotherapy, 2010. 54(9): p. 3960-3963.

123. Zimmermann, S., et al., Clinically approved drugs inhibit the Staphylococcus aureus multidrug NorA efflux pump and reduce biofilm formation. Frontiers in Microbiology, 2019. 10: p. 2762.

124. Jeong, Y.-I., et al., Ciprofloxacin-encapsulated poly (DL-lactide-co-glycolide) nanoparticles and its antibacterial activity. International journal of pharmaceutics, 2008. 352(1-2): p. 317-323.

CHAPTER 4, EXPERIMENTAL PAPER 3

5.1 Introduction

This chapter addresses Aim 3, Objectives 1 – 6 and is a first-authored experimental article accepted in Journal of Biomolecular Structure & Dynamics (Impact Factor 3.22) an ISI international journal (manuscript ID: TBSD-2020-1529). This article highlights the synthesis of a novel polymeric conjugation of FA with a biodegradable polymer; PEG, the *in vitro* toxicity evaluation, molecular dynamics simulation of the self-assembly of NPs, characterization of its physical properties, binding check for FA, bilirubin and PEG-FA molecules with HSA using MST, and *in vitro* antibacterial properties.

Graphical abstract

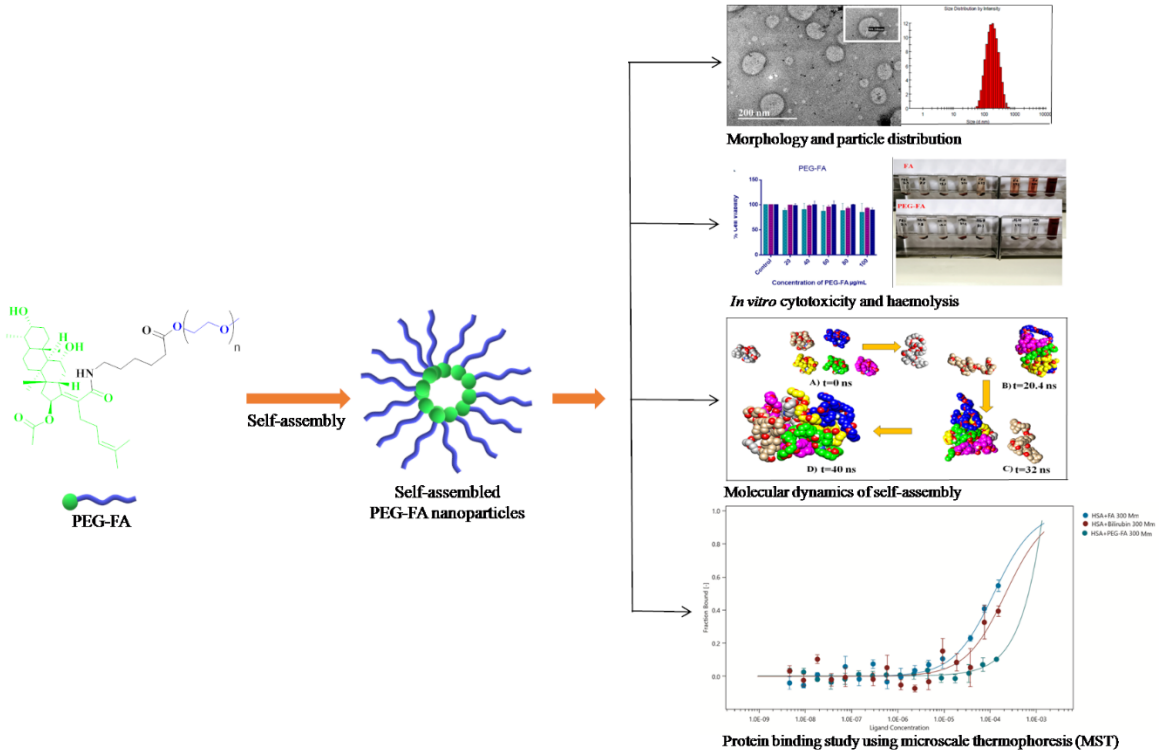

A Self-Assembled Polymer Therapeutic for Simultaneously Enhancing Solubility and Antimicrobial Activity and Lowering Serum Albumin Binding of Fusidic acid

Mohammed Salih[a], Pavan Walvekar[*,a], Calvin A. Omolo[a,c], Ahmed A Elrashedy[b], Nikita Devnarain[a] , Victoria Fasiku[a], Ayman Y. Waddad[a], Chunderika Mocktar[a], Thirumala Govender[*,a]

[a]Discipline of Pharmaceutical Sciences, College of Health Sciences, University of KwaZulu-Natal, Private Bag X54001, Durban, South Africa

[b]Department of Chemistry of Natural and Microbial Products, Division of Pharmaceutical and Drug Industries, National Research Centre, Cairo, 12622, Egypt.

[c]School of Pharmacy and Health Sciences, United States International University, P.O. BOX 14634 - 00800 Nairobi, Kenya

* corresponding author

Email address**:** govenderth@ukzn.ac.za; pavanwalvekar43@gmail.com

Abstract

The global antimicrobial resistance crisis has prompted worldwide efforts to develop new and more efficient antimicrobial compounds, as well as to develop new drug delivery strategies and targeting mechanisms. This study aimed to synthesize a novel polyethylene glycol-fusidic acid (PEG-FA) conjugate for self-assembly into nano-sized structures and explore its potential for simultaneously enhancing aqueous solubility and antibacterial activity of FA. In addition, the ability of PEG-FA to bind to HSA with lower affinity than FA is also investigated. Haemolysis and *in vitro* cytotoxicity studies confirmed superior biosafety of the novel PEG-FA compared to FA. The water solubility of FA after PEG conjugation was increased by 25-fold compared to the bare drug. PEG-FA nanoparticles displayed particle size, polydispersity index and zeta potential of 149.3 ± 0.21 nm, 0.267 ± 0.01 and 5.97 ± 1.03 mV, respectively. Morphology studies using high resolution transmission electron microscope revealed a homogenous spherical shape of the PEG-FA nanoparticles. *In silico* studies showed that Van der Waals forces facilitated PEG-FA self-assembly. HSA binding studies showed that PEG-FA had very weak or no interaction with HSA using *in silico* molecular docking (-2.93 kcal/mol) and microscale thermophoresis (K_d = 14999 ± 1.36 µM), which may prevent bilirubin displacement. Conjugation with PEG did not inhibit the antibacterial activity of FA but rather enhanced it by 2.5-fold against *Staphylococcus aureus* and methicillin-resistant *Staphylococcus aureus*, compared to the bare FA. These results show that PEG-FA can simultaneously enhance solubility and antibacterial activity of FA, whilst also reducing binding of HSA to decrease its side effects.

Keywords: Fusidic acid; Polyethylene glycol; *Staphylococcus aureus*; Methicillin-Resistant *Staphylococcus aureus*; Human serum albumin; Bilirubin; Microscale Thermophoresis

1. Introduction

Infectious diseases caused by pathogenic microorganisms, such as bacteria, impose a significant threat to global health and remain a major contributor to premature mortality. Recent statistics showed an estimated 700,000 annual deaths worldwide [18], with the United States specifically showing 2.8 million severe illnesses cases and 35,000 annual deaths in 2019 due to pathogenic resistant bacteria [221]. These numbers are significantly higher than the previous report from 2013. Factors such as high cost, lengthy process of development and regulatory approval of new drugs, and high attrition rates at final stages of testing, amongst others [35], have resulted in a 90% decline in the development and regulatory approval of new antibiotics [15]. Therefore, scientists are focusing on less time consuming and more cost-effective approaches to enhance the efficacy of old antibiotics through modification of their structures and reformulation into nanosystems [128, 222].

Nanotechnology is recognized as an effective strategy to deliver and improve the activity of different antibiotics, with some nano-drug delivery systems have already reached the market [33, 40, 41]. The most attractive feature of nanoparticles (NPs) as drug delivery vehicles are their ability to introduce a wide range of therapeutics, either attached to their large surface area or contained within the structure. This characteristic enhances the solubility of poorly soluble drugs, allowing for sustained and controlled drug release, improving cellular internalization, providing efficient delivery to the site of infection and preventing exposure of the drug to healthy cells [42, 43, 223]. Therefore, utilizing nanotechnology to fabricate a delivery system for old antibiotics, such as fusidic acid (FA), can potentiate their applications and protect the deterioration of the numbers of effective antibiotics available to treat resistant bacterial diseases.

Fusidic acid, an antibiotic which belongs to the fusidane group, was first isolated from *Fusidium coccineum* fungus in 1962 [120]. Structurally, FA is a tetracyclic triterpenoid, with a ring system similar to steroid compounds, but has no corticosteroid effect. It is a slightly hygroscopic white powder, practically insoluble in water. FA is active against *Staphylococcus aureus* (*S. aureus*) and methicillin-resistant *Staphylococcus aureus* (MRSA) strains [121]. Due to the global crisis of antimicrobial resistance, there is an increasing research focus on FA, as it has a unique mechanism of action and lacks significant cross-resistance to other classes of antibiotics [224-226]. A novel safe and effective dosing regimen for oral drug monotherapy for FA has been patented recently in the United States to fight

against MRSA [227]. Phase 2 clinical trials investigating the effectiveness of oral FA for the treatment of prosthetic joint infections in the United States are also underway, as a part of an effort to register FA in the United States, since it is yet to be approved by FDA [228].

Fusidic acid is available in different conventional dosage forms, including; tablets and suspension for oral, cream and ointment for topical and also injection for intravenous administration [121]. However, there are challenges that limit the formulation and therapeutic efficacy of FA. Due to the hydrophobic nature of FA, it has been classified as a class II drug according to the biopharmaceutical classification system (BCS) [229]. When compared to highly soluble drugs, poorly soluble drugs not only indicate *in vivo* challenges, such as reduced bioavailability and higher inter-patient variability, but also many *in vitro* obstacles associated with formulations such as restricted choice of delivery techniques and complex dissolution testing with low or weak co-relation to *in vivo* absorption [229-231]. Several techniques, such as micronization [232], solubilization [233] and salt formation [234], have been explored to solve the problem of low aqueous solubility. Despite the good water solubility of FA sodium salt, it precipitates in acidic media and its solubility often appears to vary with changes in pH in the gastrointestinal tract. Furthermore, FA binds with high affinity to human serum albumin (HSA) under normal conditions, 91% to 98% of FA molecules in circulation are bound to HSA [122]. However, it should be used with caution because one of the frequent side effects of FA is hyperbilirubinemia/jaundice, which can occur as early as two days post treatment [235]. An *in vitro* and *in vivo* study confirmed that FA is capable of causing significant displacement of bilirubin bound to HSA [236]. This adverse effect is more serious in infants as jaundice occurs in 60% to 80% of normal infants in the United States [237, 238]. Hence, a strategy that can improve the water solubility and pharmacokinetic profiles of FA, as well as reduce its side effects, whilst retaining its antimicrobial activity is of significant interest and necessity.

The drug delivery field using polymers such as polyethylene glycol (PEG), which is covalently connected to a drug is known as “polymer therapeutics” [106, 239]. Polymer therapeutics have been reported to increase plasma circulation time, reduce side effects and increase the therapeutic index of the conjugated drugs. The conjugation of drug molecules with polymers such as PEG is one of the most attractive techniques in the drug delivery field that can boost the activity of drugs [108]. Moreover, polymer therapeutic prodrugs that have the ability to self-assemble into nanosized particles have received considerable attention in drug delivery [58]. PEGylation has been reported to be a suitable technique for formulating

polymer therapeutics [110, 111], with several products such as Pegasys, Mircera and Cimzia being available in the market [107]. Therefore, PEGylation of biopharmaceutics class II drugs such as FA could offer a strategic opportunity to improve the therapeutic effects of the drugs. PEGylated polymer therapeutics have shown to enhance water solubility of poorly soluble drugs, reduce uptake by the reticulo-endothelial system (RES), target the delivery of drugs to specific sites of action and reduce HSA binding [47, 108]. In particular, PEGylated irinotecan conjugate, a polymer therapeutic that entered phase II clinical trials, showed superior anticancer activity, compared to irinotecan alone [240]. The activity enhancement was attributed to the combination of enhanced drug solubility, improved biodistribution and the enhanced permeability and retention (EPR) effect [241].

There are several reported polymer therapeutics for enhancing and improving the activity of antibiotics, such as penicillin [112, 113], fluoroquinolones [114-117], aminoglycoside [110, 118] and sulfonamides [119] using delivery systems developed through polymeric conjugation. Although there have been reports of FA conjugation with small molecules in order to enhance and broaden its spectrum [123, 124], there are no reports on polymer FA conjugation to form a self-assembling polymer therapeutic. Therefore, polymeric conjugation of FA with a biodegradable polymer such as PEG, can potentially enhance its aqueous solubility, bioavailability and antimicrobial activity.

Molecular dynamics (MD) simulations are routinely used to provide understanding and testing of novel hypotheses at the molecular scale for small molecule drug delivery research [242-244]. With recent advances in computational power such simulations can now be used in nanomedicine, for instance, to better understand assembly and biological properties of nanoparticles, such as protein binding [47, 245].

In this study, we report a novel PEGylated FA (PEG-FA), conjugated through a small spacer with an amide bond for self-assembly into a nanosystem for simultaneous improved solubility and antibacterial activity and decreased HSA binding. Moreover, we report for the first time, the quantitative binding of FA, bilirubin and PEGylated FA molecules with HSA using microscale thermophoresis (MST). Further, *in silico* studies were used to evaluate the self-assembly and binding affinity of PEG-FA to HSA at a molecular level.

2. Materials and methods

2.1. Materials

Monomethoxy PEG (MW 2,000), FA, 6-aminohexanoic acid (6-AHA), p-dimethylaminopyridine (DMAP), 1-ethyl-3-(3-dimethylaminopropyl)carbodiimide (EDC) and trifluoroacetic acid (TFA) were purchased from Sigma-Aldrich (USA). Dichloromethane (DCM) was purchased from Merck Chemicals (Pty) Ltd (Johannesburg, South Africa). Di-tert-butyl dicarbonate (BOC anhydride) was purchased from Sisco Research Laboratories Pvt. Ltd (India). 3-(4,5-dimethylthiazol-2-yl)-2,5-diphenyltetrazolium bromide (MTT) was purchased from Merck Chemicals (Germany). For cell culture, cells were purchased from Highveld Biologicals (Johannesburg, South Africa). Cell culture reagents were purchased from Whitehead Scientific (Johannesburg, South Africa). For haemolytic study, sheep blood from United scientific (Durban, South Africa). For bacterial cultures, Mueller-Hinton Broth (MHB), Nutrient Broth and Mueller-Hinton Agar (MHA) were purchased from Biolab (South Africa). *S. aureus* (ATCC 25923) and MRSA (SA Rosenbach ATCC BAA 1683) were purchased from DLD Scientific (South Africa). Purified water used in the study was produced in the laboratory with a Milli-Q water purification system (Millipore corp., USA). Bilirubin and HSA were purchased from Sigma-Aldrich (USA). Monolith protein labeling kit RED-NHS, MST buffer supplemented with 0.05% Tween 20 and Monolith NT.115 standard treated capillaries were supplied by NanoTemper Technologies (Germany). All reagents and solvents used in this study were of analytical grade.

2.2. Synthesis and characterization of PEG-FA

PEG-FA conjugate was synthesized using **Scheme 1.** Details of synthesis can be found in the supplementary material.

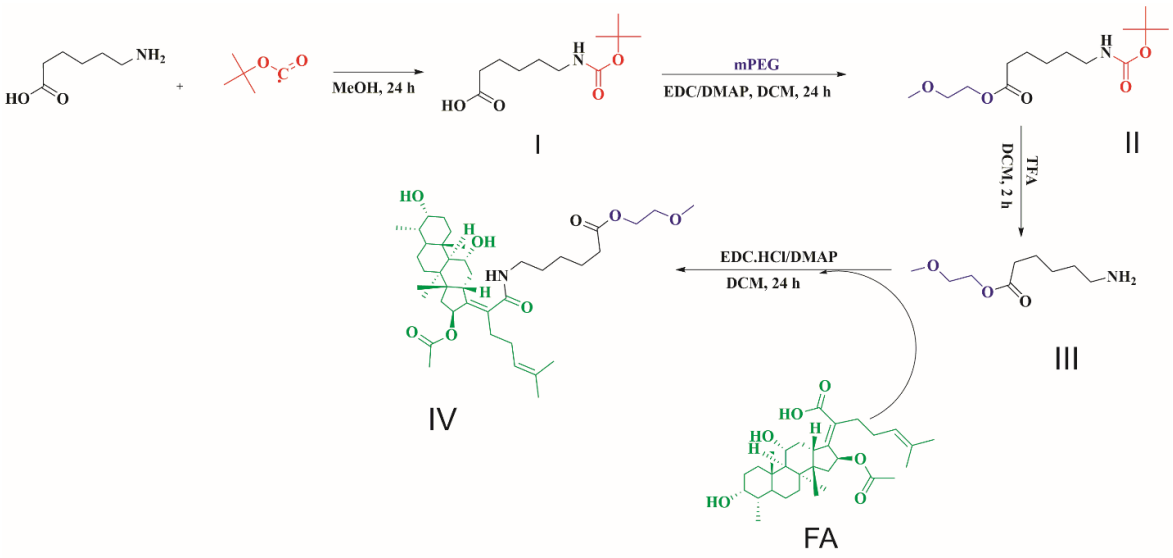

Scheme 1. Synthesis of PEG-FA. I) Methanol, room temperature, 24 h; II) EDC, DMAP, DCM, room temperature, 24 h; III) TFA, DCM, room temperature, 2 h; IV) EDC, DMAP, DCM, room temperature, 24 h.

2.3. Characterization of the synthesized PEG-FA

Fourier-transform infrared spectroscopy (FT-IR) spectra of all the compounds were recorded on a Bruker Alpha-p spectrometer with a diamond ATR (Germany). Thermal profiles of the polymer and the conjugated polymer were determined using differential scanning calorimetry (DSC) (Shimadzu DSC-60, Japan) [246]. Samples were loaded on aluminum pans (2 mg) and sealed using a crimper, followed by heating under nitrogen flow, at a constant rate of 10 °C/min to 300 °C. An empty pan was used as a reference. Proton nuclear magnetic resonance (^{1}H NMR) measurements were performed on a Bruker 400 Ultra shield™ (United Kingdom) NMR spectrometer using deuterated chloroform ($CDCl_3$) as a solvent.

2.4. Solubility studies

A comparison of the solubility enhancement between FA and PEG-FA was determined using a previously reported method [225]. Briefly, a specific amount of FA and PEG-FA was added to water in vials at a concentration of 100 µg/mL. The mixture in the vials were kept in an isothermal shaker at 37 ± 1.0 °C for 72 h. The undissolved part was filtered through a membrane filter (0.22 µm), and centrifuged for 15 min at 3000 rpm. The absorption was measured at 285 nm using a UV spectrophotometer (UV-1800, Shimadzu, Japan). The samples for solubility studies were prepared in triplicate.

2.5. *In vitro* biosafety

2.5.1. Cytotoxicity and cell viability

The *in vitro* cell viability of the conjugated PEG-FA was evaluated and compared to FA using the MTT assay [150]. Three different cell lines were used in this study: human embryonic kidney 293 (HEK 293) cells, Michigan Cancer Foundation-7 (MCF-7) breast cancer cells and human cervical cancer (HeLa) cells. All three cell lines were seeded at a concentration of 2.5 x 10^3 cells/well into a sterile 96-well plate containing 100 µL DMEM, 10% fetal bovine serum (FBS), 1% pen-strep-fungizone and 1% L-glutamine and incubated for 24 h at 37 °C in a CO_2 humidified incubator. Thereafter, different concentrations of PEG-FA and FA (20, 40, 60, 80 and 100 µg/mL) were added and incubated for a further 24 h. After the 24 h incubation period, the media were substituted with 100 µL of MTT solution (5

mg/mL in PBS) per well and incubated for 4 h. The supernatant was then aspirated and formazan crystals were solubilized using 100 µL of dimethyl sulfoxide. A microplate spectrophotometer (SpectrostarNano, Germany) was used to read absorbances at 540 nm (proportional to the number of live cells). The study was performed in hexaplicate and the formula below was used to calculate the percentage cell viability.

$$\%\ \text{Cell viability} = \left(\frac{A_{540\ \text{nm}}\ \text{treated cells}}{A_{540\ \text{nm}}\ \text{untreated cells}}\right) \text{x } 100\%$$

2.5.2. Haemolysis

A previously reported method was used for the determination of percentage hemolysis [193]. Briefly, freshly collected sheep blood was washed three times with autoclaved phosphate buffer saline (PBS, pH 7.4), followed by centrifugation at 2800 rpm for 5 min. PEG-FA was diluted with PBS to a concentration ranging from 0.05 to 0.5 mg/mL for each sample. The red blood cell (RBC) suspension (0.2 mL) was added to 1.8 mL of each sample and left for incubation at 37 °C for 30 min. Thereafter, the samples were centrifuged at 3000 rpm for 10 min. Spectrophotometric readings of the supernatant of each sample at different concentrations were taken for the determination of haemoglobin release. To obtain 0% and 100% haemolysis, 0.2 mL of RBC suspension was added to 1.8 mL PBS and distilled water, respectively. The degree of haemolysis was calculated using the formula below.

$$\%\ \text{Haemolysis} = \left(\frac{\text{ABS} - \text{ABS}_0}{\text{ABS}_{100} - \text{ABS}_0}\right) \text{x } 100\%$$

Where, ABS_{100} and ABS_0 are the absorbances of the solution at 100% and 0% haemolysis, respectively. The results of triplicate measurements were used.

2.6. Preparation of PEG-FA nanoparticles

Self-assembled PEG-FA NPs were prepared by the solvent evaporation method [143]. Briefly, PEG-FA (50 mg) was dissolved in THF (0.5 mL) and slowly added to water (10 mL) dropwise. The formed emulsion was stirred for 24 h at room temperature to ensure complete evaporation of the solvent. Thereafter, the volume was adjusted to 10 mL. The self-assembled PEG-FA nanosystem was further characterized. PEG-FA nanoparticles were prepared in triplicate.

2.7. Characterization of PEG-FA nanoparticles

2.7.1. Size, polydispersity index (PDI), zeta potential (ZP) and morphology

The molecular self-assembly of PEG-FA conjugate into its nanostructures was characterized using the dynamic light scattering (DLS) technique to determine their average size, PDI and ZP. Appropriate dilutions of the formula were made using distilled water. Measurements were recorded at room temperature using a Zetasizer Nano ZS90 (Malvern Instruments, UK) fitted with a 633 nm laser at 173° detection optics. All parameters were analyzed in triplicate. To observe the morphological structure of PEG-FA nanoparticles, a High-Resolution Transmission Electron Microscope (HRTEM, JEOL 2100) was used.

2.7.2. *In silico* study of PEG-FA self-assembly

2.7.2.1. All-atom molecular dynamic simulations of PEG-FA self-assembly

Molecular“dynamic (MD) simulation is a widely applied technique in the field of drug delivery to achieve different tasks, such as understanding the drug interaction with proteins, membranes and polymers. The spontaneous self-assembly of PEG-FA was studied using MD simulations to understand the mechanism and identify the type of interactions that played a crucial role in self-assembly. The synthesized conjugate (PEG-FA) structure composed of single FA attached through single 6AHA to PEG polymer compromising of seven repeating monomer units of ethylene glycol (EG), was drawn with ChemDraw professional software [247]. The Chimera tool was used for random insertion of six molecules of PEG-FA complex [161]. The LEAP module implemented in AMBER 14 was used to combine, neutralize and solvate the system by adding hydrogen atoms, chloride and sodium ions and suspending them in an orthorhombic box of TIP3P water molecules such that all atoms were within 10 Å of the box edges [248]. The system contained a total of 5820 water molecules and 6 molecules of PEG-FA. The system was minimized for 2500 steps with applied restraint of 100 kcal/mol Å, followed by 1000 steps of full minimization. The system was then gradually heated from 0 °K to 300 °K for 50 ps such that they maintained a fixed number of atoms and fixed volume (NVT) with a potential harmonic restraint of 10 kcal/mol Å and collision frequency of 1.0 ps^{-1}. The system was then equilibrated without restraint at a temperature of 300 °K at a constant pressure of 1 bar using the Berendsen barostat. This was followed by MD production for 40 ns per system, in which the SHAKE algorithm was used to constrict the bonds of hydrogen atoms [147]. All the MD simulations were carried out using the GPU amber 14 software package [148].

2.7.2.2. Post-dynamic analysis

To determine the binding free energy, the trajectory generated after MD simulation was saved every 1 ps, followed by analysis using the CPPTRAJ [165] module employed in AMBER 14 suite. All plots, visualizations and graphical representations were completed using Microcal Origin tools [249] and Chimera [161], respectively.

2.7.2.3. Binding free energy calculations

Binding free energy calculations is an important endpoint method that may be used to elucidate the mechanism of binding between a ligand and protein, including both enthalpic and entropic contributions [250, 251]. To estimate the binding affinity of the system, the free binding energy was calculated using the Molecular Mechanics/Generalized Born Surface Area method (MM/GBSA) [252]. Binding free energy was averaged over 1000 snapshots extracted from the 10 ns trajectory. The free binding energy computed by this method for each molecular species (complex, ligand, and receptor) can be represented as:

$$\Delta G_{\text{bind}} = G_{\text{complex}} - G_{\text{receptor}} - G_{\text{ligand}} (1)$$

$$\Delta G_{\text{bind}} = E_{\text{gas}} + G_{\text{sol}} - \text{TS} \quad (2)$$

$$E_{\text{gas}} = E_{\text{int}} + E_{\text{vdw}} + E_{\text{ele}} (3)$$

$$G_{\text{sol}} = G_{\text{GB}} + G_{\text{SA}} (4)$$

$$G_{\text{SA}} = \gamma \text{SASA} \qquad (5)$$

where:

E_{ele}	Electrostatic potential energy from Coulomb forces
E_{gas}	Gas-phase energy (based on FF14SB force field terms)
E_{int}	Internal energy
E_{vdW}	van der Waals energy
G_{sol}	Solvation free energy
G_{GB}	Polar solvation energy
G_{SA}	non-polar solvation energy
S	Total entropy of solute
SASA	Solvent accessible surface area (water probe radius of 1.4 Å)
T	Total entropy of temperature

The E_{gas} was directly assessed from the force field terms. The G_{sol}, was assessed from the energy involvement from the G_{GB}, and non-polar states (G). The G_{SA} was determined from

SASA using a water probe radius of 1.4 Å, whereas the G_{GB} contribution was assessed by solving the GB equation. S and T symbolize the total entropy of the solute and temperature, respectively [252].

2.8. Determination of the binding affinity of FA, bilirubin and PEG-FA to HSA

2.8.1. *In silico* study of the binding affinity

2.8.1.1. Molecular docking study

This study was conducted to study the effect of PEGylation of FA on the binding of HSA in comparison with bilirubin at the molecular level. This was performed using molecular modeling environment (MOE) to evaluate the binding affinities and the best binding positions between the 3 compounds (FA, bilirubin and PEG-FA) and the sub-domain IB of HSA **(Fig. 1)**.

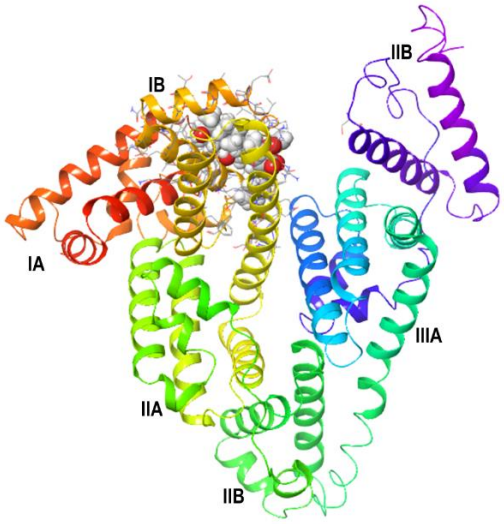

Fig. 1. The 3-D crystal structure of human serum albumin (PDB code: 2VUE).

Docking studies were performed using the MOE 2008.10 (MOE source: Chemical Computing Group Inc., Quebec, Canada, 2008). First, a Gaussian contact surface was drawn around the binding site. The surface of the molecule is occupied by van der Waals attraction forces (filling in solvent inaccessible gaps). Docking studies were performed to determine the binding free energy of FA and synthesized PEG-FA conjugate within the macromolecules. Simply, we performed molecular docking with two PEG-FA molecule sseparately with a small PEG chain (2 and 7 monomer of EG). Dock Scoring in MOE software was conducted using the London dG Scoring feature and it was improved using two separate refining methods, the Force-field and Grid-Min posing to ensure that the refined poses met the

required specified conformations. We allowed rotatable bonds; the best 10 poses were retained and analyzed for the binding pose with the best score.

2.8.1.2. Preparation of the ligands and HSA

The ligand compounds involved in this study were tested for their binding affinity to the sub-domain IB of HSA. The Molecule Builder method in MOE has been used to create a three-dimensional model of the structures. Energy minimization was carried out through Force-field MMFF94x Optimization using a gradient of 0.0001 for the determination of low energy conformations with the most suitable (lowest energy) geometry. The crystal structure of HSA in complex with 4Z,15E-bilirubin was retrieved from the Protein Data Bank [253] (PDB code: 2VUE) [254]. Hydrogen atoms and partial loads have been applied with the protonation 3D application in MOE. This application is used to assign ionization states and place hydrogen atoms in the macromolecular structure.

2.8.1.3. The binding affinities of the FA and the synthesized PEG-FA conjugate to HSA proteins

Molecular docking analysis was performed to identify the interactions between the ligands and HSA, as well as to compare the binding affinities of FA and PEG-FA conjugate towards the target sub-domain IB HSA. For docking calculations, the protein structure was first split from the inhibitor molecule and improved by molecular minimization with added hydrogen atoms. Docking calculations have been conducted using default variables for the MOE program. The binding affinity was measured by binding free energies (S-score, kcal/mol) and hydrogen bonds. All the synthesized conjugates in addition to FA were docked in the same groove of the sub-domain IB binding site of the native co-crystallized"bilirubin-ligand.

2.8.2. Microscale thermophoresis binding affinity studies

Based on the *in silico* confirmation, MST studies were undertaken to quantitatively elucidate the difference in binding. The binding parameters between FA, bilirubin and PEG-FA with HSA were measured using MST on a Monolith NT.115 (Germany) [47]. Labeling of HSA was carried out using the Monolith protein labeling kit RED-NHS according to the manufacturer's instructions. MST assay buffer supplemented with 0.05% Tween 20 was used to dilute the labeled HSA to 100 nM. A series of 16 dilutions (1:1) using the same buffer solution of the ligands (FA, bilirubin and PEG-FA) were prepared with starting concentration of 300 μM. Equivalent volume of the labeled HSA was added to each of the dilutions and

incubated for 10 min, then loaded into Monolith NT.115 Standard Treated Capillaries (Nano Temper Technologies). The measurement of the MST trace was carried out using a Monolith NT.115 instrument (Nano Temper Technologies) at a temperature of 27 °C. Parameters were adjusted to 40% MST and power 20% LED power. The strength of binding was evaluated using MO-Affinity analysis software version 2.1.3 (Nano Temper Technologies). The results of triplicate measurements were used to calculate the dissociation constant, K_d.

2.8.3. HSA protein adsorption studies

Human serum albumin adsorption studies were performed according to a previously reported protocol [47, 255]. The self-assembled PEG-FA NPs were incubated in a solution of 400 μg/mL of HSA and stirred vigorously for 2 h at 37 °C. The NPs were then centrifuged (14,000 rpm, 4 °C for 20 min) to remove any unabsorbed proteins. The samples were then diluted, and the Zetasizer was used to analyze the size and surface charge.

2.9. *In vitro* antibacterial activity

The broth microdilution method was used to determine the minimum inhibitory concentrations (MICs) of FA and PEG-FA against *S. aureus* and MRSA [153]. Briefly, an overnight culture in nutrient broth at 37 °C of *S. aureus* and MRSA, placed in a shaker incubator, was diluted to 0.5 McFarland standard, using a DEN-1B McFarland densitometer (Latvia). In a 96-well plate, a specific volume of MHB was added, followed by the addition of an equal volume of bare FA solution (positive control), and PEG-FA in the first well, then they were serially diluted. Subsequently, *S. aureus* and MRSA were further diluted to 5×10^5 colony-forming units per mL (CFU/mL) and added to the 96-well plate containing the serially diluted samples and MHB. The studies were performed in triplicate. The broth mixture was incubated for 24 h in a shaking incubator at 37 °C, then spotted on MHA plates, and incubated for 24 h at 37 °C to calculate the MICs.

2.10. Statistical analysis

The results were stated as mean ± standard deviation (SD), and the data analysis was carried out using GraphPad Prism® 5 (Graphpad Software Inc., USA). The multiple comparison test and One-way ANOVA from Bonferroni were used to evaluate the results, and the difference was considered significant when $p < 0.05$.

3. Results and discussion

3.1. Synthesis of PEG-FA conjugate

PEG was chosen as a conjugating polymer with FA due to its unique properties, such as high water solubility, biocompatibility, lack of toxicity, low immunogenicity and presence of one or two functionalizable hydroxyl groups. In this study, we used PEG, which has only one terminal hydroxyl group. The preliminary work involved conjugation of FA to PEG directly without the use of a linker, but the reaction was not successful. A similar problem with PEG conjugation with other drugs was resolved using a small linker or spacer [256]. Since primary amines are more reactive than alcohol groups (-OH), a linker with free amine groups was chosen to conjugate FA and PEG [257]. Amino acids are well-known spacers that have been used to conjugate PEG with different peptides, proteins and non-protein drugs [256, 258]. A derivative of amino acid lysine (6-aminohexanoic acid) was used as a spacer between PEG and FA. The first step was to protect the amino group of the amino acid using BOC protection as described in **Scheme 1**, to synthesize compound I. The second step was an esterification reaction, to conjugate PEG with compound I, to produce the PEG-spacer conjugate (compound II). A further cleaving step was carried out to deprotect the terminal amine group (compound III). The last step was to conjugate the carboxylic group of FA with the amine group of compound III, through amidation reaction to get the final PEG-FA (compound IV). The polymer drug conjugate product (PEG-FA) was verified and fully characterized using FT-IR, DSC and ^{1}H NMR, and compared to the individual spectra of FA and PEG-spacer.

3.2. Characterization of PEG-FA

FT-IR spectra of FA, PEG-6AHA and PEG-FA have been provided in the supplementary material (**Fig. S1**). The formation of amide bond between FA and PEG-6AHA was confirmed by the appearance of a new peak at 1640 cm^{-1}, which is characteristic of a stretching carbonyl group (C = O). Another peak was observed at 1510 cm^{-1} due to bending of (N-H) bond [259]. These results provided preliminary confirmation of successful synthesis of drug-polymer conjugate (PEG-FA). DSC can also provide evidence for the successful synthesis of PEG-FA [260]. From the thermograms (**Fig. 2A and 2B**), the PEG-6AHA polymer shows two endothermic peaks at 57.4 °C and 204.9 °C, while FA shows an endothermic peak at 191.2 °C, which corresponds to the melting point of FA (**Fig. 2A**). The DSC thermogram of the final polymer drug conjugate PEG-FA exhibited a sharp endothermic peak at 54.4 °C, similar to the main peaks in PEG-6AHA polymer. Furthermore, there are two other small peaks at 225.2 °C and 281.2 °C, whereas the peak for the melting point of FA disappeared. This confirms the conjugation of FA to PEG and absence of the free FA. The results obtained

from FT-IR and DSC were further verified using ^{1}H-NMR analysis. **Fig. 3** shows the ^{1}H-NMR peaks for FA, PEG-6AHA and the final product (PEG-FA). In both PEG-6AHA and PEG-FA, the repetitive ethylene protons can be identified at 3.6 ppm. The peaks that appeared between 2.3 ppm and 2.9 ppm in the spectra of PEG-6AHA and PEG-FA were attributed to the methylene protons (-CH_2-) of 6AHA, thus confirming the esterification between the PEG and 6AHA (**Fig. 3**). Further, the presence of protons corresponding to FA that appeared between 0.5 ppm and 2.5 ppm in the spectrum of PEG-FA confirmed the successful conjugation of PEG-6AHA to FA.

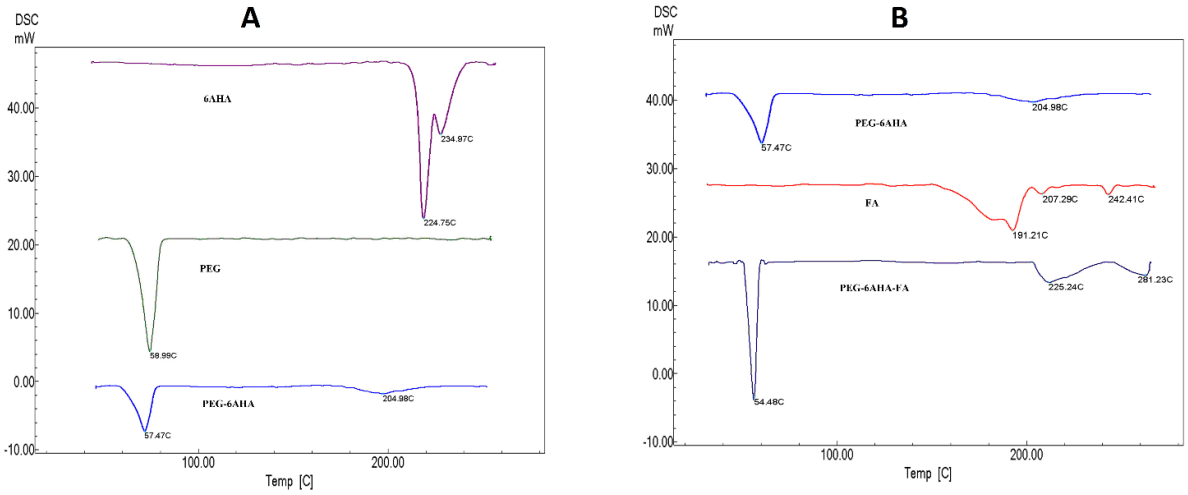

Fig. 2. DSC thermogram of **A)** 6AHA, PEG and PEG-6AHA. **B)** PEG-6AHA, FA and PEG-FA.

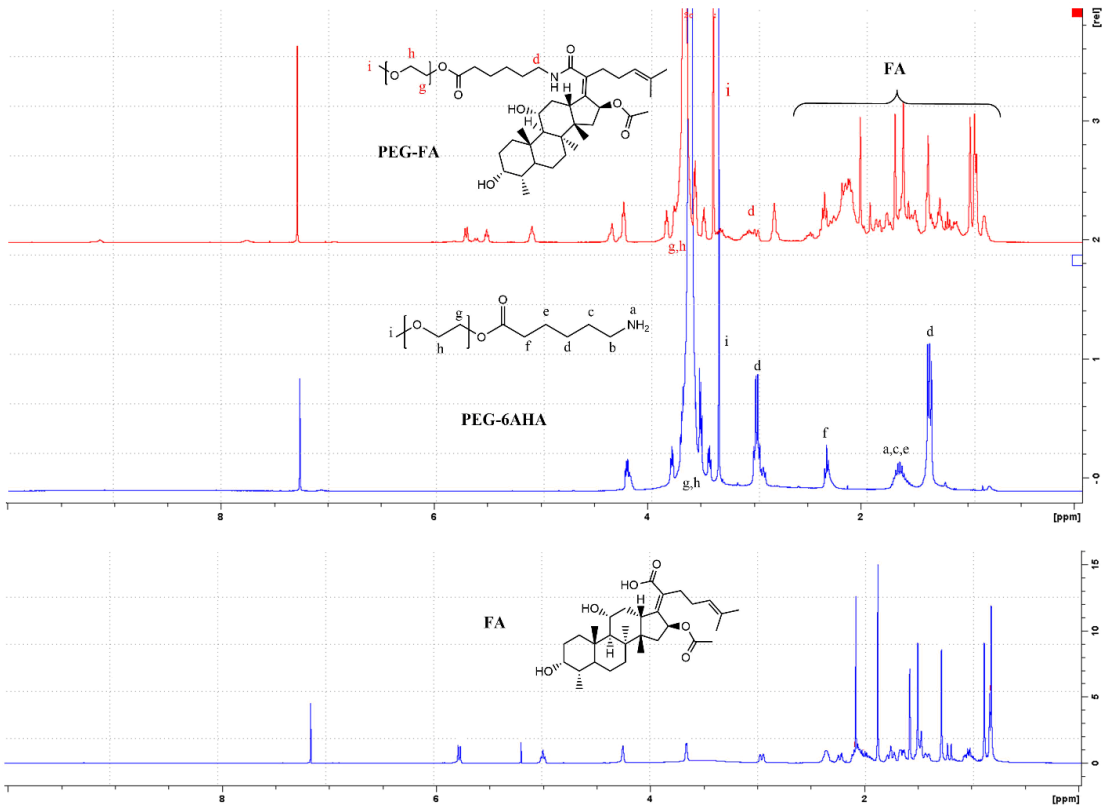

Fig. 3. ^{1}H-NMR spectra of FA, PEG-6AHA and PEG-FA in $CDCl_3$.

3.3. Solubility studies

In this study we aimed to measure solubility by measuring the dissolved compound rather than measuring the turbidity of the undissolved particles. Since absorption spectrum of PEG-FA was observed at 285 nm, solubility was measured at same wavelength [225]. Solubility studies using UV absorbance showed that PEG-FA was almost completely dissolved in water (99.6 ± 3.4 %), while only 4.1 ± 0.2 % of FA was soluble (**Fig. 4**). There was a 25-fold increase in solubility of PEG-FA when compared to the bare drug ($p< 0.05$). As previously mentioned, FA is a class II drug, according to BCS. The drugs belonging to this class suffer from poor aqueous solubility and low dissolution rates, which limits their oral bio-absorption and causes difficulty in formulating parenteral dosage forms [229, 231]. This phenomenon of solubility enhancement could be attributed to the PEGylation effect, as reported in the literature for other drugs [260, 261]. Furthermore, the self-assembly of PEG-FA into NPs could also contribute to solubility enhancement, as the solubility of particles is inversely proportional to their radius, according to Ostwald–Freundlich effect [262, 263]. In comparison with FA nanosuspension that was previously prepared by nanoprecipitation using various surfactants [246], the self-assembled PEG-FA NPs in our study showed advantageous features, such as superior solubility and smaller size. Moreover, a nanosuspension faces the

major drawback of nucleation and particle growth, which could be overcome by PEG-FA self-assembled NPs [264]. In another study, micelles were formulated with an amphiphilic dendrimer to enhance FA solubility [265]. However, encapsulation efficiency achieved was only 25%, whereas PEG-FA NPs overcame this obstacle with FA conjugated directly to the polymer without reducing the antibacterial effect. The significant increment in the aqueous solubility of FA will be highly beneficial for its bioavailability, as it will facilitate drug partitioning through biological membranes. Therefore, the enhanced water solubility of FA owing to PEGylation could potentially improve the activity of the drug.

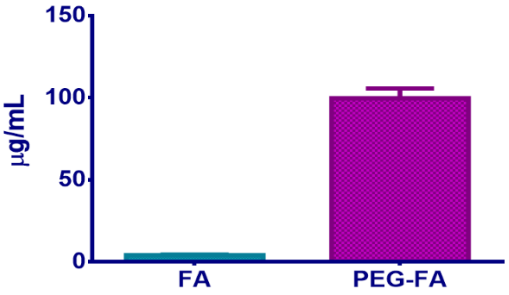

Fig. 4. The solubility of FA and PEG-FA in water, n=3.

3.4. *In vitro* biosafety

3.4.1. Cytotoxicity and cell viability

The cytotoxic effect of the synthesized PEG-FA was determined via the *in vitro* MTT cytotoxicity assay. The MTT assay measures the number of healthy, living cells based on enzymatic conversion of the yellow tetrazolium salt into the purple formazan crystal by living mammalian cells. The amount of formazan crystals produced is proportionate to viable cells present [150]. The results showed that cell viability ranged from 84% to 99%, across all concentrations on all three tested cell lines (**Fig. 5**). This is in accordance with the ISO norm for biomedical products (>75% cell viability) [190]. In this study, no dose-dependent toxicity within the concentration range to any of the three cell lines was reported for PEG-FA, while FA showed some cytotoxicity at the highest concentration (100 µg/mL) towards HEK 293 and HeLa cells with viability of 53% and 62%, respectively. FA is known to have anti-proliferative activity against some human cell lines. For this reason, FA and its chemical derivatives have been investigated as promising anticancer molecules [266, 267]. This result confirms the biocompatibility and biosafety of PEG-FA, which correlate with other reports showing a decrease in cytotoxicity of other drugs or dendrimers when attached to PEG chains [108, 110, 268].

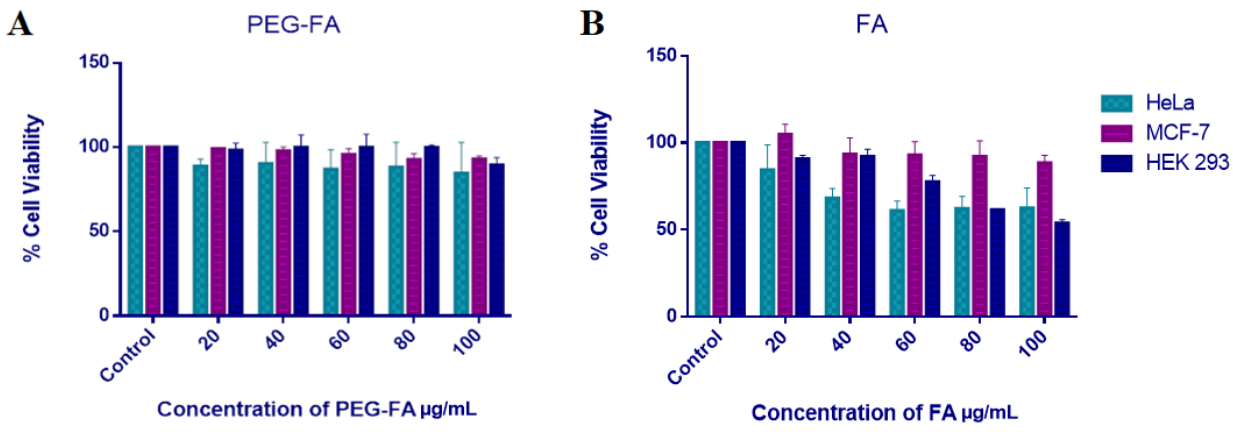

Fig. 5. MTT assay for evaluation of cytotoxicity of A) PEG-FA and B) FA, against HeLa, HEK 293 and MCF-7 cell lines.

3.4.2. Haemolysis

Blood compatibility is an essential factor for all intravenously administered pharmaceuticals to ensure they do not possess haemolytic activity [192]. Due to the nanosize, positive charge and unique physicochemical characteristics of NPs, interference with RBCs is likely to happen more than the small-molecule drugs. Therefore, an early preclinical study to confirm their biocompatibility with the blood constituents is essential [193]. Red blood cells collected from sheep blood was used to evaluate the haemolytic properties of PEG-FA conjugate and bare FA (**Fig. 6A and 6B**). Among the different concentrations used in the study (**Table 1**), the highest concentration (250 µg/mL) of PEG-FA and FA resulted in <0.3% and 8.6% haemolysis of RBCs, respectively. However, the FA plasma concentration that is sufficient for antibacterial activity is reported to be 15 - 30 µg/mL [228, 235], which is still within the non-heaemolytic concentration for both FA and PEG-FA. This result further confirms the improved biosafety profile and non-haemolytic nature of PEG-FA in comparison to bare FA.

Table 1. Haemolysis (%) for different concentrations of FA and PEG-FA, PBS (pH 7.4) and distilled water.

Concentration (µg/mL)	Haemolysis (%)	
	FA	PEG-FA
7.8	0	0
15.6	0.22	0.18
31.2	0.78	0.24
62.5	2.28	0.24
125	5.28	0.24

250	8.6	0.25
PBS (pH 7.4)	0	0
Distilled water	100	100

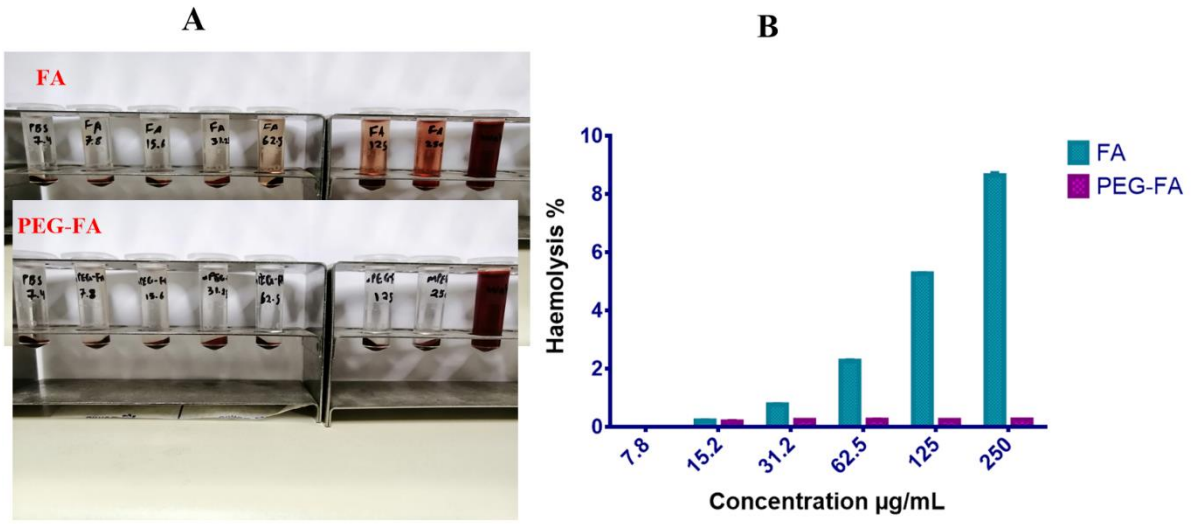

Fig. 6. Haemolysis assay of FA and PEG-FA A) Images of RBCs treated with FA and PEG-FA at various concentrations. B) % of haemolysis after exposure to various concentrations of FA and PEG-FA. Data are expressed as mean ± SD, n=3.

3.5. Preparation and characterization of PEG-FA nanoparticles

3.5.1. Size, PDI, ZP and morphology

Recently, drug polymer conjugates with amphiphilic properties that are able to self-assemble into well-defined nanostructures in aqueous solutions are showing potential for enhancing drug delivery [58, 260]. PEG-FA nanoparticles were prepared using a simple solvent evaporation technique. Following spontaneous evaporation of the solvent, FA and PEG serving as hydrophobic core and hydrophilic shell, respectively could have directed the self-assembly of amphiphilic PEG-FA under aqueous environment to form NPs. The molecular self-assembly of PEG-FA conjugate was characterized via a Zetasizer and HRTEM. The results revealed that the average hydrodynamic diameter of the self-assembled nanosystem was 149.3 ± 0.21 nm with a PDI of 0.267 ± 0.01 and surface charge of 5.97 ± 1.03 mV. The size and morphology of the assembled NPs were also investigated under HRTEM **(Fig. 7A**). The images showed that PEG-FA nanoparticles had a spherical morphology and were dispersed homogeneously with an average particle size found to be ~100 nm. This result corroborates well with obtained small PDI value (0.267 ± 0.01), indicating a high degree of

particle homogeneity. The size of the nanoparticles observed by HRTEM appeared to be smaller compared to DLS (**Fig. 7B**), because DLS represents average hydrodynamic diameter of particle, while HRTEM images relates to shrunken dehydrated particles after water evaporation [269]. Generally, nanosized structures have higher efficacy for cellular uptake, which will assist in targeting bacterial infected sites [171, 270]. The positive surface charge of PEG-FA NPs might encourage interactions with the negatively charged elements on the bacterial cell wall and create strong multivalent electrostatic-mediated binding [271]. Since PEG is known as a water-based stabilizing moiety, the PEGylated surface of the NPs would induce extra stability through steric stabilization, thus providing sufficient colloidal stability to the system [272, 273]. The results are comparable to other reported polymeric drug conjugates that self-assemble into nanostructures with improved therapeutic outcomes. In one such report, PEGylated sulfasalazine (treatment for inflammatory bowel disease) showed enhanced solubility and self-assembled into micellar structures with an average size of 212.9 ± 21.7 nm, and proved to be an efficient carrier for colonic drug delivery [261]. Unlike small drug molecules that get distributed throughout the whole body organs leading to undesirable side effects [58], NPs with an appropriate size and drug composition possess distinct physicochemical properties. These include longer circulation half-life and differential biodistribution profile compared with the free drug counterpart [58, 274]. Therefore, PEG-FA nanoparticles could hold great promise for enhancing the delivery of antibiotics.

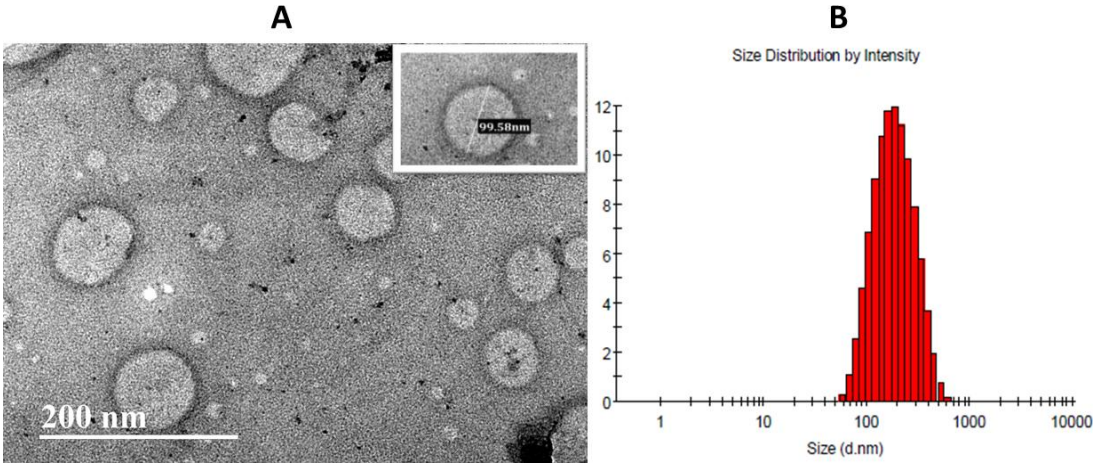

Fig. 7. A) Morphology of the self-assembled PEG-FA conjugate from HRTEM. B) Histogram for sample measurement showing size distribution measured via DLS.

3.5.2. *In silico* studies for self-assembly of PEG-FA

3.5.2.1. All-atom MD simulations of PEG-FA self-assembly

Molecular“dynamic simulations were performed to study the mechanism and forces that contributed to the self-assembly of the PEG-FA nanosystem. The total binding free energy was calculated to gain insight into the binding energetics of PEG-FA conjugates. The MM/GBSA program in AMBER was used to calculate the binding free energies by extracting snapshots from the trajectories.

Table 2. The binding energies (kcal/mol) of PEG-FA conjugates computed from the MD trajectories

	Energy Components (kcal/mol) ± SD				
	Δ E_{vdW}	**ΔE_{elec}**	**ΔG_{gas}**	**ΔG_{solv}**	**ΔG_{bind}**
PEG-FA	-65.55 ± 0.51	-11.31 ± 0.18	-76.87 ± 0.63	35.01 ± 0.30	-41.85 ± 0.36
	-55.24 ± 1.86	-13.72 ± 0.57	-68.96 ± 2.39	31.92 ± 1.10	-37.04 ± 1.31
	-34.47 ± 1.33	-7.73 ± 0.37	-42.21 ± 1.66	19.34 ± 0.72	-22.86 ± 0.95
	-63.70 ± 1.65	-14.42 ± 0.50	-78.13 ± 2.09	37.67 ± 1.03	-40.45 ± 1.08
	-47.78 ± 1.82	-10.04 ± 0.46	-57.83 ± 2.23	29.09 ± 1.10	-28.73 ± 1.15
	-69.71 ± 0.66	-24.10 ± 0.24	-93.81 ± 0.85	42.58 ± 0.38	-51.22 ± 0.49

From **Table 2**, we can conclude that binding energy components showed that vdW energy, non-polar energy and electrostatic energies led to the overall highly favorable binding energy, however polar solvation energy appeared to be highly unfavorable.

It was observed that PEG-FA amphiphilic molecules started to assemble within a few nanoseconds of simulation (**Fig. 8**). Simulation data revealed that at ~20 ns, four molecules were aggregated and at 32 ns, five molecules were formed. We observed that total aggregation was formed at 40 ns. This arrangement included the hydrophilic portions (PEG) of the PEG-FA conjugate facing the outside of the aggregates and is in contact with water molecules, while the hydrophobic segment (FA) was sandwiched in the middle and tend to be less exposed to water **(Fig. 8C and 8D)**. This aggregation could have been the possible arrangement that resulted in the formation of the NPs. Literature shows this arrangement is a

typical intermediate arrangement before the formation of NPs [275, 276]. The general structure of PEG-FA conjugate is a solvent-(philic-phobic) type structure that contains a hydrophobic part connected to a hydrophilic polymer. The philic-phobic structures have shown the ability to self-assembly in solution to form complex structures such as spherical micelles, cylindrical micelles, NPs and vesicles [276, 277]. These structures have been successfully employed in drug delivery. From a thermodynamic point of view, the self-assembled structure built from philic-phobic conjugate in solution relies heavily on the balance of three free energy contributions: chain stretching in the core, interfacial tension and repulsion interaction between coronal chains [278].

The stability of the simulated system was investigated by evaluating the differences in the root-mean-square deviation (RMSD) with respect to the minimized structure, as well as the potential energy of the complex during the simulation time. The calculation of the RMSD is considered as the time point when the conformation changes. In order to ensure a comprehensive investigation of a well-relaxed and balanced system, RMSD, kinetic energy and potential energy were monitored along the MD simulation. The system under study was properly balanced and conformational stability was observed throughout the simulations (**Fig. S2**). Overall, the results of this study supported the fact that PEG-FA could self-assemble to a stable aggregate.

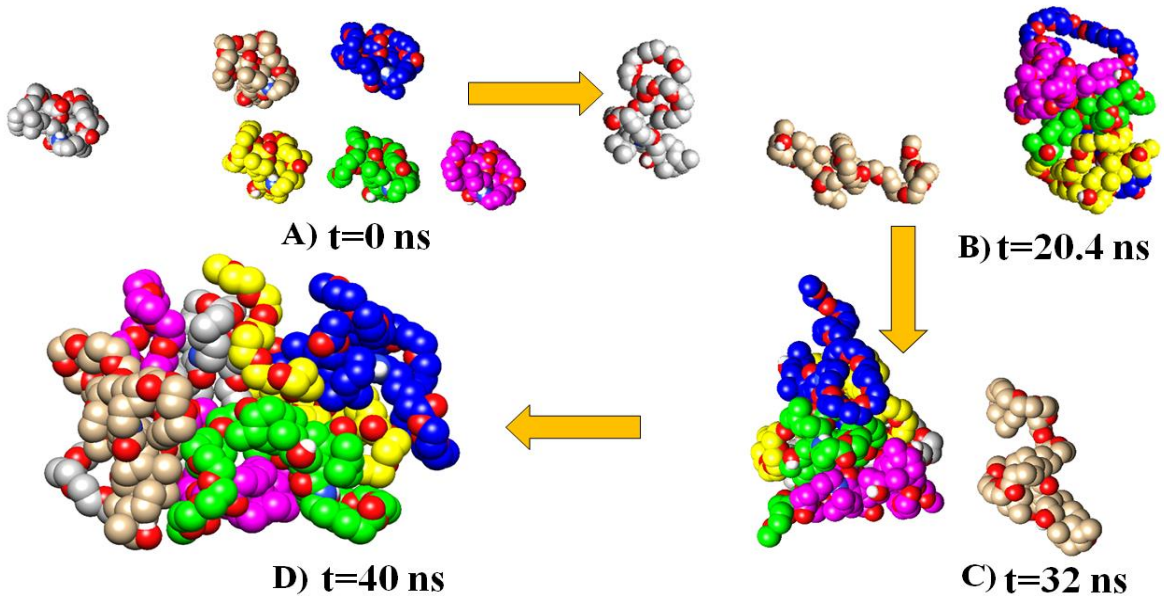

Fig. 8. Representation of the self-assembly of PEG-FA conjugates via MD simulation at different time points (t).

3.6. Determination of the binding affinity on HSA

3.6.1. Molecular docking study

This study was conducted to understand the binding of FA to HSA and the interaction with bilirubin binding, and to study the effect of PEGylation of FA on the HSA binding at a molecular level. Fusidic acid provided the best docking score based on the free energy binding (-30.10 kcal/mol), which revealed a stronger interaction between FA and HSA compared to the 4Z,15Z-bilirubin, which exhibited a lower docking score (-14.95 kcal/mol) **(Fig. 9 A1 and 9 A2)**. This correlates with previous literature, which reports the competitive binding of FA with 4Z,15Z-bilirubin for the same binding site on HSA [236, 254], due to the hydrophobicity and hydrogen bond formation of FA with the binding site residues on HSA. Besides hydrogen bonds and electrostatic interactions, no secondary structure change upon FA binding to the receptor was observed. Fusidic acid adopts an L-shaped conformation and occupies the binding pocket of sub-domain IB in a way very similar to 4Z,15Z-bilirubin (**Fig. 9 B1 and 9 B2**). The side-chain hydroxyl of TYR 161 creates equal distance hydrogen bonds (3.3 Å) with the two hydroxyl groups that are expected from the FA steroid rings. At the other end of the drug molecule, the hydrocarbon tail of methyl-heptanoic acid group is projected into the deeper part of the binding pocket. The acetyloxy and carboxylate groups of FA are positioned at the entrance of the pocket, where hydrogen bond interactions with ARG117 and ARG186 occur. Notably, the two side-chains of Arg are significantly reoriented in order to establish these specific interactions with the drug. An upward rotation of the side-chain of ARG117 by approximately 40° is required to provide room for the increased bulk of the steroid moiety of FA. In contrast, when the synthesized PEG-FA was docked with 2 EG monomers (2-PEG-FA), significant weak contacts with binding site amino acid residues ARG186 and ARG 117 were observed. Also, it showed unfavorable contact with Ala 126, Phe 143, Lys 190, Leu 115, Lys 137 and Leu 139 with very low docking score (-6.85 kcal/mol) **(Fig. 9 C1and 9 C2)**. Further docking with longer PEG polymer conjugate using 7 PE monomers (7-PEG-FA) did not show any binding or inter-molecular interactions at the binding site with a negligible docking score (-2.93kcal/mol) **(Fig. 10).** Therefore, the ligand interaction binding has shown a weak conformation change especially at the binding site. Accordingly, as the PEG chain increased, the interaction of ligand decreased at the HSA binding pocket. Hence, since the average molecular weight of PEG that was used for synthesis is 2000 g/mol, the conjugate will be unfavorable to fit the binding pocket. This

indicates the potential of PEG to reduce the affinity of FA binding to HSA, and thus preventing bilirubin displacement.

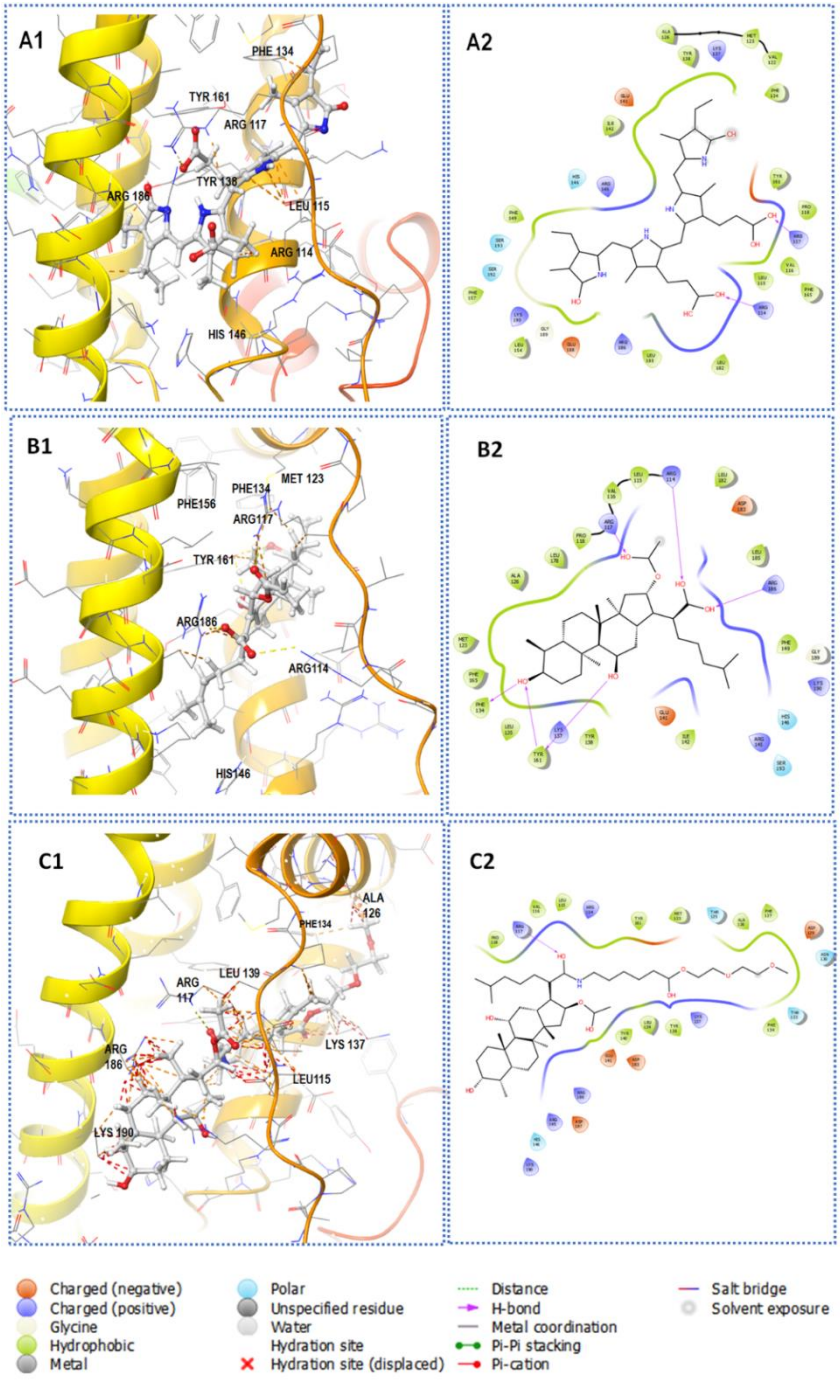

Fig. 9. Molecular visualization of bilirubin, FA and 2-PEG-FA at the sub-domain IB of HSA [A1], [B1] and [C1], respectively. Inter-molecular interactions between bilirubin, FA and 2-PEG-FA with sub-domain IB of HSA are shown in [A2], [B2] and [C2], respectively.

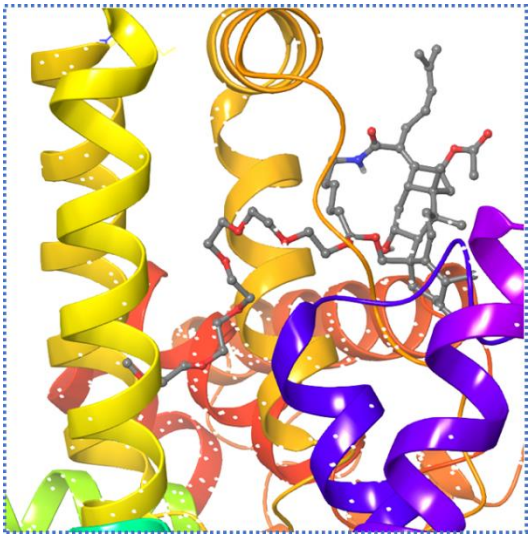

Fig. 10. Structural orientation of the 7-PEG-FA at the sub-domain IB of HSA showing the unfavorable binding site.

3.6.2. Microscale thermophoresis binding affinity studies

Microscale thermophoresis is a relatively new quantification technique for biomolecular interactions. The technique is based on the gradient change in sample temperature induced by infrared (IR) laser, causing thermophoresis of the molecules, which can be detected and quantified using the change in the normalized fluorescence [279]. MST offers an elastic, robust and fast method for molecular interaction studies. A constant concentration of the labelled HSA protein was incubated with increasing concentrations of the test samples (FA, bilirubin and PEG-FA). Thermophoresis was then induced and detected due to a created temperature gradient by the IR laser. The strength of binding was evaluated by calculating the dissociation constant K_d. The smaller the K_d, the stronger is the binding force. **Table 3** represents the K_d value for each material when they were tested for binding with HSA. FA showed a K_d value of 120.03 ± 0.53 µM, which is in good agreement with the K_d value derived from the surface plasmon resonance method reported for FA binding with HSA [280]. This K_d value is 1.7-fold lower than the bilirubin K_d value (p= 0.0006) and approximately 120-fold lower than PEG-FA (p<0.0001), which can be interpreted as strongest binding properties to HSA protein. Moreover, this result is in accordance with literature reports for FA binding to HSA and interaction with the binding of bilirubin, which showed that FA is bound strongly and competitively with bilirubin to HSA [236]. Conversely, PEG-FA showed an inflated value of 14999 ± 1.36 µM for K_d; this value is barely enough to conclude binding (**Fig. 11**), which is similar to previously reported study for

the binding affinity of PEG to HSA using MST [47]. **Fig. 11** illustrates the F_{norm} % curve against the concentration of FA, bilirubin, and PEG-FA from MST experiments. PEG-FA curve is a nearly straight line and not showing any dose dependant response in comparison to FA and bilirubin. The inhibition of PEG-FA binding to HSA is due to the steric hindrance of PEG polymer [281]. This evidence supports the inhibition of binding affinity to HSA for the novel PEGylated FA, which will prevent bilirubin displacement and decrease the risk of jaundice in infants. Furthermore, the binding affinities of the different molecules to HSA that was obtained from this MST study are in line with the calculated binding energies from the MD study.

The MST results were further confirmed by a Zetasizer, where the self-assembled PEG-FA conjugate was incubated with HSA, and its effect on the size, PDI and ZP were investigated [47, 282]. There was no significant impact on the physical characteristics of the nanosystem after incubation of PEG-FA NPs with HSA (**Table 4**). This could be attributed to the PEG forming a shell around the nanostructure, which is considered not to bind with HSA [47], suggesting long circulating and stealth offering capabilities to the NPs [255]. Furthermore, these results also provide proof of concept that PEG-FA NPs could remain stable in serum environment by not binding to human serum albumin and maintaining its structural integrity [283].

Table 3. Binding affinity parameters of FA, bilirubin and PEG-FA with HSA protein.

Name	K_d (μM) ± SD	Response amplitude	Unbound	Bound
HSA + FA	120.03 ± 0.53	6.953	931.697	924.744
HSA + Bilirubin	215.8 ± 0.30	5.263	932.620	927.357
HSA + PEG-FA	14999 ± 1.36	0.568	960.265	960.833

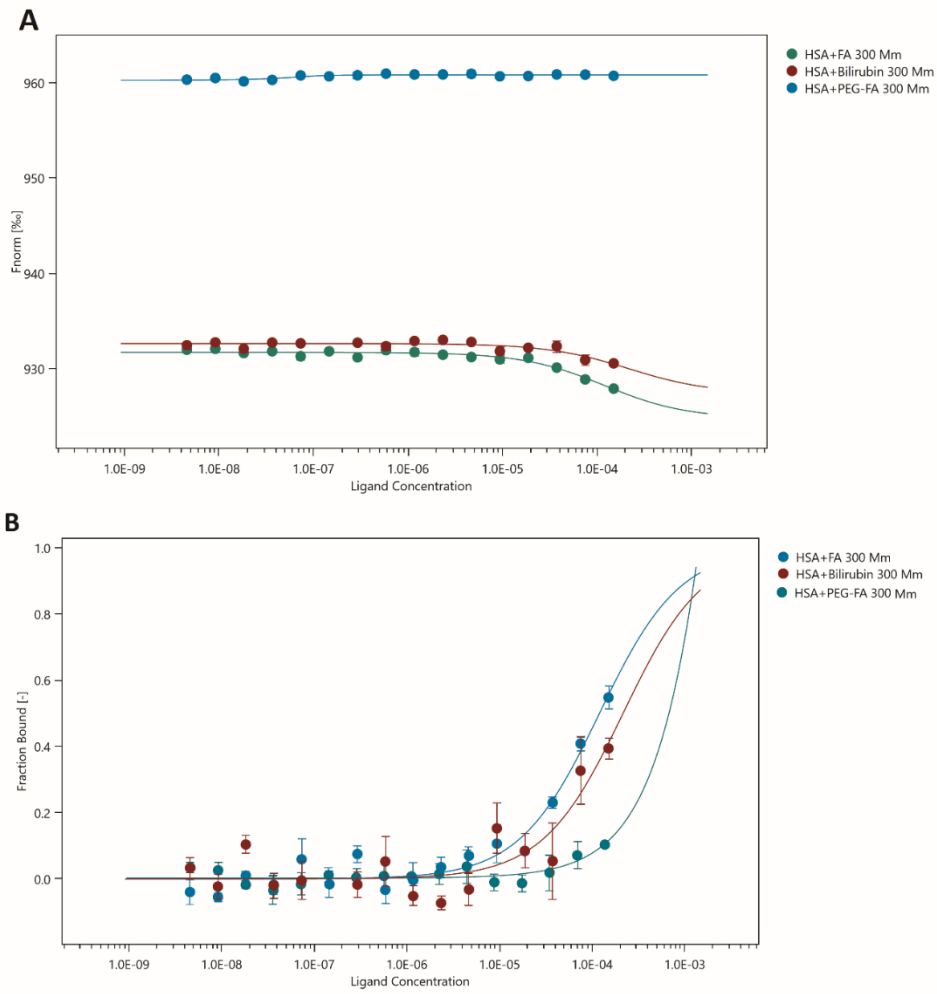

Fig. 11. A) The plot of the normalized fluorescence F_{norm} (%) vs. the concentration of FA, bilirubin, and PEG-FA from MST experiments. Data were derived from the T-Jump signal. Lines represent fits of the data points using the K_d model. **B)** Quantitative comparison of the different ligands shown in (A) to the HSA in fraction bound, (n=3).

Table 4. The effect of HSA on self-assembled PEA-FA conjugate after incubation (n=3).

Sample	size (nm)	PDI	ZP (mV)
Before	146.4 ± 0.8	0.225 ± 0.01	8.11 ± 1.2
After	129.7 ± 1.8	0.261 ± 0.01	6.02 ± 1.5

3.7. *In vitro* antibacterial activity

Following the modification of FA to PEG-FA, carboxyl groups were converted to amide bonds to couple FA to PEG. The antibacterial activity of FA could be deactivated by this coupling. In order to prove that modified FA was still available to inhibit bacterial growth after hydrolysis, *in vitro* antibacterial activity of PEG-FA conjugate against *S. aureus* and

MRSA was determined. The broth dilution method was employed and MICs were calculated for bare FA (control) and the PEG-FA conjugate. The results in **Table 5** show the MIC values in μmol/L for FA and PEG-FA against *S. aureus* and MRSA. PEGylation increased the molecular mass by approximately 5-6 times [284]. After 24 h, the MIC values for FA against both *S. aureus* and MRSA were 15.119 μmol/L, whereas PEG-FA had MIC values of 5.936 μmol/L against both the tested bacterial strains displaying 2.5 fold improved antibacterial activity. After 48 h, there was 1-fold reduction in MICs for both FA (30.239μmol/L) and PEG-FA (11.873) against *S. aureus* and MRSA, and the trend was continued until the studied time period of 72 h. Therefore, PEGylated FA showed enhanced antibacterial activity against both *S. aureus* and MRSA compared to FA, with 2.5-fold reduced molar MIC values. The Modification of FA through PEGylation to improve its solubility could have adversely affected the activity of FA, since some studies have reported a reduction in the activity of polymer conjugated antibiotics [284-286]. However, in our study, this modification led to better antibacterial activity. This improved antibacterial activity could be due to the smaller size of the nanoparticles and the electrostatic attraction between the positively charged PEG-FA NPs and the oppositely charged bacterial cell membrane [57, 287]. The enhanced FA activity via polymeric conjugation with PEG and self-assembly into NPs underlines PEGylation as a promising strategy to develop novel antibacterial delivery systems to address the crisis of deterioration of new antibiotics.

Table 5. MIC values for bare FA and PEG-FA.

Time (h)	24	48	72	24	48	72
	S. aureus (MIC μmol/L)			MRSA (MIC μmol/L)		
FA	15.119	30.239	30.239	15.119	30.239	30.239
PEG-FA	5.936	11.873	11.873	5.936	11.873	11.873

The values are expressed as mean, n=3.

4. Conclusion

Recently, there has been a surge of interest in the development of novel drug carrier systems for antibiotic delivery. In this study, a novel PEGylated FA was successfully synthesized and structurally characterized. *In vitro* cytotoxicity and haemolysis studies confirmed the biosafety of the synthesized PEG-FA with it being superior to FA. The synthesized PEG-FA conjugate was not only freely dispersible in water but also formed nanostructures following self-assembly. These nanostructures displayed a suitable particle size, PDI, ZP and

morphology for targeted antibiotic therapy. Self-assembly of PEG-FA into NPs was confirmed using MD simulations. MST and molecular docking studies confirmed that PEG-FA did not have any adsorption and binding affinity towards HSA, which indicated its potential for preventing bilirubin displacement and reducing side effects. *In vitro* antibacterial study confirmed that conjugation of FA with PEG did not reduce but rather enhanced the activity of FA against *S. aureus* and MRSA. These findings confirmed the potential of the self-assembled PEG-FA conjugate as a novel polymer therapeutics to combat multi-drug resistant bacteria. In addition, the proposed conjugate can be further explored to encapsulate other classes of antibiotics and investigate the synergistic antibacterial effect.

5. Acknowledgment

The authors acknowledge the College of Health Sciences, University of KwaZulu-Natal (UKZN), and the UKZN Nanotechnology Platform, the National Research Foundation (NRF) of South Africa (Grant No. 106040) and the Medical Research Council (MRC) of South Africa for financial support. We also acknowledge the Microscopy and Microanalysis Unit (MMU) and the Department of Human Physiology at UKZN, for use of their facilities, as well as the Centre for High-Performance Computing (CHPC), Cape Town, for supercomputing resources.

6. Conflict of Interest

The authors declare that there is no conflict of interest.

7. References

1. Willyard, C., The drug-resistant bacteria that pose the greatest health threats. Nature News, 2017. 543(7643): p. 15.

2. Centers for Disease Control Prevention, Antibiotic Resistance Threats in the United States 2019, US Department of Health and Human Service: Atlanta.

3. Singer, A.C., C. Kirchhelle, and A.P. Roberts, (Inter) nationalising the antibiotic research and development pipeline. Lancet Infect. Dis., 2019. 20(2): p. 54-62.

4. Boucher, H.W., et al., White paper: developing antimicrobial drugs for resistant pathogens, narrow-spectrum indications, and unmet needs. J. Infect. Dis, 2017. 216(2): p. 228-236.

5. Okano, A., N.A. Isley, and D.L. Boger, Peripheral modifications of [Ψ [CH2NH] Tpg4] vancomycin with added synergistic mechanisms of action provide durable and potent antibiotics. PNAS, 2017. 114(26): p. 5052-5061.

6. Kalhapure, R.S., et al., Nanoengineered drug delivery systems for enhancing antibiotic therapy. Journal of Pharmaceutical Sciences, 2015. 104(3): p. 872-905.

7. Caster, J.M., et al., Investigational nanomedicines in 2016: a review of nanotherapeutics currently undergoing clinical trials. Wiley Interdiscip. Rev. Nanomed. Nanobiotechnol., 2017. 9(1): p. 1416.

8. Hamblin, K.A., et al., Inhaled liposomal ciprofloxacin protects against a lethal infection in a murine model of pneumonic plague. Frontiers in Microbiology, 2017. 8(1): p. 91.

9. Gupta, A., et al., Combatting antibiotic-resistant bacteria using nanomaterials. Chemical Society Reviews, 2019. 48(2): p. 415-427.

10. Pissuwan, D., T. Niidome, and M.B. Cortie, The forthcoming applications of gold nanoparticles in drug and gene delivery systems. Journal of Controlled Release, 2011. 149(1): p. 65-71.

11. Barth, J.V., G. Costantini, and K. Kern, Engineering atomic and molecular nanostructures at surfaces, in Nanoscience and Technology: a Collection of Reviews from Nature Journals. 2010, World Scientific p. 67-75.

12. Mokaberi, P., et al., Analysis of the interaction behavior between Nano-Curcumin and two human serum proteins: Combining spectroscopy and molecular stimulation to understand protein-protein interaction. J Biomol. Struct. Dyn., 2020(just-accepted): p. 1-20.

13. Godtfredsen, W., et al., Fusidic acid: a new antibiotic. Nature, 1962. 193(4819): p. 987-987.

14. Curbete, M.M. and H.R.N. Salgado, A critical review of the properties of fusidic acid and analytical methods for its determination. Crit. Rev. Anal. Chem., 2016. 46(4): p. 352-360.

15. Farrell, D.J., et al., Activity of fusidic acid tested against staphylococci isolated from patients in US medical centers in 2014. Antimicrobial Agents and Chemotherapy, 2016. 60(6): p. 3827-3831.

16. Eid, A.M., et al., Antibacterial Activity of Fusidic Acid and Sodium Fusidate Nanoparticles Incorporated in Pine Oil Nanoemulgel. Int. J. Nanomedicine, 2019. 14(1): p. 9411.

17. Lemaire, S., et al., Activity of fusidic acid against extracellular and intracellular Staphylococcus aureus: influence of pH and comparison with linezolid and clindamycin. Clinical infectious diseases, 2011. 52(suppl_7): p. 493-503.

18. Craft, J.C., et al., A randomized, double-blind phase 2 study comparing the efficacy and safety of an oral fusidic acid loading-dose regimen to oral linezolid for the treatment of acute bacterial skin and skin structure infections. Clinical infectious diseases, 2011. 52(suppl_7): p. S520-S526.

19. Fernandes, P. and D. Pereira, Efforts to Support the Development of Fusidic Acid in the United States. Clinical Infectious Diseases, 2011. 52(suppl_7): p. 542-546.

20. Hosey, C.M., R. Chan, and L.Z. Benet, BDDCS predictions, self-correcting aspects of BDDCS assignments, BDDCS assignment corrections, and classification for more than 175 additional drugs. AAPS J., 2016. 18(1): p. 251-260.

21. Merisko-Liversidge, E.M. and G.G. Liversidge, Drug nanoparticles: formulating poorly water-soluble compounds. Toxicologic pathology, 2008. 36(1): p. 43-48.

22. O'driscoll, C. and B. Griffin, Biopharmaceutical challenges associated with drugs with low aqueous solubility—the potential impact of lipid-based formulations. Adv. Drug Deliv. Rev., 2008. 60(6): p. 617-624.

23. Zhang, Z.-B., et al., Micronization of silybin by the emulsion solvent diffusion method. International journal of pharmaceutics, 2009. 376(1-2): p. 116-122.

24. Chen, H., et al., Nanonization strategies for poorly water-soluble drugs. Drug discov. today, 2011. 16(7-8): p. 354-360.

25. Serajuddin, A.T., Salt formation to improve drug solubility. Adv. Drug Deliv. Rev., 2007. 59(7): p. 603-616.

26. Rieutord, A., et al., In vitro study of the protein binding of fusidic acid: a contribution to the comprehension of its pharmacokinetic behaviour. International Journal of Pharmaceutics, 1995. 119(1): p. 57-64.

27. Christiansen, K., Fusidic acid adverse drug reactions. International Journal of Antimicrobial Agents, 1999. 12(1): p. 3-9.

28. Brodersen, R., Fusidic acid binding to serum albumin and interaction with binding of bilirubin. Acta Pædiatr., 1985. 74(6): p. 874-880.

29. Gubernick, J.A., et al., US approach to jaundice in infants and children. Radiographics, 2000. 20(1): p. 173-195.

30. Baodong, Y., Effect of fusidic acid on bilirubin level in neonates and infants. Chinese J. Infect. Chemother., 2017. 17(3): p. 249-252.

31. Knop, K., et al., Poly (ethylene glycol) in drug delivery: pros and cons as well as potential alternatives. Angew. Chem. Int. Ed., 2010. 49(36): p. 6288-6308.

32. Greenwald, R., PEG drugs: an overview. Journal of Controlled Release, 2001. 74(1-3): p. 159-171.

33. Banerjee, S.S., et al., Poly (ethylene glycol)-prodrug conjugates: concept, design, and applications. J. Drug Deliv., 2012. 2012(1): p. 1-17.

34. Cheetham, A.G., et al., Self-assembling prodrugs. Chemical Society Reviews, 2017. 46(21): p. 6638-6663.

35. Bahamondez-Canas, T.F., et al., PEGylation of tobramycin improves mucus penetration and antimicrobial activity against Pseudomonas aeruginosa biofilms in vitro. Mol. Pharm., 2018. 15(4): p. 1643-1652.

36. Du, J., et al., Improved biofilm antimicrobial activity of polyethylene glycol conjugated tobramycin compared to tobramycin in pseudomonas aeruginosa biofilms. Molecular Pharmaceutics, 2015. 12(5): p. 1544-1553.

37. Duncan, R. and M.J. Vicent, Polymer therapeutics-prospects for 21st century: the end of the beginning. Adv. Drug Deliv. Rev., 2013. 65(1): p. 60-70.

38. Omolo, C.A., et al., A hybrid of mPEG-b-PCL and G1-PEA dendrimer for enhancing delivery of antibiotics. Journal of Controlled Release, 2018. 290(1): p. 112-128.

39. Patnaik, A., et al., Phase I dose-escalation study of EZN-2208 (PEG-SN38), a novel conjugate of poly (ethylene) glycol and SN38, administered weekly in patients with advanced cancer. Cancer Chemotherapy and Pharmacology, 2013. 71(6): p. 1499-1506.

40. Joralemon, M.J., S. McRae, and T. Emrick, PEGylated polymers for medicine: from conjugation to self-assembled systems. ChemComm, 2010. 46(9): p. 1377-1393.

41. Nathan, A., et al., Copolymers of lysine and polyethylene glycol: a new family of functionalized drug carriers. Bioconjugate Chemistry, 1993. 4(1): p. 54-62.

42. Turos, E., et al., Antibiotic-conjugated polyacrylate nanoparticles: new opportunities for development of anti-MRSA agents. Bioorganic & Medicinal Chemistry Letters, 2007. 17(1): p. 53-56.

43. Gac-Breton, S., et al., Norfloxacin-poly (L-lysine citramide imide) conjugates and structure-dependence of the drug release. Journal of Drug Targeting, 2004. 12(5): p. 297-307.

44. Sobczak, M., Synthesis and characterization of polyester conjugates of ciprofloxacin. European Journal of Medicinal Chemistry, 2010. 45(9): p. 3844-3849.

45. Sobczak, M., et al., Synthesis and study of controlled release of ofloxacin from polyester conjugates. International Journal of Pharmaceutics, 2010. 402(1-2): p. 37-43.

46. Kugel, A., et al., Antimicrobial polysiloxane polymers and coatings containing pendant levofloxacin. Polym. Chem., 2010. 1(4): p. 442-452.

47. Chen, M., et al., Multifunctional hyperbranched glycoconjugated polymers based on natural aminoglycosides. Bioconjugate Chemistry, 2012. 23(6): p. 1189-1199.

48. Chang, H.-P., et al., Synthesis and characterization of a new polymer–drug conjugate with pH-induced activity. Polymer, 2012. 53(16): p. 3498-3507.

49. Njoroge, M., et al., Semisynthetic Antimycobacterial C-3 Silicate and C-3/C-21 Ester Derivatives of Fusidic Acid: Pharmacological Evaluation and Stability Studies in Liver Microsomes, Rat Plasma, and Mycobacterium tuberculosis culture. ACS Infect. Dis, 2019. 5(9): p. 1634-1644.

50. Espinoza-Moraga, M., et al., Synthesis and biological characterisation of ester and amide derivatives of fusidic acid as antiplasmodial agents. Bioorganic & Medicinal Chemistry Letters, 2017. 27(3): p. 658-661.

51. Mokaberi, P., et al., New insights into the binding behavior of lomefloxacin and human hemoglobin using biophysical techniques: binary and ternary approaches. New Journal of Chemistry, 2019. 43(21): p. 8132-8145.

52. Sohrabi, T., et al., Probing the binding of lomefloxacin to a calf thymus DNA-histone H1 complex by multi-spectroscopic and molecular modeling techniques. Journal of Molecular Liquids, 2018. 256: p. 127-138.

53. Li, Y. and T. Hou, Computational simulation of drug delivery at molecular level. Current medicinal chemistry, 2010. 17(36): p. 4482-4491.

54. Sharifi-Rad, A., et al., Oil-in-water nanoemulsions comprising Berberine in olive oil: biological activities, binding mechanisms to human serum albumin or holo-transferrin and QMMD simulations. Journal of Biomolecular Structure and Dynamics, 2020: p. 1-15.

55. Omolo, C.A., et al., Formulation and Molecular Dynamics Simulations of a Fusidic Acid Nanosuspension for Simultaneously Enhancing Solubility and Antibacterial activity. Mol. Pharm., 2018. 15(8): p. 3512-3526.

56. Mosmann, T., Rapid colorimetric assay for cellular growth and survival: application to proliferation and cytotoxicity assays. Journal of Immunological Methods, 1983. 65(1-2): p. 55-63.

57. Dobrovolskaia, M.A., et al., Method for analysis of nanoparticle hemolytic properties in vitro. Nano Lett., 2008. 8(8): p. 2180-2187.

58. Rabani, E., et al., Drying-mediated self-assembly of nanoparticles. Nature, 2003. 426(6964): p. 271.

59. Cousins, K.R., Computer review of chemdraw ultra 12.0. 2011, ACS Publications.

60. Pettersen, E.F., et al., UCSF Chimera—a visualization system for exploratory research and analysis. Journal of Computational Chemistry, 2004. 25(13): p. 1605-1612.

61. Shao, Y., et al., Advances in methods and algorithms in a modern quantum chemistry program package. Physical Chemistry Chemical Physics, 2006. 8(27): p. 3172-3191.

62. Ryckaert, J.-P., G. Ciccotti, and H.J. Berendsen, Numerical integration of the cartesian equations of motion of a system with constraints: molecular dynamics of n-alkanes. J. Comput. Phys., 1977. 23(3): p. 327-341.

63. Case, D.A., et al., The Amber biomolecular simulation programs. Journal of Computational Chemistry, 2005. 26(16): p. 1668-1688.

64. Roe, D.R. and T.E. Cheatham III, PTRAJ and CPPTRAJ: software for processing and analysis of molecular dynamics trajectory data. Journal of Chemical Theory and Computation, 2013. 9(7): p. 3084-3095.

65. Seifert, E., OriginPro 9.1: Scientific Data Analysis and Graphing Software Software Review. 2014, ACS Publications. p. 1552-1552.

66. Raha, K. and K.M. Merz Jr, Calculating binding free energy in protein–ligand interaction. Annual Reports in Computational Chemistry, 2005. 1(1): p. 113-130.

67. Ylilauri, M. and O.T. Pentikäinen, MMGBSA as a tool to understand the binding affinities of filamin–peptide interactions. Journal of Chemical Information and Modeling, 2013. 53(10): p. 2626-2633.

68. Hou, T., et al., Assessing the performance of the MM/PBSA and MM/GBSA methods. 1. The accuracy of binding free energy calculations based on molecular dynamics simulations. Journal of chemical information and modeling, 2011. 51(1): p. 69-82.

69. Berman, H.M., et al., The protein data bank. ACTA CRYSTALLOGR. D, 2002. 58(6): p. 899-907.

70. Zunszain, P.A., et al., Crystallographic analysis of human serum albumin complexed with 4Z, 15E-bilirubin-IXα. Journal of molecular biology, 2008. 381(2): p. 394-406.

71. Parveen, S. and S.K. Sahoo, Long circulating chitosan/PEG blended PLGA nanoparticle for tumor drug delivery. European journal of pharmacology, 2011. 670(2-3): p. 372-383.

72. Jorgensen, J.H. and J.D. Turnidge, Susceptibility test methods: dilution and disk diffusion methods, in Manual of Clinical Microbiology, Eleventh Edition. 2015, American Society of Microbiology. p. 1253-1273.

73. Schiavon, O., et al., PEG–Ara-C conjugates for controlled release. European Journal of Medicinal Chemistry, 2004. 39(2): p. 123-133.

74. Yang, H. and S.T. Lopina, Penicillin V-conjugated PEG-PAMAM star polymers. Journal of Biomaterials Science, Polymer Edition, 2003. 14(10): p. 1043-1056.

75. Esposito, P., et al., PEGylation of growth hormone-releasing hormone (GRF) analogues. Adv. Drug Deliv. Rev., 2003. 55(10): p. 1279-1291.

76. Kuang, J., et al., Grafting of PEG onto lanthanum hydroxide nanowires. Mater. Lett., 2008. 62(25): p. 4078-4080.

77. Rostamizadeh, K., et al., Methotrexate-conjugated mPEG–PCL copolymers: a novel approach for dual triggered drug delivery. New J. Chem., 2018. 42(8): p. 5937-5945.

78. Priyam, A., et al., Enhanced solubility and self-assembly of amphiphilic sulfasalazine-PEG-OMe (S-PEG) conjugate into core-shell nanostructures useful for colonic drug delivery. Colloids Surf. A Physicochem. Eng. Asp., 2018. 547: p. 157-167.

79. Wais, U., et al., Nanoformulation and encapsulation approaches for poorly water-soluble drug nanoparticles. Nanoscale, 2016. 8(4): p. 1746-1769.

80. Leitner, J. and D. Sedmidubský, Enhanced solubility of nanostructured paracetamol. Biomed. Phys. Eng. Express, 2016. 2(5): p. 055007.

81. Wang, Y., et al., Stability of nanosuspensions in drug delivery. Journal of Controlled Release, 2013. 172(3): p. 1126-1141.

82. Sikwal, D.R., et al., Non-ionic self-assembling amphiphilic polyester dendrimers as new drug delivery excipients. RSC Advances, 2017. 7(23): p. 14233-14246.

83. Standard, I., Biological Evaluation of Medical Devices. Tests for in vitro Cytotoxicity. Switzerland, Geneva: ISO. TC, 2009. 194.

84. Ni, J., et al., Discovery, synthesis of novel fusidic acid derivatives possessed amino-terminal groups at the 3-hydroxyl position with anticancer activity. European Journal of Medicinal Chemistry, 2019. 162(1): p. 122-131.

85. Zhu, Y. and J.E. Weldon, Evaluating the influence of common antibiotics on the efficacy of a recombinant immunotoxin in tissue culture. BMC Res. Notes, 2019. 12(1): p. 293.

86. Lopez, A.I., et al., Antibacterial activity and cytotoxicity of PEGylated poly (amidoamine) dendrimers. Molecular BioSystems, 2009. 5(10): p. 1148-1156.

87. Yalkowsky, S.H., J. Krzyzaniak, and G. Ward, Formulation- related problems associated with intravenous drug delivery. Journal of Pharmaceutical Sciences, 1998. 87(7): p. 787-796.

88. Xie, Z., et al., A novel polymer–paclitaxel conjugate based on amphiphilic triblock copolymer. Journal of Controlled Release, 2007. 117(2): p. 210-216.

89. Auría-Soro, C., et al., Interactions of nanoparticles and biosystems: microenvironment of nanoparticles and biomolecules in nanomedicine. Nanomaterials, 2019. 9(10): p. 1365.

90. Gao, W., et al., Nanoparticle approaches against bacterial infections. Wiley Interdiscip. Rev. Nanomed. Nanobiotechnol., 2014. 6(6): p. 532-547.

91. Radovic-Moreno, A.F., et al., Surface charge-switching polymeric nanoparticles for bacterial cell wall-targeted delivery of antibiotics. ACS Nano, 2012. 6(5): p. 4279-4287.

92. Wu, L., J. Zhang, and W. Watanabe, Physical and chemical stability of drug nanoparticles. Adv. Drug Deliv. Rev., 2011. 63(6): p. 456-469.

93. Meier, W. and J. Schreiber, Intelligent polymers and self organizing liposome gel delivery systems, in Delivery System Handbook for Personal Care and Cosmetic Products. 2005, Elsevier. p. 587-602.

94. Baptista, P.V., et al., Nano-Strategies to Fight Multidrug Resistant Bacteria—"A Battle of the Titans". Frontiers in Microbiology, 2018. 9(1441): p. 1-26.

95. Woo, S.Y. and H. Lee, Molecular dynamics studies of PEGylated α-helical coiled coils and their self-assembled micelles. Langmuir, 2014. 30(29): p. 8848-8855.

96. Zhang, Q., et al., Theoretical modeling and simulations of self-assembly of copolymers in solution. Prog. Polym. Sci., 2017. 75(1): p. 1-30.

97. Yang, R., et al., Biodegradable polymer-curcumin conjugate micelles enhance the loading and delivery of low-potency curcumin. Pharmaceutical Research, 2012. 29(12): p. 3512-3525.

98. Zhang, L. and A. Eisenberg, Formation of crew- cut aggregates of various morphologies from amphiphilic block copolymers in solution. Polym. Adv. Technol, 1998. 9(10- 11): p. 677-699.

99. Jerabek-Willemsen, M., et al., MicroScale Thermophoresis: Interaction analysis and beyond. Journal of Molecular Structure, 2014. 1077(1): p. 101-113.

100. Banères-Roquet, F., et al., Use of a surface plasmon resonance method to investigate antibiotic and plasma protein interactions. Antimicrobial agents and chemotherapy, 2009. 53(4): p. 1528-1531.

101. Gref, R., et al., The controlled intravenous delivery of drugs using PEG-coated sterically stabilized nanospheres. Adv. Drug Deliv. Rev., 1995. 16(2-3): p. 215.

102. Thiele, L., et al., Competitive adsorption of serum proteins at microparticles affects phagocytosis by dendritic cells. Biomaterials, 2003. 24(8): p. 1409-1418.

103. Walvekar, P., et al., Self-assembled oleylamine grafted hyaluronic acid polymersomes for delivery of vancomycin against methicillin resistant Staphylococcus aureus (MRSA). Colloids Surf. B, 2019. 182: p. 110388.

104. Pintér, G., et al., Synthesis and antimicrobial activity of ciprofloxacin and norfloxacin permanently bonded to polyethylene glycol by a thiourea linker. J. Antibiot, 2009. 62(2): p. 113-116.

105. Turos, E., et al., Penicillin-bound polyacrylate nanoparticles: restoring the activity of β-lactam antibiotics against MRSA. Bioorganic & medicinal chemistry letters, 2007. 17(12): p. 3468-3472.

106. Ustariz-Peyret, C., et al., Labile conjugation of a hydrophilic drug to PLA oligomers to modify a drug delivery system: cephradin in a PLAGA matrix. Journal of Microencapsulation, 2000. 17(5): p. 615-624.

107. Fernandes, M.M., et al., Nanotransformation of vancomycin overcomes the intrinsic resistance of gram-negative bacteria. ACS Appl. Mater. Interfaces, 2017. 9(17): p. 15022-15030.

108. Zhu, C., et al., Multifunctional Cationic Poly (p- phenylene vinylene) Polyelectrolytes for Selective Recognition, Imaging, and Killing of Bacteria Over Mammalian Cells. Adv. Mater., 2011. 23(41): p. 4805-4810.

CHAPTER 5, CO-AUTHORED PAPERS

5.1 Introduction

In addition to the first authored experimental papers in Chapters, 2, 3 and 4 focusing on aims 1, 2 and 3, I have also been involved in other papers within our group as a Ph.D. student. As these papers also focused on the broad aim of this PhD project to improve treatment of bacterial infections, these papers have been included in the thesis. This chapter therefore includes one published experimental paper and one review article in an ISI International Journals: Colloids and Surfaces B: Biointerfaces (Impact Factor = 3.973) and WIREs Nanomedicine & Nanobiotechnology (Impact Factor = 7.689).

5.2 Co-authored paper 1

Self-assembled oleylamine grafted hyaluronic acid polymersomes for delivery of vancomycin against methicillin resistant *Staphylococcus aureus* (MRSA)

Walvekar, Pavan, Ramesh Gannimani, Mohammed Salih, Sifiso Makhathini, Chunderika Mocktar, and Thirumala Govender. Colloids and Surfaces B: Biointerfaces. 2019 Oct 1;182:110388. (Appendix IV)

5.2.1 Abstract

MRSA infections are a major global healthcare problem associated with high morbidity and mortality. The application of novel materials in antibiotic delivery has efficiently contributed to the treatment of MRSA infections. The study aimed to develop novel hyaluronic acid oleyl amine (HA-OLA) conjugates with 25-50% degrees of conjugation, for application as a nano-drug carrier with inherent antibacterial activity. The biosafety of synthesized novel HA-OLA conjugates was confirmed by *in vitro* cytotoxicity assay. The drug loading ability of HA-OLA conjugates was confirmed by 26.1-43.12% of vancomycin (VCM) encapsulation in self-assembled polymersomes. These polymersomes were dispersed in nano-sized range (196.1-360.9 nm) with a negative zeta potential. Vancomycin loaded polymersomes were to found have spherical and bilayered morphology. The VCM loaded polymersomes displayed sustained drug release for 72 h. *In vitro* studies showed moderate antibacterial activity for HA-OLA conjugates against both *S. aureus* and MRSA with minimum inhibitory concentration (MIC) of 500 μg/mL. The VCM loaded HA-OLA polymersomes displayed four-fold lower MIC (1.9 μg/mL) than free VCM (7.8 μg/mL) against MRSA. Furthermore, synergism was observed for VCM and HA-OLA against MRSA. Flow cytometry showed 1.8-fold higher MRSA cell death in the population for VCM loaded polymersomes relative to free drug, at concentration of 1.95 μg/mL. Bacterial cell morphology showed that the drug loaded polymersomes had stronger impact on MRSA membrane, compared to free VCM. These findings suggest that, HA-OLA conjugates are promising nano-carriers to function as antibiotic delivery vehicles for the treatment of bacterial/MRSA infections.

5.3 Co-authored paper 2

Intrinsic Stimuli-Responsive Nanocarriers for Smart Drug Delivery of Antibacterial Agents – An In-Depth Review of the Last Two Decades

Nikita Devnarain, Nawras Osman, Victoria Fasiku, Sifiso Makathini, Mohammed Salih, Usri Ibrahim and Thirumala Govender. (2020). WIREs Nanomedicine & Nanobiotechnology. Manuscript ID: NANOMED-651 (In Press).

5.3.1 Abstract

Antibiotic resistance due to suboptimal targeting and inconsistent antibiotic release at bacterial infection sites has driven the formulation of stimuli-responsive nanocarriers for antibacterial therapy. Unlike conventional nanocarriers, stimuli-responsive nanocarriers have the ability to specifically enhance targeting and drug release profiles. There has been a significant escalation in the design and development of novel nanomaterials worldwide; in particular, intrinsic stimuli-responsive antibiotic nanocarriers, due to their enhanced activity, improved targeted delivery and superior potential for bacterial penetration and eradication. Herein, we provide an extensive and critical review of pH-, enzyme-, redox- and ionic microenvironment-responsive nanocarriers that have been reported in literature to date, with an emphasis on the mechanisms of drug release, the nanomaterials used, the nanosystems constructed and the antibacterial efficacy of the nanocarriers. The review also highlights further avenues of research for optimising their potential and commercialisation. This review confirms the potential of intrinsic stimuli-responsive nanocarriers for enhanced drug delivery and antibacterial killing.

CHAPTER 6, CONCLUSION

6.1 General conclusions

Resistance to antibiotics has reached extreme levels throughout the world, with available treatment options gradually becoming ineffective to treat MDR bacteria. The development of new strategies such as nanotechnology-derived formulations are showing great potential to improve the efficacy of existing antibiotics. The severity of bacterial resistance demands new materials to develop novel drug delivery systems that can alter the physicochemical properties of drugs, and thus, counteract antibacterial resistance and improve the efficiency of the drugs. The broad aim of this study was to design advanced materials and explore nano-based strategies for preparations of self-assembling delivery systems to treat *S. aureus* and MRSA infections. The specific research aims of this study were, therefore to: (1) synthesize and formulate a novel supramolecular amphiphile, BCD-OLA, via inclusion complexation for the enhancement of VCM delivery; (2) synthesize and formulate a VCM/TS SADDs and explore its potential for enhancing the antibacterial activity of VCM against *S. aureus* and MRSA; and (3) to synthesize and formulate a novel PEGylated FA and to explore its potential for simultaneously enhancing the solubility and antimicrobial activity of FA and lowering its binding to HSA.

The main conclusions generated from the research data are summarised below:

Aim 1

- The supramolecular amphiphile of BCD and OLA was successfully synthesized. FT-IR, DSC, ^{1}H NMR, and 2D NMR analyses confirmed the successful synthesis and structure of BCD-OLA amphiphile.

- A 1:1 stoichiometric inclusion complex was found in the BCD-OLA amphiphile.

- Cytotoxicity studies performed using the MTT assay on three mammalian cell lines, viz; adenocarcinoma alveolar basal epithelial cells (A549), cervical cancer cell-lines (HeLa) and human embryonic kidney cells 293 (HEK 293), revealed the BCD-OLA amphiphile to be biosafe.

- The synthesized BCD-OLA amphiphile was employed to formulate VCM loaded nanovesicles, which displayed a size of 119.8 ± 1.12 nm with a PDI of 0.220 ± 3.98, and ZP of 25.8 ± 6.96 mV, with an encapsulation efficiency of 40.2 ± 4.5%. The

VCM release from the drug loaded nanovesicles was found to be sustained, with an 80% release throughout 48 h.

- The MD simulations showed spontaneous insertion of OLA into the BCD core and formation of stable inclusion complex. Further simulation confirmed the self-assembly of BCD-OLA amphiphile.

- The *in vitro* antibacterial test revealed that the VCM-loaded BCD-OLA nanovesicles had 2- and 4-fold lower MIC against *S. aureus* strains and MRSA respectively, compared to the free drug. Furthermore, synergism was observed for VCM and BCD-OLA against MRSA.

- The efficacy of the BCD-OLA nanovesicles in eliminating the intracellular MRSA was determined by infecting the macrophages (TPH-1) and HEK 293, followed by further treatment with the nanovesicles. BCD-OLA nanovesicles showed an 8- and 459- fold reduction of intracellular bacteria in TPH-1 and HEK 293 infected cells, respectively, when compared to bare VCM.

Aim 2

- Screening for the proper ratio of complexation between VCM and TS using solvent evaporation revealed the preferred ratio to be 1:3 as it displayed the best balance between small size, low PDI and the high drug loading capacity. The sizes of the formed NPs with the selected ratio were 85.15 ± 0.4 nm, surface charge and drug loading were -27 ± 1.3 mV and 68.8 ± 2.8%, respectively.

- Haemolytic effect and cytotoxicity studies using MTT assay performed on three mammalian cell lines MCF-7, A549 and HEK 293, revealed the formulated VCM/TS NPs to be non-haemolytic and >75% cell viability was observed, which confirmed their biosafety.

- Molecular dynamics simulation under the same conditions of the experiment, confirmed a continued and stable binding between VCM and TS, which was mainly governed by hydrophobic interactions, followed by van der Waals and electrostatic forces. A further MD simulation of multiple VCM/TS complexes showed spontaneous self-aggregation of the complexes.

- Structural analysis using FT-IR and DSC showed that only physical binding such as hydrophobic interactions contributed to the formation of VCM/TS NPs, without the formation of new chemical bonds.

- The formulated VCM/TS NPs with the selected ratio showed a sustained release of VCM from the NPs, with a 52.2% release after 48 h. The *in vitro* antibacterial test showed a 2-fold decrease in MIC against both *S. aureus* and MRSA, Additionally, it was observed that there was a significantly higher reduction in MRSA biofilms compared to bare VCM. Further *in vivo* study using mice skin infection models showed a 9.5-fold reduction in bacterial load after treatment with VCM/TS NPs, in comparison with bare VCM ($p = 0.0077$).

- Molecular dynamics simulations studies showed the potential of TS to stably interact with MRSA NorA and NorB efflux pumps at a molecular level, indicating its potential as an effective constituent in a delivery system to inhibit efflux pumps for enhancing antibacterial activity.

Aim 3

- A novel PEGylated FA was successfully synthesized and the structure was confirmed by FT-IR, DSC, and ^{1}H NMR analysis.

- Haemolytic effect and cytotoxicity studies using MTT assay was performed on three mammalian cell lines MCF-7, HeLa and HEK 293 respectively. Results revealed the non-haemolytic effect of the synthesized PEG-FA and >75% cell viability, which confirmed its biosafety.

- The self-assembled PEG-FA NPs displayed an average hydrodynamic diameter of 149.3 ± 0.21 nm with PDI of 0.267 ± 0.012 and a surface charge of 5.97 ± 1.03 mV. HRTEM images revealed a homogenous spherical shape of the PEG-FA NPs.

- The conjugation of PEG with FA successfully increased the water solubility of FA by 25-fold. The *in vitro* antibacterial activity revealed that the conjugation of FA with PEG did not inhibit the antibacterial activity of FA but rather enhanced it by 2.5-fold against *S. aureus* and MRSA respectively, compared to the bare FA.

- Human serum albumin binding studies using MST showed that PEG-FA had a very weak or no interaction with HSA (K_d = 14999 µM). In addition, molecular docking revealed that the binding of FA to HSA was more favourable compared to bilirubin, while PEG-FA did not fit into the HSA binding pocket. Thus, PEG-FA conjugation shows potential in reducing the risk of bilirubin encephalopathy in newborn infants due to bilirubin displacement.

The results of this study, therefore, confirmed the potential of novel BCD-OLA, VCM/TS and PEG-FA self-assembling nano-delivery systems to be biosafe and superior in treating *S. aureus* and MRSA infections as compared to the bare antibiotics. The additional experimental paper presented in Chapter 5 as a co-author, confirmed the potential of a novel self-assembled polymeric conjugate (HA-OLA) for the treatment of bacterial infections. Also, the review article in Chapter 5 elucidates the potential of different intrinsic stimuli-responsive nanocarriers for treatment of bacterial infections.

6.2 Significance of the findings in the study

The newly synthesized materials and designed nano formulations comprising; BCD-OLA nanovesicles, VCM/TS NPs, and PEG-FA conjugate were successfully employed to address the limitations associated with conventional dosage forms of antibiotics and antibacterial resistance. The significance of the findings in this study include the following:

New pharmaceutical products: This study has generated new pharmaceutical materials, viz; novel BCD-OLA amphiphile for drug delivery and PEG-FA as a polymer theraputic. Also, a new medicine, self-assembled VCM/TS NPs for enhancement of VCM delivery was generated. This will expand the range of the available pharmaceutical excipient for preparing new medicines, which can stimulate local pharmaceutical industries to manufacture superior cost-effective medicines.

Improved patient therapy and disease treatment: The newly designed BCD-OLA amphiphile, VCM/TS NPs, and PEG-FA nanosystems were successfully formulated with improved antibacterial potential against *S. aureus* and MRSA. The novel systems lowered the MIC of the loaded drugs and can effectively control bacterial infections with reduced dosing frequency without affecting therapeutic outcomes. Additionaly, unlike FA, PEG-FA did not have any binding affinity to the HSA, which indicated its potential for preventing bilirubin displacement and reducing side effects. These findings, therefore, prove the potential of these

systems in improving patient therapy and treatment of bacterial infections, thereby ultimately improving the quality of life as well as saving lives.

Creation of new knowledge to the scientific community: The various studies and their findings have contributed to the pharmaceutical sciences knowledge database in several ways. These include the following:

- New knowledge on the synthesis, characterization and determination of the toxicity profiles of the supramolecular BCD-OLA complex and PEG-FA conjugate was generated. The physicochemical, *in vitro*, *in silico*, and *in vivo* properties of the drug-loaded BCD-OLA nanovesicles, VCM/TS NPs, and PEG-FA NPs delivery systems were identified.
- Molecular mechanism of the interactions between BCD/OLA and VCM/TS with different ratios were identified. The process of spontaneous aggregation of BCD-OLA amphiphiles, PEG-FA conjugate and VCM/TS self-assembling complexes in water, were successfully confirmed. The ability of TS in the VCM/TS NPs to interact with NorA and NorB efflux pumps in MRSA at a molecular level, showed its potential to inhibit efflux pumps, which resulted in enhanced antibacterial activity.
- Formulation and processes parameters for preparation of BCD-OLA nanovesicles, VCM/TS NPs and PEG-FA conjugate were identified using various experimental techniques.
- The binding affinity of FA to HSA in comparison to bilirubin and PEG conjugation on the binding affinity of FA was quantified using MST.
- The detailed antimicrobial testing from MIC determination, flow cytometry, time killing assay, elimination of intracellular bacteria and *in vivo* antibacterial infection models successfully identified the *in vitro* and *in vivo* correlation of the designed and formulated nano-drug delivery systems.

Stimulation of new research: The research findings of the various studies and the successful development of BCD-OLA amphiphile, VCM/TS NPs and PEG-FA conjugate can stimulate new research areas, including the following:

- The newly synthesized BCD-OLA can be utilized for delivering other classes of drugs to treat various disease conditions, such as cardiovascular diseases, HIV/AIDS, gene therapy-related diseases, metabolic diseases amongst others. Also, PEG-FA can be

explored to encapsulate other classes of antibiotics and investigate the synergistic antibacterial effect.

- The newly designed carrier-free VCM/TS NPs (SADDs), could stimulate the application of this strategy to develop new nano-systems based on hydrophobic interaction for delivery other drugs with similar physicochemical properties.
- The successful formulation and *in vitro* and *in vivo* characterization of the reported nano-drug delivery systems in this study could stimulate research into the formulation of other nano-drug delivery systems for other classes of drugs to treat other diseases.
- The improved antibacterial activity of FA via polymeric conjugation with PEG and self-assembly into NPs, underlines PEGylation as a promising strategy to develop novel antibacterial delivery systems to combat the crisis of AMR and enrich the field of new antibiotics.

6.3 Recommendations for future studies

Although, these approaches have demonstrated the potential of BCD-OLA amphiphile, VCM/TS NPs and PEG-FA conjugate as novel nano-drug delivery systems to eradicate the problem of bacterial resistance, additional studies are necessary to improve the formulations to ensure eventual regulatory approval for patient use.

The following studies are proposed:

- In the case of BCD-OLA and PEG-FA, there is a need for coarse-grain MD simulations in order to build a system that can completely self-assemble into drug-loaded nanovesicles and to simulate the release of drug from the system.
- The successfully developed BCD-OLA nanovesicles for VCM delivery and PEG-FA conjugate system can be loaded with different classes of antibiotics. In addition, the simultaneous delivery of multiple antibiotics and their ability to achieve enhanced and synergistic activities can be explored.
- The MD simulation studies for interaction between TS and MRSA efflux pumps NorA and NorB can be upgraded with a quantitative determination of a specific protein using techniques, such as western blot or dot blot analysis.
- In the case of the VCM/TS NPs, the next phase would be to formulate other antibiotics using this simple technique, as well as trying other efflux inhibiting molecules that are already FDA-approved and available in the market to enhance the antimicrobial activity of other antibiotics further.

- Long-term stability studies using international conference of harmonization (ICH) conditions to assess the physical and chemical stability of optimized formulations must be undertaken to confirm their shelf life.
- *In vivo* acute, intermediate and long-term toxicity studies could be performed to determine the full toxicological profile of the material and the formulations reported in this study.
- *In vivo* IV infection model, bioavailability and pharmacokinetic studies, and clinical trials could be performed on the developed nano-systems to achieve approval for market introduction.
- Validated scale-up method for production of the nano-systems presented in this study could be developed in order to enable their applications in pharmaceutical industries.

6.4 Conclusion

The findings of this study specifically demonstrate the potential of the newly developed BCD-OLA amphiphile, VCM/TS NPs and PEG-FA conjugates as nano-carriers with inherent antibacterial activity, as well as their drug delivery potential, for improving the treatment of *S. aureus* and MRSA infections. This current research has thus, made significant contributions to nano-based approaches to overcome limitations of current/conventional dosage forms. The study further directed an approach towards the synthesis of novel antibacterial amphiphiles to develop multifunctional nano-systems to treat bacterial infections. The understanding of novel antibacterial materials and nano-technology in addressing the current global antibiotic drug therapy crisis will be dependent on future intensive and multidisciplinary research. This approach will play a vital role in improving the treatment of diseases associated with bacterial infections, with a tremendous impact on public health.

APPENDICES

Appendix I

Supplementary material for experimental paper One

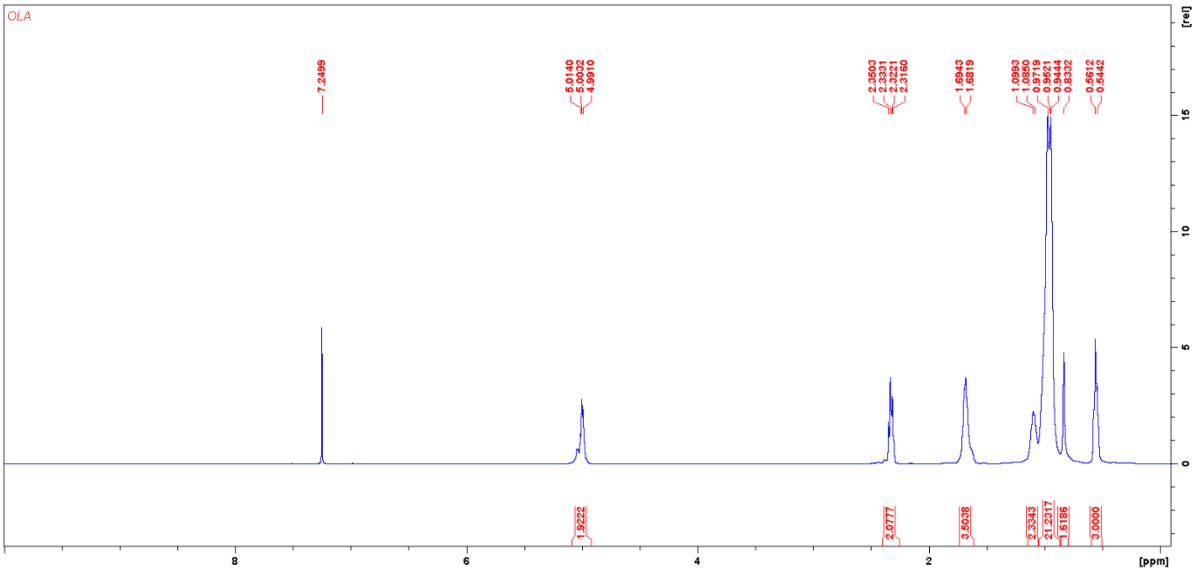

Figure S1. ^{1}H NMR (400 MHz) spectra in $CDCl_3$ at 300 K of OLA.

Table S1: FIC index

Result	Synergy	Additive	Indifference	Antagonism
Index	≤0.5	>0.5 to 1	>1 to <2	≥2

Table S2: Chemical Shifts in ppm of the Protons of BCD, OLA alone and BCD-OLA complex from ^{1}H NMR (400 MHz).

δ (ppm) of BCD protons	BCD alone	OLA alone	BCD-OLA (1:1)	Change in chemical shift
H-1	5.111		5.083	-0.028
H-2	3.6941		3.6657	-0.028
H-3	4.008		3.932	-0.076
H-4	3.628		3.6319	0.004
H-5	3.899		3.7433	-0.156
H-6	3.926		3.898	-0.028
a	-	5.344	5.481	0.137
b	-	2.615	3.001	0.386
c	-	2.041	2.110	0.069
d	-	1.426	1.685	0.259
e, f	-	1.313	1.342	0.029
g	-	0.929	0.936	0.007

Table S3: Average Binding Energy and its components obtained from the MM-PBSA Calculation for BCD and OLA complex

Model	Equation	R^2	RMSE	Release exponent (n)	β
First Order	$Q = Q_0 . e^{kt}$	0.647	13.725	-	-
Higuchi	$Q = k. t^{½}$	0.758	11.372	-	-
Korsmeyer-Peppas	$Q = k . t^n$	0.943	5.519	0.327	-
Hixson-Crowell	$Q^{⅓} = kt + Q_0^{⅓}$	0.492	16.453	-	-
Weibull	Q = 1 exp [-(t)a/b]	0.978	4.079	-	0.473

R2 = linear regression coefficient, RMSE = Root mean square error.

Table S4: Drug release kinetics data for BCD-OLA/VCM nanovesicles

Contribution	Energy (kJ/mol)
ΔE_{vdw}	-78.59 ± 2.73
ΔE_{elec}	-1.28 ± 0.13
ΔG_{polar}	37.46 ± 1.04
$\Delta G_{nonpolar}$	-10.80 ± 0.30
ΔG_{total}	-53.25 ± 1.93

Table S5: ΣFIC of (BCD-OLA)/VCM for the in vitro antibacterial activity against SA and MRSA

	ΣFIC against SA	**ΣFIC against MRSA**
(BCD-OLA)/VCM	0.50 (Synergistic)	0.24 (Synergistic)

Appendix II

Supplementary material for experimental paper Two

Table S1: Size and PDI of different dilutions of VCM/TS NPs in PBS measured using Zetasizer. N=3

VCM/TS NPs Conc (µg/ml)	Size (nm)	PDI
1000	96.12 ± 3.2	0.142 ± 0.11
100	96.11 ± 2.5	0.174 ± 0.13
10	97.96 ± 2.1	0.150 ± 0.25
0.1	520.6 ± 16.2	0.774 ± 4.55

Table S2: Haemolysis (%) for different concentrations of VCM/TS NPs, PBS (pH 7.4) and distilled water.

VCM/TS NP (mg/ml)	Haemolysis (%)
0.05	0.08
0.1	0.07
0.2	0.30
0.3	0.41
0.4	0.58
0.5	0.78
PBS (pH 7.4)	0.00
Distilled water	100.00

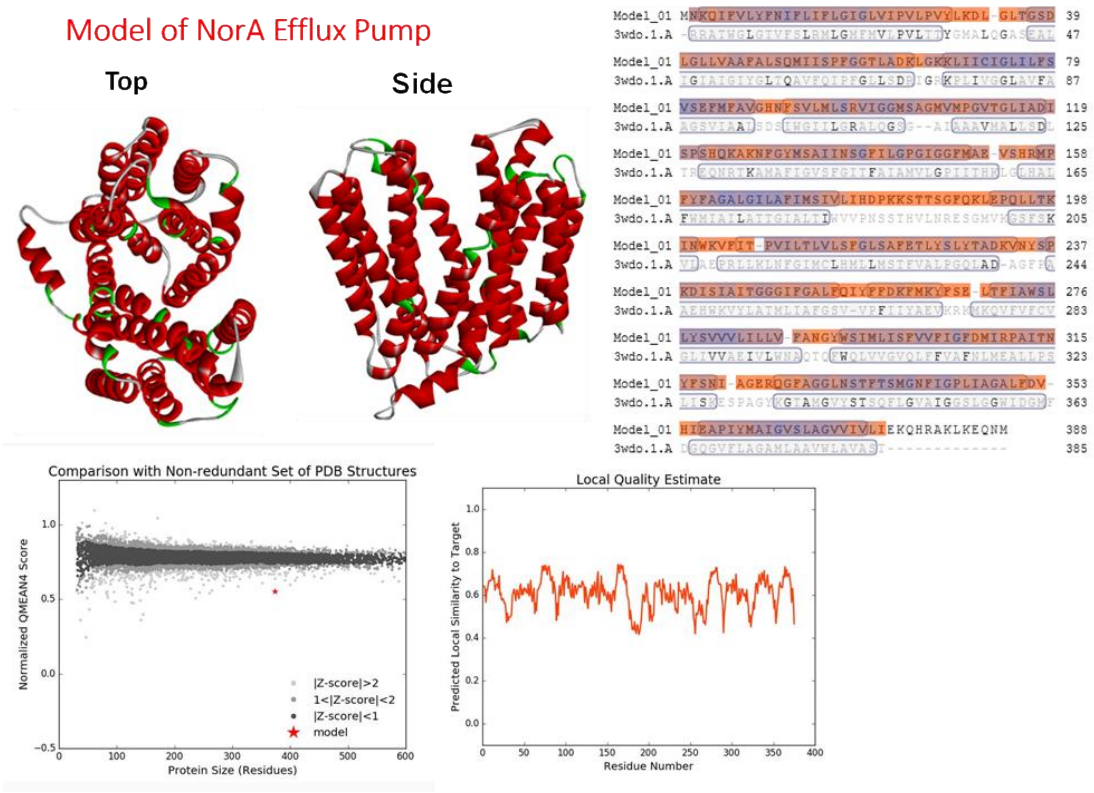

Figure S1: Homology model of NorA efflux pump (top left) including alignment of NorA FASTA sequence with its template (top right). The comparison with nonredundant PDB structures (bottom left) and the predicted local similarity to its target (bottom right) are shown.

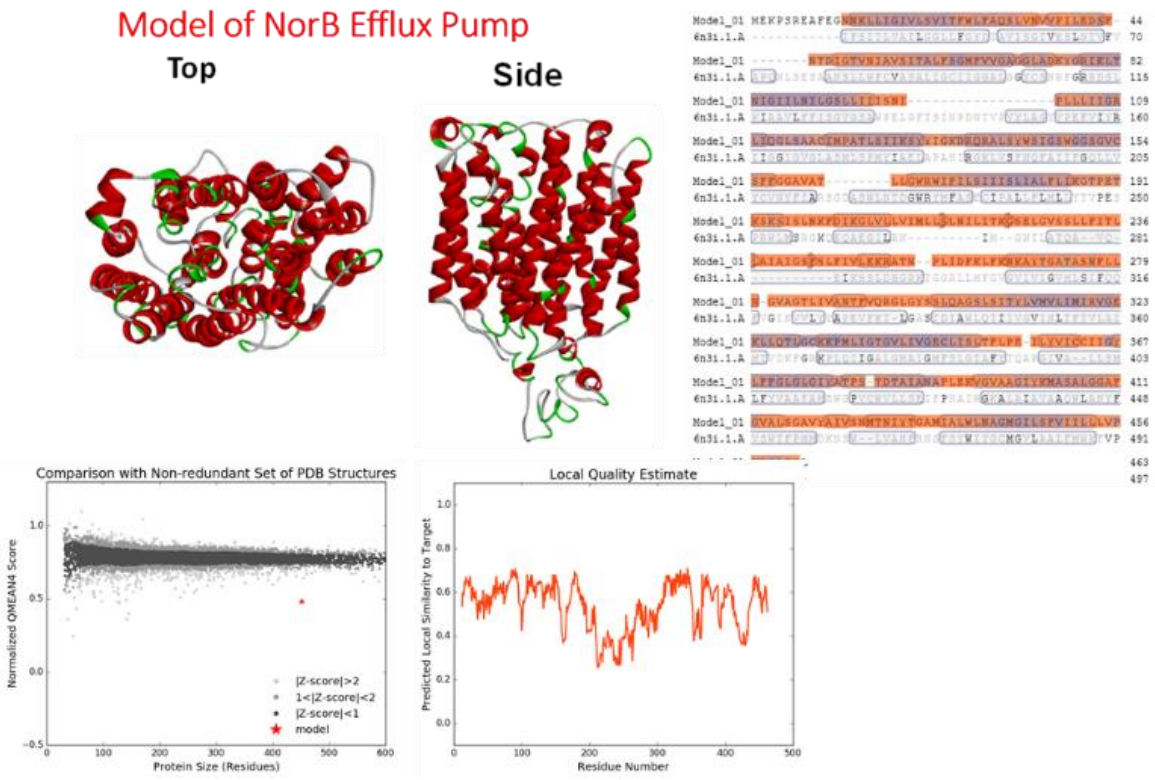

Figure 2: Homology model of NorB efflux pump (top left) including alignment of NorB FASTA sequence with its template (top right). The comparison with nonredundant PDB structures (bottom left) and the predicted local similarity to its target (bottom right) are shown.

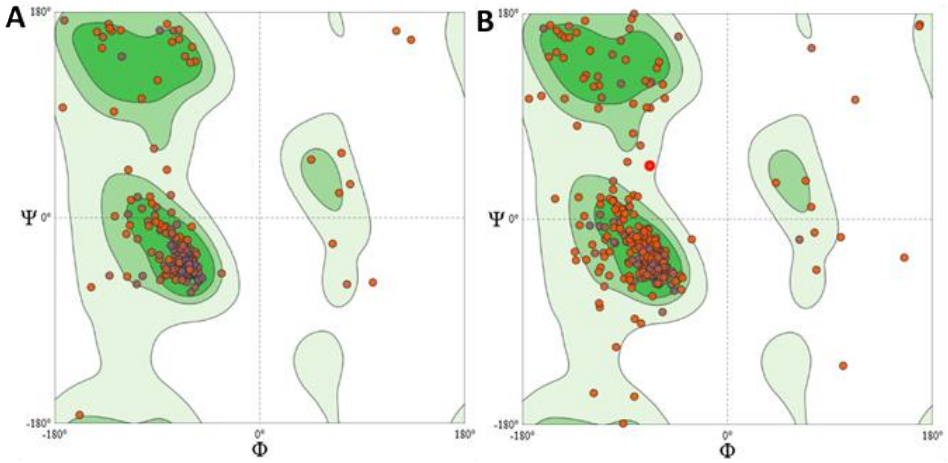

Figure S3: Ramachandran Plots generated from MolProbity for Homology models of NorA (A) and NorB (B).

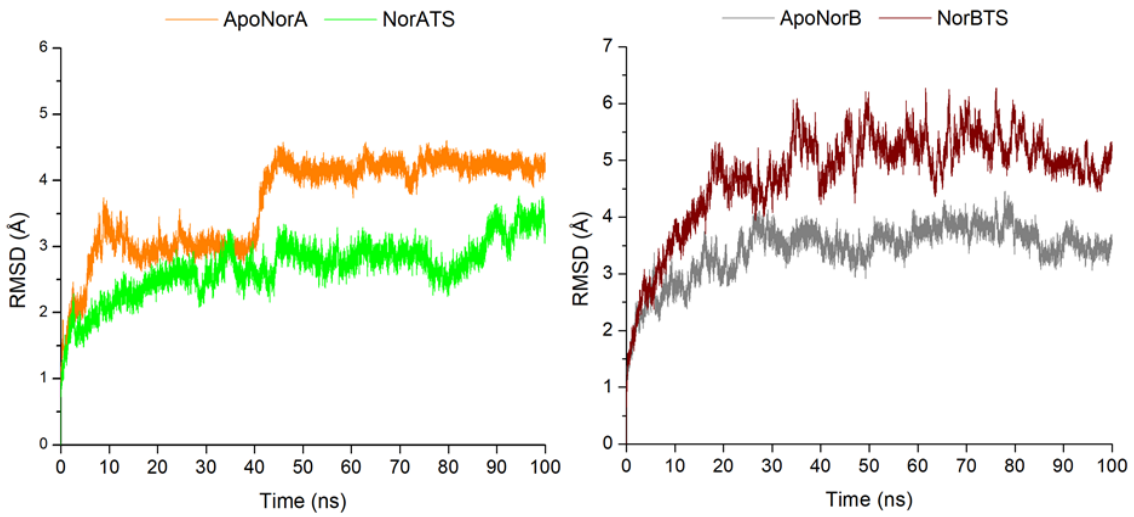

Figure S4: Root-mean-square deviation of all systems remained within a stable 2Å range.

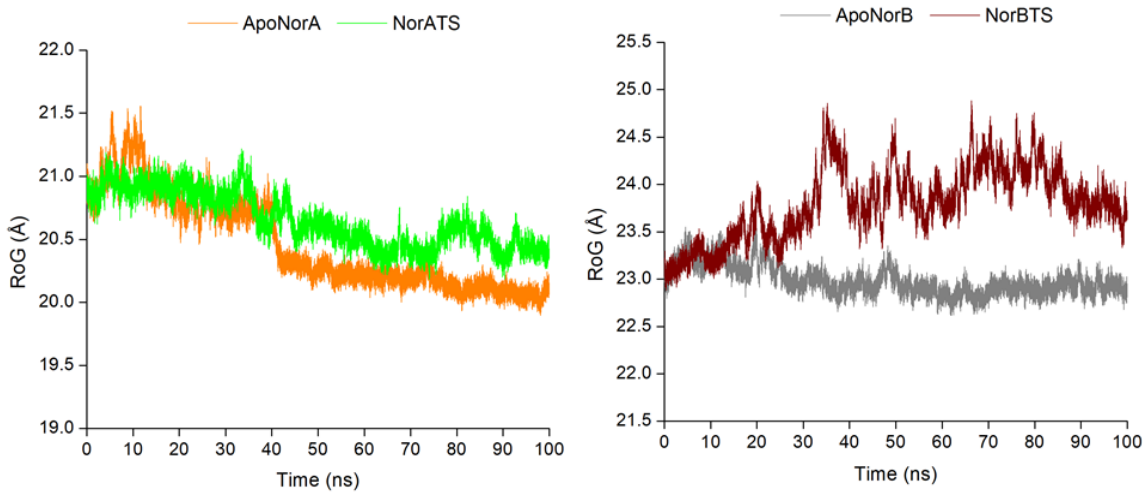

Figure S5: Radius of gyration of all systems indicating that NorA and NorB proteins expand to allow TS to bind more efficiently.

Appendix III

Supplementary material for experimental paper Three

Method of Synthesis of PEG-FA

1- Synthesis of (I)
BOC protection of 6-aminohexanoic acid (6AHA):
To a stirring solution of 6AHA (0.6 g, 4 mmol) in 25ml methanol, tert-butyl decarbonate (1.08 g, 5 mmol) added and the reaction mixture was stirred overnight at room temperature. After this time, the solvent was evaporated to complete dryness to give a white crude product which was purified by flash chromatography (5 % MeOH/CH2Cl2) to yield a crystal white solid (98% yield).

2- Synthesis of (II)
Conjugation of BOC-6AHA (spacer) to 2000 Polyethylen glycol monoether (PEG):
PEG-6AHA-BOC was synthesized, by addition of BOC-6AHA (0.462g, 2 mmol) to a stirring reaction mixture of PEG 2000 (4g, 2 mmol), DMAP (0.293 g, 2.4 mmol), EDC (0.46 g, 2.4 mmol) in dry DCM. The reaction mixture was stirred for 24 h at room temperature under inert conditions (N2(g)). After this time, acidic water wash was used to removed EDC/DMAP and the organic solvent was evaporated. TLC was used to monitor the reaction and complete removal of DMAP, then the product was precipitated in cold ether, solid white product product was obtained at Yield above 80%.

3- Synthesis of (III)
Cleaving of BOC:
To synthesized PEG-6AHA, a reaction mixture of PEG-6AHA-BOC (3.5 g, 1.5 mmol) in 25% trifluoroacetic acid (TFA) in DCM was stirred for 2 h at room temperature. After this time, TFA was removed under reduced pressure. The traces amount of TFA remaining was removed by re-dissolving the crude product in ethyl acetate and washed with saturated solution of Na_2CO_3 and followed by washing with brine solution separately. The organic layer was dried over anhydrous MgSO4 to remove traces amount of water and filtered off. The solvent was vacuum dried to give the final product at yield above 75 %.

4- Synthesis of (IV)
Coupling of FA with PEG-6AHA:
PEG-6AHA-FA was synthesized, by addition of FA (0.591g, 1.1 mmol) to a stirring reaction mixture of PEG-6AHA (2.2 g, 1.04 mmol), DMAP (0.152 g, 1.24 mmol), EDC (0.239 g, 1.24 mmol) in dry DCM. The reaction mixture was stirred for 24 h at room temperature under inert conditions (N2(g)). After this time, acidic water wash was used to removed EDC/DMAP and the organic solvent was evaporated. TLC was used to monitor the reaction and complete removal of DMAP, then the product was precipitated in cold ether, faint yellow product was obtained at Yield above 80%.

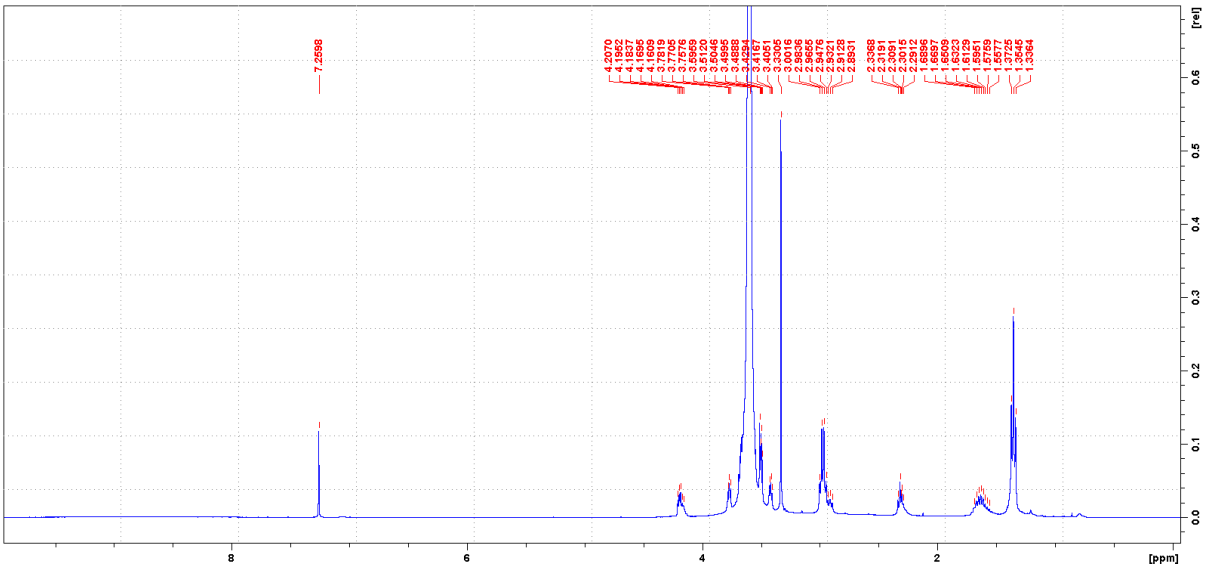

Figure S1. ^{1}H NMR (400 MHz) spectra in $CDCl_3$ of PEG-6AHA

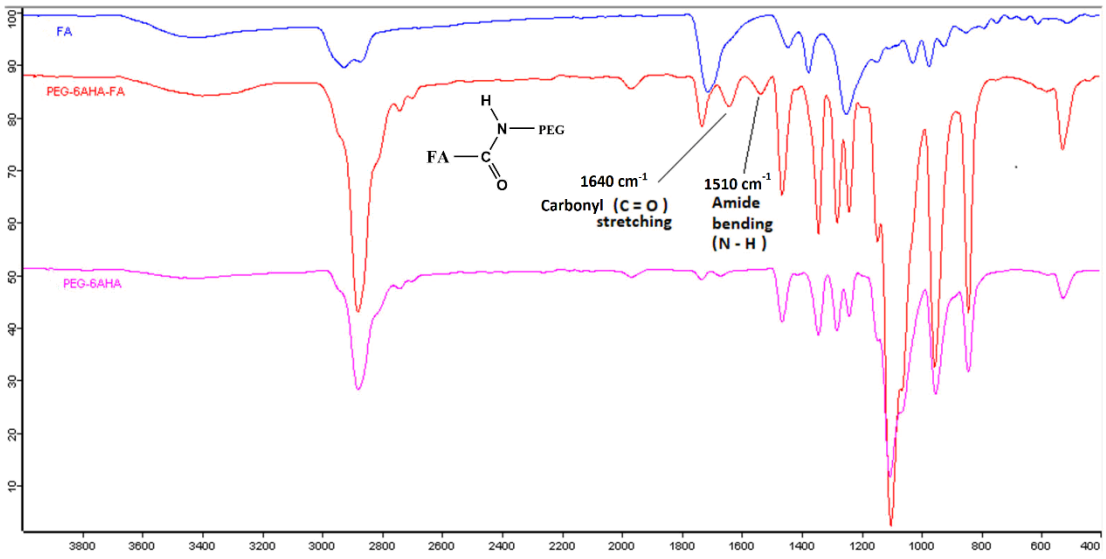

Figure S2: IR spectrum of FA, PEG-6AHA, and PEG-FA.

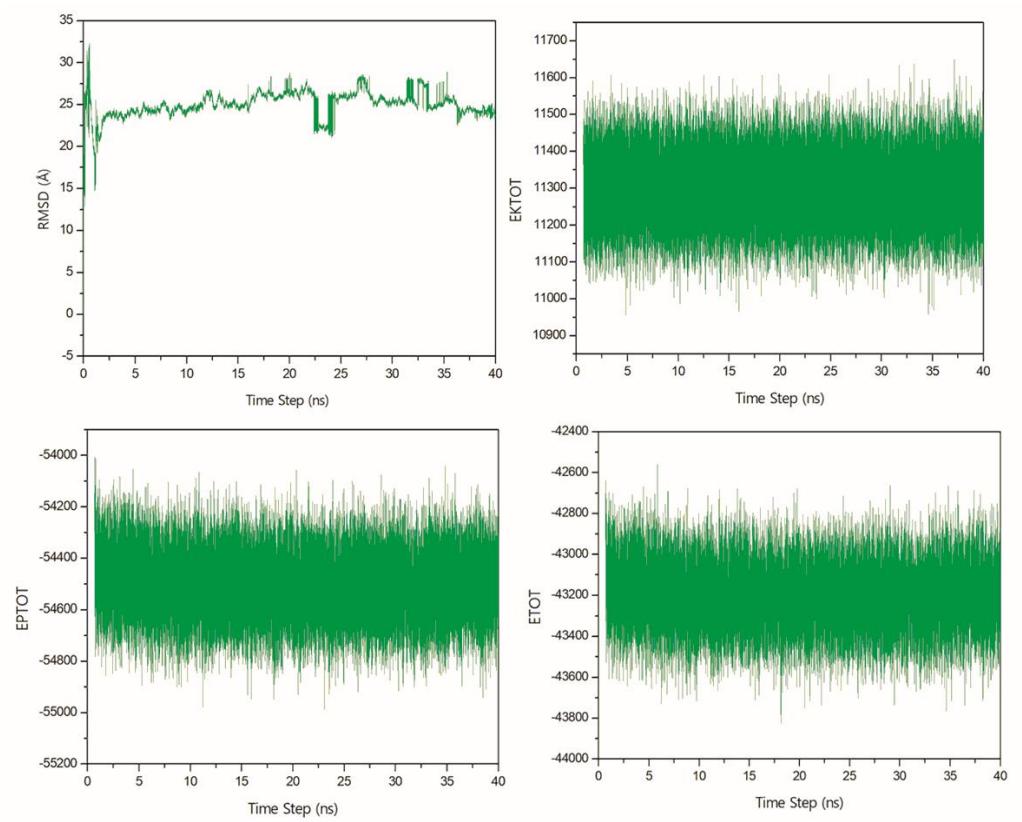

Figure S3: The plots for the RMSD, kinetic (EKTOT), potential (EPTOT), and total energy (ETOT) for FA-PEG complexes during the MD.

Proof of acceptance for experimental paper Three:

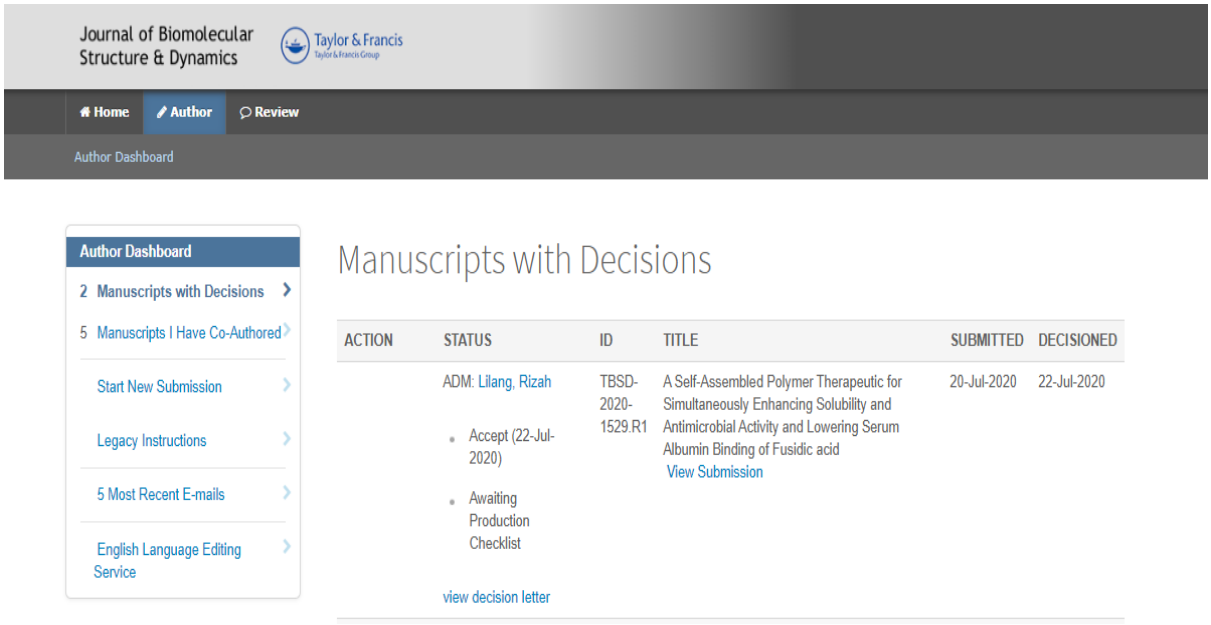

Appendix IV

Colloids and Surfaces B: Biointerfaces 182 (2019) 110388

Contents lists available at ScienceDirect

Colloids and Surfaces B: Biointerfaces

journal homepage: www.elsevier.com/locate/colsurfb

Self-assembled oleylamine grafted hyaluronic acid polymersomes for delivery of vancomycin against methicillin resistant *Staphylococcus aureus* (MRSA)

Pavan Walvekar, Ramesh Gannimani, Mohammed Salih, Sifiso Makhathini, Chunderika Mocktar, Thirumala Govender*

Discipline of Pharmaceutical Sciences, School of Health Sciences, University of KwaZulu-Natal, Private Bag X54001 Durban, 4000, South Africa

ARTICLE INFO

Keywords:
Hyaluronic acid-oleylamine conjugates
Inherent antibacterial activity
Self-assembly
Vancomycin delivery
Enhanced antibacterial activity

ABSTRACT

MRSA infections are a major global healthcare problem associated with high morbidity and mortality. The application of novel materials in antibiotic delivery has efficiently contributed to the treatment of MRSA infections. The aim of the study was to develop novel hyaluronic acid-oleylamine (HA-OLA) conjugates with 25–50% degrees of conjugation, for application as a nano-drug carrier with inherent antibacterial activity. The biosafety of synthesized novel HA-OLA conjugates was confirmed by *in vitro* cytotoxicity assay. Drug carrying ability of HA-OLA conjugates was confirmed by 26.1–43.12% of vancomycin (VCM) encapsulation in self-assembled polymersomes. These polymersomes were dispersed in nano-sized range (196.1–360.9 nm) with a negative zeta potential. Vancomycin loaded polymersomes were found to have spherical and bilayered morphology. The VCM loaded polymersomes displayed sustained drug release for 72 h. *In vitro* studies showed moderate antibacterial activity for HA-OLA conjugates against both *S. aureus* and MRSA with minimum inhibitory concentration (MIC) of 500 μg/mL. The VCM loaded HA-OLA polymersomes displayed four-fold lower MIC (1.9 μg/mL) than free VCM (7.8 μg/mL) against MRSA. Furthermore, synergism was observed for VCM and HA-OLA against MRSA. Flow cytometry showed 1.8-fold higher MRSA cell death in the population for VCM loaded polymersomes relative to free drug, at concentration of 1.95 μg/mL. Bacterial cell morphology showed that the drug loaded polymersomes had stronger impact on MRSA membrane, compared to free VCM. These findings suggest that, HA-OLA conjugates are promising nano-carriers to function as antibiotic delivery vehicles for the treatment of bacterial/MRSA infections.

1. Introduction

Resistant strains of *Staphylococcus* bacteria are currently a significant factor contributing to deterioration of the health status in infected individuals, thus causing premature mortality [1]. Predominantly, MRSA has acquired resistance to virtually all potent antibiotics, making it extremely difficult to eliminate from the host, thus challenging current drug therapy [2]. Vancomycin (VCM) being the drug of choice to treat MRSA infections, has also capitulated to resistance to some of the isolates, known as vancomycin resistant *Staphylococcus aureus* [3]. Therefore, there is a need for novel and innovative approaches to treat MRSA infections effectively. In recent years, nano drug delivery systems have attracted large interest in the treatment of bacterial infections, because of their ability to target specific infection sites, thus increasing localized drug concentration; to provide sustained drug release, thus lowering the frequency of administration; and to improve physico-chemical properties of drugs *etc*. This can lead to improved therapeutic outcomes and patient compliance and can overcome drug resistance mechanisms [4]. Numerous antibiotic-loaded nano-systems are being reported for combating bacterial infections [5–7]. Therefore, antibiotic loaded nano-systems may efficiently overcome MRSA infections.

Among the various nano drug delivery systems, polymeric nano-systems have gained considerable interest to deliver therapeutic agents and treat many diseases. Polymeric nano-systems are considered to be more stable and reliable than other organic nano-platforms such as lipidic systems [8,9]. For example, liposomes tend to lose their structural configuration upon storage thus resulting in leakage of encapsulated payloads. However, polymeric nano-systems are comparatively more robust and stable, and do not lose their integrity during long term

* Corresponding author at: Private Bag X54001 Durban, 4000, KwaZulu-Natal, South Africa.
E-mail address: govenderth@ukzn.ac.za (T. Govender).

https://doi.org/10.1016/j.colsurfb.2019.110388
Received 9 May 2019; Received in revised form 15 July 2019; Accepted 23 July 2019
Available online 25 July 2019
0927-7765/ © 2019 Published by Elsevier B.V.

storage. Furthermore, polymeric nano-systems can facilitate sustained/controlled, targeted and intracellular drug delivery to improve the therapeutic efficacy of encapsulated payloads [7,10]. In addition to these advantages, polymers with surface functionalities can be easily structurally modified with other compounds to make graft or block copolymers that can suit various drug delivery applications. For example, hyaluronic acid was grafted with poly(L-histidine) for the preparation of pH responsive and tumor-targeted amphiphilic copolymer for use as a carrier for anticancer drugs [11].

Various naturally occurring, synthetic and semi-synthetic polymers such as chitosan, dextran, polylactic acid, polyglycolic acid, poly(lactic-co-glycolic acid), polyacrylic acid, methyl cellulose *etc*, have been used to construct nano-drug delivery systems to deliver therapeutic agents. These nano-systems have shown promising outcomes thus far in treating many diseases including bacterial infections [6]. Recently, hyaluronic acid (HA), a naturally occurring biodegradable hydrophilic polymer has captured considerable attention in designing various drug delivery nanotherapeutics. Many reports on HA-based nano-systems can be found in the literature to deliver anticancer drugs [12]. The application of HA to construct antibiotic loaded nano-systems may display improved and synergistic antibacterial activity because of its inherent bacteriostatic and antibiofilm effects against certain strains [13,14]. Some evidences have also been documented where, polycarboxylic acids such as HA are shown to lower the pH of infection, thus creating an environment where pathogens find it difficult to survive [15]. Furthermore, HA is also known to possess wound healing, tissue regeneration and anti-inflammatory properties, which may help to cure dermal infections and facilitate quick recovery [16]. Recently, Zhu et al. reported HA-based nanogel loaded with chlorhexidine diacetate (an antibacterial agent) to demonstrate prolonged antimicrobial activity against *S. aureus* and *E. coli* followed by accelerated hemostasis and wound healing [16]. Therefore, there is a need for novel HA-based polymeric nano-systems to be used as antibiotic carriers to combat bacterial infections.

Self-assembling amphiphiles are considered as one of the most prominent and promising candidates for drug delivery applications [17]. HA is a completely hydrophilic polymer, and cannot self-organise to form nano-assemblies on its own. Therefore, an additional support is needed from a hydrophobic moiety to make it an amphiphile. Biodegradable hydrophobic long fatty chains are one class of compounds that have been frequently used to make amphiphiles [18]. Furthermore, long fatty chains have also been reported to enhance the activity of other antibacterial agents [19,20]. The grafting of these hydrophobic long fatty chains with hydrophilic HA can make ideal amphiphilic drug cargoes. HA can be grafted with oleylamine (a long fatty chain) at certain degrees of conjugation to synthesize hyaluronic acid-grafted-oleylamine amphiphiles. To date, no HA-fatty amine conjugates have been used to deliver antibiotics.

Our research group has primarily been focussing on developing various novel nano-systems to deliver VCM for combating MRSA infections. Amongst, various other nano-systems, we have developed polyacrylic acid, chitosan and dextran sulphate based polymeric nano-systems to deliver VCM, and fight MRSA infections [21–23]. In these findings, we have achieved decent entrapments for VCM with sustained and improved antibacterial activities against MRSA. In addition, these nano-formulations also enabled ease of preparation with good physical stability, which may enable the future commercialization of these VCM nano-systems. In continuation of our efforts to develop novel polymers, in this study, hydrophilic HA was grafted with hydrophobic oleylamine (OLA) to promote self-assembly and simultaneous encapsulation of VCM to combat MRSA infections. To the best of our knowledge, VCM has not been delivered using HA based polymeric nano-system to fight MRSA infections. Therefore, this research undertaken aimed to synthesize a novel amphiphile comprising of hydrophilic HA and hydrophobic oleylamine (fatty chain) for the formulation of self-assembled nano-carriers to deliver VCM and treat MRSA infections.

2. Materials and methods

Hydrochloride form of vancomycin was purchased from Sinobright Import & Export Co. Ltd. (China). 1-Ethyl-3- (3-dimethylaminopropyl) carbodiimide hydrochloride (EDC.HCl) was acquired from Carbosynth (UK). Oleylamine (≥ 98%) and Mueller Hinton Broth-2 (MHB) was procured from Sigma Aldrich (USA). N-Hydroxysuccinimide (NHS) was purchased from Sigma-Aldrich (Japan) Sodium hyaluronate (9.47 KDa) was purchased from Spec-Chem IND. INC. MTT (3-(4, 5-dimethylthiazol-2-yl)-2, 5-diphenyltetrazolium bromide) was purchased from Alfa Aesar (UK), Mueller Hinton Agar (MHA), Nutrient Agar and Nutrient Broth were obtained from Biolab (South Africa). The dialysis tube (MWCO 14,000 Da) was purchased from Sigma-Aldrich (USA) for drug release studies. Double distilled water obtained from a Direct-Pure EDI water system was used throughout the experiment. Gram positive bacteria, *Staphylococcus aureus* (*S. aureus*, ATCC 25923) & methicillin resistant *Staphylococcus aureus* (MRSA, ATCC 700699) were used to study the antibacterial activity.

2.1. Synthesis and characterization of HA-OLA conjugates

As sodium hyaluronate was not freely soluble in formamide, sodium salt of HA was converted to HA, to facilitate the reaction. Briefly, 2 g of sodium hyaluronate was dissolved in water, and 48 mL of 1 M HCl was added slowly to the solution, followed by stirring for two hours. The obtained solution was freeze dried to obtain HA. Synthesis of HA-OLA with various degrees of conjugation (50%, 33% and 25%) was planned to evaluate the self-assembling behaviour of HA after conjugation with OLA. Synthesis of HA-OLA conjugates were performed in one pot reaction as indicated in Scheme 1. EDC/NHS coupling chemistry was used to graft OLA to carboxylic acid groups of HA. Considering the molecular

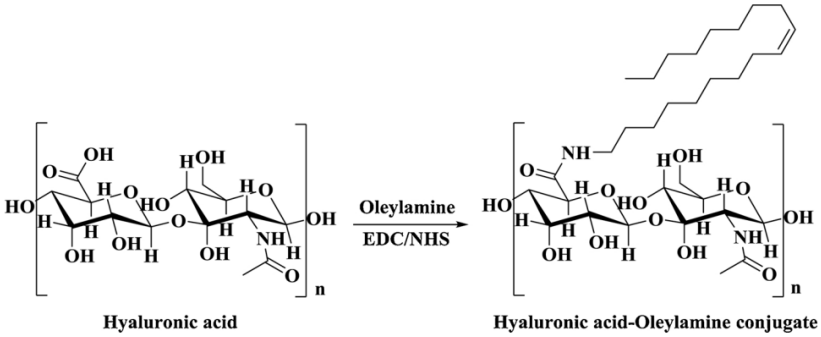

Scheme 1. Synthesis of HA-OLA conjugates.

weight of HA, ~24 carboxylic acids were calculated per molecule. As OLA conjugated to 50% of carboxylic acids of HA became too hydrophobic, and did not self-assemble, it was not considered suitable for the present study. To synthesize 33% of conjugation, briefly, 500 mg of HA was allowed to completely dissolve in formamide, followed by sequential addition of 113 mg (8 equivalents) of OLA, 48.6 mg (8 equivalents) of NHS and 162 mg (16 equivalents) of EDC, and allowed to react for 48 h. The resulting reaction mixture was dialysed (MWCO = 3500 Da) against water for two days to purify the polymer. Further, the polymer solution was freeze dried to obtain HA-OLA conjugates. To yield 25% of conjugation, the same procedure was followed, where OLA, NHS and EDC used were 84.8 mg (6 equivalents), 36.4 mg (6 equivalents) and 121.7 (12 equivalents) respectively. As twelve, eight and six carboxylic acids were targeted for conjugation, HA-OLA conjugates with 50%, 33% and 25% of conjugation were termed as HA-OLA12, HA-OLA8 and HA-OLA6 respectively. The HA-OLA conjugates were characterized by FTIR and ^{1}H NMR spectroscopy (D_2O).

2.2. MTT assay

To evaluate the biosafety of the synthesized novel HA-OLA conjugates, MTT assay was performed on human embryonic kidney cells (HEK-293), human cervix adenocarcinoma (HeLa) cells and human breast adenocarcinoma cells (MCF-7) according to previously published method [24]. Briefly, cell lines grown at 37 °C under humidified atmosphere of 5% CO_2 were seeded at a density of 3.0×10^3 cells in 96-well plates and incubated for 24 h. Thereafter, cells were treated with test compounds (HA-OLA6 and HA-OLA8) at various concentrations (20–100 µg/mL) and allowed to incubate for 48 h. Thereafter, the spent culture medium was replaced with 100 µL of fresh medium and 20 µL of MTT (5 mg/mL in PBS) in each well and incubated for 4 h, followed by the removal of the used medium and addition of 100 µL of DMSO to dissolve the MTT formazan crystals. The absorbance was recorded at 570 nm using a microplate spectrophotometer (Spectrostar nano, Germany). Untreated cells in the culture medium was used as negative control. The study was performed in pentaplicates, and the percentage cell viability was calculated as follows.

$$\%\ \text{Cell viability} = \left(\frac{\text{A570 nm treated cells}}{\text{A570 nm untreated cells}}\right) \text{X } 100\%$$

2.3. Preparation of VCM loaded HA-OLA polymersomes

The VCM loaded polymersomes were prepared using a probe ultrasonication technique [25]. Since, HA-OLA12 became highly hydrophobic, and did not self-assemble, it was therefore not included in the optimization process of polymersomes. Briefly, specified amounts of HA-OLA6 or HA-OLA8 conjugates were dispersed in 10 mL of water containing VCM (5/10 mg). The resulting mixture was ultrasonicated at 30% amplitude for 10 min under, cold water bath to obtain VCM loaded polymersomes of nano-sized range. Empty polymersomes were prepared using the same procedure by excluding VCM. All formulations in optimization process were prepared in triplicate.

2.4. Size, polydispersity index (PDI), zeta potential (ZP), morphology and stability

The determination of size, PDI and ZP of polymersomes was achieved through a zeta sizer (Nano ZS90, Malvern Instruments Ltd., UK) at 25 °C, without further dilution. Prior measurement, the polymersomes suspension were filtered through a 0.45 µm membrane filter to obtain a dust-free nano-system. Morphological characterisation of drug loaded polymersomes was investigated using a transmission electron microscopy (TEM - Jeol, JEM-1010, Japan). The samples were prepared and captured as previously reported [26].

A previously reported protocol was followed to assess the stability of polymersomes [25]. The stability of HA-OLA6 polymersomes in the presence of 10% FBS was measured by dynamic light scattering (DLS) technique at 37 °C. HA-OLA6 polymersomes were dissolved in DMEM containing 10% FBS, and incubated in a shaking incubator at 100 rpm and 37 °C. The mean particle diameter (n = 3) of polymersomes were obtained every 24 h for three consecutive days.

2.5. Entrapment efficiency (%EE) and drug loading capacity (DLC)

An ultrafiltration method was employed for the determination of % EE of VCM loaded polymersomes. Briefly, 2 mL of drug loaded polymersomes was placed in Amicon® Ultra-4 centrifugal filter tubes (MWCO, 10 kDa), and centrifuged at 3000 rpm at 25 °C for 30 min. The un-entrapped drug in the filtrate was assayed using reversed-phase high performance liquid chromatography (HPLC), Shimadzu Prominence DGU-20A3 with UV detection at 280 nm. A Nucleosil 120-5 C18 column (4 × 150 mm, 5 µm) was used, and the mobile phase consisted of acetonitrile:0.1% TFA in water (15:85 v/v). The flow rate and injection volume were 1 mL/min and 100 µL, respectively. The %EE and DLC were determined using the following equations [26].

$$\%\text{EE} = \left(\frac{\text{Amount of VCM in polymersomes}}{\text{Amount of VCM added}}\right) \text{X } 100$$

$$\%\text{DLC} = \left(\frac{\text{Amount of VCM in polymersomes}}{\text{Total weight of polymersomes}}\right) \text{X } 100$$

2.6. Differential scanning calorimetry (DSC)

DSC (Shimadzu DSC-60, Japan) was employed to study the thermal behaviours of free VCM, HA-OLA6, physical mixture (drug and the polymer) and lyophilized drug loaded polymersomes. Approximately, two mg of samples were transferred and sealed in an aluminium pan, which was further heated to 300 °C at a constant rate (10 °C/min) under a constant nitrogen flow (20 mL/min) using an empty pan as reference.

2.7. In vitro drug release

The release profiles of free VCM and VCM loaded polymersomes were studied using the dialysis bag method in PBS (pH 7.4) at 37 °C [27]. Both free VCM and VCM loaded polymersomes, each of 1 mL were loaded separately into dialysis bags (MWCO 14,000 Da). The loaded tubings were tightly sealed and dialyzed against 40 mL of PBS at 37 ± 0.5 °C in a shaking incubator at 100 rpm. At defined time intervals, 3 mL samples were withdrawn from the dissolution media and replaced with an equal amount of fresh PBS to maintain a uniform volume and sink condition. The amount of VCM present in the samples was measured spectrophotometrically at 280 nm using HPLC (as specified in Section 2.5). The study was performed in triplicate. *In vitro* drug release kinetics and analysis were determined using DD Solver. Zero order, first order, Higuchi, Hixon-Crowell, Korsmeyer-Peppas and Weibull models. The parameters such as correlation coefficient (R^2), root mean square error (RMSE) and mean dissolution time (MDT) were calculated to determine the release kinetics and best fit model.

2.8. Antibacterial activity

2.8.1. In vitro antibacterial activity

The *in vitro* antibacterial effects of free VCM, free HA, HA-OLA6, HA-OLA8, and VCM loaded polymersomes (made up of HA-OLA6 and HA-OLA8) were studied against *S. aureus* and MRSA by determining MIC using broth dilution technique [28]. *S. aureus* and MRSA cultures were grown overnight in Nutrient Broth at 37 °C in a shaking incubator at 100 rpm. The overnight grown cultures were diluted with sterile distilled water to achieve a concentration equivalent to 0.5 MacFarland

standard using a DEN-1B densitometer (Latvia). MHB (135 µL) was added to 96 well plates. Further, 135 µL of test samples were added in the first well and were serially diluted. The 0.5 MacFarland bacterial suspension were further diluted to 1:150 with sterile distilled water to achieve a final concentration equivalent to 5×10^5 colony forming units (CFU)/mL. The diluted bacterial culture (15 µL) was added to 96 well plates containing the mixture of MHB and the test samples. The plates were placed in a shaking incubator (100 rpm) at 37 °C for 24 h. MIC was determined as the lowest concentration that inhibited bacterial growth. The MIC was determined by spotting 10 µL of each broth on MHA plates followed by incubation for 24 h at 37 °C. The spotting was repeated for the next two days, *i.e.*, at 48 h and 72 h. The study was performed in triplicate.

Σ Fractional Inhibitory Concentration (FIC) was used to study the combined effect of novel HA-OLA6 and VCM in VCM loaded polymersomes against both *S. aureus* and MRSA. ΣFIC was calculated on the basis of MIC data that was generated by *in vitro* antibacterial study. A previously reported method was followed to calculate the FIC [26]. The ΣFIC was calculated using the following equations and Table S1 (Supplementary material).

FIC (VCM) = MIC of VCM in combination with HA-OLA6/MIC of HA-OLA6

FIC (HA-OLA6) = MIC of HA-OLA6 in combination with VCM/MIC of VCM

ΣFIC = FIC (VCM) + FIC (HA-OLA6)

2.8.2. Flow cytometry bacterial cell viability

A flow cytometry assay was employed to study the cell viability of MRSA cells after treatment with free VCM and VCM-loaded polymersomes for 18 h [29]. The bacterial cultures were prepared as previously described in Section. 2.8.1. Sterile distilled water (135 µL) was added to the 96 well plate. Further, 135 µL of free VCM (positive control) and VCM-loaded polymersomes were added to the plate, and were serially diluted. Thereafter, bacterial suspension (15 µL) containing 5×10^5 CFU/mL was added at respective MICs of test samples, and incubated at 37 °C in a shaking incubator (100 rpm). To flowcytometry tubes containing 350 µL of the sheath fluid, free VCM and VCM loaded polymersomes treated broths were added and vortexed for five minutes. The tubes containing sheath fluid and test samples were further incubated for 30 min with 5 µL of propidium iodide (PI) and Syto9, which served as cell wall impermeable and permeable dyes, respectively. The fluorescence of PI was excited at 455 nm and collected through a 636 nm bandpass filter (red wavelength), whereas Syto9 excited at 485 nm, and collected at 498 nm (green wave length). Pure untreated MRSA cells were used as a negative control. A flow cytometer (BD FACSCanto II, Becton Dickinson, USA) was used for the experiment. Sheath fluid and sample flow rate were set at 16 mL/min and 0.1 mL/min, respectively. BD FACSDiva v8.0.1 (a flow cytometer software) was used to collect the data for fixed cells [30]. To analyse fluorescence-activated cell sorting, the voltage settings were, 731, 538, 444 and 451 for forward scatter, side scatter, PI and Syto9, respectively. The MRSA cells were initially gated using forward scatter, further, cells of appropriate size were gated and at least 10,000 cells were collected. The study for each sample was performed in triplicate, and position of the 'live' and 'dead' cells gates were determined. The detection threshold was set to 1000 in side scatter analysis to avoid any background signal from particles smaller than bacteria [31].

2.8.3. Bacterial killing kinetics

Free VCM and VCM-PS6 were added at concentrations equivalent to five times the MIC to the MRSA culture (5×10^5 CFU/mL). Sterile water was added to MRSA broth, which served as a control. Bacterial killing kinetics was monitored from 0 h to 24 h. At defined time periods (0, 1, 2, 4, 6, 8, 12 and 24 h), the samples were collected in sterile eppendorf tubes and serially diluted three times (1 : 10) with sterile water. The diluted broths were plated in triplicate on Mueller Hinton Agar plates, and incubated for 48 h at 37 °C. Thereafter, the total number of colonies were counted and converted to $\log_{10}$ values, followed by plotting a graph [32].

2.8.4. Bacterial cell morphology

VCM acts on the cell-wall of bacteria therefore, a membrane disruption study was undertaken using high resolution transmission electron microscopy (HRTEM). The study was performed for free VCM, VCM-PS6 and untreated MRSA, where, the former and latter served as positive and negative controls, respectively. Briefly, MRSA suspension (5×10^5 CFU/mL) was incubated with free VCM (500 µg/mL) and VCM-PS6 containing 500 µg/mL of VCM, at 1:1 ratio separately for 4 h. The test samples were fixed onto the surface of copper grids followed by drying. The images were captured using JEOL HRTEM 2100 (brightfield, darkfield, STEM diffraction).

2.9. Statistical analysis

The results obtained were reported as mean ± standard deviation (SD) and the data analysis was performed using GraphPad Prism®5 (Graphpad Software Inc., USA). Bonferroni's Multiple Comparison Test and One-way ANOVA were used to analyse the data and the difference was considered significant when $p < 0.05$.

3. Results and discussion

3.1. Synthesis

The conjugation of OLA to the carboxylic groups of HA was confirmed by FTIR and ^{1}H NMR studies. The spectra included in the supplementary material shows the comparative FTIR and ^{1}H NMR spectra of free HA and HA-OLA conjugates. The changes that appeared in the infrared vibrational frequencies of HA chemical bonds, provided a preliminary confirmation of the grafting of OLA to HA. The parent HA was characterised by the presence of peaks at 1725 $cm^{-}1$ and 1648 $cm^{-}1$ in the FTIR spectra, which corresponded to the carbonyl groups of carboxylic acids and acetamide bonds, respectively. After the grafting of HA with OLA, the peak at 1648 $cm^{-}1$ was shifted to 1643 $cm^{-}1$. In addition, the intensity of the peak was increased, which was due to the increase in the number of amide bonds after the conjugation of OLA to HA. Both HA and HA-OLA conjugates contained broad peaks at ~3298 and sharp peaks at ~2923 $cm^{-}1$, which corresponded to OH and NH groups of amides respectively. These small shifts in bands were observed after the conjugation of OLA to HA. The results observed in FTIR were further verified by ^{1}H NMR studies. The appearance of new peaks at δ 0.903 and δ 1.30 in the ^{1}H NMR spectra of HA-OLA6 was attributed to the aliphatic protons of OLA, thus confirming the successful conjugation of OLA to HA.

3.2. MTT assay

Determining bio-safe dosages of novel materials is critical for any biomedical applications [33]. The *in vitro* cytotoxicity study demonstrated that both HA-OLA6 and HA-OLA8 displayed cell viability over 78% on HEK-293, HeLa and MCF-7, at all tested concentrations (Fig. 1A and B). The percentage cell viability of HA-OLA6 and HA-OLA8 ranged between 79.96–96.66%, 78.08–100.95% and 78.01–88.50% for HEK-293, HeLa and MCF-7, respectively, with no dose dependent toxicity observed at the tested concentrations. The percentage cell viability displayed on all tested cell-lines was above 75%, thus HA-OLA6 and HA-OLA8 can be considered as biologically safe and non-toxic to human cells [34].

3.3. Preparation of VCM loaded HA-OLA polymersomes

Self-assembled VCM loaded HA-OLA polymersomes were prepared

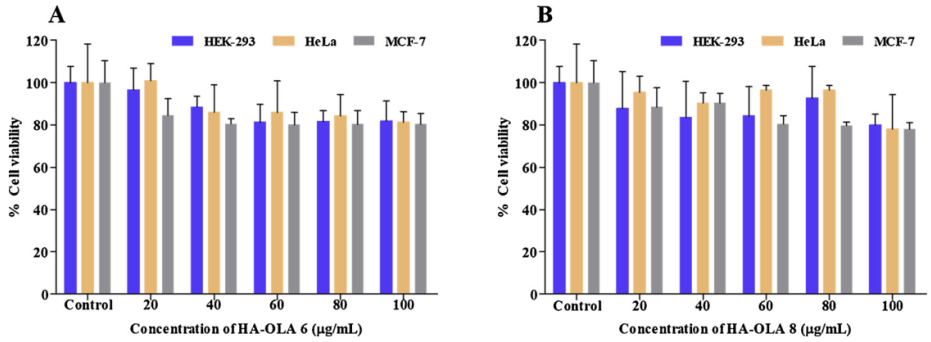

Fig. 1. *In vitro* cytotoxicity of A) HA-OLA6 and B) HA-OLA8 on HEK-293, HeLa and MCF-7 (n = 5).

using a simple probe ultrasonication technique without the use of any organic solvent, surfactant, stabilizer or emulsifier. HA and oleylamine serving as the hydrophilic backbone and grafted hydrophobic chains, respectively, could have influenced the self-assembly of amphiphilic HA-OLA, under aqueous conditions to form polymeric vesicles (polymersomes), thereby encapsulating VCM in hydrophilic cores. This green approach to formulate polymersomes may circumvent the toxic effects of surfactants and residual organic solvents [35].

Several VCM loaded polymersomes were prepared using both HA-OLA6 and HA-OLA8 by varying the amounts of polymer and drug to optimize in terms of size, PDI, ZP and %EE. A combination of 5 mg and 20 mg of VCM and HA-OLA 6, respectively, showed satisfactory results with respect to size, PDI, ZP and %EE (Table 1). The results obtained from DLS revealed that, VCM (5 mg) loaded HA-OLA6 (20 mg) polymersomes (VCM-PS6) had a mean particle diameter of 248.7 ± 3.08 nm with a narrow size distribution of 0.189 ± 0.01 and a negative ZP of -17.6 ± 0.6 mV. The %EE and DLC of VCM-PS6 were found be 43.12 ± 2.18% and 8.62 ± 0.91% respectively, which were comparable with the reports for other VCM encapsulated vesicles [36,37]. The polymersomes made up of HA-OLA8 were of smaller size compared to HA-OLA6 at all respective concentrations of polymer and drug. A similar trend was observed by Qui et.al, where, the diameter of micelles decreased with the increase in grafting of octadecylamine on HA [25]. Furthermore, polymersomes made up of HA-OLA8 displayed lower %EE compared to VCM-PS6 at all respective concentrations of polymer and drug (Supplementary material, Table S2). We assume that, smaller particle size and increased hydrophobicity in HA-OLA8, due to the presence of greater number of oleylamines might have reduced the encapsulation of hydrophilic VCM. Since, VCM-PS6 exhibited good results in terms of size and %EE compared to other formulations, it was therefore considered as the optimized formulation to perform other studies.

The surface morphology of VCM-PS6 was studied using TEM imaging. The images revealed a bilayered vesicular morphology with particles being spherical, and dispersed discretely and homogeneously (Fig. 2A). The polymersomes were found to be in the size range obtained with DLS (Fig. 2B).

The stability of nanoparticles in serum environment is important, as serum proteins can interact with them and may adversely affect *in vivo* efficacy [11]. The stability of polymersomes was investigated by measuring the change in their particle size as a function of time in the presence of a complete medium with FBS at 37 °C. As shown in Fig. 2C, the polymersomes were found to be stable after incubation in FBS for 72 h, with average diameter remaining almost the same on all three days with no significant difference ($p > 0.05$). The results indicate that the hydrophilic anionic shell present in HA-OLA6 polymersomes might have prevented the adsorption of serum proteins on polymersomes [25].

3.4. Differential scanning calorimetry (DSC)

DSC studies were performed to confirm the loading of VCM into HA-OLA6 polymersomes. The thermal behaviour of VCM, HA-OLA6, physical mixture of VCM and HA-OLA6 and lyophilised drug loaded formulation were studied (Fig. 3). As many chemical and physical transitions are associated with consumption or generation of heat, an abrupt change in the thermal behaviour may indicate a possible interaction between the excipients [38,39]. A broad endothermic peak was observed for free VCM at 129.96 °C, which displayed its thermal decomposition, while for HA-OLA6, a similar peak was noticed at 203.93 °C. Two separate endothermic peaks with slightly upward shifts were observed for VCM and HA-OLA6 mixture at 137.25 °C and 208.68 °C respectively, whereas, the thermogram of VCM loaded HA-OLA6 polymersomes (VCM-PS6) did not display any thermal peaks for neither VCM nor HA-OLA6. This disappearance of VCM suggested that the drug was encapsulated into the polymersomes in non-crystalline form [40].

3.5. In vitro drug release

The drug release behaviour of free VCM and VCM-PS6 were studied in PBS 7.4, and are represented in Fig. 4. The cumulative percentage release for free VCM and VCM from polymersomes at 12 h was 75% and 57%, respectively, displaying ˜22% of difference in the release pattern between free VCM and VCM in polymersomes, respectively. After 24 h, almost 90% of free VCM was released, whereas, it took 72 h for the

Table 1
Effect of various concentrations of VCM and HA-OLA6 on formulation optimization (n = 3).

VCM	HA-OLA6	Size (nm)	PDI	ZP	%EE
5	10	201.4 ± 3.25	0.196 ± 0.01	−20.4 ± 1.84	33.12 ± 2.11
5	20	248.7 ± 3.08	0.189 ± 0.01	−17.6 ± 0.61	43.12 ± 2.18
5	40	339.5 ± 3.37	0.222 ± 0.01	−18.8 ± 1.42	41.04 ± 1.85
10	10	203.7 ± 3.81	0.181 ± 0.01	−19.2 ± 0.89	27.68 ± 2.41
10	20	251.3 ± 1.21	0.202 ± 0.01	−18.4 ± 1.26	36.48 ± 2.06
10	40	360.9 ± 5.84	0.225 ± 0.01	−18.5 ± 1.11	38.34 ± 4.74

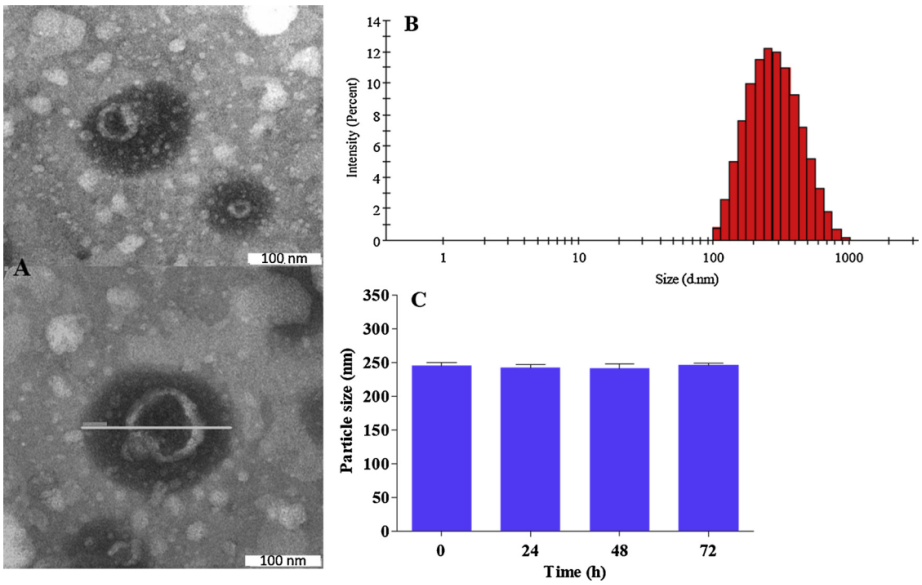

Fig. 2. A) TEM images of VCM-PS6 showing bilayered morphology. B) Size distribution of VCM-PS6 determined by DLS. C) Stability of HA-OLA6 polymersomes in 10% FBS (n = 3).

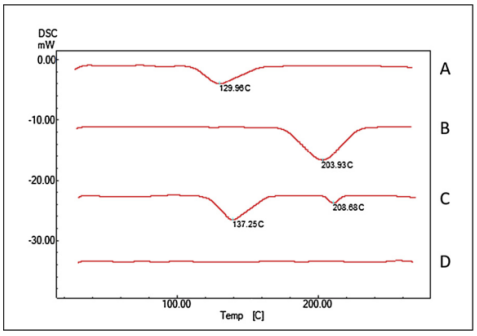

Fig. 3. Thermograms of (A) Free VCM; (B) HA-OLA6; (C) physical mixture of VCM and HA-OLA6 and (D) Lyophilized VCM-PS6.

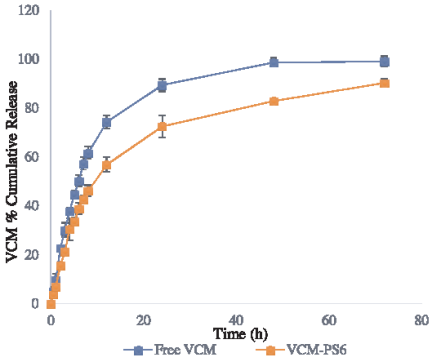

Fig. 4. *In vitro* drug release profiles of free VCM and VCM-PS6.

polymersomes to release same amount of drug. Although, the release profiles of free VCM and VCM from polymersomes were comparable at initial hours, a sustained drug release was observed with nano-formulation after 6 h. The initial quick release could have been governed by diffusion and greater concentration gradient of drug, whereas, sustained drug release might have been due to polymer erosion and degradation [41]. From these observations, it was evident that, polymersomes made from HA-OLA6 were able to release the encapsulated VCM in a sustained manner, compared to free drug. Considering, the ability of polymersomes to release VCM in a slow manner, this formulation could provide required lethal doses of encapsulated antibiotic in bacterial microenvironment for a prolonged period of time to facilitate improved and sustained antibacterial activity. Furthermore, this sustained release of VCM may also overcome the development of resistance.

Various mathematical models were used to understand the release kinetics of VCM from HA-OLA6 polymersomes (Table 2). Among the studied mathematical models, the release of VCM from polymersomes was found to fit in Weibull model with a higher co-relation coefficient of 0.994 and a lower root mean square error of 2.433. The '*n*' exponent (0.488), that was obtained from Korsmeyer-Peppas equation indicated that the release mechanism was anomalous or non-fickian transpot [42]. Apart from drug diffusion, polymer erosion and degradation may have significant roles in releasing VCM slowly from polymersomes. The MDT values calculated for the release of free VCM and VCM polymersomes were 9.76 and 15.06, respectively, indicating slower release of

Table 2
Various mathematical models for drug release from VCM-PS6.

Model	Equation	R^2	RMSE	Release exponent (*n*)
Zero order	$Q = k.\ t + Q_0$	0.2724	24.581	–
First order	$Q = Q_0.\ e^{kt}$	0.9579	5.9115	–
Higuchi	$Q = k.\ t^{½}$	0.9100	8.6468	–
Hixon-Crowell	$Q^{⅓} = kt + Q_0^{⅓}$	0.9045	8.9037	–
Korsmeyer-Peppas	$Q = k.\ t^n$	0.9460	6.2425	0.488
Weibull	$Q = 1\ exp - (t)^{a/b}]$	0.9940	2.4334	–

Table 3
MIC values of free VCM, free HA, HA-OLA6, HA-OLA8, VCM-PS6 and VCM-PS8.

Time (h)	24	48	72	24	48	72
	S. aureus (μg/mL)			MRSA (μg/mL)		
Free VCM	1.95	250	NA	7.8	NA	NA
Free HA	NA	NA	NA	NA	NA	NA
HA-OLA6	500	500	500	500	500	500
HA-OLA8	500	500	500	500	500	500
VCM-PS6	1.95	1.95	1.95	1.95	1.95	1.95
VCM-PS8	1.95	1.95	1.95	1.95	1.95	1.95

NA = No activity, n = 3.

VCM from polymersomes.

3.6. Antibacterial activity

3.6.1. In vitro antibacterial activity

The *in vitro* antibacterial studies were performed for free VCM, free HA, HA-OLA6 and optimized drug loaded formulation, *i.e.*, VCM-PS6 against *S. aureus* and MRSA (Table 3). Since OLA is an antibacterial enhancer, MIC values were determined for HA-OLA8 and VCM (5 mg) loaded HA-OLA8 (20 mg) polymersomes (VCM-PS8) as well. There was no antibacterial activity observed for free HA against the tested strains of *S. aureus* and MRSA. Interestingly, the novel amphiphilic polymers synthesized in this study, HA-OLA6 and HA-OLA8 displayed moderate antibacterial activities against both *S. aureus* and MRSA with MIC values of 500 μg/mL, over the studied period of 72 h. The MIC values for free VCM against *S. aureus* and MRSA were 1.95 and 7.8 μg/mL, respectively at 24 h. Although, the MIC values for VCM-PS6 and VCM-PS8 remained same as free VCM against *S. aureus*, enhanced activities were observed against MRSA with MIC values of 1.95 μg/mL, displaying 4-fold improvement. At 48 h, free VCM started to lose its potential antibacterial activity, displaying an increased MIC value (250 μg/mL) against *S. aureus* and complete bacterial growth against MRSA. At the end of day three, free VCM had no activity against both *S. aureus* and MRSA. In contrast, VCM-PS6 and VCM-PS8 retained the activity of VCM at 48 h and 72 h against both bacterial strains with MIC values (1.95 μg/mL), remaining same as day one. From these results, both VCM-PS6 and VCM-PS8 showed better activity than free VCM against the tested bacterial strains. The nano-formulations preserved the antibacterial potency of VCM for three days against both strains, while free VCM lost its activity after 24 h. The improved and sustained antibacterial activity of VCM loaded polymersomes can be attributed to slow and controlled release of VCM in bacterial environment over a prolonged period of time. This sustained antibacterial potential of VCM-PS6 and VCM-PS8 can efficiently control infection with reduced frequency of dose and adverse effects. Although, HA-OLA6 and HA-OLA8 were not as potent as VCM, they were able to improve the antibacterial activity of VCM against both *S. aureus* and MRSA. Therefore, the grafted polymers synthesized in this study can make promising nano-carriers to deliver antibiotics and treat MRSA infections.

To understand the combined effect of HA-OLA6 and VCM in VCM loaded HA-OLA6 polymersomes (VCM-PS6) against *S. aureus* and MRSA, FIC values were calculated. As free VCM had lost its potential activity at the end of 24 h, FIC values for both free VCM and free HA-OLA6 were determined at 24 h. The calculated FIC values for VCM-PS6 were found to be 1.01 and 0.25 against *S. aureus* and MRSA, indicating that there was indifference and synergistic antibacterial activity

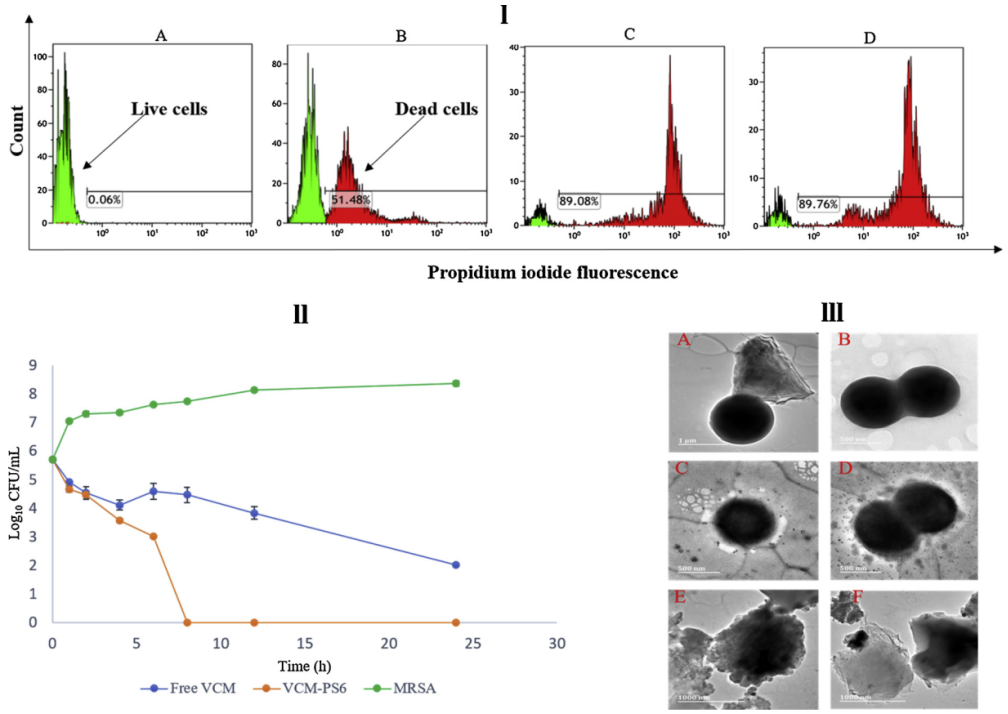

Fig. 5. (I) MRSA cell counts *vs* PI uptake histogram where, A represents untreated MRSA (live cells); B, C and D represents percentage of dead cells in the population after incubation with free VCM at MIC of 1.95 μg/mL, free VCM at its MIC (7.8 μg/mL) and VCM-PS6 at its MIC (1.95 μg/mL) respectively; (II) Bacterial killing kinetics of MRSA exposed to 5 x MIC of free VCM, VCM-PS6 and sterile water; (III) HRTEM images showing morphological differences of untreated MRSA (A and B); VCM treated MRSA (C and D) and VCM-PS6 treated MRSA (E and F).

respectively (Table S3, supplementary material).

3.6.2. Flow cytometry bacterial cell viability

The rapid cell viability of MRSA cells was analysed using a Flow cytometry technique [29]. The MRSA cells were incubated with free VCM and VCM-PS6. The bacterial cells, upon incubation with antibiotics, change their morphology and cell-division cycle, which can be measured using special dyes. PI, a cell-wall non-permeant dye and Syto9, a non-selective cell wall permeant dye were used to detect dead and live cells, respectively [43]. Kaluza-2.1 (Beckman Coulter USA) flow cytometer software was used to analyse the data. Two gates were created to differentiate viable cells (green) and dead cells (red). VCM acts by interfering with the cell wall integrity, which enables the uptake of PI in bacterial cells. The PI inside the cell, intercalate the DNA showing a shift in PI fluorescence, indicating bacterial cell death. Whilst, untreated MRSA showed ~100% viable cells, the bacteria treated with free VCM and VCM-PS6 showed a shift in PI fluorescence, where two distinct populations of live and dead bacteria were observed (Fig. 51). The free VCM (Fig. 51 C) and VCM-PS6 (Fig. 51 D) showed 88.7 ± 1.21% and 89.2 ± 0.60% dead MRSA cells in the population, after treating at their MICs of 7.8 and 1.95 µg/mL respectively. However, the MRSA treated with free VCM at a concentration same as of MIC of VCM-PS6 (1.95 µg/mL), had reduced killing percentage of bacterial cells, *i.e.*, 51.22 ± 1.21% ($p < 0.05$) (Fig. 51 B). VCM-PS6 proved to be more efficient than free VCM at concentration of 1.95 µg/mL, showing 1.8-fold more dead cells. These results further supported the antibacterial superiority of VCM-PS6.

3.6.3. Bacterial killing kinetics

Time-kill curve for free VCM and VCM-PS6 at 5 x MIC against MRSA is presented in Fig. 5II. Rapid bactericidal activity was observed for VCM-PS6 after eight hours of exposure, displaying 3-log reduction (99.9% clearance). In contrast, free VCM displayed slow killing rate (2-log reduction) after 24 h treatment. A complete bacterial inhibition was not observed for free VCM over the studied period of 24 h. It was worth noting that, VCM-PS6 at four times lower concentration than free VCM, achieved bactericidal activity within eight hours of treatment. This may lead to rapid elimination of bacteria, thus reducing the dose and course of treatment.

3.6.4. Bacterial cell morphology

The ability of free VCM and VCM-PS6 to disrupt bacterial cell membrane was determined by assessing the morphological changes/differences induced in MRSA cells after four hours of treatment. The HRTEM images showed that, untreated MRSA, which was used as negative control exhibited smooth and integrated cell membrane with intact cocci (Fig. 5III A and III B). The MRSA cells that were treated with VCM alone displayed a deformed and impaired cell membrane after four hours (Fig. 5III C and III D). In contrast, after same incubation period, the MRSA cells treated with VCM-PS6 were damaged and ruptured intensely (Fig. 5III E and III F). The closer view of VCM-PS6 treated cells revealed that, the drug loaded formulation had a strong impact on the integrity of MRSA cell membrane. Furthermore, the membrane and shape of cocci was completely altered with distinguished perforations and leakage of cytosol (Fig. 5III E and III F). VCM-PS6 were found to be more potent than free VCM in disrupting MRSA membrane. These results corroborate well with *in vitro* antibacterial activity, flow cytometry analysis and bacterial killing kinetics.

4. Conclusions

Recently, there has been a surge of interest to develop novel drug carrier systems for antibiotic delivery. In this study, conjugates of HA and OLA were synthesized depending on various percentage of conjugation. The novel HA-OLA conjugates were proven to be bio-safe on the cell lines tested and exhibited moderate antibacterial activity against *S. aureus* and MRSA. VCM loaded HA-OLA6 polymersomes (VCM-PS6) were dispersed in nano-sized range with particle sizes < 250 nm and entrapment efficiency of 43.12 ± 2.18%. The polymersomes exhibited slow and sustained release for VCM throughout the studied period of 72 h. The *in vitro* antibacterial activity against MRSA revealed that, VCM-PS6 had 4-fold enhanced activity, compared to free VCM. Furthermore, synergism was observed for VCM and HA-OLA6 against MRSA. The antibacterial studies using flow cytometry revealed that, VCM-PS6 showed 1.8-fold more dead cells of MRSA, compared to free VCM, when samples were treated at MIC of 1.95 µg/mL. Bacterial cell morphology showed that, VCM loaded polymersomes had a stronger impact on MRSA membrane disruption compared to free VCM. These results indicate that, VCM-PS6 was more potent than free VCM against MRSA in all performed antibacterial studies. In summary, these findings suggest that, HA-OLA conjugates can make promising antibiotic nano-carriers to combat multi-drug resistant bacterial strains. In addition, these novel conjugates can be further explored to encapsulate other classes of pharmacologically active agents to manage various disease conditions effectively.

Declaration of Competing Interest

The authors declare no conflict of interest.

Acknowledgments

The authors acknowledge the College of Health Sciences, University of KwaZulu-Natal (UKZN) and UKZN Nanotechnology Platform, National Research Foundation of South Africa (Grant No. 106040) and Medical Research Council of South Africa for financial support. We acknowledge Microscopy and Microanalysis Unit and Department of Human Physiology at UKZN for use of facilities and Ms. Charlotte Ramadhin for proof reading.

Appendix A. Supplementary data

Supplementary material related to this article can be found, in the online version, at doi:https://doi.org/10.1016/j.colsurfb.2019.110388.

References

[1] T. Foster, Staphylococcus, in: S. Baron (Ed.), Medical Microbiology, 1996.
[2] D.C. Kaur, S.S. Chate, Study of antibiotic resistance pattern in methicillin resistant Staphylococcus aureus with special reference to newer antibiotic, J. Glob. Infect. Dis. 7 (2015) 78.
[3] A. Gupta, S. Mumtaz, C.-H. Li, I. Hussain, V.M. Rotello, Combatting antibiotic-resistant bacteria using nanomaterials, Chem. Soc. Rev. 48 (2019) 415–427.
[4] L. Zhang, F. Gu, J. Chan, A. Wang, R. Langer, O. Farokhzad, Nanoparticles in medicine: therapeutic applications and developments, Clin. Pharmacol. Ther. 83 (2008) 761–769.
[5] M.-H. Xiong, Y. Bao, X.-Z. Yang, Y.-H. Zhu, J. Wang, Delivery of antibiotics with polymeric particles, Adv. Drug Deliv. Rev. 78 (2014) 63–76.
[6] A.J. Huh, Y.J. Kwon, "Nanoantibiotics": a new paradigm for treating infectious diseases using nanomaterials in the antibiotics resistant era, J. Control. Release 156 (2011) 128–145.
[7] W. Gao, S. Thamphiwatana, P. Angsantikul, L. Zhang, Nanoparticle approaches against bacterial infections, Wiley Interdiscip. Rev. Nanomed. Nanobiotechnol. 6 (2014) 532–547.
[8] H. Pinto-Alphandary, A. Andremont, P. Couvreur, Targeted delivery of antibiotics using liposomes and nanoparticles: research and applications, Int. J. Antimicrob. Agents 13 (2000) 155–168.
[9] W.S. Cheow, K. Hadinoto, Factors affecting drug encapsulation and stability of lipid–polymer hybrid nanoparticles, Colloids Surf. B Biointerfaces 85 (2011) 214–220.
[10] U.S. Toti, B.R. Guru, M. Hali, C.M. McPharlin, S.M. Wykes, J. Panyam, J.A. Whittum-Hudson, Targeted delivery of antibiotics to intracellular chlamydial infections using PLGA nanoparticles, Biomaterials 32 (2011) 6606–6613.
[11] L. Qiu, Z. Li, M. Qiao, M. Long, M. Wang, X. Zhang, C. Tian, D. Chen, Self-assembled pH-responsive hyaluronic acid–g-poly (l-histidine) copolymer micelles for targeted intracellular delivery of doxorubicin, Acta Biomater. 10 (2014) 2024–2035.
[12] J.M. Wickens, H.O. Alsaab, P. Kesharwani, K. Bhise, M.C.I.M. Amin, R.K. Tekade, U. Gupta, A.K. Iyer, Recent advances in hyaluronic acid-decorated nanocarriers for targeted cancer therapy, Drug Discov. Today 22 (2017) 665–680.

[13] P. Pirnazar, L. Wolinsky, S. Nachnani, S. Haake, A. Pilloni, G.W. Bernard, Bacteriostatic effects of hyaluronic acid, J. Periodontol. 70 (1999) 370–374.
[14] L. Drago, L. Cappelletti, E. De Vecchi, L. Pignataro, S. Torretta, R. Mattina, Antiadhesive and antibiofilm activity of hyaluronic acid against bacteria responsible for respiratory tract infections, APMIS 122 (2014) 1013–1019.
[15] B.S. Nagoba, N.M. Suryawanshi, B. Wadher, S. Selkar, Acidic environment and wound healing: a review, Wounds 27 (2015) 5–11.
[16] J. Zhu, F. Li, X. Wang, J. Yu, D. Wu, Hyaluronic acid and polyethylene glycol hybrid hydrogel encapsulating nanogel with hemostasis and sustainable antibacterial property for wound healing, ACS Appl. Mater. Interfaces 10 (2018) 13304–13316.
[17] A. Rösler, G.W. Vandermeulen, H.-A. Klok, Advanced drug delivery devices via self-assembly of amphiphilic block copolymers, Adv. Drug Deliv. Rev. 64 (2012) 270–279.
[18] J.-P. Douliez, C. Gaillard, Self-assembly of fatty acids: from foams to protocell vesicles, New J. Chem. 38 (2014) 5142–5148.
[19] A. Desbois, K. Lawlor, Antibacterial activity of long-chain polyunsaturated fatty acids against Propionibacterium acnes and Staphylococcus aureus, Mar. Drugs 11 (2013) 4544–4557.
[20] T. Kitahara, N. Koyama, J. Matsuda, Y. Aoyama, Y. Hirakata, S. Kamihira, S. Kohno, M. Nakashima, H. Sasaki, Antimicrobial activity of saturated fatty acids and fatty amines against methicillin-resistant Staphylococcus aureus, Biol. Pharm. Bull. 27 (2004) 1321–1326.
[21] D.R. Sikwal, R.S. Kalhapure, S. Rambharose, S. Vepuri, M. Soliman, C. Mocktar, T. Govender, Polyelectrolyte complex of vancomycin as a nanoantibiotic: preparation, in vitro and in silico studies, Mater. Sci. Eng. C 63 (2016) 489–498.
[22] R.S. Kalhapure, M. Jadhav, S. Rambharose, C. Mocktar, S. Singh, J. Renukuntla, T. Govender, pH-responsive chitosan nanoparticles from a novel twin-chain anionic amphiphile for controlled and targeted delivery of vancomycin, Colloids Surf. B Biointerfaces 158 (2017) 650–657.
[23] D. Hassan, C.A. Omolo, R. Gannimani, A.Y. Waddad, C. Mocktar, S. Rambharose, N. Agrawal, T. Govender, Delivery of novel vancomycin nanoplexes for combating methicillin resistant staphylococcus aureus (MRSA) infections, Int. J. Pharm. (2019).
[24] C.A. Omolo, R.S. Kalhapure, N. Agrawal, S. Rambharose, C. Mocktar, T. Govender, Formulation and molecular dynamics simulations of a fusidic acid nanosuspension for simultaneously enhancing solubility and antibacterial activity, Mol. Pharm. 15 (2018) 3512–3526.
[25] L. Qiu, M. Zhu, Y. Huang, K. Gong, J. Chen, Mechanisms of cellular uptake with hyaluronic acid—octadecylamine micelles as drug delivery nanocarriers, RSC Adv. 6 (2016) 39896–39902.
[26] P. Walvekar, R. Gannimani, S. Rambharose, C. Mocktar, T. Govender, Fatty acid conjugated pyridinium cationic amphiphiles as antibacterial agents and self-assembling nano carriers, Chem. Phys. Lipids 214 (2018) 1–10.
[27] S.J. Sonawane, R.S. Kalhapure, S. Rambharose, C. Mocktar, S.B. Vepuri, M. Soliman, T. Govender, Ultra-small lipid-dendrimer hybrid nanoparticles as a promising strategy for antibiotic delivery: in vitro and in silico studies, Int. J. Pharm. 504 (2016) 1–10.
[28] M. Balouiri, M. Sadiki, S.K. Ibnsouda, Methods for in vitro evaluating antimicrobial activity: a review, J. Pharm. Anal. 6 (2016) 71–79.
[29] N.M. O'Brien-Simpson, N. Pantarat, T.J. Attard, K.A. Walsh, E.C. Reynolds, A Rapid and Quantitative flow cytometry method for the analysis of membrane disruptive antimicrobial activity, PLoS One 11 (2016) e0151694.
[30] A.R.C. Duarte, M.S. Costa, A.L. Simplício, M.M. Cardoso, C.M. Duarte, Preparation of controlled release microspheres using supercritical fluid technology for delivery of anti-inflammatory drugs, Int. J. Pharm. 308 (2006) 168–174.
[31] S. Renggli, W. Keck, U. Jenal, D. Ritz, Role of autofluorescence in flow cytometric analysis of Escherichia coli treated with bactericidal antibiotics, J. Bacteriol. 195 (2013) 4067–4073.
[32] P. Vaudaux, A. Gjinovci, M. Bento, D. Li, J. Schrenzel, D.P. Lew, Intensive therapy with ceftobiprole medocaril of experimental foreign-body infection by methicillin-resistant Staphylococcus aureus, Antimicrob. Agents Chemother. 49 (2005) 3789–3793.
[33] S. Choksakulnimitr, S. Masuda, H. Tokuda, Y. Takakura, M. Hashida, In vitro cytotoxicity of macromolecules in different cell culture systems, J. Control. Release 34 (1995) 233–241.
[34] X. Cao, C. Cheng, Y. Ma, C. Zhao, Preparation of silver nanoparticles with antimicrobial activities and the researches of their biocompatibilities, J. Mater. Sci. Mater. Med. 21 (2010) 2861–2868.
[35] I. Hussain, N. Singh, A. Singh, H. Singh, S. Singh, Green synthesis of nanoparticles and its potential application, Biotechnol. Lett. 38 (2016) 545–560.
[36] J. Liu, Z. Wang, F. Li, J. Gao, L. Wang, G. Huang, Liposomes for systematic delivery of vancomycin hydrochloride to decrease nephrotoxicity: characterization and evaluation, Asian J. Pharm 10 (2015) 212–222.
[37] M. Jadhav, R.S. Kalhapure, S. Rambharose, C. Mocktar, S. Singh, T. Kodama, T. Govender, Novel lipids with three C18-fatty acid chains and an amino acid head group for pH-responsive and sustained antibiotic delivery, Chem. Phys. Lipids 212 (2018) 12–25.
[38] G. Höhne, W.F. Hemminger, H.-J. Flammersheim, Differential Scanning Calorimetry, Springer Science & Business Media, 2013.
[39] G. Ceschel, R. Badiello, C. Ronchi, P. Maffei, Degradation of components in drug formulations: a comparison between HPLC and DSC methods, J. Pharm. Biomed. Anal. 32 (2003) 1067–1072.
[40] C.G. Pupe, M. Villardi, C.R. Rodrigues, H.V.A. Rocha, L.C. Maia, V.P. de Sousa, L.M. Cabral, Preparation and evaluation of antimicrobial activity of nanosystems for the control of oral pathogens Streptococcus mutans and Candida albicans, Int. J. Nanomedicine 6 (2011) 2581.
[41] J. Ritsema, E. Herschberg, S. Borgos, C. Løvmo, R. Schmid, Y. Te Welscher, G. Storm, C.F. van Nostrum, Relationship between polarities of antibiotic and polymer matrix on nanoparticle formulations based on aliphatic polyesters, Int. J. Pharm. 548 (2018) 730–739.
[42] P.L. Ritger, N.A. Peppas, A simple equation for description of solute release I. Fickian and non-fickian release from non-swellable devices in the form of slabs, spheres, cylinders or discs, J. Control. Release 5 (1987) 23–36.
[43] M. Fittipaldi, A. Nocker, F. Codony, Progress in understanding preferential detection of live cells using viability dyes in combination with DNA amplification, J. Microbiol. Methods 91 (2012) 276–289.

Proof of acceptance for Co-authored paper 2

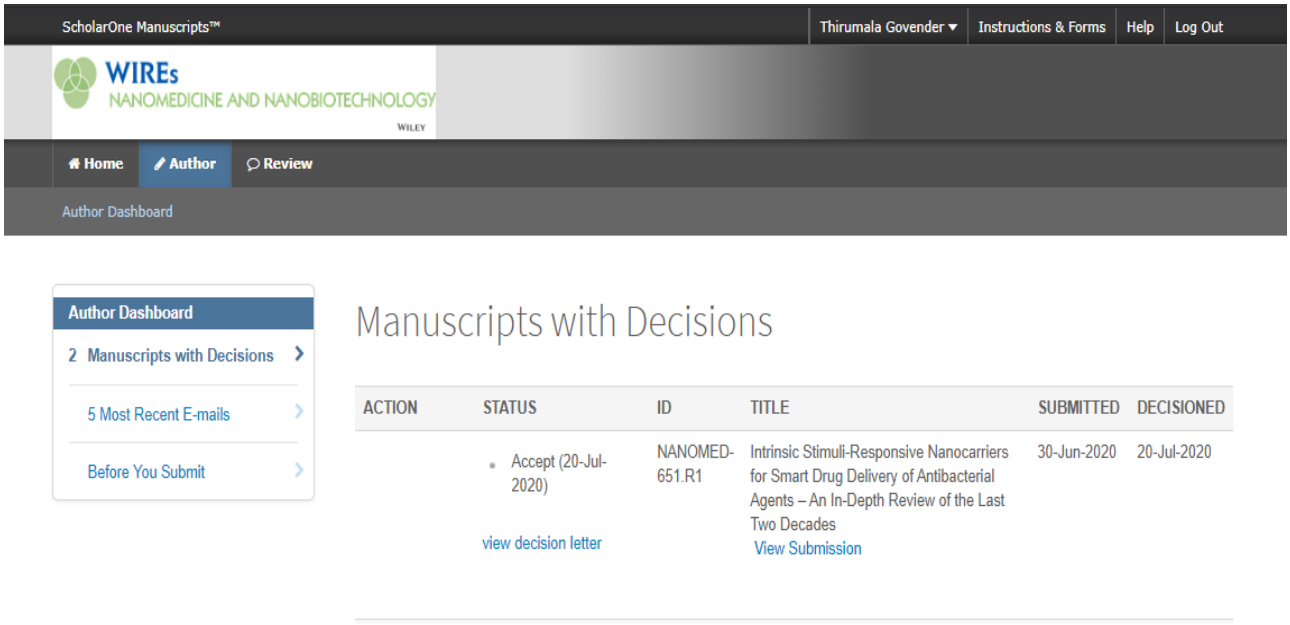

Appendix V

Poster for ICONAN 2019 conference, Munich, Germany

UNIVERSITY OF KWAZULU-NATAL
INYUVESI YAKWAZULU-NATALI

SUPRAMOLECULAR AMPHIPHILE OF BETA-CYCLODEXTRIN AND OLEYLAMINE TO ENHANCE VANCOMYCIN DELIVERY

*Mohammed Salih, Calvin A. Omolo, Nikhil Agrawal, Pavan Walvekar, Ayman Y. Waddad, Chunderika Mocktar, Thirumala Govender**

Discipline of Pharmaceutical Sciences, College of Health Sciences, University of KwaZulu-Natal, Private Bag X54001, Durban, South Africa

Introduction

- Emergence of Multi drug resistant (MDR) bacteria is a major reason for increased mortality.
- Among drug resistance strains, Methicillin resistant *Staphylococcus aureus* (MRSA) continue to threaten the potency of current antibiotics (1).
- New strategies for the design of novel nano-systems are required to improve antibiotic therapy.
- Nano delivery systems (liposomes, solid lipid nanoparticles, polymersomes, etc.) have shown to improve the activity of antibiotics due to their advantages such as, targeted drug delivery, sustained release and improved therapeutic efficacy (2).
- Cyclodextrins (CDs) are cyclic oligosaccharides with a hydrophobic cavity that can act as a host for many micro/macro molecules. β-CD (BCD) has been extensively studied to prepare various drug loaded nano-structures (3).
- Oleylamine (OLA) is a long hydrophobic chain fatty alkyl amine which has been used in the preparation of various nano-materials due to its biodegradability and easy availability (4).
- In this work, we designed a new sugar-based amphiphile derivative from BCD head and long C-18 carbon chain with a terminal amine (OLA) using green chemistry. This novel amphiphile can be used to prepare an antibiotic loaded nano-delivery system to combat bacterial infections.

Aims and Objectives

Aims:

- To prepare vancomycin (VCM) loaded nano-vesicles using BCD-OLA, a novel supramolecular complex formed by noncovalent bonding.
- To characterize BCD-OLA amphiphile in terms of *in vitro* physicochemical and antibacterial properties.

Objectives

- To prepare and characterize novel supramolecular complex amphiphile from BCD-OLA.
- To explore the potential efficacy of the newly developed VCM loaded BCD-OLA nano-vesicles against SA & MRSA.

Methods

Preparation and Characterization of VCM loaded BCD-OLA nano-vesicles

- Suspension method was used to prepare the inclusion complexes.
- Molecular Dynamic (MD) simulation was performed to determine the mechanism of complexation of BCD and OLA.
- DSC, 1H NMR, 2D NMR NOESY spectrum and FT-IR were used to characterize the complex.
- MTT assay was performed to determine the bio-safety of BCD-OLA.
- Self –assembly in water was used to formulate the Nano system.
- *In vitro* drug release study was performed using dialysis bag method.
- Size, PDI and ZP of assembled nano-vesicles were measured using dynamic light scattering technique using Zetasizer.
- Ultrafiltration method was used to determine entrapment efficiency (EE%).
- TEM was used to study the Morphology of assembled nano-vesicles.
- Broth dilution method was used to determine the MIC of VCM loaded BCD-OLA nano-vesicles against SA and MRSA.
- *In vitro* intracellular antibacterial activity of BCD-OLA was evaluated on HEK-293 and THP1 cell lines.

Results and Discussion

Molecular Dynamic Simulation

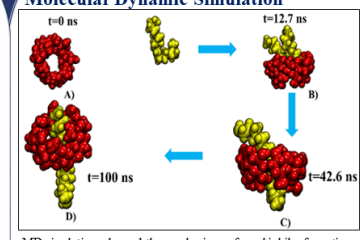

MD simulation showed the mechanism of amphiphile formation through hydrophobic interactions between BCD and OLA.

In vitro Cytotoxicity

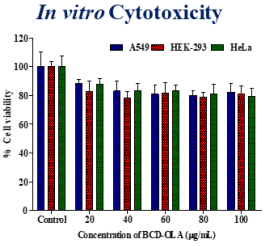

MTT assays showed a cell viability of 75-100% confirming the nontoxic nature of BCD-OLA complex.

Size, PDI, ZP and EE% of VCM loaded BCD-OLA nano-vesicles

VCM : BCD-OLA	Size (nm)	PDI	ZP (mV)	EE%
Only BCD-OLA (blank)	104.6 ± 0.6	0.251 ± 0.01	45 ± 0.95	-
1 : 1	123.3 ± 10.5	0.211 ± 0.04	25.6 ± 1.5	31.0 ± 1.0
1 : 3	125.1 ± 8.3	0.231 ± 0.05	19.3 ± 9.2	40.2 ± 4.5
1 : 6	210.9 ± 50	0.433 ± 0.08	28.5 ± 6.0	51.6 ± 2.3

Surface Morphology

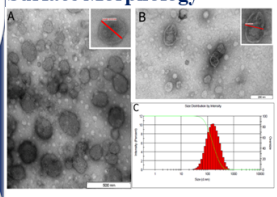

TEM images showed the self-assembled structures to be vesicles

In Vitro Release study

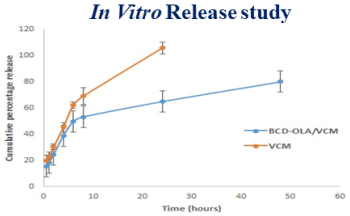

Drug release from nano-vesicles was sustained, with 80 % of VCM released over a period of 48 h.

In Vitro Antimicrobial Activity (MIC)

Time in hours	24	48	72	24	48	72
Material	SA (MIC µg/ml)			MRSA (MIC µg/ml)		
Bare VCM	3.90	3.90	N/A	31.25	31.25	N/A
(VCM - BCD-OLA)	1.95	3.90	3.90	7.81	7.81	7.81
BCD-OLA	93.75	187.5	187.5	93.75	187.5	187.5

VCM-BCD-OLA had 2 and 4-fold lower MIC against SA and MRSA respectively compared to the free VCM.

Bacterial killing kinetics

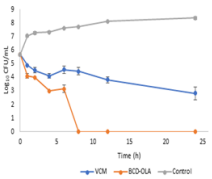

VCM loaded BCD-OLA nano-vesicles exhibited faster bacterial killing.

Bacterial membrane disruption

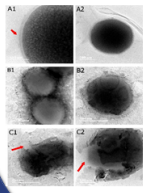

From HRTEM images: BCD-OLA loaded nano-vesicles showed cracked and disrupted membrane and released cytoplasmic materials in compare to bare VCM.

In Vitro Intracellular Activity

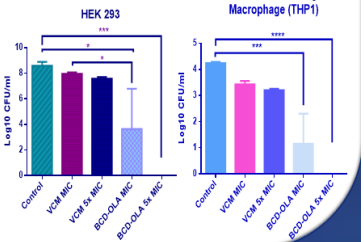

- BCD-OLA at 5x the MIC, eradicated all intracellular infections in both HEK-293 and TPH1 cell lines.
- The nan system had 459-fold reduction of intracellular bacteria from the HEK-293 cell, and 8-fold reduction in infected macrophages (THP1) compared to free VCM.

Conclusion

- These findings confirmed the potential of the BCD-OLA complex as a promising, biosafe, effective nanocarrier for antibiotic delivery to combat bacterial resistance to antibiotics, thus encouraging its application as a nanocarrier for delivery of other antibiotic classes.

REFERENCES & ACKNOWLEDGMENT

References

1- Magill, S.S., et al., Multistate point-prevalence survey of health care-associated infections. N Engl J Med, 2014. 370(13): p. 1198-208.
2- Xu, X., et al., Cancer nanomedicine: from targeted delivery to combination therapy. Trends Mol Med., 2015. 21(4): p. 223-232.
3- Martin, V.I., et al., Host-guest interactions between cyclodextrins and surfactants with functional groups at the end of the hydrophobic tail. J. Colloid Interface Sci., 2017. 491: p. 336-348..
4- Mourdikoudis S, Liz-Marzán LM. Oleylamine in nanoparticle synthesis. Chemistry of Materials. 2013 Feb 27;25(9):1465-76.

Acknowledgements

- **UKZN Nanotechnology Platform, CHS, CAES.**
- **NRF, MRC.**
- **NDDU research group members**

Appendix VI

UNIVERSITY OF KWAZULU-NATAL
INYUVESI YAKWAZULU-NATALI

15 April 2019

Dr Ayman Waddad (60072)
School of Health Sciences
Westville Campus

Dear Dr Waddad,

Protocol reference number: AREC/104/015PD
Project title: *In vivo* antibacterial activity of antimicrobial based nanoantibiotic formulations in BALB/c mice

Full Approval – Renewal Application

With regards to your renewal application received on 05 November 2018 and your response on 20 March 2019 to our letter of 05 November 2019. The documents submitted have been accepted by the Animal Research Ethics Committee and **FULL APPROVAL** for the protocol has been granted with the following conditions:

Please note: Any Veterinary and Para-Veterinary procedures must be conducted by a SAVC registered VET or SAVC authorized person.

Any alteration/s to the approved research protocol, i.e Title of Project, Location of the Study, Research Approach and Methods must be reviewed and approved through the amendment/modification prior to its implementation. In case you have further queries, please quote the above reference number.

Please note: Research data should be securely stored in the discipline/department for a period of 5 years.

The ethical clearance certificate is only valid for a period of one year from the date of issue. Renewal for the study must be applied for before 15 April 2020.

Attached to the Approval letter is a template of the Progress Report that is required at the end of the study, or when applying for Renewal (whichever comes first). An Adverse Event Reporting form has also been attached in the event of any unanticipated event involving the animals' health / wellbeing.

I take this opportunity of wishing you everything of the best with your study.

Yours faithfully

.....
Dr Sanil D Singh, PhD
Acting Chair: Animal Research Ethics Committee

/ms

cc Supervisor: Professor Thirumala Govender
Cc Academic Leader Research: Dr Brenda de Gama
Cc Registrar: Mr Simon Mokoena
Cc BRU – Dr Linda Bester

Animal Research Ethics Committee (AREC)
Ms Mariette Snyman (Administrator)
Westville Campus, Govan Mbeki Building
Postal Address: Private Bag X54001, Durban 4000
Telephone: +27 (0) 31 260 8350 **Facsimile:** +27 (0) 31 260 4609 **Email:** animalethics@ukzn.ac.za
Website: http://research.ukzn.ac.za/Research-Ethics/Animal-Ethics.aspx

1910 - 2010
100 YEARS OF ACADEMIC EXCELLENCE
Founding Campuses: Edgewood Howard College Medical School Pietermaritzburg Westville